Phase Equilibria of the Pd-rich Fe-Pd Eutectoid Region:

Shockley's Controversial L1' Phase and Order to Order Transformations

---

A Dissertation

Presented to
the faculty of the School of Engineering and Applied Science University of Virginia

---

In partial fulfillment
of the requirements for the degree

Doctor of Philosophy by

Adrian Savovici

December 2023

Table of Contents

Acknowledgements

First and foremost I'd like to thank my advisor Prof. Jerrold Floro, who has the rare combination of both precision and passion. I'm grateful he took a chance on me and helped me see this serious undertaking to completion. His openness to impromptu scientific conversations allowed me to 'think aloud' many of the problems tackled in this dissertation.

The countless hours spent discussing science with Prof.'s Soffa and Floro over pizza and soda were in no doubt the most edifying part of this journey. I am forever grateful for both the sage advice and gentle nudges these gentlemen and scholars have had on my education.

I'd like to thank my committee members, Prof. Bi-Cheng Zhou and Prof. Sean Agnew, for their support. Prof. Bi-Cheng Zhou has been particularly helpful to me, again allowing me to make a make a fool of myself as I tried to understand his work. I'd also like to thank Prof. Andreas Beling who agreed to sit in on this dissertation defense and lend his time and ear to this work.

Lastly, I cannot say enough *thank yous* to my family, and friends who have substituted for family during these last few years. I'm particularly indebted to the 'Sandwich Science Squad' who regularly discussed the more philosophical points of life and science over a warm lunch. The many pizza parties and warm teas gave greater comfort than imaginable to a weary soul during this journey. For those and many other kind gestures and evenings, I am forever grateful.

“Science, my lad, is made up of mistakes,
but they are mistakes which it is useful to make,
because they lead us little by little to the truth.”

Journey to the Center of the Earth

Jules Verne

Chapter 1. Introduction & Background

This chapter will begin at the most general levels before progressing to Fe-Pd specifics. A history of ordering and phase stability in FCC substitution alloys will be given, followed by an explanation of recent computational results. Ordering and microstructural development of $L1_0$ will be explained, followed by a brief survey of Fe-Pd analogue systems (Fe-Pt, Co-Pt). This chapter also covers an introduction to magnetism and cubic→cubic + tetragonal decomposition.

Ordering in alloys was first hypothesized in 1919 by Tamman[1]. Subsequent work by Bain[2] in 1923 showed the existence of ordering with X-ray diffraction. Shortly thereafter, CuAu[3], Fe_3Al[4], and CuZn[5] ordered compounds were all investigated. These early results spurred the burgeoning field of order/disorder in alloys. Although X-ray techniques afforded crystallographic information, in-depth microstructural analysis was lacking, as the electron microscope was still in its infancy. Only in 1958, with work done by Ogawa, Watanabe and Komodoa[6] were anti-phase boundaries first observed in a microscope. In quick succession, analysis of stacking faults and dislocations were investigated by Marckinowski[7]. Researchers were driven to understand and document the transformation pathways and crystallographic underpinnings of these order-disorder transformations, which were generally studied to exploit their material (ferromagnetic, ferroelectric, hardness) properties. It is with the same intrepid spirit of these early scientists that we present the work done on the $L1_0 + L1_2$ Fe-Pd eutectoid region.

1.1. Research Goals

Despite nearly a century's worth of study in the Fe-Pd system (equiatomic $L1_0$ was first identified by X-ray methods in 1938[8)], no explicit investigation of the Pd-rich eutectoid region has ever been undertaken.

The research contained within these chapters attempts to answer and explain several key things:

- What phases are in equilibria in/near the Pd-rich Fe-Pd eutectoid region?
- What morphologies do these different two-phase equilibria present in? Can we properly characterize them?
- Can we identify the L1' phase? What is its microstructure? What stabilizes it?
- Can we identify an order/disorder boundary for L1' ?
- What magnetic properties can be ascribable to the phases / morphologies present?
- How can we explain the *order* → *order* + *order* transformation observed for two-phase samples?

1.2. Order – Disorder Transformations

The transformation from disordered to ordered structures below a critical temperature is considered a hallmark of cooperative phenomena[9]. Broadly speaking there are two types of transformations, which are distinguished on the basis of thermodynamics. First order transformations exist, where the derivative of the free energy G, with respect to T and P are discontinuous at a critical temperature T_C, and 2nd/Higher order (in the Ehrenfest sense) transformations for which $(\frac{\mathrm{dG}}{\mathrm{dT}})_P = -S$, and $(\frac{\mathrm{dG}}{\mathrm{dP}})_T = V$ are continuous at T_C. First order transformations involve a latent heat of transformation, where as second-order (or higher) transformations rigorously do not. For a first order transformation, as the chemical potential is varied, the relative amounts of the two phases change while the temperature remains constant, where the respective fractions of the different phases are determined by the lever-rule. However, for a second-order (or higher) transformation, there is no such partitioning into disorder & ordered regions: the transformation can be described as being '*large in extent but small in degree'*.

The distinction between these type of transformations (denoted as 1st/2nd order above) was first discussed by Gibbs in 1875[10] when he discussed changes in what is commonly regarded as an order parameter in today's parlance. An order parameter can be used to measure changes in the difference in composition, atomic order, or magnetization (for example) within a phase as progression towards an entirely new phase is made[10]. Schematic order parameter vs temperature plots are given in Figure 1.1, where a clear distinction between discontinuous (Fig. 1.1a, '1st order') vs continuous (Fig. 1.1b, '2nd/higher order) transformations can be made. In Fig. 1.1a, a large fluctuation in the order parameter is observed, showing a 'discontinuity' at the critical temperature.

In Fig. 1.1b however, infinitesimal changes in the order parameter occur, such that the transformation continues ‘continuously’. These simple schematics articulate the fundamental differences between these different types of transformations. More rigorously however, these type of transformations differ significantly in their: thermodynamic, kinetic, and microstructural features[10]. Thermodynamic functions differ between the types of transformations, as shown in the first paragraph of this section where derivatives of the free energy G with respect to T,P may be discontinuous/continuous. Kinetically speaking, continuous transformations do not change as a function of time, however discontinuous transformations begin slowly and ramp up[10] . The same distinctions are found microstructurally, where continuous transformations begin within the entirety of the sample at once, while discontinuous transformations begin within a distinct region, creating a heterophase interface between the two phases (parent / product). This final point was discussed by Christian[10], who used the terms heterogeneous and homogeneous transformations, with regard to spatial portioning (for heterogeneous) and no partitioning (for homogeneous transformations). Nucleation & growth processes (whether nucleating homogeneously or heterogeneously at specific sites) is always considered a heterogeneous transformation, whereas continuous transformations are always homogeneous transformations.

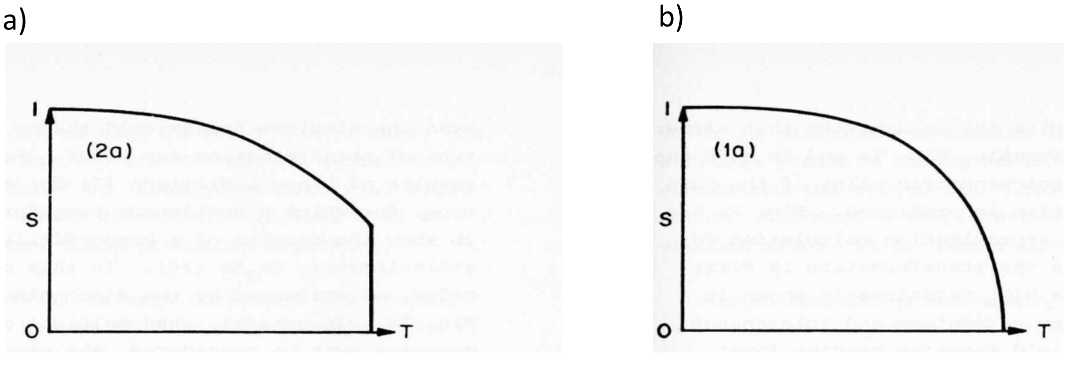

Figure 1.1. These schematics show long-range order (given here *S,* but may η classically) vs. temperature for Bragg-Williams first (a) and second (b) order transitions. A discontinuity in order parameter is observed in a), while none is observed in b).

The formation of a solid solution at elevated temperatures is a hallmark phenomenon of physical metallurgy and materials science[10]. Atomic ordering occurs when atomic species preferentially order to specific sites, giving rise to different properties of the metal. While solute atoms may enter the solid solution interstitially, the following section on is focused on substitutional solid alloys. Interatomic interactions dictate the non-random placement of atoms on sites: for a binary alloy containing *A,B* atoms there then exist *A-A, B-B, and A-B* interactions. When bonding is preferred between similar atoms (i.e. A-A or B-B bonds), the system is said to exhibit clustering. When dissimilar bonds are preferred (A-B – type), the system is said to exhibit ordering. The atomic lengthscale over which this preferential (A-B-type) site placement occurs determines whether the system exhibits short-range (few to several atomic distances) or long-range (many times the unit cell length) ordering. When long-range order is observed, the atomic arrangement can be envisioned as interpenetrating sublattices which are occupied preferentially by A or B atoms, creating what is now referred to as a superlattice[10]. Superlattices tend to form around stoichiometric compositions, and are classically referred to as intermetallic compounds. However, as observed in this dissertation, off-stoichiometric compositions do not disqualify superlattice formation. Long range order can be quantified with an order parameter as described above (see Fig. 1a,b), where deviations in composition (among other variables) will affect the degree to which the system can observe perfect order[10].

Treatments of cooperative phase phenomena are based upon lattice models where the potential energy change associated with the interchange of A & B atoms is assumed to arise from changes in A-A, B-B, and A-B bonds, whose energies are assumed to be independent of composition and lattice parameter[9]. The interchange energy parameter can be described $\varepsilon = \varepsilon_{AB} - \frac{\varepsilon_{AA}+\varepsilon_{BB}}{2}$ where

$\varepsilon_{AB}, \varepsilon_{AA}$, and ε_{BB} correspond to the energies of A-B,A-A, and B-B bonds. These expressions will have 1st and 2nd nearest neighbors. When $\varepsilon < 0$ the system will observe ordering, where as when $\varepsilon > 0$ clustering is said to occur. These pairwise interactions can, in common parlance, be replaced by a mean field of the Weiss type[9] (as developed for ferromagnetism). While the Mean field theory is relatively successful at predicting interatomic potentials, since the effective interparticle interaction is of infinite range, experiment and theories tend to deviate significantly near the critical temperature T_C. However, recent advances with Ising models have satisfactory results, including in systems such as liquids, ferromagnets, superconductors, and others[9].

Using a relatively simple thermodynamic model, Bragg and Williams introduced a long-range order parameter based on "right" and "wrong" site placement in substitutional alloys[10]. "Right" site placement ws defined when all A atoms sat on $\alpha - sites$, and B atoms on $\beta - sites$, whereas "wrong" site placement occurred when B atoms sat on $\alpha - sites$, and A atoms on $\beta - sites$. Their model was relatively elementary, as it did not account for short-range forces or pairwise interaction energies. However, many important features were captured, especially with respect to AB and A_3B ordering. Their model is considered a zeroth approximation of the quasichemical approach. The long range order parameter is given below, with an accompanying schematic showing A2/B2 crystal structures, where A2 is the disordered BCC solid solution, and B2 an ordered cubic phase exhibit exhibiting specific α , β sites as shown.

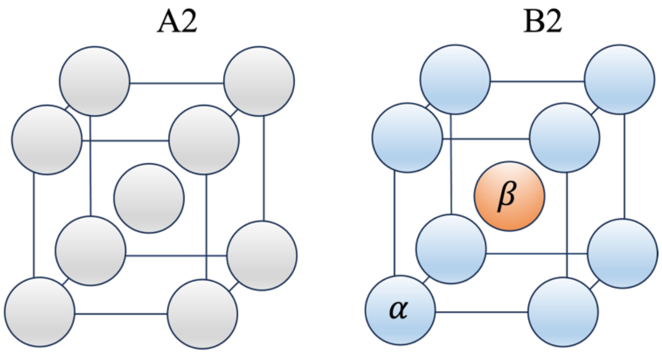

Figure 1.2. Unit cell schematics of the disordered solution A2 phase, and an ordered cubic B2 phase, with α, β sites marked. Grey spheres represent average A/B ratio given by composition, whereas Blue/orange spheres correspond to A/B atoms

$$\eta = \frac{(r_\alpha - X_A)}{Y_\beta} = \frac{(r_\beta - X_B)}{Y_\alpha}$$

In the expression above, r_α, r_β are the fraction of $\alpha, \beta - sites$ occupied by A,B atoms respectively, X_A X_B is the atomic fraction of A,B atoms in the alloy, and Y_β, Y_α is the fraction of β, α -sites in the ordered structure. This expression can be used for both stoichiometric and non-stoichiometric compositions. At equiatomic compositions, the B2 compound should exhibit perfect order: that is, $\eta = 1$. In perfectly disordered alloys, $\eta = 0$. The "maximum" allowed long-range order that can be observed is a function of composition.

Additionally, a short range order parameter may be employed, as given below:

$$\sigma_{AB}(\bar{\bar{r}}_i) = \frac{P_{AB}(\bar{\bar{r}}_i) - 2X_AX_B}{P_{AB}(\bar{\bar{r}}_i)(\text{max.}) - 2X_AX_B}$$

In the following expression $P_{AB}(\bar{\bar{r}}_i)$ is the observed number of A-B bonds, $P_{AB}(\bar{\bar{r}}_i)(\text{max.})$ is the maximum possible value of P_{AB}, and $2X_AX_B$ is the number of A-B bonds randomly occurring in a solution, as defined by the compositions. As such, the values of σ_{AB} can range from 0 to 1, where $(\bar{\bar{r}}_i)$ is the interatomic vector connecting first nearest-neighbor atoms.

Schematic phase diagrams for first and second order transformations are included below, in Figure 1.3a,b respectively. For a first order transformation, a latent heat is found: upon cooling the disordered region in Fig.1.3a below the critical temperature T_C, but above the instability temperature, a discontinuous nucleation & growth process is the only way in which the system can order. Below the instability temperature T_i^- though, the thermodynamic restorative force (energetic barrier) vanishes, and the disordered phase becomes unstable with respect to small energetic fluctuations. The system will order continuously, mimicking a continuous/homogeneous transformation. However, while this transformation may be thermodynamically predicted, strain energy considerations may increase the enegetic barrier and lead to a suppression of a continuous transformation. In Fig. 1.3a, the T_0 line corresponds to the congruent ordering transformation[11] boundary. Figure 1.3b shows the schematic phase diagram for a system undergoing a 2nd order transformation, where $T_C=T_i^-$. The solid solution will order continuously: no latent heat is observed for these type of transformations.

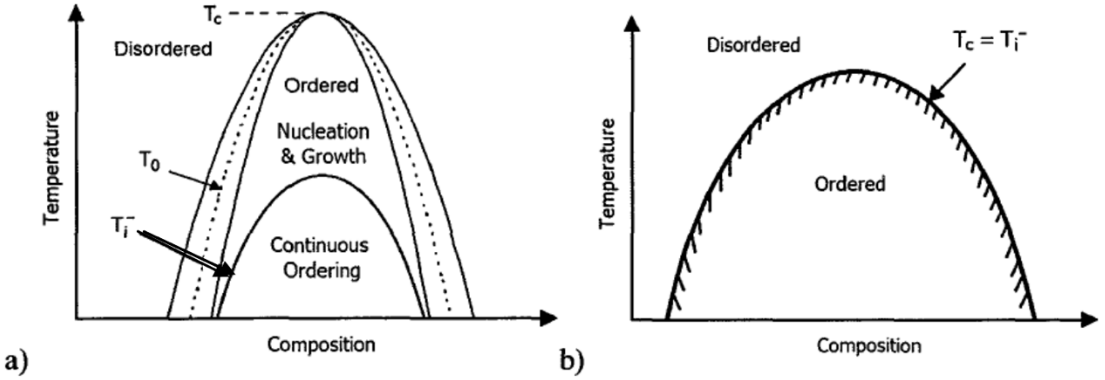

Figure 1.3. Schematic phase diagram for a) 1st order and 2) 2nd order transformations. T_C is the critical temperature in these diagrams. T_i^- is the instability temperature, below which transformations may occur continuously.

A change in free energy upon ordering can be described by a Landau order parameter, which is given by the Taylor series expansion as :

$$G(\eta) - G(0) = \alpha\eta^2 + \beta\eta^3 + \tau\eta^4 + \cdots$$

Where $G(\eta)$ is the free energy for the ordered phase and $G(0)$ is the free energy of the disordered phase. In this expression, α, β, τ essentially constants. Figure 4 shows Landau free energy curves for both (a) and 1st order (b) 2nd order type of transitions. In Figure 1.4a, for $T = T_C$, a second minimum is found for $\eta > 0$, in addition to the minimum found at $\eta = 0$, separated by a thermodynamic restorative force. For $T \leq T_i^-$ conditions, the thermodynamic restorative force is seen to disappear, and only one minimum is found, for $\eta > 0$. For this level of undercooling, the system can order continuously (although it may not, given elastic strain conditions): however, In Fig. 4b (corresponding to a 2nd order transformation), there is no thermodynamic restorative force such that $T_C = T_i^-$. Ordering can occur in this system unimpeded. Landau theory dictates that in order for a transformation to be continuous, the symmetry elements of the ordered phase must comprise a sub-group of the point group which describes the disordered phase. Most transformations in nature are 1st order in nature. Certain transformations, such as the normal to superconducting state transformation is 2nd/higher order.

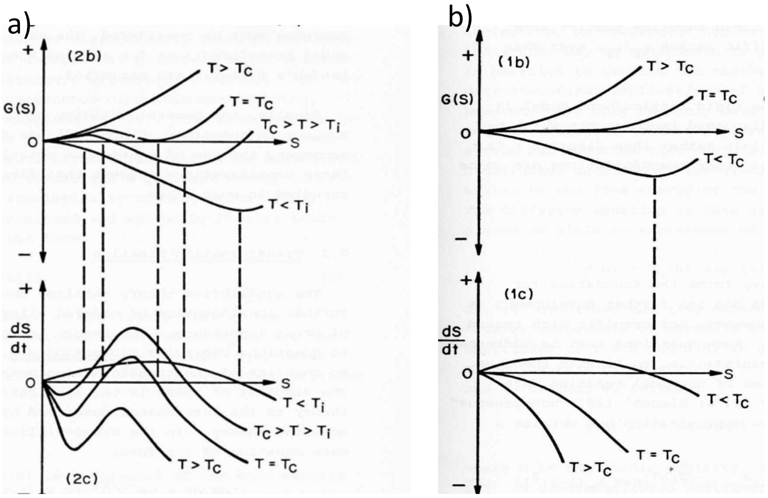

Figure 1.4. This schematic shows Landau free-energy curves for different temperatures vs. order parameter (*S*), for both 1st order (a) and second order transofmrations (b). . Below each schematic is the first derivative with respective to temperature.

1.3. A Brief Primer on FCC Phase Diagram Calculations

In order to properly couch the results presented in this dissertation, a brief primer on the history of phase stability calculations on the FCC lattice will be presented, as adapted from Ducastelle's *Order and Phase Stability in Alloys*[12]. Cu-Au is oftentimes considered the prototypical FCC ordering system, and was the system chosen by Shockley[13] in 1938 who used nearest-neighbor interactions to compute ordered structures on the FCC lattice in what is now referred to as a mean-field. Shockley's calculated phase diagram is shown in Fig. 5a, where three ordered phases are identified (η $(L1_2), \xi_2, (L1_0),$ $\xi_1(L1')$) and is markedly different from the accepted phase-diagram of Cu-Au[14]. A reproduction of Shockley's phase diagram by Ducastelle[12] is given in Fig. 1.5b. Interestingly, the phase field bounded by *¼<c<1/2* shows two ordered phases: ξ_1 (low temperatures, away from equimolar compositions) and ξ_2 (high temperatures). Both $L1_0$ (ξ_2) & L1' (ξ_1) are ordered tetragonal phases which Shockley said 'may be lumped together in one'[13]. However, there are key distinctions between $L1_0$ (ξ_2) and L1' (ξ_1), which this dissertation will

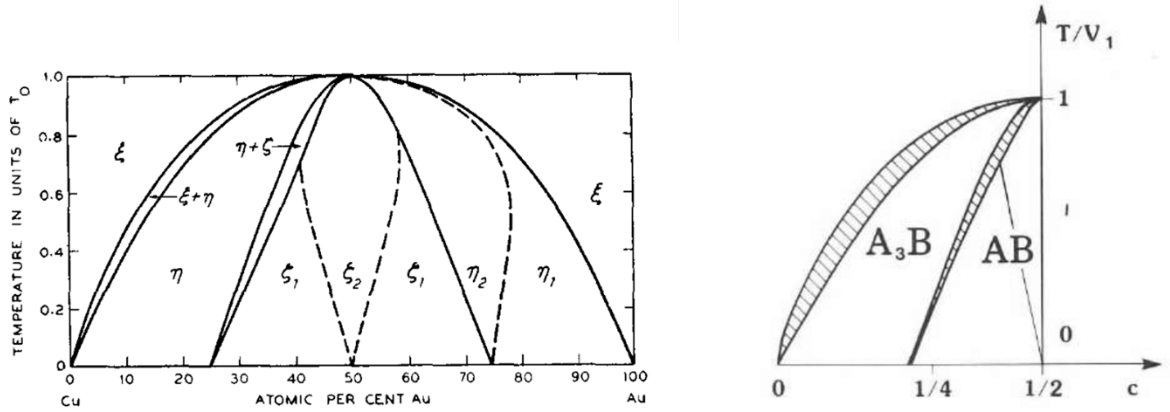

Figure 1.5. In a) the phase diagram produced by Shockley[13] in 1938 using nearest neighbor interactions in what is now referred to as a mean-field approximation. An identical phase diagram is provided in b), reproduced by Ducastelle[12.] Three low-temperature ordered phases are shown: η $(L1_2), \xi_2, (L1_0),$ $\xi_1(L1')$.

explore and discuss: namely, the placement of off-stoichiometric atoms in L1' is strictly limited to the (001) center site (1/2,1/2,0) as shown in Fig. 1.6, where two schematic unit cells for (equiatomic) $L1_0$ and L1' are given.

In $L1_0$, there is equal distribution of off-stoichiometric atoms across all complementary atom sites. The order/disorder transition at $c=0.5$ (for FCC → $L1_0$) was calculated to be 2nd/higher order in Shockley's work. Subsequent calculations show that this transition becomes 1st order when strain is incorporated into free energy model[15].

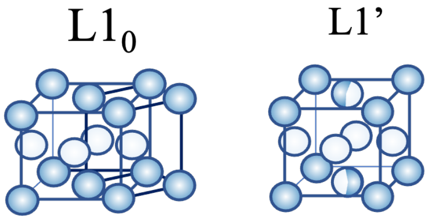

Figure 1.6. Unit cells of $L1_0$ (ξ_2) and L1' (ξ_1).

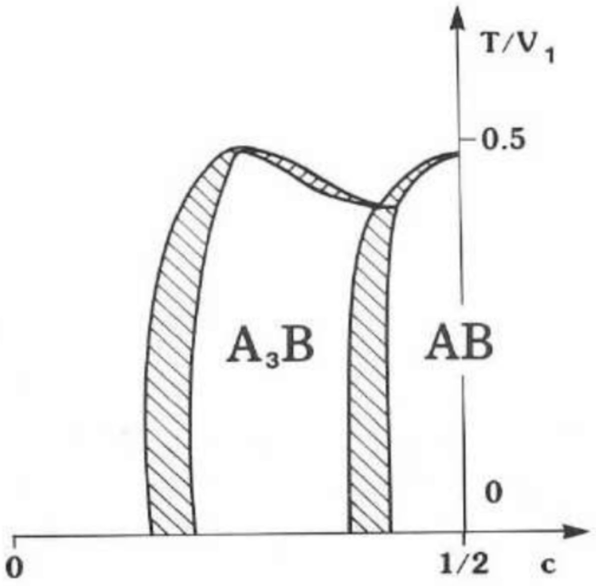

Figure 1.7. The CVM-Tetrahedron phase diagram produced by Van Baal[18] in 1973, which gave a satisfactory topology: both $L1_0$ and $L1_2$ are found, but not L1'.

Unfortunately, the topology of Shockley's phase diagram above deviated significantly from experimental observations, and was thus considered unsatisfactory. Li[16] employed a quasi-chemical approach, and while $L1_0$ and $L1_2$ were both found, he did not find low-temperature the L' (L1') phase. Golosov[17] did not find this phase either, with tetrahedron CVM calculations. However, the

Cluster Variation Method was considered to be a better approximation than the quasi-chemical approach given by Li. The phase diagram calculated using a CVM-tetrahedron approach is given in Figure 1.7, done in 1973 by Van Baal[18], employing the Kikuchi adaptations to the Ising model (incorporation of higher-order interactions between more particles and pairs of more distant particles). In general, incorporation of more than nearest-neighbors led to a favorable overall topology of the phase diagram and adequately captured relevant order/disorder phenomena[18]. Interestingly, this phase diagram predicted a 1st order order/disorder transition at *c*=0.5 without employing strain energy considerations.

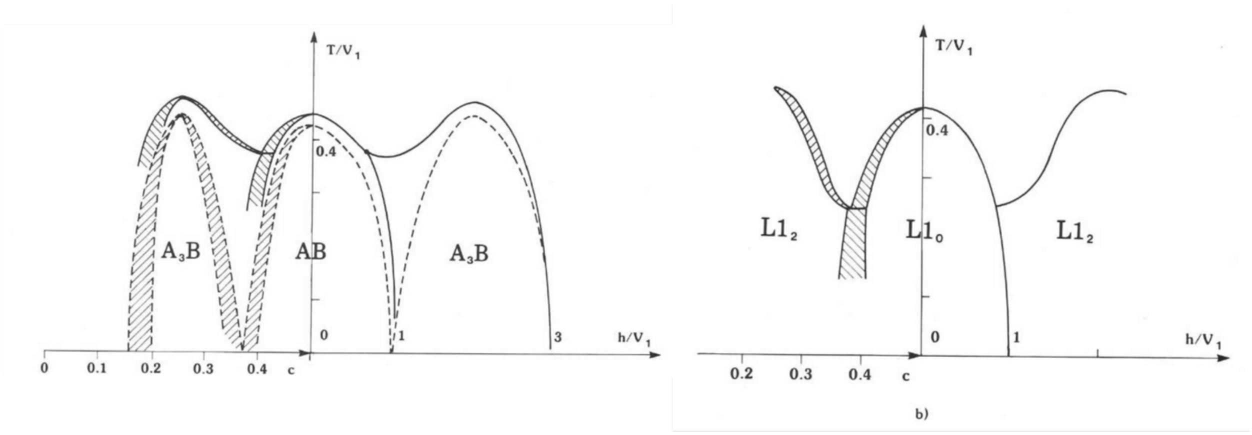

Figure 1.8. In a) Binder's[19] Monte Carlo calculations results (dashed line) show existence of the disordered phase at 0K. Solid lines show the CVM tetrahedron-octahedron approximation and Monte Carlo results of Finel & Ducastelle[21] with a finite temperature triple point. In b) subsequent Monte Carlo calculations[12] do not find any such degeneracy for the triple points.

Generally speaking, the Ising models suffer considerable inconsistencies with experimental results when near the order/disorder critical temperature T_C. In particular, triple-points present significant modeling issues, as shown by Monte Carlo simulations undertaken by Binder[19] who found significant inaccuracies for regions between $L1_0$ and $L1_2$. Binder[19] undertook these calculations because there was significant uncertainty about whether the shortcomings in phase stability calculations were inherent to the Ising model, or due to shortcomings in the approximations. Binder found that the disordered phase existed all the way to *0K (*dashed lines in Fig. 8a) at triple point regions (where FCC, $L1_0$, and $L1_2$ meet). The solid lines superimposed on Fig. 8a show the CVM results of Finel & Ducastelle[20], which have incorporated tetrahedron-octahedron configurations, and show a finite temperature for the triple point mentioned: resolving the issue.

Calculations surrounding the triple-point have generated much debate in the past[12] . Monte Carlo simulations are difficult to perform at low temperatures, and they are 'particularly useless' at superdegenerate points[12]. As such, special low temperature expansions have been carried out, where the competition between $L1_0$ and more complicated structures deduced from $L1_0$-type ordering have been studied. Ducastelle[12] points out that that the structures of the CuAu-family are the most stable structures at *0K,* especially in the presence of repulsive nearest-neighbour interactions. The presence of more complicated structures at intermediate temperatures cannot be ruled out though[12], and is considered of import to increase compatibility between computations and experimental observations. In particular, this dissertation is primarily concerned with a low-temperature ordered phase (L1' or L') which has been seen on some Ising model phase diagrams, but not others. Ducastelle makes note that more general structures with different occupancies on the four simple interpenetrating lattices should be considered[12].

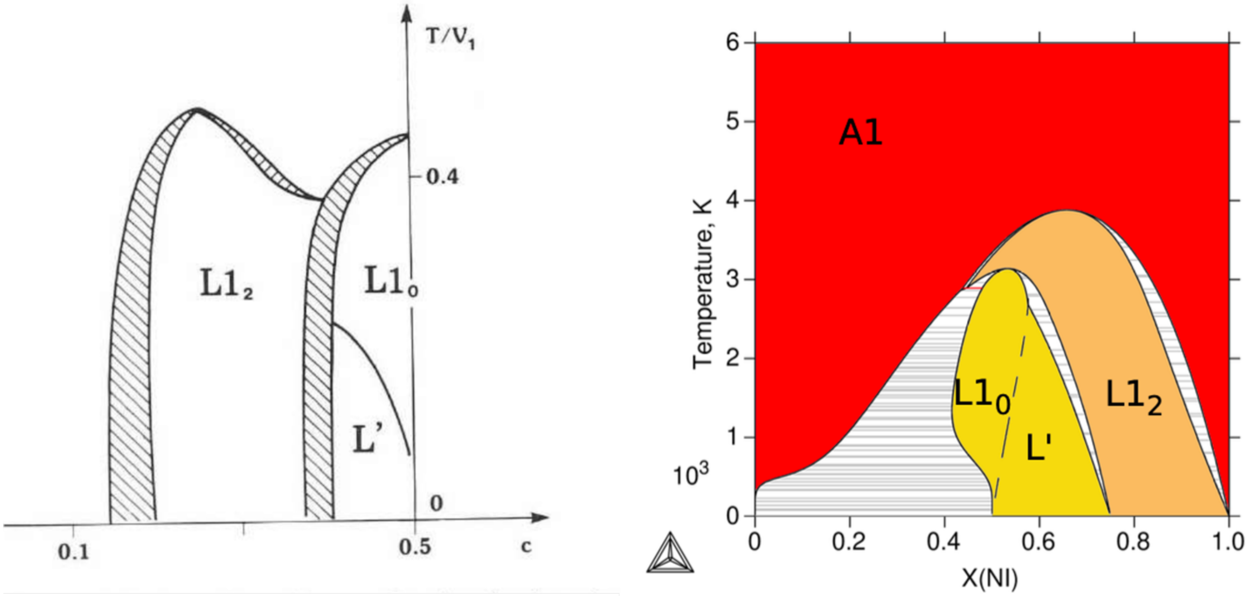

Figure 1.9. In a) the CVM tetrahedron-octahedron approach by Finel & Ducastelle[20] shows again three ordered phases on the FCC lattice. In b) Fries shows a metable phase diagram computed with ThermoCalc for Al-Ni with existence of $L1_0$, $L1_2$, and L1' for Ni-rich regions.

Figure 1.9a shows the FCC phase diagram utilizing CVM tetrahedron-octahedron approach by Finel and Ducastelle[20] from 1986, where at low temperatures the L1' (or L') phase is found to be more energetically stable than $L1_0$ (as predicted by Shockley). Subsequent Monte Carlo simulations undertaken by Finel & Ducastelle[21] also found L' to be stable at low temperatures, although they found energetic differences between ordering configurations to be very small (on the order of 10^{-6} J/atom). In many ways, the work carried out by Finel & Ducastelle showed that CuAu-family should be the stable ordered structures at all compositions & temperatures, that triple-points exist at finite temperatures, and that the three-sublattice structure L1' (L') is stable at finite temperatures.

So far, these calculations have been carried out in hypothetical *AB* systems, (disregarding the early work in Cu-Au). However, certain recent calculations (e.g. 2020) in other functional material systems (Ni-Al) purport the existence or insist consideration of L1' stability at finite temperatures. For example, Fries et al.[22] generated a metastable phase diagram for Al-Ni at finite temperatures, where DFT-generated formation energies at 0K (utilizing a Bragg-Williams-Gorsky configurational entropy parameter) were input into ThermoCalc v.2020a (shown in Fig. 1.9b). They found at low temperatures, ordering on the FCC lattice to form L1' (or L') instead of $L1_0$. This ordering was preferred on the Ni-rich side but not the Al-rich side (see Fig. 9b). It is worth pointing out thought, that 3rd law considerations should exclude the possibility for L1' (L') existence at 0K (as a ground state structure). At the ground state, entropy must be 0: as such, a shared (1/2, ½, 0) site would be disallowed rigorously. In short: only at finite temperatures could L1' ordering be stabilized or considered on phase diagrams (equilibrium or metastable).

In summary, the study of finite temperature phase stability on the FCC lattice has employed various techniques (Mean-Field, Quasi-chemical approximation, Cluster Variation Method, Monte Carlo calculation), and found general agreement with stability of $L1_0$ & $L1_2$ ordering around *c=0.5 & 0.25*,0.75 respectively. The stability of other ordered structures at finite temperatures has also been considered, with particular attention paid to L1' (or L'). Experimentally however, the L1' sublattice ordering may be stabilized by other interactions not classically included within free energy models (magnetic or phononic contributions). As the study of computational phase stability at finite temperatures progresses, incorporation of more non-classical energies should allow for better prediction of phases *and* better agreement with experimental observations.

1.4. Overview of the Computationally-Determined Fe-Pd System

The Fe-Pd phase diagram has largely been studied at equiatomic compositions due to the relatively large uniaxial magnetocrystalline anisotropy[23] of the ordered $L1_0$ compound and its good corrosion resistance. In general, the $L1_0$ structure has found direct application in ultra-high density magnetic recording media[24]. However, Fe-Pd also appears to be one of the most promising ferromagnetic shape memory alloys for magnetic sensors or magneto-thermoelastic actuators, because of its high magnetic-field induced strains[25]. The Fe-Pd system has also been investigated for use in catalytic applications[26].

As articulated by Zunger[26], the Fe-Pd system is relatively unique in that unlike other binary compounds exhibiting all paramagnetic, all FCC (e.g. Cu-Au) alloys, or all-BCC (e.g. Mo-Ta) alloys, there exists a competition in Fe-Pd between BCC and FCC structures as well as para- and ferro-magnetic phases. The stability of these different structural & magnetic regions is shown schematically on the classically accepted phase diagram[27] of Figure 1.10a, where FCC (BCC) regions are Pd-rich (Pd-lean), and para- (ferro-) magnetic coupling appears at high (low) temperatures. These different phase stability regions are labelled (1) – (4), where: (1) ferromagnetic FCC and/or ferromagnetic FCC + ferromagnetic BCC; (2) paramagnetic FCC; (3) ferromagnetic BCC + paramagnetic FCC; (4) paramagnetic BCC + paramagnetic FCC. While this structural (and magnetic) phase diagram is readily accepted as standard in the literature, this dissertation will show that the unexplored Pd-rich two-phase region yielded unexpected (by this phase diagram) ordering behavior. Figure 1.10b is a compiled experimental + calculated phase diagram of Fe-Pd (solid lines are calculated) done by Ghosh[28], where again, general agreement is found amongst experimental studies.

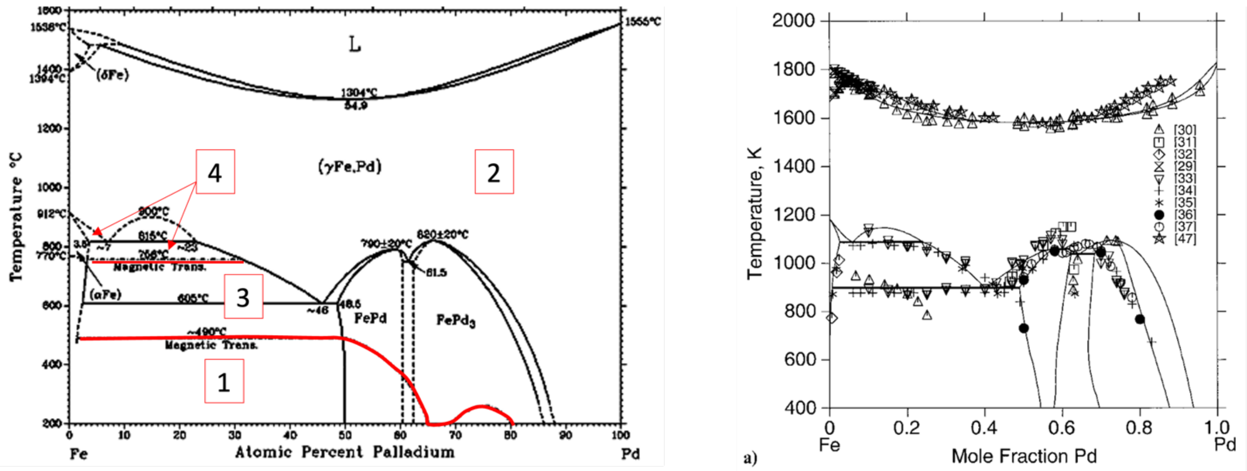

Figure 1.10. In a) the classically accepted phase diagram by Massalski[27] is given, where superimposed red lines separate magnetic phase stability regions. In b) a composite phase diagram is given by Ghosh[28], where solid lines are computationally-generated.

This interplay between competing para/ferro-magnetic coupling & BCC/FCC structures was explored in depth by Zunger[26], who set out to answer the question: <u>what would finite temperature ordering and phase stability in Fe-Pd alloys look like in the absence of magnetic contributions?</u> Their work shows that magnetic excitations play a critical role in stabilizing many of the compounds observed experimentally. In fact, many of the lowest-energy ground states they report have never been reported experimentally. Zunger[26] makes pains to increase accuracy from other calculation methods, and argues his results are not linked to assumptions in his models. In broad strokes, Zunger generated DFT formation energies of ground states as a function of composition and employed final cluster expansion calculations at *T=0K*, which were subsequently incorporated into Monte Carlo simulations to create a finite-temperature phase diagram.

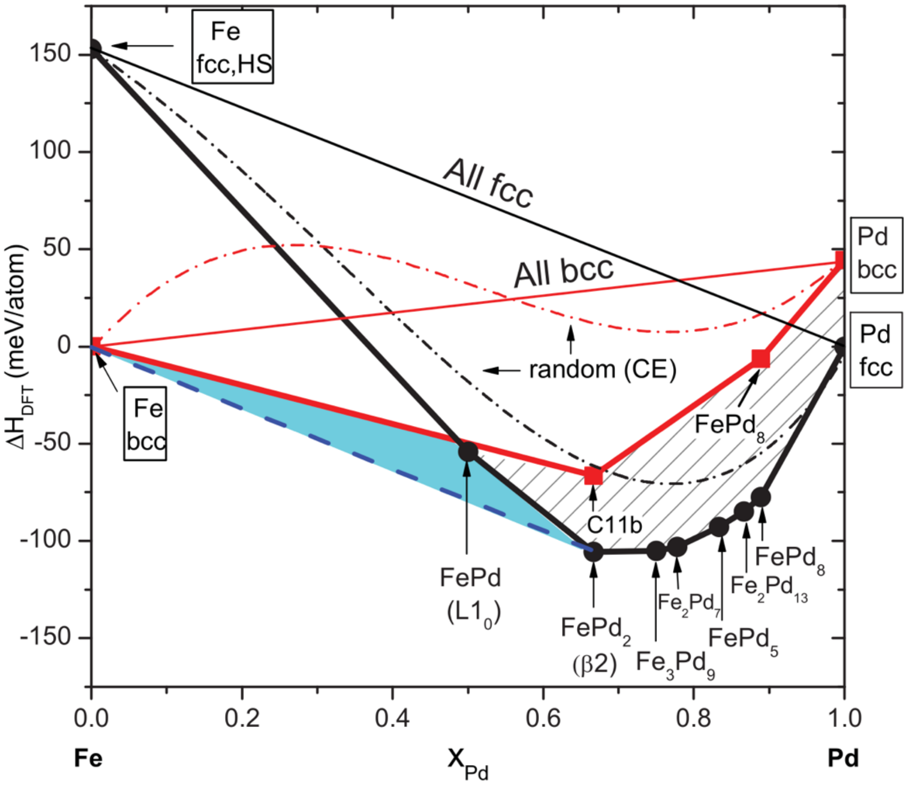

Figure 1.11. The convex hull for BCC (red line) and FCC (black line) structures in Fe-Pd, given by Zunger[26].

In their work, formation energies of Fe-Pd compounds using the pseudopotential momentum-space total energy and force formalism within the plane-augmented-wave (PAW) method in DFT-GGA of the VASP package were carried out. The ground-state structures are shown in Figure 11. This image is a composite of both FCC (black lines and dots) and BCC (red lines and dots) ground-state structures given across composition space, where BCC-Fe and FCC-Pd are included as reference states. Of significant importance in the results of Fig. 1.11, is the blue region showing decomposition of $L1_0$ into two-phase coexistence of BCC-Fe and FCC β_2. This result is very shocking, as at finite-temperatures, all experimentally determined equiatomic compositions report the existence of only the $L1_0$ phase[23,29–31]. For clarity, this two-phase coexistence is only considered when both FCC + BCC ground state structures are considered: when only ordered structures on the FCC lattice are considered, $L1_0$ is still the lowest structure at this composition.

There are other interesting results found on the convex hull reported in Fig. 1.11. For example, on the Pd-rich side the experimentally reported L1$_2$ structure is not found at all (namely at AB_3 composition). Instead, a series of ordered $\beta_2 -$based compounds are found (FePd$_2$, Fe$_3$Pd$_9$, Fe$_2$Pd$_7$, FePd$_5$, Fe$_2$Pd$_{13}$, FePd$_5$, and pure Pd (FCC)). Again, these results are confusing as no experimental reports of these long period superlattice structures exist in the literature. At many of these compositions L1$_2$ is found (or expected) to form. However, if all FCC + BCC-derivative structures are considered, the only BCC structure considered 'ground state' is pure Fe (BCC). Temperature-induced entropic considerations should always prefer FCC-based structures (for example, as observed in the allotropic transitions of Fe)[32].

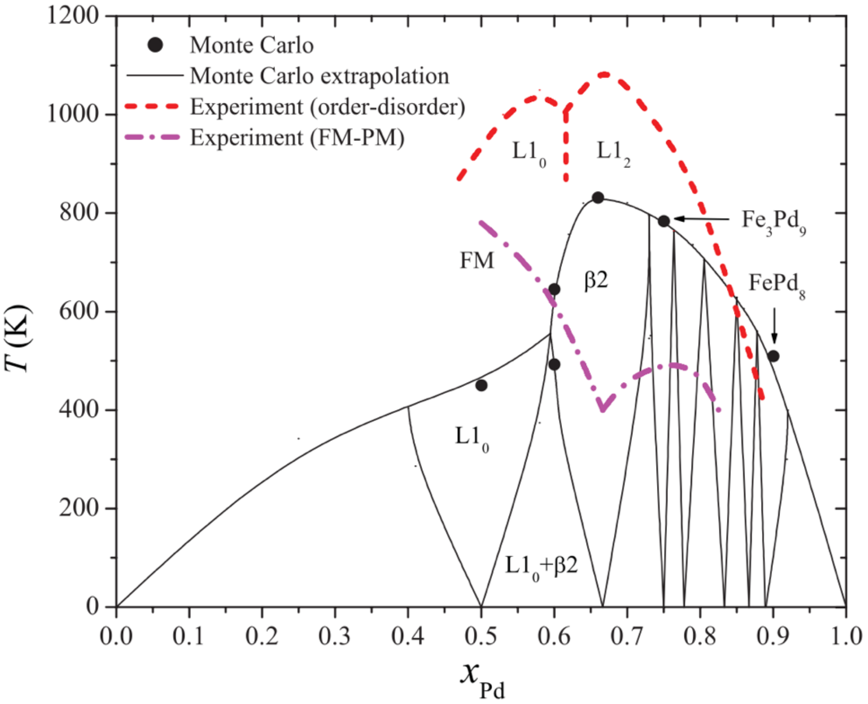

Figure 1.12. The phase diagram generated for Fe-Pd by Monte Carlo simulations (using only the FCC lattice) as given by Zunger[26], where order/disorder and curie temperatures are superimposed (red and purple lines respectively).

The phase diagram predicted from Zunger's results is shown in Fig. 12, which was calculated by inputting final FCC cluster expansion results into a canonincal Monte Carlo simulation of only the

FCC alloy states. In Figure 1.12, the experimentally-determined order/disorder & curie temperatures (*T_C)* are included as a guide to the eye (in red & purple respectively). Broadly speaking, there are significant disagreements between the computed phase diagram of Zunger and the experimentally observed values. Zunger[26] attributes the mismatch between order/disorder temperature at equiatomic compositions, the complete disappearance of $L1_2$ from the phase diagram, and the preference for β_2-based ordering for Pd-rich compositions to all be due to the lack of magnetic energy contributions in their simulations. In fact, Zunger reiterates this critical point on several occasions. Out of consternation, Zunger simulated XRD diffractograms for the β_2 structure at the observed compositions in Fe-Pd, to qualitatively rule out if there had been mistakes in Phase ID for alloys within that composition space (and finds no potential for mismatch in identification). Interestingly, β_2 ordering has been observed in DFT calculations for analogous ordered FCC systems: Cu-Au[33], Fe-Pt[34], and Co-Pt[35]. However, no experimental evidence of these phases have reinforced these findings. It is worth reiterating again here, that the analysis provided here to explore first-principles calculations of phase stability was given in order to reiterate the significance of magnetic contributions to phase stability.

The following table (Table 1.1) compiled by Zunger[26] gives the list of FCC (Lifshitz) structures: these are the ordered structures with ordering vectors exclusively at high-symmetry ***k*** points. These are included as reference. The final structure L1' is included though it is not a Lifshitz structure. It is simply included as an ordered phase on the FCC lattice.

Structure	**L1$_2$**	**L1$_0$**	**L1$_1$**	**D4**	**CH, A$_2$B$_2$**
	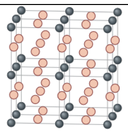	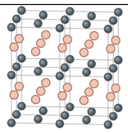	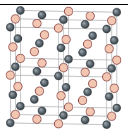	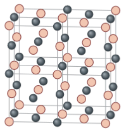	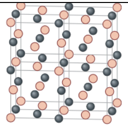
Prototype	Cu$_3$Au	CuAu-I	CuPt		NbP
Bravais Lattice	Simple Cubic	Simple Tetragonal	Rhombohedral	Face-Centered Cubic	Body-Centered Tetragonal
Unit Cell Basis Vectors	(1,0,0) , (0,1,0), (001)	(1/2, ½, 0), ($\underline{1/2}$, ½, 0), (0,0,1)	(1/2,1/2,0) (1/2,0,1/2) (1, $\underline{½}$, $\underline{½}$)	(1,1,0) (1,$\underline{1}$,0) (1,0,$\underline{1)}$	(1,0,0) (0,1,0) (1/2, ½, 1)
Atomic Positions	**A:** (0,0,0) **B**: (1/2,1/2,0) **B:** (1/2, 0, ½) **B:** (0, ½, ½)	**A:** (0,0,0) **B:** (0, ½, ½)	**A:** (0,0,0) **B:** (1,0,0)	**A:** (0,0,0) **A:** (1/2,1/2,0) **A:** (3/2, 0, $\underline{1/2)}$ **A:** (1, ½, $\underline{½)}$ **B:** (1, $\underline{½}$, $\underline{1/2}$) **B:** (1/2, 0, $\underline{½}$) **B:** (1/2, $\underline{½}$, 0) **B:** (1, 0, 0)	**A:** (0,0,0) **A:** (1/2, 1, ½) **B:** (1/2, ½, 0: **B:** (1, ½, ½)
Space Group	Pm$\underline{3}$m	P4/mmm	R$\underline{3}$m	Fd$\underline{3}$m	I4$_1$/amd
Pearson Symbol	cP4	tP2	hR32		tI8

Table 1.1. These two tables show all high-symmetry (***k)*** structures, commonly referred to as Lifshitz structures on the FCC lattice. The prototype, lattice, unit cell basis vectors, atomic positions, space group, & Pearson symbol are included. Only three will be considered in depth for this thesis (L1$_0$, L1$_2$, and L1'). The final structure L1' is not a high-symmetry structure, but is included as an ordered phase on the FCC lattice.

Structure	**D1 (A_7B); D7 (AB7**	**L1$_3$**	**DO$_{22}$**	**D3 (A_5B_3); D5 (A_3B_5)**	**L1'**
	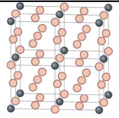	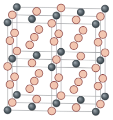	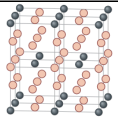	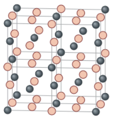	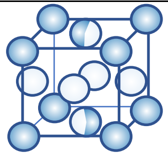
Prototype	CuPt$_7$	CuPt$_3$			
Bravais Lattice	Face-centered Cubic	Base-centered Orthorhombic	Body-centered Tetragonal	Rhombohedral	Simple Tetragonal
Unit Cell Basis Vectors	(1,1,0) (1,$\underline{1}$,0) (1,0,$\underline{1}$)	(1/2, ½, 0) (1/2, $\underline{½}$, 1) (1/2, $\underline{½}$, $\underline{1}$)	(1,0,0) (0,1,0) (1/2, ½, 1)	(1, 1, 0) (1, $\underline{1}$, 0) (1, 0, $\underline{1}$)	(1,0,0) (0,1,0) (0,0,1)
Atomic Positions	**A:** (0,0,0) **B:** (1,0,0) **B**:3/2, 0, $\underline{½}$) **B:** (1, $\underline{½}$, $\underline{½}$) **B:** (1, ½, $\underline{1/2}$) **B:** (1/2, 0, $\underline{½}$), **B:** (1/2, $\underline{½}$, 0) **B:** (1/2, ½, 0)	**A:** (0,0,0) **B:** (1/2, $\underline{½}$, 0) **B:** (½, 0, ½) **B:** (1/2, 0, ½) **B:** (1/2, 0 $\underline{½}$)	**A:** (0,0,0) **B:** (1/2, ½, 0) **B:** (1/2, 1, ½) **B:** 1, ½, ½)	**A:** (0,0,0) **A:** (1/2, ½, 0) **A:** (3/2, 0, $\underline{½}$) **B:** (1/2, 0, $\underline{½}$) **B:** (1/2, $\underline{½}$, 0) **B:** (1, 0, 0) **B:** (1, ½, $\underline{1/2}$) **B:** (1, $\underline{½}$, $\underline{½}$)	**A:** (0,0,0) **A:**(1/2,½,0) **B:**(1/2,½,0) **B:**(1/2,0,½)
Space Group	Fm$\underline{3}$m	Cmmm	I4/mmm	R$\underline{3}$m	P4/mmm
Pearson Symbol	cF32	cF4	tI8		tP4

Table 1.1 (continued). These two tables show all high-symmetry (***k***) structures, commonly referred to as Lifshitz structures on the FCC lattice. The prototype, lattice, unit cell basis vectors, atomic positions, space group, & Pearson symbol are included. Only three will be considered in depth for this thesis (L1$_0$, L1$_2$, and L1'). The final structure L1' is not a high-symmetry structure, but is included as an ordered phase on the FCC lattice.

1.5. The A1→ $L1_0$ Transformation

The A1→ $L1_0$ transformation is rigorously a first order transformation, usually involving nucleation + growth of ordered regions within the disordered FCC matrix. However, several other transformation pathways exist (although they will not be discussed in depth here): continuous ordering when supercooled below the instability temperature T_i^- , and by massive transformation when volume diffusion is sluggish[10]. As the A1→ $L1_0$ transformation is a cubic → tetragonal transformation, the transformation accrues significant strain in the process: the *c/a* ratio of Fe-Pd $L1_0$ (degree of tetragonality) is 0.966[23,31] The following transformation description will focus on the regime above the instability temperature, but below the critical temperature: $T_i^- < T < T_C$. As such, the ordering transformation prototypically begins with formation of tetragonal nanodomains (in the language of Khachaturyan[36]) or embryos (in the language of Muto[37,38] aligned along {110} planes, which constitutes the 'tweed' pre-transition state, strain contrast, or 'microstructure'. These nanodomains of the tetragonal phase correspond to small {110}<110> atomic shear displacements. At the moment, there is no widely accepted model that explains the origin of the tweed pre-transition state: Kartha[39]suggests it is a disorder-driven process, initiated by fluctuations in free-energy landscape brought about by disorder in the chemical environments. However, a dynamical strain wave model suggests that long elastic waves (i.e. phonons) are responsible for the periodic modulations between more and less tetragonally distorted regions. In both theories, the 'tweed' microstructure constitutes a pre-transition state, where point-group symmetry requires twinning in the transformed state. A more involved handling of the tweed pre-transition state is presented in Chapter 5 of this dissertation.

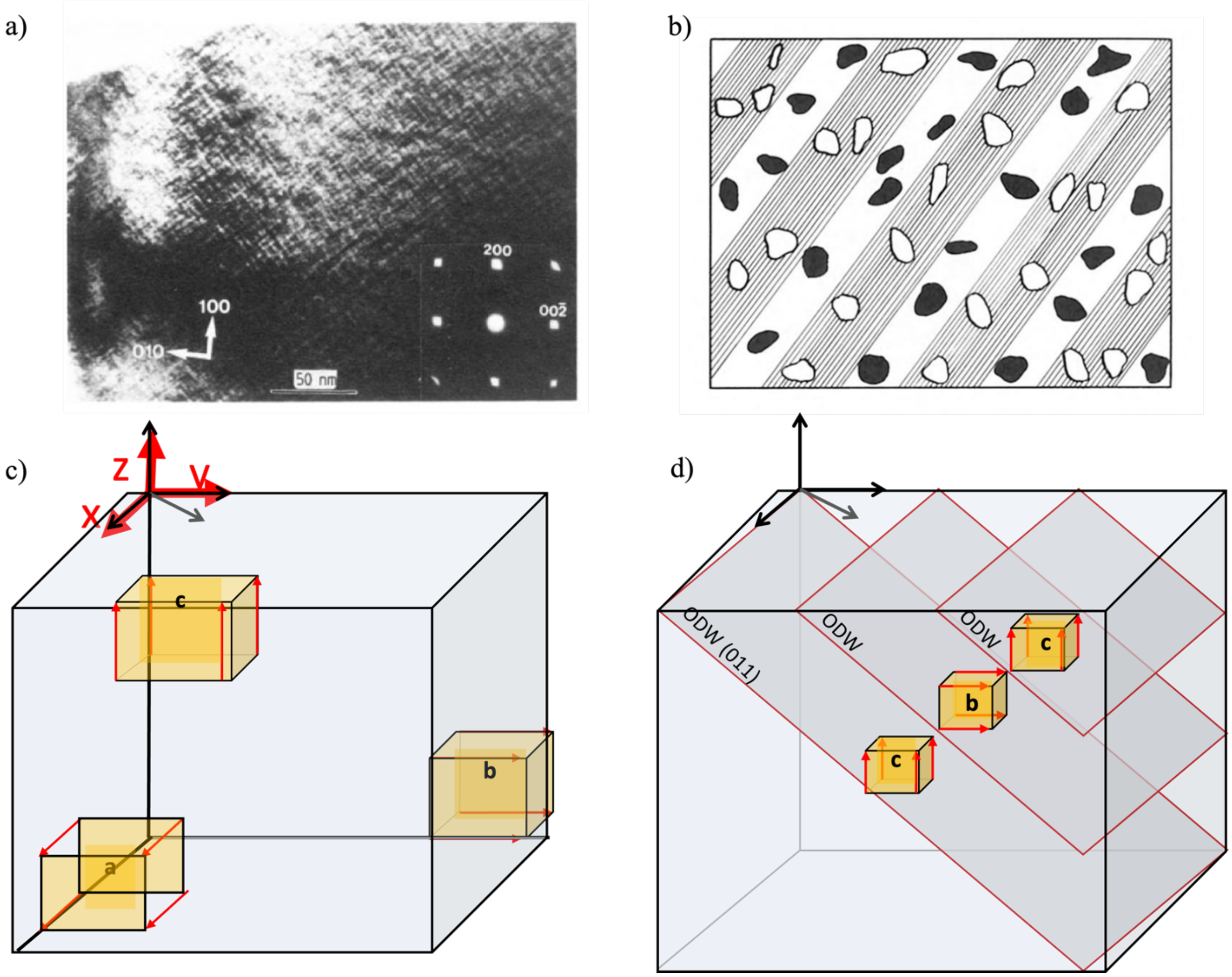

Figure 1.13. The tweed pre-transition sate is shown in a), where striations along <110> can be seen. Corresponginly in c), tetragonal domains (yellow cubes) represent nanodomains aligned along all three <100> of the parent phase. In b) and d), a representation of tetragonal nuclei banding, with interfaces between domains along{110}. In b) black and white correspond to [100] and [010] oriented $L1_0$ particles , respectively.

The tetragonal nanodomains are formed with their respective *c*-axes aligned along all three of the principal <100> directions of the A1 parent matrix. This is observed experimentally in Fig. 1.13a, and schematically in Fig. 1.13c (the orange squares denote tetragonal domains where the red arrows articulate *c*-axis direction). As the transformation proceeds, two of the domains will emerge dominant, through stress-affected growth and coarsening[23], and will align along alternating {110} bands (this is seen in Fig. 1.13b & d). In Fig. 1.13b, the white and black particles correspond to $L1_0$ regions whose *c*-axes are aligned along [100] and [010] respectively. As the individual particles within these bands grow, they impinge and coalesce, resulting in anti-phase boundaries.

The alternating {110} bands lead to a twinned relationship, where *c*-domains are nearly orthogonal to one another (~88°) [23,40]. This is observed graphically in Fig. 1.14b, where red/blue lines continue unimpeded between orientation variants. In Fig. 1.14a, a schematic of conjugate-pairings of

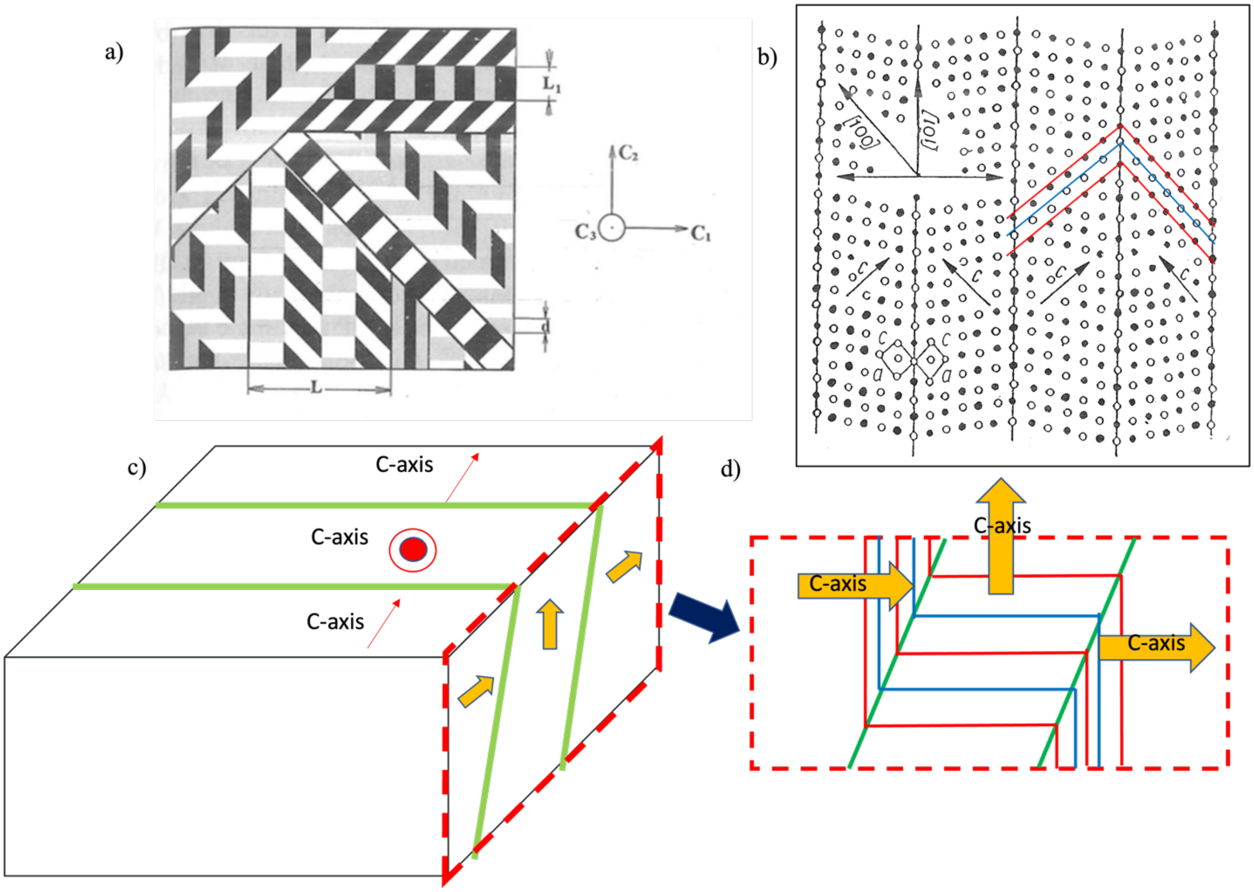

Figure 1.14. In a) a schematic alignment of conjugate *c*-domains for all pairings of orientation variants (X,Y,Z-type) when viewed down [001] (given by Vlasova[41]). Cross sections of a polytwinned section are shown in c) and d), where A/B atomic sheets (red /blue) connect across {110} orientation domain boundary. A similar atomic-level schematic[23] is shown in b) articulating coherency across {110} interfaces.

orientation domains is shown, as viewed down a [001] zone axis. In this schematic, the white, black, grey regions correspond to orientation domains aligned along [100], [010], and [001] respectively. In c) and d), further schematics articulate the structure of twinned orientation variants along {110}, where in d) atomic A/B-rich sheets show twinning relationship.

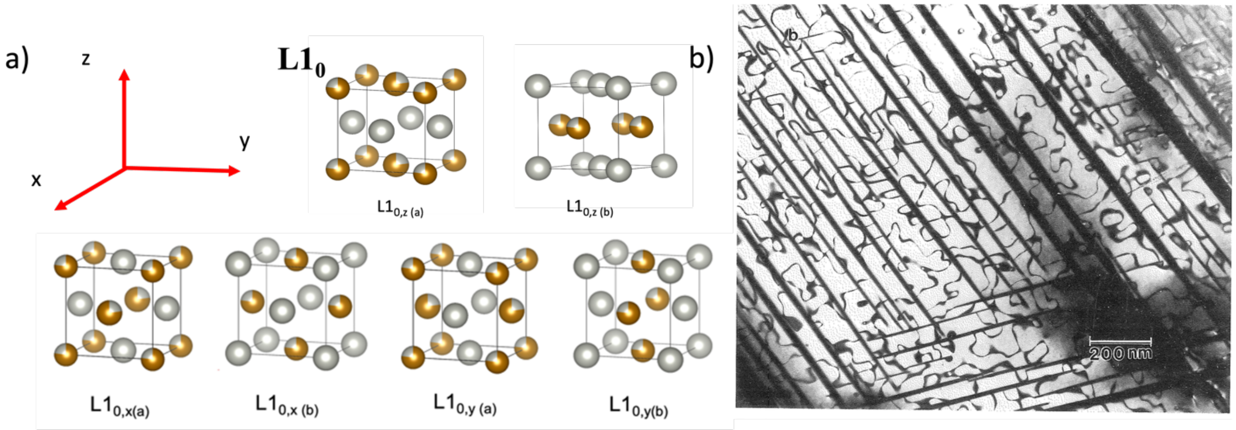

Figure 1.15. In a) all orientation & translation variants are shown for $L1_0$ (6 possible structures). When similarly oriented but out-of-phase particles meet, an anti-phase boundary is formed, as shown by the black fringes in b)[23].

As similarly oriented particles coalesce within segregated {110} bands (see Fig. 1.13b,d), a boundary may form between them if the incipient ordering site on the FCC lattice differs. For example, as will be discussed in greater detail in Chapter 4 of this thesis, each orientation variant of $L1_0$ has two translation variants (see Fig. 1.15a). When similarly oriented (*c*-axes aligned) but out-of-phase variants (different translation variants) meet, an anti-phase boundary will form. An equiatomic Fe-Pd $L1_0$ twinned region is displayed in Fig. 1.15b, as given by Soffa[23]. The regions separated by an APB may be connected by a translation vector $\vec{r}$. While there are four sublattice sites on the FCC lattice, for $L1_0$ there are only two meaningful translation vectors : $\vec{r} = \frac{1}{2}a < 101 >, \frac{1}{2}a < 011 >$ (where *a* is the lattice constant, which we will assume for the pseudo-cubic unit cell). An important distinction however, needs to be made with the existing nomenclature in

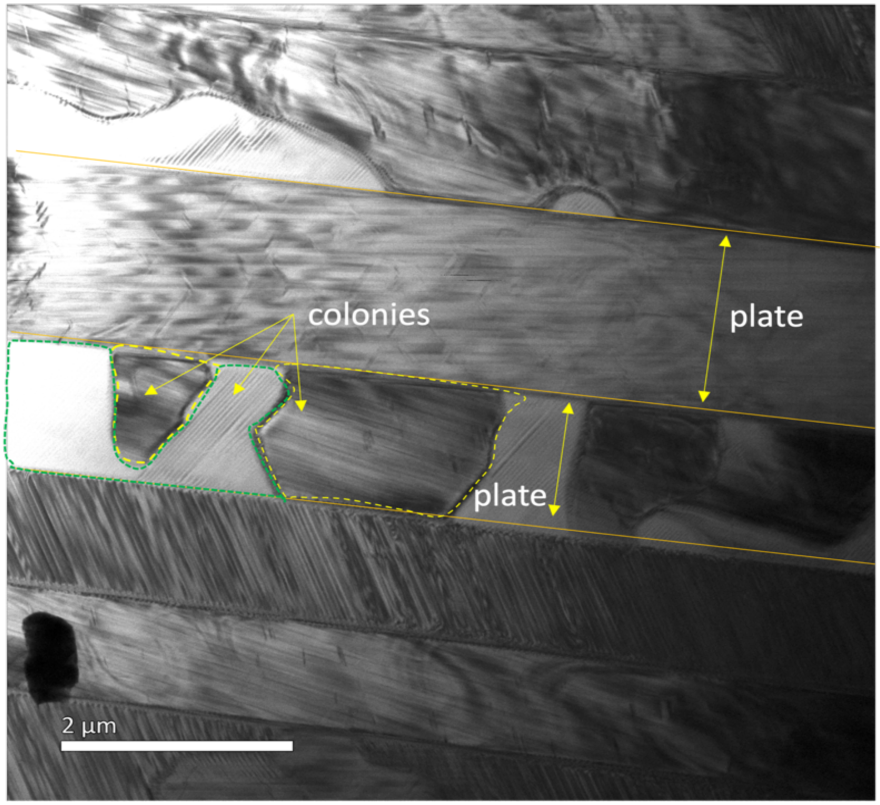

Figure 1.16. This section of polytwinned $L1_0$ shows hierarchical structuring of polytwinned microstructures: *c-domain* pairings make up a colony, and one or more colonies make up a plate. The entire collection of plates constitutes a bundle.

the literature for polytwinned structures. In this dissertation, we will refer to groupings of individual *c*-domains (or orientation variants as 'colonies' (see Fig. 1.16), and one or more colonies may make a plate. Groupings of plates are called bundles, or blocks, as expressed by Vlasova. This distinction is necessary, as oftentimes throughout the investigations provided we find plates with multiple colonies within. This so far, presents a significant disagreement with the language used by Vlasova[41], who did not consider multiple colonies as residing within a plate. Thickness of *c*-domains is typically found to be around 100nm, plates to be roughly 1-5μm[41] (although we have found plates to be as small as 500nm), and bundles of plates to reach anywhere between 50 – 100μm. When the local rate of nucleation of tetragonal domains is very high, a highly dispersive polytwinned structure will be formed, with blocks of *c*-domains comparable to the sizes of *c*-

domains themselves[41]. When the growth rate surpasses the nucleation rate, large bundles of plates will form, which have begun from different centers of ordering. When a bundle of plates is grown from the same center, the *c*-domain boundaries are invariant: there are no internal stresses for them. When blocks, plates, or bundles have grown from different centers, their boundaries may be noninvariant, coherent or incoherent[41]. These types of boundaries typically involve internal stresses, dislocations, vacancies or other defects, which suppress magnetic exchange interaction of moments across the boundaries.

1.6. Magnetic Properties

While typical explanations on the theory of magnetism require electron band theory, a simplistic model can be provided where magnetic moments are generated by two atomic contributions: 1) the orbital motion of electrons, and 2) the spin of the electron. It is the sum of these two moments that gives the moment of the atom, and the vector sum of all magnetic moments of atoms in a material that give the magnetization **M** (per unit volume). If in the absence of an applied field, the magnetic moments sit randomly and the sum magnetization is zero, the system exhibits paramagnetism. If however, there are strong positive exchange interactions ***(A)*** between neighboring atoms, the system exhibits ferromagnetism. Thermal fluctuations tend to misalign some of the atomic moments, such that their vector sum is less than theoretically possible. It is also common for ferromagnetic materials to break apart into magnetic domains, with the vector sum of the moments in different domains aligned along different directions: cancelling or reducing the overall magnetization. The magnetocrystalline anisotropy **(K)** or crystal anisotropy influences the magnetization such that moments of atoms prefer to be aligned along specific crystallographic directions, which are commonly referred to as “easy” axis directions. For the $L1_0$ phase, the “easy” magnetization axis is along its *c*-axis. In addition to these energies, ferromagnetic materials also possess a magnetostatic energy, which is associated with the demagnetizing field of the sample (the internal field produced in a sample opposite in direction to that of its magnetization). The demagnetizing field (and magnetostatic energy) can be reduced by the formation of domains. Domain walls are formed when the increase in interfacial energy is less than the magnetostatic energy reduced.

	FePd	**FePt**	**CoPt**
Curie Temp. **T_C** (K)	730	750	720
Saturation Magnetization **M_S** (emu/cm^3**)**	1100	1150	800
Magnetocrystalline Anisotropy Constant **K** (10^7 ergs/cm^3)	2.0	6.6	4.9
Exchange Constant **A** (10^{-6} erg/cm)	2.7	2.7	2.7

Table 1.2. Relevant magnetic property values taken from Vlasova, for the $L1_0$ containing ferromagnetic alloys.

Domain walls are inherently regions of increased exchange energy, as spin alignment must vary in the wall. The direction of magnetization varies within the wall between two domains, in a fashion such that there is a gradual transition between one domain and the next. Domain wall widths are determined by the balance between magnetocrystalline and exchange energies: magnetocrystalline anisotropy prefers spin alignment along its easy-axis (thinning the wall), while the exchange energy prefers to minimize misorientation between adjacent spins (thickening the wall). Bloch and Neel walls are two different domain wall types: Bloch walls involve magnetization rotation within the plane of the wall, while Neel walls involve magnetization rotations in a plane perpendicular to the domain wall.

For magnetic materials which are sufficiently large to allow domain wall formation, magnetization reversal proceeds by domain wall motion. Under an applied field, domains with magnetization directions closest to the applied field direction will grow at the expense of other domains. As the domain wall progresses through the material, local energy minima can hinder or pin the domain wall. Pinning sites may take the form of defects, inclusions (second phase particles), or other local changes in magnetic properties brought about by cracks, holes or residual microstresses. Unpinning of domain walls requires additional energy from the applied field. A material with many imperfections will require a higher reverse field to reduce internal magnetization to zero.

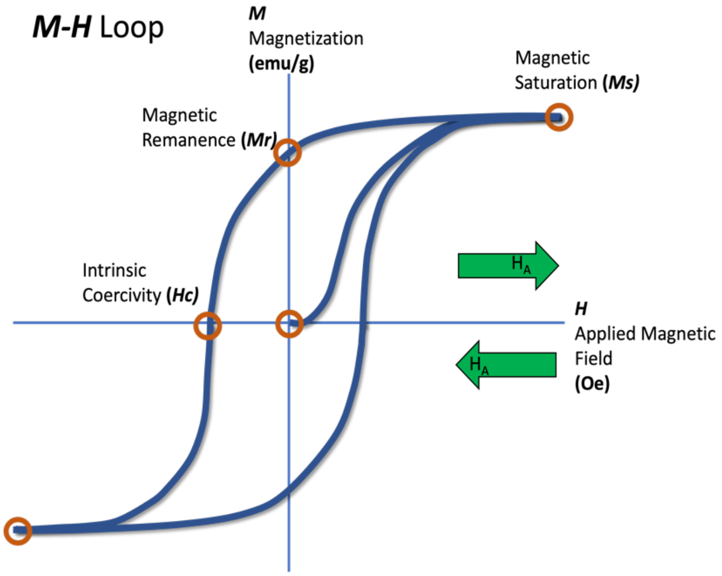

Figure 1.17. Schematic major hysteresis loop (M-H), where Magnetic saturation, magnetic remanence, and intrinsic coercivity are defined.

Anti-phase boundaries also serve as local variations in the magnetic properties, and are classically regarded as the fundamental pinning mechanism in polytwinned microstructures[23,42]. Within polytwinned microstrucutres, both 1) frozen domain walls found along macrotwin boundaries, and 2) mobile serrated 180° domain walls are found to exist.

In Fig. 1.17 a magnetic hysteresis loop is shown, where the magnetic moment per unit volume (magnetization M) is measured as a function of the applied external magnetic field (H). The initially demagnetized sample is saturated at the value $M=M_S$. When the field is reversed to 0 Oe, the residual magnetic moment is called the remanence M_R. The amount of applied field required to reduce magnetization to zero is called the intrinsic coercivity H_C. Materials that exhibit high coercivities are referred to as "hard" magnets: when the inverse is true, they are referred to as "soft" magnets.

1.7. The Fe-Pd System

While the computationally-determined phase diagram may be significantly troubled by unaccounted for energetic interactions[26,34], experimental results in Fe-Pd have also been anomalous at times. Loebich[29] found unexpected ordering phenomena near the Pd-rich eutectoid region. Loebich reports that for nominally on-eutectoid compositions (Fe – 62 at% Pd), two-phase $L1_0 + L1_2$ equilibria was seen at 600°C but only single-phase $L1_0$ when annealed at 500°C. While their finding *could* be explained by retrograde solvus boundary (as in Ni-Al[43]), this behavior is relatively anomalous and may be an unlikely explanation. Our results will later show that this ordering phenomena may be caused by the existence of L1' ordering (and an attendant strain-related solvus boundary shrinkage).Other peculiar phenomena have been reported in Fe-Pd. For example, Vlasova[44] observed a metastable disordered tetragonal phase (A6) in the transformation pathway for equiatomic Fe-Pd alloys. Laughlin[45] studied the effect of ordering on the Curie temperature for Fe-Pd $L1_0$, and found an inverse relationship between Pd-composition & T_C. However, more importantly, Laughlin commented on the discrepancies found between reported Curie temperatures (T_C) in the literature. These were later explained by Vlasova[46] to be a function of the temperature and length of annealing time. Vlasova[46] also found a trend between the dependence of magnetic anisotropy constant on temperature $K(T)$ of Fe-Pd single crystals which contradicted the standard (two-ion anisotropy) model: analogous Fe-Pt & Co-Pt samples are satisfactorily explained by this model.

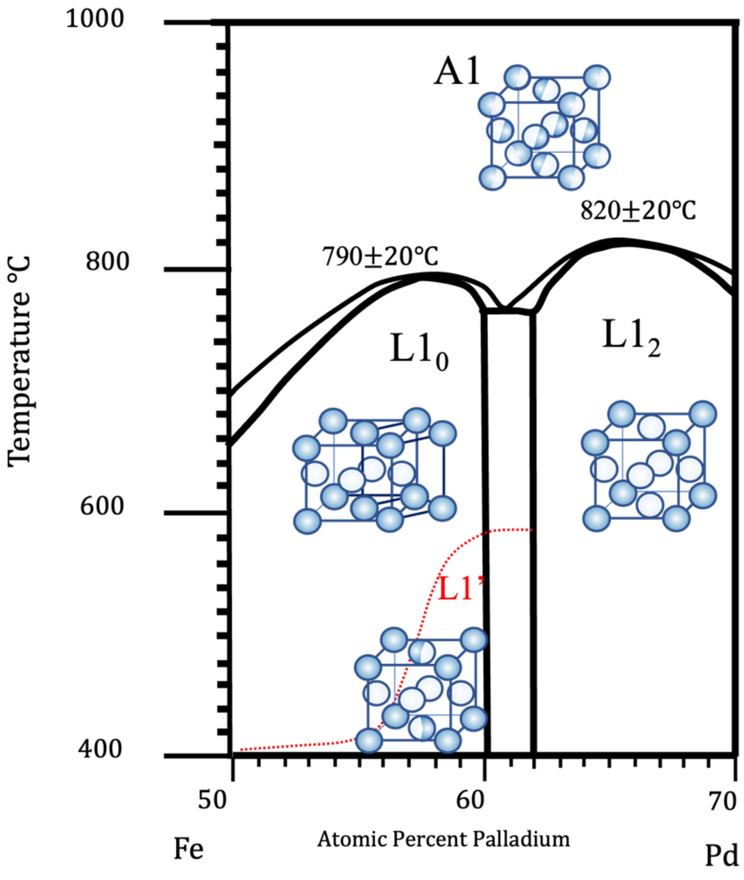

Figure 1.18. The eutectoid region (A1 → L1$_0$ + L1$_2$) of the Fe-Pd phase diagram. At low termperatures L1' ordering is observed, and is the central focus of chapter 3 in this dissertation.

A snippet of the eutectoid-region phase diagram is given in Figure 1a, with accompanying unit cells for the phase of interest in Fig. 1.18a. As a brief primer, the solid solution FCC A1 phase decomposes into two-phase L1$_0$ + L1$_2$ below the eutectoid isotherm of ~760±30°C. As given in table 1, L1$_0$ is an ordered tetragonal phase (P4/mmm space group, tP2 Pearson symbol), whereas L1$_2$ is an ordered cubic phase (Pm$\underline{3}$m space group, cP4 Pearson symbol). L1' is a low-temperature ordered tetragonal phase, but has different translational symmetry than L1$_0$ (P4/mmm space group, tP4 Pearson symbol).

As shown in Chapters 3,4 of this dissertation, we show that at low temperatures (and as predicted in the preceding phase diagrams of Shockley[13], Finel & Ducastelle[20,21]) there exists a second ordered tetragonal phase exhibiting different ordering of off-stoichiometric atoms (relative to equimolar) labelled L1'. The $L1_0$ phase in Fe-Pd has typically been studied at or near equiatomic compositions. For example, Soffa et al.[23,31] studied magnetic hardening and coercivity mechanisms in Fe-Pd $L1_0$. Wiezorek et al.[47–50] studied combined reaction processing to increase magnetic coercivity of equiatomic $L1_0$ in Fe-Pd. Fe-Pd $L1_0$ thin films have also been studied extensively for their use in nanoscale applications, where their large magnetocrystalline anisotropy constant (K) can overcome the superparamagnetic limit at small volumes[51]. Fe-Pd thin films have been grown with a varied assortment of techniques: molecular beam epitaxy[52,53] , pulsed laser deposition[54], and electrochemical methods[55].

The closest studies done on/near the Fe-Pd $L1_0$ + $L1_2$ eutectoid region was done with thin films. Steiner[56] grew $Fe_{38.5}Pd_{61.5}$ thin films and found that depositing at 650℃ or 600℃ yielded a single phase L1' (Steiner says tetragonality distorted $L1_2$), whereas for films aged at 550℃ a two-phase mixture of $L1_2$ + Fe-rich FCC thought to arise from a metastable extension of the FCC + $L1_2$ region induced by epitaxial strain. In a subsequent report done on on-eutectoid composition thin films, Steiner[57] explored the L1' ordering postulated earlier, and envisioned a two-order order parameter to study Fe & Pd sublattice ordering rigorously. Interestingly, in Steiner's work[56], $L1_2$ was shown to order first, before any $L1_0$ formation – as we show in subsequent chapter on two-phase coexistence in Fe-Pd bulk, this may be due to continuous ordering for samples sufficiently undercooled below the critical temperature T_C and instability temperature T_i^-.

1.8. Analogue Binary Alloys (Co-Pt, Fe-Pt)

The Pt-rich Co-Pt eutectoid region was first explored by Leroux et al.[58] in 1991, where continuous cooling experiments through the eutectoid isotherm led to the unique nanochessboard microstructure (see Fig. 1.19a). For the eutectoid reaction in Co-Pt A1 → $L1_0 + L1_2$, strain-driven self assembly led to patterning of $L1_0$ *c*-domain rods within an $L1_2$ matrix such that when viewed end-on, this structure resembled a chessboard. In Fig. 1.19a, a DF-TEM image of the nanochessboard is shown, where the illuminated 'light' regions correspond to the $L1_2$ matrix, whereas the dark regions correspond to "X" and "Y" pairing of $L1_0$ domains. This alignment of "X" and "Y" $L1_0$ domains is visible clearly in the complementary schematic attached in Fig. 1.19b, where the red arrows show the direction of the *c*-axis for the respective $L1_0$ domains (this image

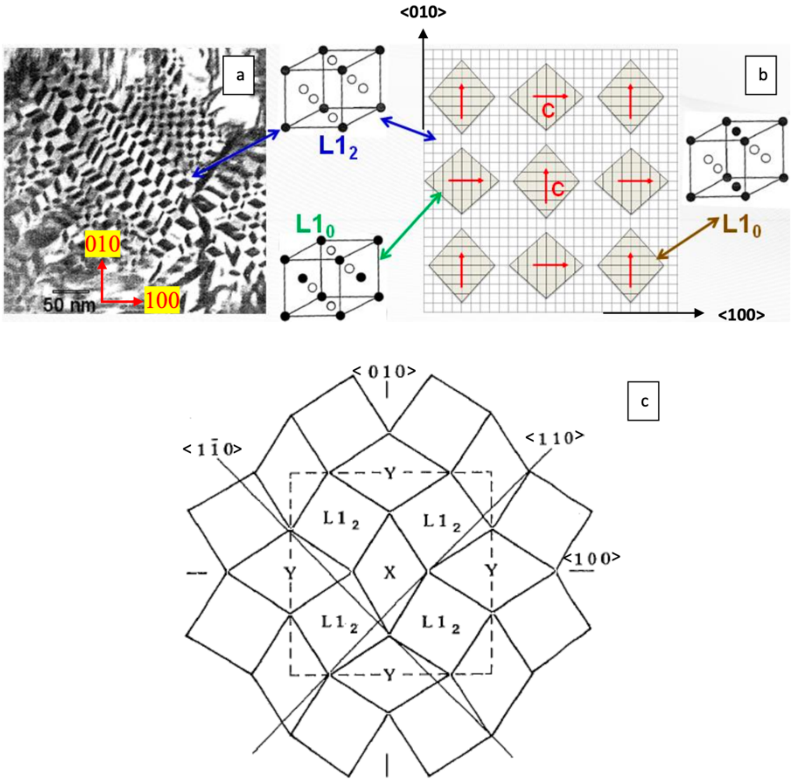

Figure 1.19. A DF-TEM micrograph of the nanochessboard found in Co-Pt[58] is shown in a), where black (white) regions correspond to $L1_0$ ($L1_2$). The orientation of the $L1_0$ variants is shown in b), where red arrows correspond to *c*-axis direction. In c) enmeshment of $L1_0$ variants "X" & "Y" in the $L1_2$ matrix is shown.

is in direct correspondence to Fig. 1.19a). The orthogonal patterning of $L1_0$ domains is further highlighted in Fig. 19c, where “X” and “Y” correspond to $L1_0$ domains aligned along [100] and [010] respectively, and the $L1_2$ square regions correspond to the ordered cubic matrix phase.

Although Leroux[58] first identified the nanochessboard microstructure, the magnetic properties of this two-phase structure were not probed until work done by Prof. Floro. By changing continuous cooling rates (40°C/Day - 80°C/Day) through the eutectoid isotherm, Vetter et al.[59,60] found fungibility of chessboard-tiling lengthscale (from 10-40nm) which in turn dictated degree of exchange coupling between the $L1_0$ domains and $L1_2$ matrix. Vetter found, that when $L1_2$ domains were kept below a critical lengthscale (~ 20nm), the $L1_2$ magnetically soft-phase would exchange-

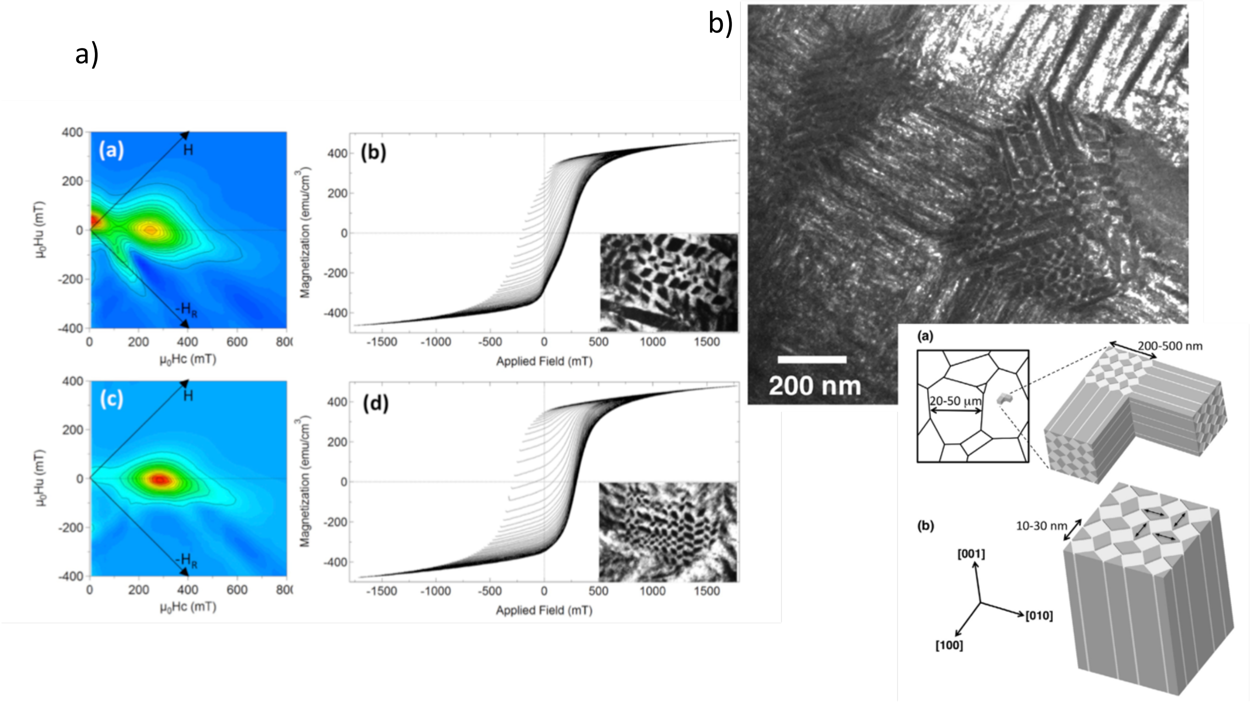

Figure 1.20. In a) two major hysteresis loops are shown, done on samples exhibiting microstructural lengthscals above a critical dimension (b) and below (d). The density plots of a) correspond to b,d, respectively and qualitatively show the existence of two reversal events (a) and one (b), which are measures of degree of exchange coupling. In b), a DF-TEM shows the nanochessboard and the hierarchical construction of a chessboard where nanrods align along al;l three <100> directions of the A1 parent matrix (per grain).

couple[61] to the magnetically hard $L1_0$ phase and a single magnetic phase was observed. When magnetic phases are properly exchange coupled, there is a single magnetization reversal event. However, when lengthscales approached or increased the critical lengthscale dimension, coupling between magnetic phases was not observed and two reversal events (corresponding to $L1_2$ and $L1_0$ respectively) were observed. This is seen in Figure 1.20a), where first order reversal curves (FORCs) and hysteresis loops of these differently processed $Co_{40}Pt_{60}$ samples exhibit large, un-coupled magnetic behavior (top) and single-phase, coupled behavior (bottom). Ghatwai[62]studied the magnetic behavior of Co-Pt compositions bracketing the eutectoid region. Floro[63] also showed that the hierarchical nature of nanochessboards leads to a demagnetization field at chessboard boundaries which influences reversal mechanisms and coercivities.

The Fe-Pt eutectoid regions of Fe_3Pt + FePt , or FePt + $FePt_3$ have never probed for microstructure – magnetic property optimization, despite exhibiting higher magnetocrystalline anisotropy and magnetic saturation. Nose[64]re-examined the Fe-Pt phase diagram. However, Fe-Pt $L1_0$ has been studied, and maximum coercivities were observed at non-stoichiometric compounds. Tanaka[40,65] found maximum coercivity for $L1_0$ samples at Fe – 39.5 at% Pt with the 'tweed' pretransition state (coarsened tetragonal nanodomins). Watanabe[66,67] also found maximum coercivity for Fe-Pt alloys at off-stoichiometric compositions (Fe – 36 at% Pt), where he (incorrectly[23] suggested microtwinning in the $L1_0$ domains prevented domain wall motion.

1.9. Cubic → Cubic + Tetragonal Trasnformations

A general three-dimensional phase-field model to study $cubic \rightarrow cubic + tetragonal$ decomposition was formulated by Khachaturyan[36]. Figure 1.21a gives free-energy curves (G vs *c)* for cubic & tetragonal phases, with equilibrium comcpositions c_α and c_β. Included in the schematic are regions labelled A and B, white denote relationship to the critical composition c_0. Khachaturyan[36] finds that the transformation pathways differ significantly in regions A and B.

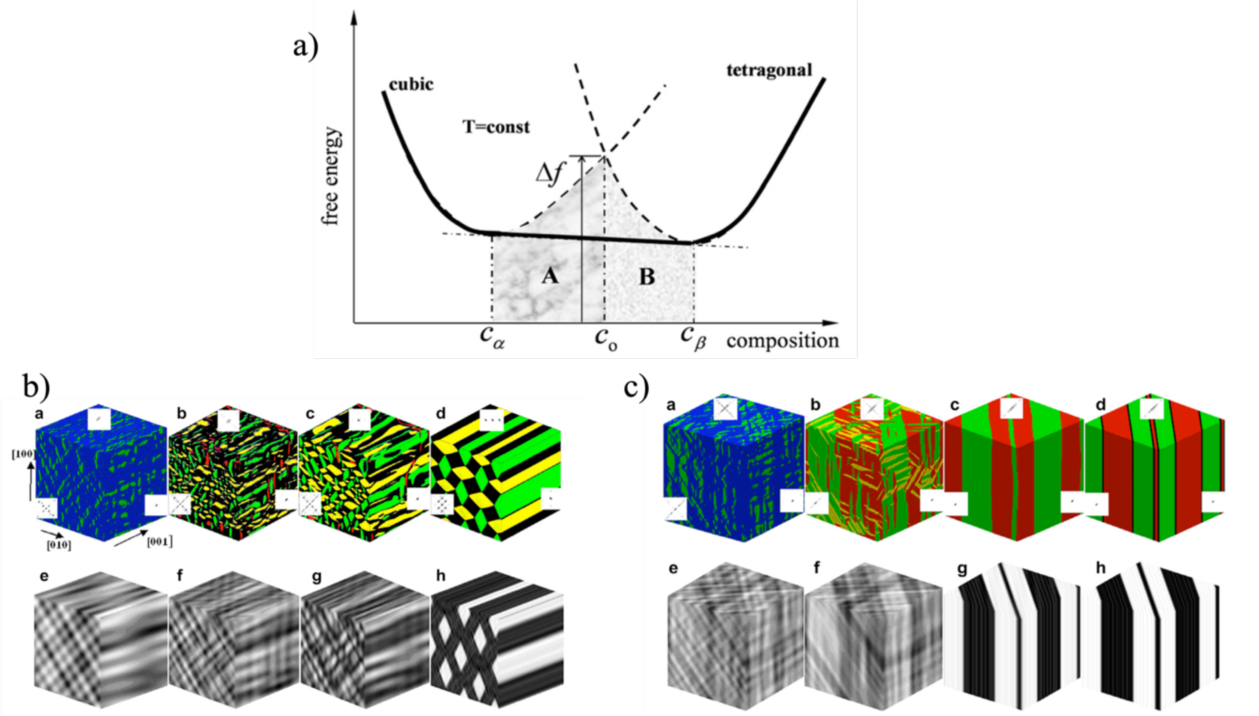

Figure 1.21. Free energy curves of cubic → cubic + tetragonal transformation as given by Khachaturyan[36]. Decomposition transformations differ signifncantly between regions A and B, as shown in the end-state microstructures of b) and c). In b) the nanochessboard is formed, while in c) polytwinned microstructure with cubic wetting layers are observed.

In region A (*c* <0.5), a diffusionless cubic → tetragonal transformation is not permitted, since the tetragonal curve is situated with a higher free energy than the cubic curve. Instead, the transformation progresses by fluctuations of composition and long-range orders parameters[36]. As shown in Fig. 1.21b, tetragonal nanodomains (constituting the tweed pre-transition state) are nucleated, oriented along the principal <100> directions (shown by the range of colors in Fig. 1.21b,(b)). The progression in Fig. 1.21b,(c-d) shows how as tetragonal nanodomains impinge and coalesce, diamond tetragonal domains are formed followed by precipitation of the cubic phase. This shows the formation of the chessboard microstructure. Interestingly, experimental results in Ghatwai's dissertation[68] suggest an alternative pathway for nanochessboard formation in Co-Pt, with $L1_2$ (matrix) formation first. The spatial organization of cubic + tetragonal domains into the chessboard structure is strain-driven, and relieves internal stresses accrued during the nucleation of the tetragonal domains.

In region B ($c\sim0.55$), a similar tweed pre-transition state is formed (as shown in Fig. 1.21c,(a)). Only after long times (needed to reach equilibrium), does the tweed transition state change evolve to form the polytwinned microstructure. Khachaturyan finds this congruent (isocompositional) transformation to be a diffusionless, displacive transformation. Again, only after long aging times (within the phase field model) does the cubic phase appear, wetting the (110) interfaces of the tetragonal phase. This two-phase microstructure is depicted by the tetragonal green + red domains and thin black lines (cubic domains) separating them in the end-state given in Fig. 1.21c,(d).

Grain-boundary segregated phases were first discussed in the context of complexion phases, as proposed by E.W. Hart[69,70] who suggested that grain boundary transitions may be responsible for temper embrittlement and segregation along the grain boundary in steels. Grain boundary complexion phase engineering is currently being explored as an avenue to improve the performance of polycrystalline materials. For example, nanostructuring of Ti alloys[71] is currently being explored where thermal phase transformations form an orthorhombically twinned structure with a thin hexagonal layer sandwiched at their hetero-interfaces.

Figure 1.22 shows the above mentioned transformation in the Ti alloy[71], where a DF-TEM image is used to highlight the 'wetting' hexagonal layer. It is suggested, that interface 'engineering' with complexion phases may be a critical step forward to achieving optimal material properties[72]. In addition, a better understanding of these grain-boundary and interface phases may explain current issues in the field of materials science, such as abnormal grain growth in organic materials[72].

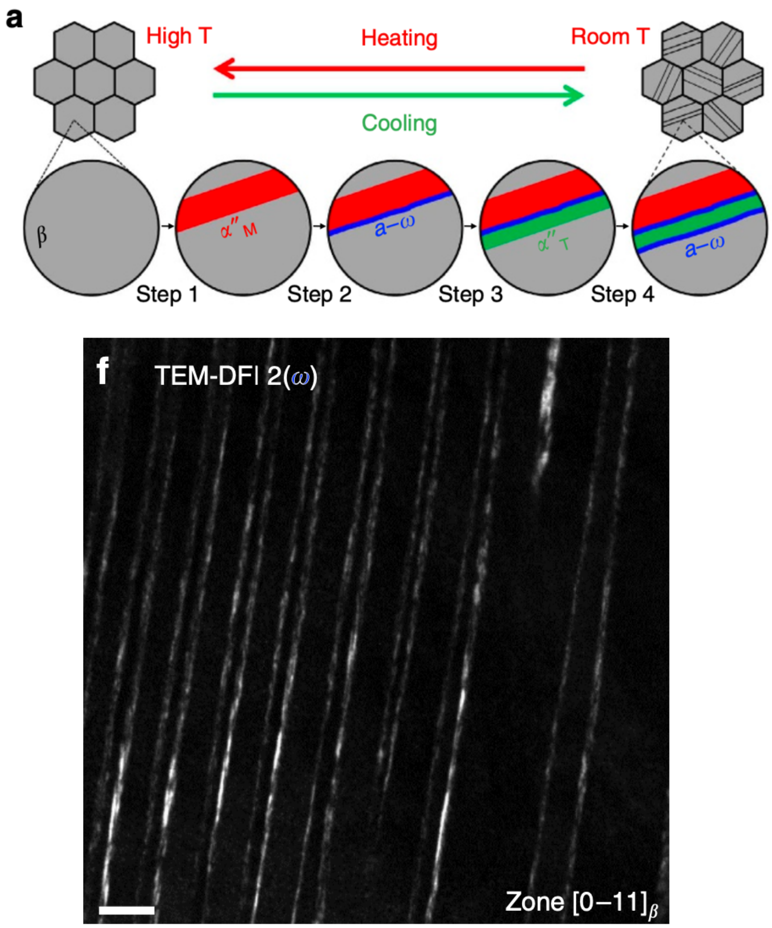

Figure 1.22. Transformation pathway in Ti alloys where the orthorhombic phase (α'') develops a hexagonal complexion phase at the interphase (via a martensitic transformation).[71]

Chapter 2. Experimental Techniques

2.1. Alloy Preparation

High purity iron chunks and 99.9% Palladium pieces were cleaned ultrasonically, then rinsed with acetone and ethanol. The elemental pieces were melted in a makeshift arc melter, using a sharpened tungsten electrode with a water cooled copper hearth. The chamber was evacuated to <50 mTorr with a roughing pump, then backfilled with high purity argon to ~500mTorr: this process was cycled 2-3 times to properly remove any remaining oxygen within the chamber. A small titanium 'oxygen getter' was placed within the center of the copper hearth, to limit any remaining oxygen present within the evacuated chamber. The melted boule (button) was flipped 2-3 times and re-melted to ensure macroscale chemical segregation was mitigated.

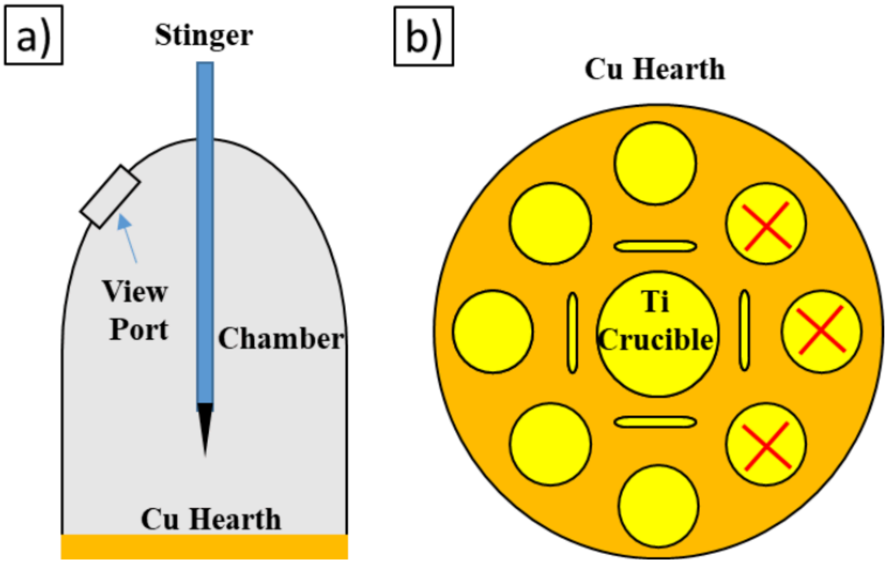

Figure 1. Schematic of the arc-melter as made by Wade Jensen[113], where red X's mark where you cannot strike.

2.2. Encapsulation Procedure for Heat Treatments

For heat treatment at elevated temperatures all samples were placed within a fused quartz ampule which was sealed at both ends. In order to form the fully sealed quartz ampule, the fused quartz tubes were attached to a vacuum manifold (after placing sample within and forming a neck) and evacuated to <5 millitorr before backfilling with forming gas (5% hydrogen + 95% Nitrogen mixture). A flushing procedure was repeated roughly 2-3 times, to ensure the ampule had limited oxygen remaining. In addition to using forming gas, a piece of Zr foil (~3cm x 3mm) was placed within the fused quartz ampule serving as an oxygen getter. Care was made such that the pieces of material (Zr and Sample) were separated during the anneal, to prevent diffusion of species. A final backfill with forming gas used, and the top of the fused quartz tube was sealed off using an oxy-acetylene torch. Shade 8 glasses were used, in addition to leather fire-resistant gloves (PPE).

2.3. Homogenization and Disordering Anneal

The as-cast boules (buttons) were cut with a Mager Cut-Off saw using a silicon-carbide blade into halves (if the mass of the initial melt was >15g). For specimens with small initial melt mass, the sample was passed through a cold-roller up to a thickness reduction of no greater than 60%, with the specimen going length-wise and in the same direction with the parallel surfaces of the samples touching the rollers. These samples were then encapsulated (as presented in the procedure above) then placed within an MTI tube furnace for 1000°C for roughly 24 hours before quenching within room-temprature water. If the samples did not break upon contact with water, rapid measures were taken to break the ampule with tongs: proper PPE was worn during this procedure if it was required (masks, gloves, lab jacket).

2.4. Inductively Coupled Optical Emission Spectra

Bulk compositional analysis was performed on as-cast samples by Inductively Coupled Plasma – Optical Emission Spectroscopy (Thermo Scientific iCap 6200). 25mg from the sample of interest was digested in heated aqua regia (3:1 HCl + HNo3 by volume), within a fume hood. The solution was then diluted to 50-200 ppm with DI water, for analysis. The reported measurements (the author did not perform these measurements) were said to be Fe 61.8 at% Pd, and Fe 62.2 at% Pd. The error from this method was found to be ~1 at% for all components. A note should be made here that compositional measurements are non-trivial, and involve fundamentally a rigorous calibration curve. High fidelity standard measurement of relevant elemental materials (in this case Fe, Pd) at intervals of 0 ppm (reference), 0.1 ppm, 1ppm, 10ppm, 100ppm, and 1000ppm should be made. Calibration curves 'fit' the points: interpolation between points is typically done. The quality of the calibration curve determines the quality of the compositional measurement. If elemental standards are not measured down to low levels (0.1, 1 ppm) the calibration curve may be considered poor quality. While typically bulk compositional measurements may not suffer with deviations of up to 1 at %, two-phase regions may be as narrow as 1-2 at % : as such, minute deviations can non-negligibly alter veritable composition measurements.

2.5. X-ray Diffraction Measurements

X-ray diffraction measurements were made on a Panalytical Empyrean X-ray diffractometer, operating at 40kV, 40mA with Cu-Kα (1.54 Å wavelength) radiation. Prior to operation, samples were polished with successive series of polishing paper: 600, 800, 1200 grit sizes were used. Polishing was carried out in cross-hatch fashion, to ensure damage accumulated during one direction was removed during polishing performed at a direction orthogonal to the previous direction. Following the grit polishing, the samples were polished with a suspended diamond slurry of $3\mu m$ dimensions, to give a satisfactory 'mirror' shine. Powder diffraction geometry was used (Bragg-Bentano), a multi-purpose sample stage (typically rotating stage, though not in rotation mode), and a zero-diffraction Silica backscatter plate. Incident / diffracted beam optic settings were adjusted for each geometry, to ensure maximum diffraction area was probed. For general phase identification measurements, the sample was scanned from low to high angles : 15° – $100°\ 2\theta$. For high-fidelity measurements, typically the smallest step size was chosen (0.007°) and scanned for ~1hr, for a given 2θ of 2-5°. Phase identification and peak assignment was typically done post-measurement with calculated structure factors: lattice constants were either extracted from individual families of reflections for tetragonal ({200}/(002)) or from satisfactory Rietveld refinements done in the GSAS-II[73] software package.

2.6. Transmission Electron Microscopy

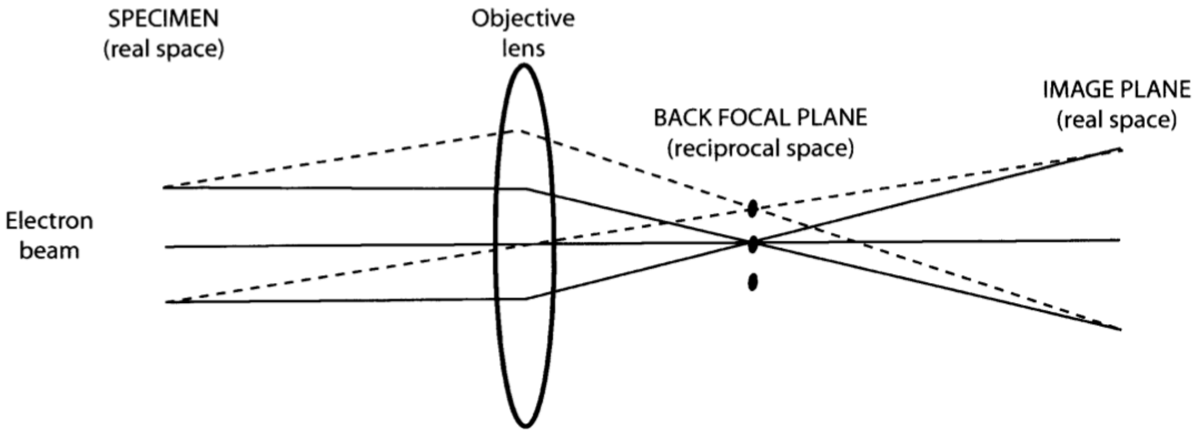

Figure 2. Optical ray diagram showing the general operation of the transmission electron microscope.[74]

The optical ray diagrams of Figure 2 shows the main principle of electron microsopy2. Diffraction spots are formed from diffracted waves on after being focused by the objective lens onto the back focal plane. These waves are then recombined to form an image on the image plane. Electromagnetic lenses can be used to focus the diffracted electrons into a regular arrangement of diffraction spots that can be projected and recorded as the electorn diffraction pattern. When the transmitted and diffracted beams interfere on the image plane, a magnified image of the sample can be made.

3mm discs were first cut from samples hand polished down to ~100μm. Following this, they were electrochemically etched in a Fischione twin-jet electropolisher with an electrolyte solution of 82% acetic acid, 9% perchloric acid, and 8% ethanol by volume in an ice bath at roughly 30V. The microscope used was a ThermoFisher Titan operating at 300kV with a GATAN double tilt specimen holder capable of tilting +/- 40 degrees in α.

Two measurement techniques were employed beyond conventional electron microscopy: both bright field (BF) and dark-field (DF) imaging was employed. Objective apertures are used to control the contrast in the image. The objective aperture can also allow certain reflections to contribute to the image (negating others). In bright-field mode, a small objective aperture is placed around the incident beam only, to form the final image[75]. Contrast arises from thickness or compositional variations (or structural anomalies). In dark-field imaging mode, the diffracted beam is moved such that only the diffracted beam only is allowed within the center of the objective aperture[75]. With DF-imaging condition, only the regions of material which generated the diffraction point (which have satisfied the Bragg diffraction condition $\vec{g}$) will be viewed, which is useful for material characterization. Typically a superlattice reflection is chosen to view ordered materials from within a disordered parent / matrix.

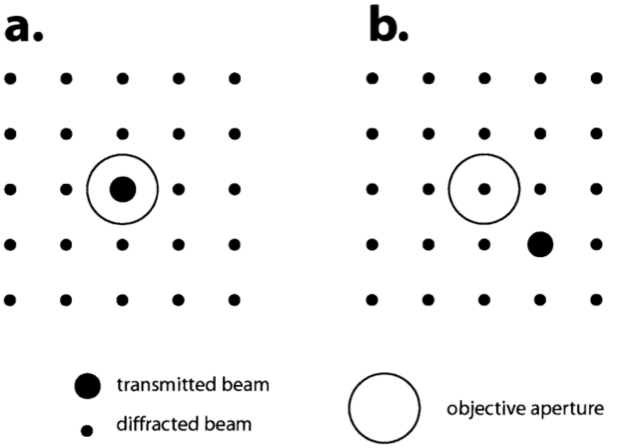

Figure 3. The objective aperture can be placed to view: only the incident beam (bright field) in a), or only a diffracted beam (dark-field) in b).[74]

2.7. Magnetic Measurements

Hysteresis loops were made on a VSM 7400 Vibrating Sample magnetometer (VSM) operating with a computer controlled, menu0-driven program. Fields were applied +/- 20 kOe (2 Tesla) in forward and reverse direction. All measurements were made on 3mm discs to ensure minimum demagnetizing fields were applied to the samples. All measurements were performed at room temperature, so temperature dependency was not explored / controlled.

Chapter 3. Evidence and Characterization of L1’

The Fe-Pd phase diagram near the eutectoid region is show below in Figure 3.1a, with accompanying unit cells for the phases of interest in Fig. 3.1b where Blue(White) atoms are Fe(Pd) respectively. For compositions between the $0.50 < c < 0.60$ in Fe-Pd alloys, there exists at low temperatures an ordered tetragonal phase, L1’, first predicted by William Shockley in 1938[13]. The remaining section will show how at low temperatures, the readily accepted $L1_0$ phase is replaced by L1’, where accommodation of excess (relative to equimolar) atoms (in this case Palladium) is placed solely on the (½, ½, 0) site for L1’, in contrast to $L1_0$ where it is distributed equally amongst all Fe-sites. While both $L1_0$ and L1’ share the P4/mmm space group, their Pearson symbols differ. For $L1_0$ the tetragonal structure reduces to Pearson symbol tP2, while for L1’ the Pearson symbol is tP4.

This chapter first aims to prove the existence of the L1’ phase found when aging ~Fe- 62 at% Pd samples at 525°C. Evidence is provided first by quantitative X-ray diffraction analysis. Superlattice peak assignment and long-range order comparison against the $L1_0$ phase gives significant justification for L1’ phase identification. Following this, the polytwinned microstructure of L1’ will be examined in detail, where electron diffraction pattern and dark-field microscopy analysis further supports the existence of L1’. Lastly, magnetic measurements for $L1_0$ & L1’ are compared, where observed differences may be ascribed to magnetic ordering variation between the phases.

3.1. Ordering

The following interpretation of X-ray diffraction results rests upon correct assignment of superlattice reflection of the two ordered phases ($L1_0$ and L1'). As such, it is important to understand the allowed reflections of the two phases. Table 1 shows the reflections for both structures to the $2\theta = 100°$, showing both superlattice (ordered) and fundamental reflections. Although both structures are tetragonal, and thus exhibit certain fundamental split reflections (e.g. {200}/(002) or (220)/{202}) the allowed superlattice reflections will differ as the periodicity has changed along the [110](001). This change is observed in the relaxation of the allowed ordered reflections for L1', which mirror those of $L1_2$. For $L1_0$, the allowed superlattice reflections must satisfy the criteria of $H + K = 2N$. Included in Table 3.1, for all of the allowed reflections of L10 & L1', the 2θ value for this composition in Fe-Pd is given next to it. In addition to the placement, the intensity is attached on the right, generated from the Vesta software package. While intensities attached were taken from this open-source package, our calculations using structure factors were in direct agreement with ratios of computed intensities, showing concordance between our model and Vesta. In addition to showing the reflections and their position/intensity, we shall also provide the structure factors generated for the L1' phase, as the calculation of order for this phase has only been reported by our work[76] .

L1$_0$ 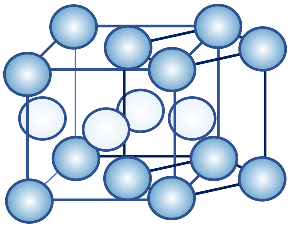			**L1’** 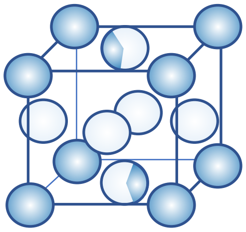			
hkl	**2θ**	**F$_{hkl}$ (Cu Kα)**	***hkl***	**2θ**	**F$_{hkl}$ (Cu Kα)**	**F$_{hkl}$ (300 kV e$^-$)**
~~**100**~~	~~23.067~~	-	**100**	23.0674	8.9585	0.705
001	23.9929	28.6909	**001**	23.7265	28.7811	2.266
110	32.8446	25.3674	**110**	32.8466	25.3674	2.500
~~**101**~~	~~33.523~~	-	**101**	33.328	7.7771	0.790
111	41.0862	94.7423	**111**	40.922	95.0313	16.434
200	47.1367	84.4197	**200**	47.1367	84.4197	14.681
002	49.1271	81.1798	**002**	48.5547	82.103	14.356
~~**210**~~	~~53.1075~~	-	**210**	53.1075	5.51544	13.225
201	53.5695	17.7055	**201**	53.4354	17.7488	1.873
~~**102**~~	~~54.9391~~	-	**102**	54.4109	5.38596	1.849
~~**211**~~	~~59.0753~~	-	**211**	58.9496	4.95641	1.719
112	60.3626	15.6342	**112**	59.8655	15.777	1.696
220	68.8688	54.0179	**220**	68.8688	54.0179	1.453
202	70.4496	52.2457	**202**	69.9916	52.7531	1.428
~~**300**~~	~~73.7059~~	-	**300**	73.7059	3.7801	1.337
221	74.0916	12.1515	**221**	73.9796	12.1764	1.332

~~**212**~~	~~75.2443~~	-	**212**	74.7982	3.7056	1.316
003	77.1522	11.4939	**003**	76.1555	11.7036	1.289
310	78.4262	11.232	**310**	78.4262	11.232	1.236
~~**301**~~	~~78.8042~~	-	**301**	78.6943	3.45282	1.231
~~**103**~~	~~81.8118~~	-	**103**	80.8308	3.32254	1.193
311	83.441	39.7854	**311**	83.3326	39.8748	1.142
113	86.4174	37.4189	**113**	85.4452	38.1734	1.109
222	89.147	35.3931	**222**	88.7159	35.7041	1.052
~~**320**~~	~~92.2455~~	-	**320**	92.2455	2.71805	0.997
~~**302**~~	~~93.7297~~	-	**302**	93.2979	2.66949	0.983
203	95.5887	8.3118	**203**	94.6151	8.45003	0.967
~~**321**~~	~~97.2145~~	-	**321**	97.106	2.5028	0.930
312	98.3365	7.9374	**312**	97.9012	7.99525	0.921
~~**213**~~	~~100.214~~	-	**213**	99.23	2.41579	0.906
400	106.2	25.444	**400**	106.2	25.444	0.823

Table 3.1. This table shows the allowed reflections (both superlattice and fundamental) for the two tetragonal structures in question: L10 and L1'. For the L10 superstructure, superlattice reflections are allowed but must satisfy the *H+K=2n* criteria. For the L1' structure, superlattice reflection conditions are relaxed, and match those of the ordered cubic L12 phase. The placement of the reflections are given, in addition to the intensities generated from the Vesta package.

An order parameter for the L1' phase was first attempted by Steiner[57], who showed that a two-order parameter model would suffice, essentially combining the L1$_0$ and L1$_2$ Bragg-Williams[77] order parameter. Typically, long-range order parameters are defined using the Bragg-Williams c, where in an example binary alloy with A,B atoms, a perfectly-ordered stoichiometric crystal would have all A-atoms populate α-sites and B-atoms populate β sites. There exists a relationship between the concentration of these atoms in the crystal, such that $X_A + X_B = 1$, where X_A, X_B are the concentrations of A,B atoms respectively. In addition, the sum of the A and B concentrations on any lattice site must equal unity: that is, $A_\alpha + B_\alpha = 1$ and $A_\beta + B_\beta = 1$, where$A_\alpha, B_\alpha$are A,B on the α site. This then allows us to write scattering factors for the α and β sites respectively, as:

$$f_\alpha = A_\alpha f_A + B_\alpha f_B$$

$$f_\beta = A_\beta f_A + B_\beta f_B$$

In order to construct an order parameter, the general quantity of species given with the crystal is also defined, such that for an ordered crystal with AB composition (i.e. L1$_0$), the quantities $y_\alpha = y_\beta = 0.5$. However, for an ordered crystal with AB$_3$ composition (while this is typically referred to as L1$_2$, L1$_2$ may also form at A$_3$B compositions), $y_\alpha = 0.25$, and $y_\beta = 0.75$ (for the A$_3$B composition the values would be flipped, $y_\alpha = 0.75$, and $y_\beta = 0.25$). As one can see, $y_\alpha + y_\beta = 1$. This allows us to re-write the concentration of the species in the crystal as follows:

$$X_A = y_\alpha A_\alpha + y_\beta A_\beta$$

$$X_B = y_\alpha B_\alpha + y_\beta B_\beta$$

This allows for the construction of a long-range order parameter, S, where S=1 for a stoichiometric, fully ordered material, and S=0 for a completely disordered material:

$$S = \frac{A_\alpha - X_A}{1 - y_\alpha} = \frac{B_\beta - X_B}{1 - y_\beta}$$

This order parameter is composition-dependent, and allows for calculation of structure factors for superlattice reflections, (ordered reflections). These are helpful, and ensure that the values generated from structure factors are directly proportional to the composition. Generally speaking, for $L1_0$ the structure factor for fundamental reflections is given as $2(f_\alpha + f_\beta)$, which are of intensity $4(X_A f_A + X_B f_B)$, while superlattice reflections have intensity $2S(f_A - f_B)$. Likewise, for the $L1_2$ crystal structure, we have fundamental intensities of $(f_\alpha + 3f_\beta)$ and superlattice intensities of $S(f_A - f_B)$.

While these parameters are useful for calculating structure factors for off-stoichiometric specimens, we aim to show briefly that for L1', the two-order parameter model proposed is identical to the structure factor for a pseudo-cubic lattice with 4-atom basis. While Steiner[57] shows, rigorously, a mixed long-range order parameter, incorporating both $L1_0$ and $L1_2$ order parameters into one, we show here briefly, that such an expansion is not necessary, as they are identical.

Without worrying too much about defining an order parameter, we can calculate a structure factor for L1' using the different sites listed in Figure 2, and the constituent species present on those sites as follows.

$$f(L1')_{hkl} = f_\alpha(1) + f_\beta\left(e^{i\pi(h+l)} + e^{i\pi(k+l)}\right) + f_\gamma(e^{i\pi(h+k)})$$

Steiner nicely shows, in his dissertation and publication, that a long range parameter can be constructed as a superposition of the $L1_0$ and $L1_2$ order parameters, which he terms an *Smixed*:

$$S_{mixed} = \frac{A_\alpha + A_\gamma - 2A_\beta}{2} = \frac{A_\alpha + A_\gamma}{2} - A_\beta$$

This is used to calculate ordered reflections for L1' where the intensity is $2S_{mixed}(f_A - f_B)$, while the fundamental reflections are $4(X_A f_A + X_B f_B)$. We can show briefly, that while this may have been useful to characterize order in a strained system which did not show the characteristic L1' reflections (e.g. {100}/(001), (110)/{101} splitting), we can measure the degree of order in our L1' system by comparing calculated intensities of superlattice/fundamentals and comparing against measured (integrated) intensities of superlattice/fundamental reflections. We provide a brief example below of how the order parameter and the simple model are identical, for example of both {100} and the {101} L1'-only reflections. For $Fe_{38.2}Pd_{61.8}$ we have four atoms in our basis, divided as such: 1.528 Fe atoms, and 2.472 Pd atoms, which are distributed throughout the sites. Solving for the structure factors on each of the four sites α, β, γ we find that $f_\alpha = A_\alpha f_A + B_\alpha f_B = 1 f_A$ and $f_\beta = A_\beta f_A + B_\beta f_B = 2 f_B$ as there are two β sites, and $f_\gamma = A_\gamma f_A + B_\gamma f_B = 0.528 f_A + 0.472 f_B$. When solving the structure factor for the ordered reflections:

$$f(L1')_{100} = f_\alpha(1) + f_\beta\left(e^{i\pi(1)} + e^{i\pi(0)}\right) + f_\gamma(e^{i\pi(1)})$$

$$f(L1')_{100} = 1f_A + 2f_B(-1+1) - 0.528f_A + 0.472f_B(-1)$$

$$f(L1')_{100} = 1f_A - 0.528f_A - 0.472f_B = 0.472f_A - 0.472f_B = 0.472(f_A - f_B)$$

If we decide to calculate utilizing the Steiner two-order-parameter model, we find that $2S_{mixed}(f_A - f_B)$ for {100} gives us $2(\frac{A_\alpha - 2A_\beta + A_\gamma}{2})(f_A - f_B)$, where $A_\alpha = 1, A_\beta = 0, A_\gamma = 0.528$. Solving for $S_{mixed} = \frac{A_\alpha - 2A_\beta + A_\gamma}{2} = \frac{1-0+0.528}{2} = \frac{0.472}{2}$. Plugging into the intensity, we find

$$2S_{mixed}(f_A - f_B) = 2(\frac{0.472}{2})(f_A - f_B) = 0.472(f_A - f_B)$$

This shows that the order parameter, while useful for interpreting L1’ as a hybrid-ordered phase that encompasses both $L1_0$ and $L1_2$ order parameters, can be simplified by treating L1’ as a pseudocubic unit cell with 4-atom basis.

3.2. X-Ray Diffraction Structural Evidence

Key results from the samples which were isothermally aged after an A1-quench at high (650°C) and low (525°C) temperatures are shown below in Figure 3.3. The resulting phase after annealing for 10 days at high temperatures (650°C) is shown to be the expected, tetragonal $L1_0$ phase (P4/mmm, Pearson symbol tP2). After aging for 10 days at low temperatures, an ordered tetragonal phase was also observed, however we assign this to be the L1’ phase (P4/mmm, Pearson symbol tP4).

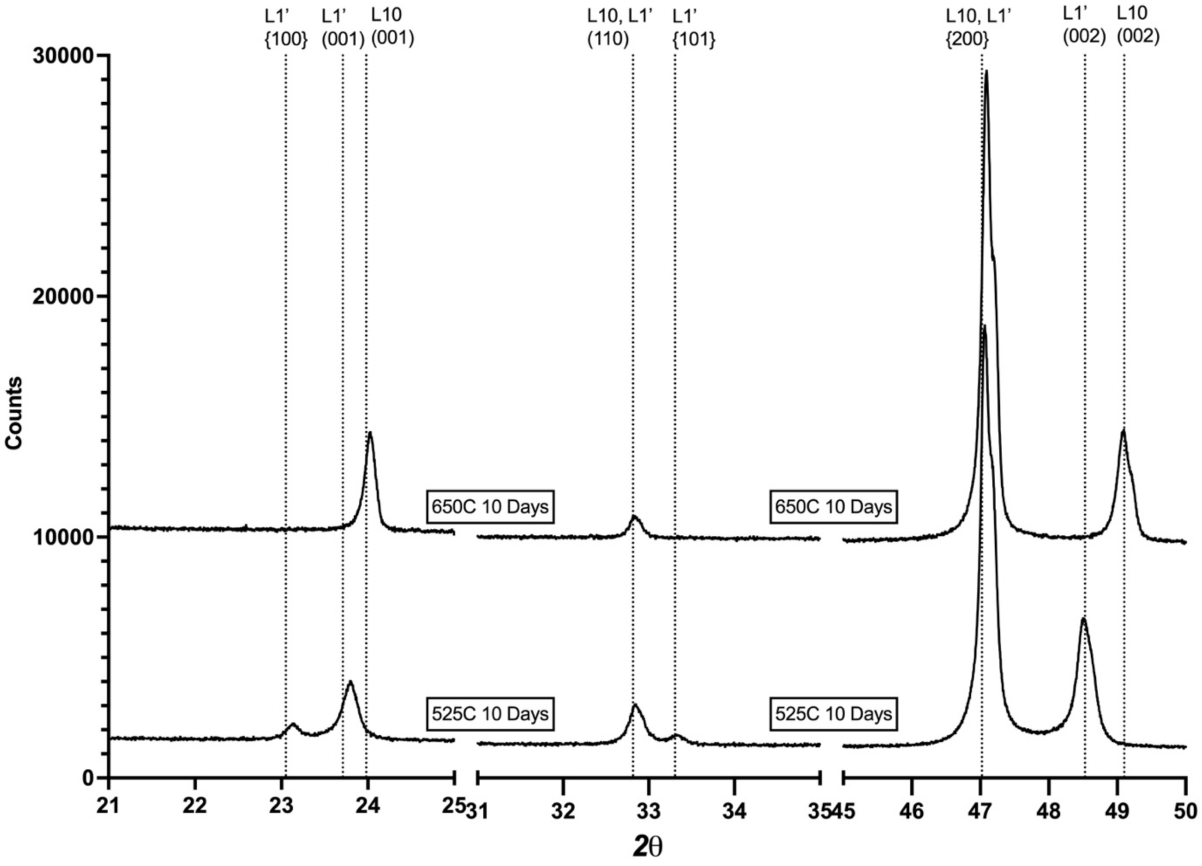

Figure 3.3. X-ray diffractograms of the two tetragonal phases aged at high (650°C) and low (525°C) temperatures displaying single-phase L10 and L1' behavior.

There are a number of key differences observed between these two phases, which will be pointed out below. First, there are the two prominent superlattice reflections observed for L1', not observed in $L1_0$ samples: the {100} and {101}. In addition, the c/a ratio has changed. Keeping in mind the tetragonal unit cell for $L1_0$, we expect the L1' *c/a* ratio to be more cubic. While the L1' is not a metastable $L1_0$/$L1_2$ hybrid phase, it does structurally 'sit' between $L1_2$ (*c/a*=1) and $L1_0$ (in this example *c/a* = 0.961) with respect to degree of tetragonality. The lattice parameters determined from {200} are a_{L1_0} = *3.853 Å*, c_{L1_0}= *3.706 Å*, and $a_{L1'}$ = *3.853 Å*, $c_{L1'}$ = *3.747 Å*. The *c/a* ratios are c/a_{L10} ≈*0.961*, while $c/a_{L1'}$ ≈ *0.972*. Interestingly, the L10 and L1' lattice parameters and *c/a* values are in agreement with the reported values from Steiner's[57] work.

Characterizing the degree of order for these differently aged specimens relies on the ratio of superlattice:fundamental integrated intensities, chiefly the $\frac{I_{(001)}}{I_{(002)}}$. These measured intensities are then compared against theoretical maximums generated from structure factor calculations (see as shown in Section 3.1). The table below (Table 2) shows key ratios: the ratios of $\frac{I_{\{100\}}}{I_{(001)}}$ & $\frac{I_{\{101\}}}{I_{(110)}}$ are used as proxy measurements for the degree of L1'-ordering. If their ratio exceeds the maximum as determined from structure factor calculations, the likelihood of L1' is diminished. However, as shown below, these values fall within the acceptable range. The overall degree of order within the system, taken as $\frac{I_{(001)}}{I_{(002)}}$, is lower in L1' than $L1_0$, most likely ascribable to sluggish diffusion for the system at lower temperatures. The $\frac{I_{(001)}}{I_{(002)}}$ ratio is chosen as a general measure of order as the (001) reflection is a strictly ordered reflection, while the (002) reflection is fundamental and appears regardless of ordering when tetragonal distortion is present. These two reflections are chosen in particular since they arise from the same set of grains, and therefore the ratio is not influenced by texture.

Table 3.2 *This table shows ratios of measured / calculated intensity ratios for the hallmark L1' superlattice reflections, and a general superlattice/fundamental ordering parameter for* $L1_0$ *& L1'.*

Crystal Structure	$\frac{I_{\{100\}}}{I_{(001)}}$	$\frac{I_{\{101\}}}{I_{(110)}}$	$\frac{I_{(001)}}{I_{(002)}}$
	$Measured/Maximum$	$Measured/Maximum$	$Measured/Maximum$
$L1'$	0.854	0.731	0.825
$L1_0$	-	-	0.945

While the correspondence of $L1_0$ & L1' to high vs. low aging temperatures for our samples, it would be prudent to eliminate the possibility of any existence of $L1_2$ in our work. Since $L1_2$ is an ordered cubic structure, with a 4-atom basis we expect to see fundamental & superlattice reflections appear, at intensity ratios set by structure factors and all angle-dependent variables. While the {100} and {101} may ascribable to a strained $L1_2$ phase within our sample, the absence of any fundamental reflections, namely around {200} discredits this idea.

3.3. The Order/Disorder Boundary for L1'

In order to probe the transformation from the solid solution A1 phase, an isothermally aged sample (after A1-quench) was probed structurally at various times during an anneal at 525℃ to probe the evolution. The results shown below (Figure 3.4) suggest that $L1_0$ does not need to form first: L1' can form directly from the high temperature A1 phase. This is seen by the slight but non-negligible {100} & {101} reflections which appear as a minute peak and broad shoulders in the red ellipses of 3.4a) and b), respectively.

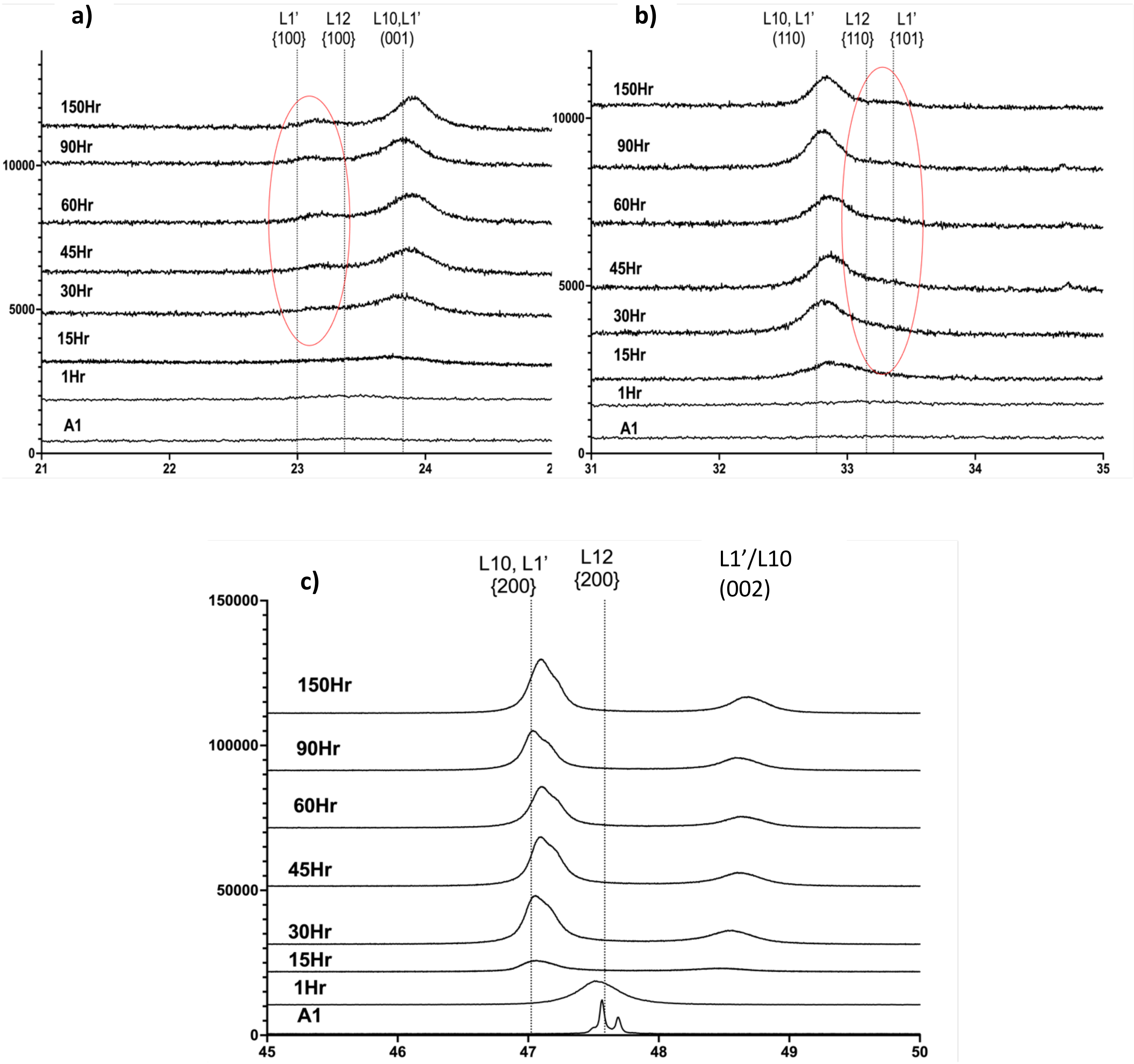

Figure 3.4. This series of diffractograms shows the temporal evolution of the transformation A1 → L1' during aging at 525 ºC. Each panel highlights a different range of 2θ, corresponding to a) {100}, b) {110} and c) {200} reflections. The ordered tetragonal L1' gives distinct superlattice reflections {100} & {101}, in addition to the $L1_0$ reflections (001) & (110). The L1'-only reflections begin to appear around 30hr, as noticed by the small hump in a) and the broad shoulder on the high-angle side of the (110) reflection in b). This evolution coupled with the fundamental reflections seen in c), as the A1 {200} peak quickly spreads by the 1hr mark and is replaced by {200}/(002) peak splitting near the 15hr mark, but becomes more pronounced near 30hr. These results again suggest that the L1' does not need to proceed through an $L1_0$ ordering process prior to the basal plane (1/2,1/2,0) ordering.

The boundary separating $L1_0$ & L1' phase fields has been contested in the past. Shockley[13] first predicted a latent heat for the transformation (see Fig. 3.7) between the $L1_0$ field and the L1' field. However, Ducastelle & Finel[21], in later CVM calculations, showed the transformation to be a 2nd order transformation (in the Ehrenfest sense). In order to probe not only the transformation order but the existence of this boundary, the fully ordered $L1_0$ sample displayed in Figure 3.3 was aged within the expected L1' phase-field (525°C) for a long duration in order to track any changes in structure or ordering. The results are shown in Figure 3.5. As can be seen, the sample was aged a total of 1000 hrs (~41 days) and probed at various times throughout this protocol. There were no observed changes in the superlattice reflection behavior near the {100} or {101} locations; no structural changes (*c/a* increase) were recorded either. However, all peaks appeared to 'shift' toward higher-angles, most likely caused by strain-relieving coarsening within the polytwinned system. This transformation did produce a number of interesting magnetic properties changes which were recorded and will be discussed in section 3.4.

It is important to note though, that in the CVM & Monte Carlo simulations performed by Finel & Ducastelle[21], the energetic differences calculated between $L1_0$ and L1' were minute. That is, CVM calculations showed that the free energy differences for site placements between the phases were f_{L10}=-2.01319451J and $f_{L1'}$= -2.01319611J, which is a change in the order of 10^{-6}J. The calculations were made with accuracy better than 10^{-10}J: as such, the results were significant. These results shed light on the why the transformation for $L1_0 \rightarrow L1'$ may not have been observed here – the driving force is small, and the kinetics are sluggish. In addition, sluggish diffusion in an ordered phase may explain the lack of significant structural or ordering changes.

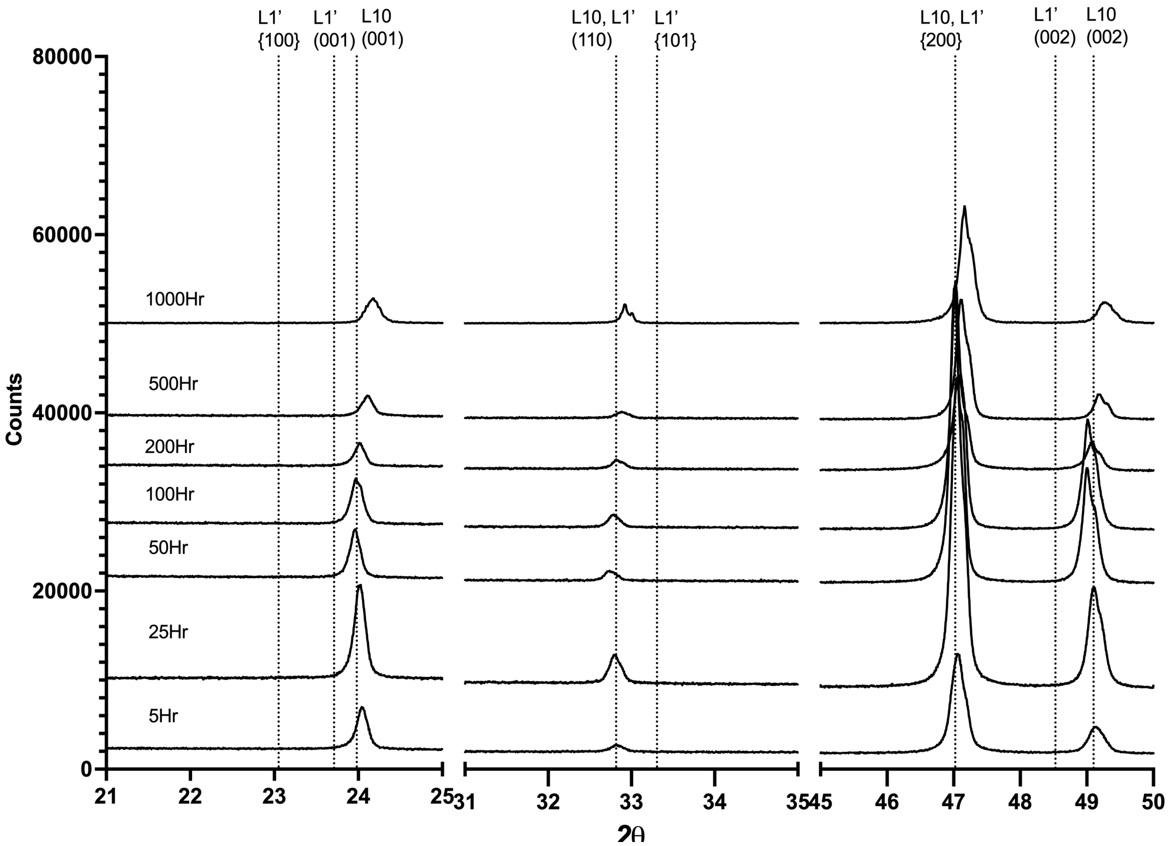

Figure 3.5. The fully ordered A1 -> $L1_0$ aged sample was aged for various times at 525C in order to probe structural & ordering changes observed at this low temperature induced by the L1'-phase field. As shown above, while the reflections did slightly shift, most likely relieving any strain accrued during the cubic -> tetragonal transformation, we do not the L1'-only reflections {100} and {101}.

The reverse thermal protocol does produce a phase change. Figure 3.6 shows that, starting with the L1'phase, aging for ~1000Hrs at 700°C promotes a decomposition reaction, L1' → $L1_0$ & $L1_2$. The {200} reflection for $L1_2$ is visible after the aging protocol, in addition to shifts in the {100} and {110} reflections, which are a result of $L1_2$ formation. This is an interesting result, as this proves that within the eutectoid region the solvus of L1' is Pd-rich than the $L1_0$ solvus found at 650°C. Following this observation, it is clear that L1' should in fact be Pd-rich with respect to the $L1_0$ formed at higher temperatures.

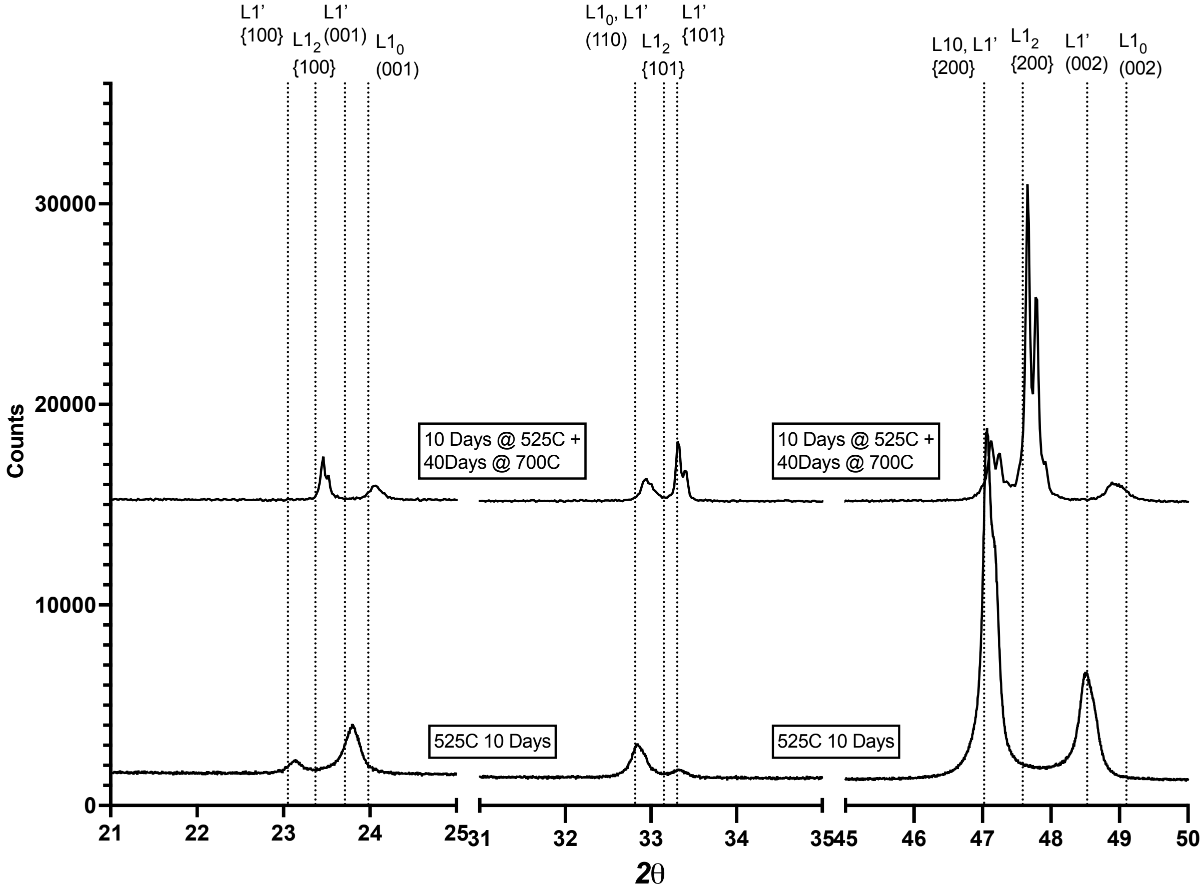

Figure 3.6. This shows the transformation of single-phase L1’ into two-phase L1$_2$ + L1$_0$. An isothermally aged (post A1 quench-in) sample of Fe – 62.0 at% Pd material exhibited single-phase L1’, however upon aging for 1000Hrs (~41 days) @ 700C transformed into L1$_2$ + L1$_0$.

This disordering transformation (Fig. 3.6) is consistent with the existence of an order/disorder boundary between the low-temperature L1’ phase-field and the higher-temperature ordered phases. While direct observation of L1$_0$→L1’ has not been recorded, the decomposition of L1’ into two ordered phases further suggests an order/disorder boundary exists. To probe the order (in the Ehrenfest sense) of the transformation, a combination of in-situ heated diffraction or microscopy experiments could be performed (as observed in Cu-Au)[78], allowing direct observation of the rearrangement or discrete formation of the superlattice & fundamental peaks. However, sluggish diffusion has so far prevented meaningful inquiry into this behavior, as time scales required for diffusion of order days-to-weeks. Interestingly, Finel and Ducastelle[79] calculated different types of transformations for L1’ to $L1_0$ and $L1_2$: the former occurred as a 2nd order transformation, while the latter is calculated to be a 1st order transformation. The latent heat for the $L1_0$ → L1’ transformation as calculated by Shockley[13] is given in Figure 3.7, where (as a function of composition) the latent heat (y axis is specific heat in units of R per gram atom) is shown for A1 → $L1_0$ → L1’ in a), and $L1_0$ → L1’ in b).

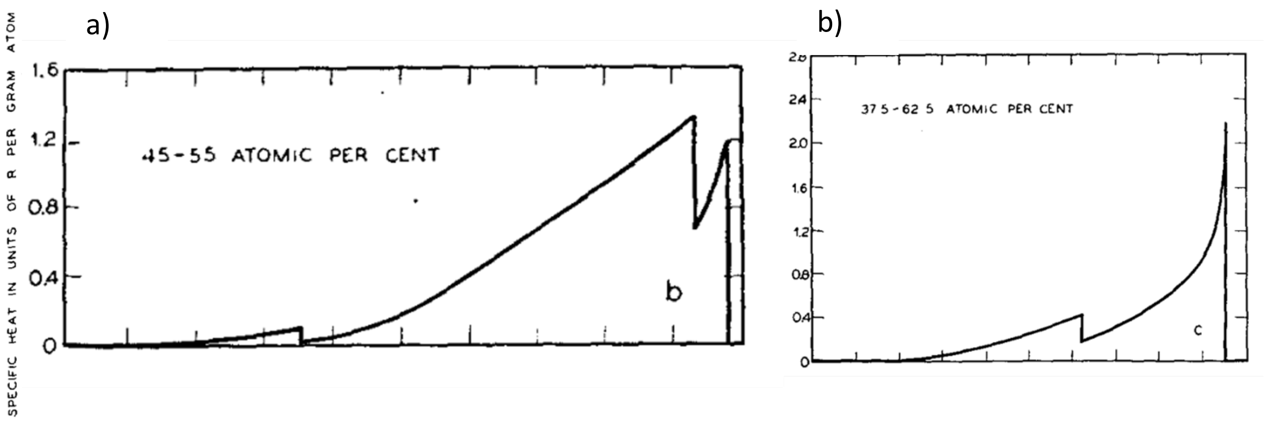

Figure 3.7. These are the latent heats calculated for $L1_0$ -> L1’ in Shockley’s original 1938 manuscript. This implies that the transition is in fact 1st order when account for simple nearest-neighbor interactions.

Table 3 below shows the relative degree of order measured from the L1’ sample and the $L1_0$ + $L1_2$ specimen (see Fig. 3.6) formed after aging for ~41days at elevated temperatures. The $L1_0$ sample is relatively completely ordered, while only partial ordering present for the $L1_2$ within the sample.

Table 3.3 *This table shows ratios of measured / calculated intensity ratios for the hallmark L1' superlattice reflections, and a general superlattice/fundamental ordering parameter for $L1_0$ & L1'. The data for a fully L1' sample, and the same sample after aging at 7000 ºC for 41 days.*

Crystal Structure	$\frac{\boldsymbol{I_{\{100\}}}}{\boldsymbol{I_{(001)}}}$	$\frac{\boldsymbol{I_{\{101\}}}}{\boldsymbol{I_{(110)}}}$	$\frac{\boldsymbol{I_{(001)}}}{\boldsymbol{I_{(002)}}}$	$\frac{\boldsymbol{I_{\{100\}}}}{\boldsymbol{I_{\{200\}}}}$
	$Measured/_{Max.}$	$Measured/_{Max.}$	$Measured/_{Max.}$	$Measured/_{Max.}$
$L1'$	0.854	0.731	0.825	-
$L1_0$ + $L1_2$	-	-	1.053	0.493

The transformation mechanism can only be speculated upon at this point. However, given the final microstructures of this $L1_0$ and $L1_2$ sample (chapter 4), it is suggested that $L1_2$ would have to not only re-order existing L1', but most likely remove orientation domain boundaries between L1' domains. Furthermore, as L1' transforms into $L1_0$, the composition of the L1' would slowly transform to that of the equilibrium composition as dictated by the solvus boundary in the two-phase region.

3.4. Microstructural Studies of L1’

3.4.1. Phase Identification with TEM

Proof of L1’ ordering is provided in Figure 3.8 where a series of darkfield micrographs were taken on a polytwinned L1’ region. The associated SADP for this region is shown in Fig 3.8d along a [001] zone axis. Herein, all planes and indices are referred to the original A1 matrix unless

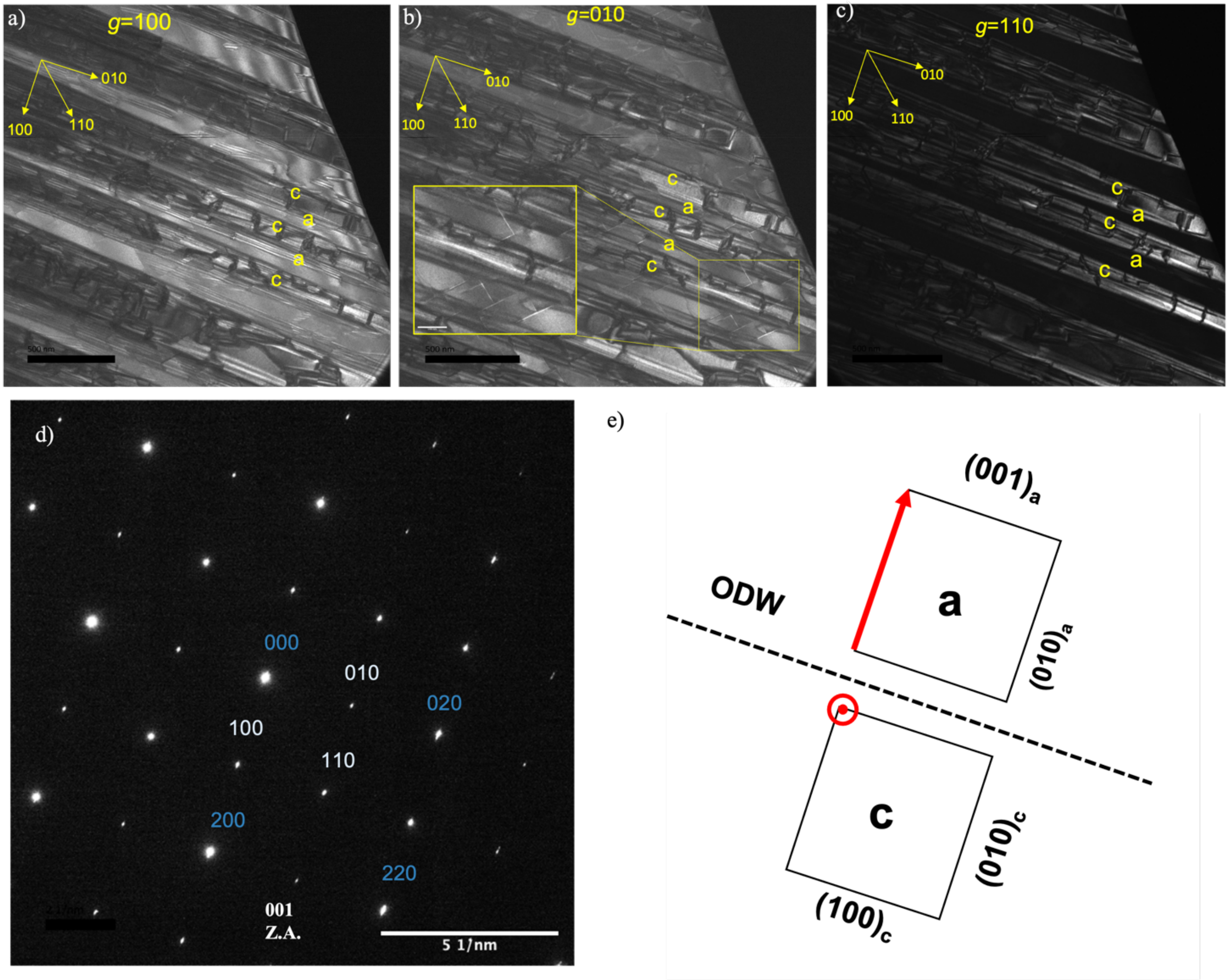

Figure 3.8. Here we have the prototypical L1’ polytwin, exhibiting two orientation variants, denoted in e) as **a** and **c**-type (*c-axis* aligned along the parent FCC [100] and [001] directions respectively), separated by a {110}-type orientation domain boundary. The series of DF-micrographs in a-c shows that under imaging conditions both pairs of orientation variants will alight. For example, in a) the g=100 has intensity formed by the (001) reflection in the a-variant, and intensity from the (100) reflection in the c-variant. Likewise in b), where g=110 creates a grey-like intensity in both variants as they contribute from the (101) and (110) reflection respectively. However in c) the image appears to be

otherwise noted. The ODWs in Fig. 3.8 are along (101) planes, tilted at 45° to the image plane. See Fig. 3.8e for the arrangement of the variant unit cells. In a prototypical $L1_0$ polytwin microstructure imaged under dark-field conditions, the orientations of the domain variants may be individually identified using specific *g*-vectors (*g* is the reciprocal lattice vector satisfying Bragg diffraction) that isolate reflections from a single variant. However, in L1', superlattice reflections not allowed in $L1_0$ will create contrast in an otherwise 'dark', or non-contributing $L1_0$ variant. For example, in Fig. 3.8a, the *g*=100 condition aligns perfectly with the strong $(001)_a$ superlattice reflection of the a-variant. In addition, this *g*-vector imaging condition will have intensity contributions from the c-variant $(100)_c$ reflection, as the reciprocal lattice points partially overlap. The contribution from the two distinct planes of the different orientation variants creates the noticeable intensity variation between the white (*c*-variants) and grey (*a*-variants) regions that constitute the L1' polytwin microstructure (whereas in L10 we would expect white and black contrast). This is consistent with Table 3.1, column 7, which indicates that the diffracted intensity from $(001)_a$ is about 3x stronger than that from $(100)_c$. Figure 3.8b shows the *g*=010 dark field imaging condition, where a more uniform grey contrast is seen across both *a* and *c*-variants. This is II the intensity found for this condItion (in both vaIiants) is created by the weakly diffracting, L1'-only, superlattice reflection, (010). Similar results are obtained in Fig. 3.8c for the *g*=110 condition from the strong $(110)_c$ vs. weak $(011)_a$ reflections (while the a-reflections appear black in Fig. 3.8c, this is the result of overall underexposure of the entire image). Again, this is consistent with structure factor calculations in Table 1 for 300 kV electrons.

In addition, the SADP of Figure 3.8d shows three superlattice reflections, 100, 010, and 110. As demonstrated in the analysis above, the dark-field imaging using these g-vectors lights up extended regions of the micrograph, so none of these reflections arises solely from a minority phase. For $L1_0$, one block of polytwin *c*-domains in a mature structure can only contain *two* *c*-axis orientation variants; in which case all three superlattice reflections will not be present simultaneously in $L1_0$. However, for L1', restrictions on missing reflections are greatly reduced (Table 1), and mature L1' polytwin blocks are expected to produce the SADP shown in Fig. 3.8d. The inset of Fig. 3.8b also shows the presence of faceted antiphase boundaries (APBs). These APBs have polygonised along a subset of {110} planes and dark-field imaging in the inset of Fig 3.8b indicates that the APBs are decorated by plates a few nm thick of another phase or orientation variant.

The above analysis of microstructure from TEM, combined with the XRD results earlier in this chapter, makes a strong and self-consistent case that the L1' ordered phase is present in Fe-Pd alloys.

The DF images that follow in Fig. 3.9a,b,c incorporate the identical analysis included for the above Fig. 3.8a,b,c. The region included in Fig. 3.9a,b,c was also imaged down a [001] zone axis, with the SADP shown in Fig. 3.9d. Dark-field superlattice imaging conditions were cycled, from *g=010,110,100*. These DF imaging conditions allowed for proper identification of $L1'_Y$ (or $L1'_B$), $L1'_X$ (or $L1'_A$) variants. For the mixed condition (*g=110)*, neither variants' (001) plane contributed to this imaging condition. Instead, the $(0\underline{1}1)_A$ and $(011)_B$ planes contribute equally, yielding the uniform grey contrast. The unit cell schematic for these regions is shown in Fig. 3.9e, with real space unit cells of the conjugate pair of L1' variants, and the corresponding *c*-axis direction given by the red arrow. The higher-magnification image of Fig. 3.9f shows a highlight of Fig. 3.9f where 'grey' intensity is generated from the $L1'_X$ variants which would normally be extinct for $L1_0$.

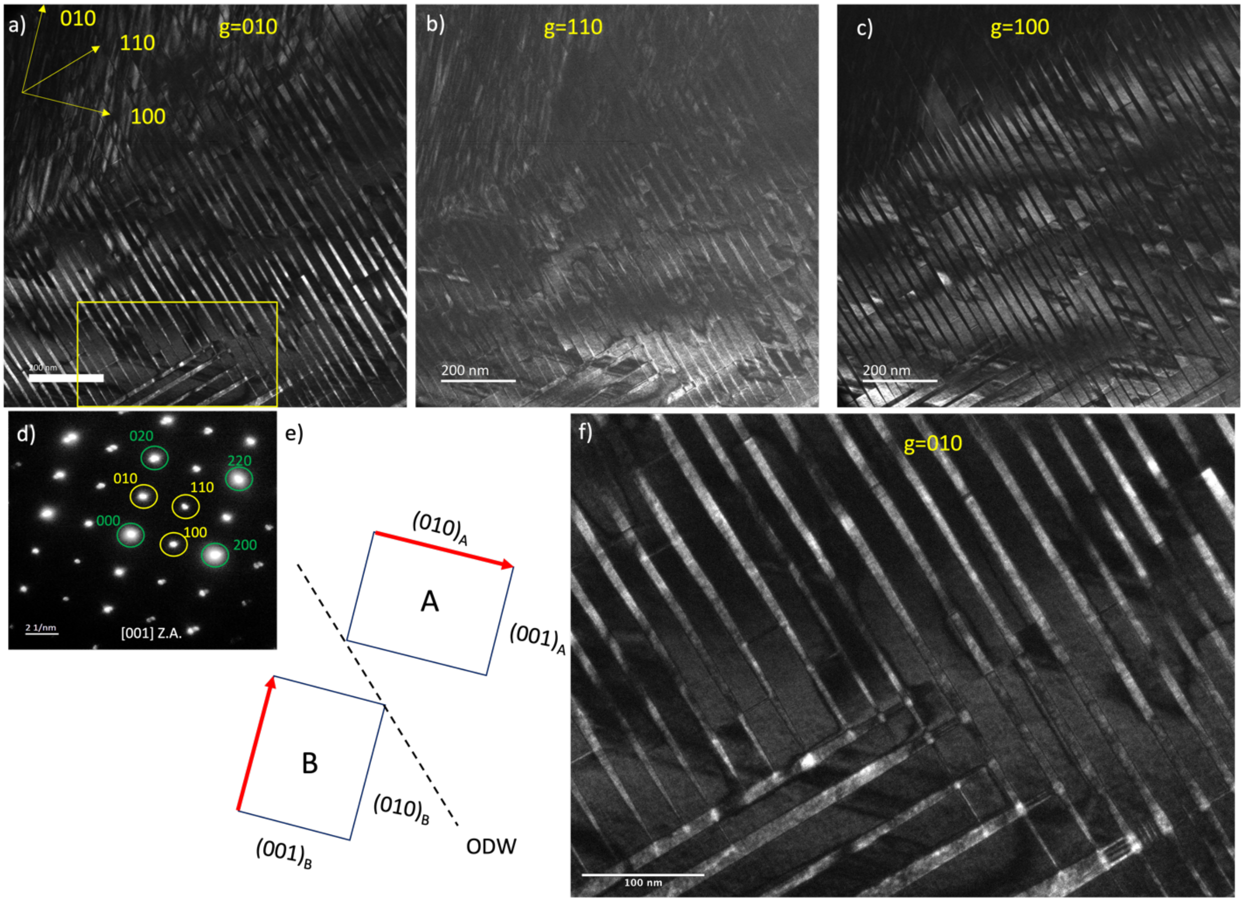

Figure 3.9. In a,b,c another L1' polytwin region is shown, with DF-TEM imagin conditions cycled, allowing for phase identification. D) shows the SADP down [001] zone axis, e) shows the real space unit cell construction of L1' variants , and f) shows a magnified region where a grey contrast is observed instead of complete extinction for one of the variants.

The micrographs captured from this region afford two important observations: namely, that L1' polytwin microstructures appear to be nominally different (between Fig 3.8 & Fig. 3.9) with *c*-domain thickness variation (~200nm in Fig. 3.8 and ~10nm in Fig. 3.9) and APB density (very high in Fig. 3.8 and negligible in Fig. 3.9). The following section will explore and discuss the microstructure observed for bulk L1'.

3.4.2. Bulk Morphology and Intra-Phase Growth of L1’

Examples of the resultant microstructure for single-phase L1’ are shown below in Figure 3.10a and b, where bright field electron microscopy affords an overview of the microstructure for L1’. The cubic → tetragonal transformation present for A1 → L1’ samples produced the polytwinned structure, where conjugate pairs of c-domains are twinned along the habit {110} planes. Figure 3.10a shows multiple plates which are bounded by yellow dashed lines, constituting a bundle. Within each plate, Fig. 3.10a also shows evidence of multiple colonies: regions where *c*-domain conjugate pairings change {110}-type habit planes (this is shown by the yellow arrows in Fig. 3.10a). In Fig. 3.10b, another polytwinned region is shown, with narrow *c*-domains.

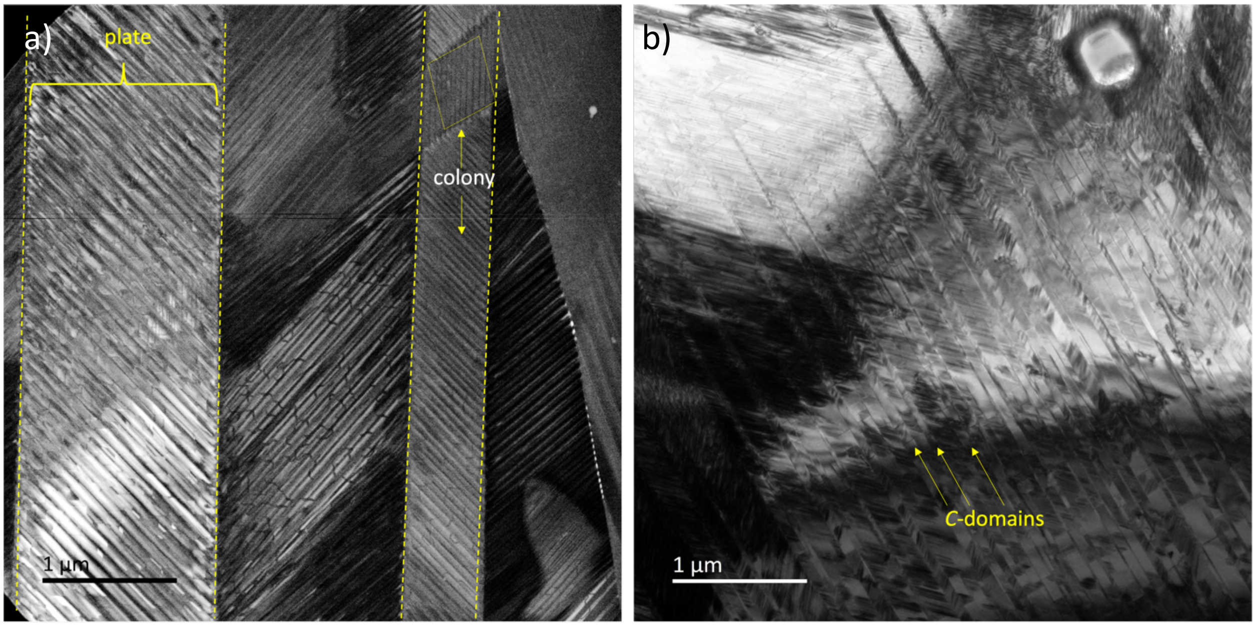

Figure 3.10. BF macroscale images of bulk L1’ polytwin, typical morphology on left where bundles are made up of plates, which contain one or more individual colonies of conjugately paired c-domains. In b), a slightly different morphbology is observed, where c-domains appear to be verry narrow.

Fig. 3.11a is important as it shows ‘edge-on’ regions where different “colonies” co-exist within a single plate (see green lines and markers in Fig. 3.11a). The yellow rectangle included in Fig. 3.11a is magnified in Fig. 3.11b. The region probed in Fig. 3.11c is at the boundary between boundary the colony with ‘edge-on’ c-domains and an adjacent colony, separated by the green line in Fig.

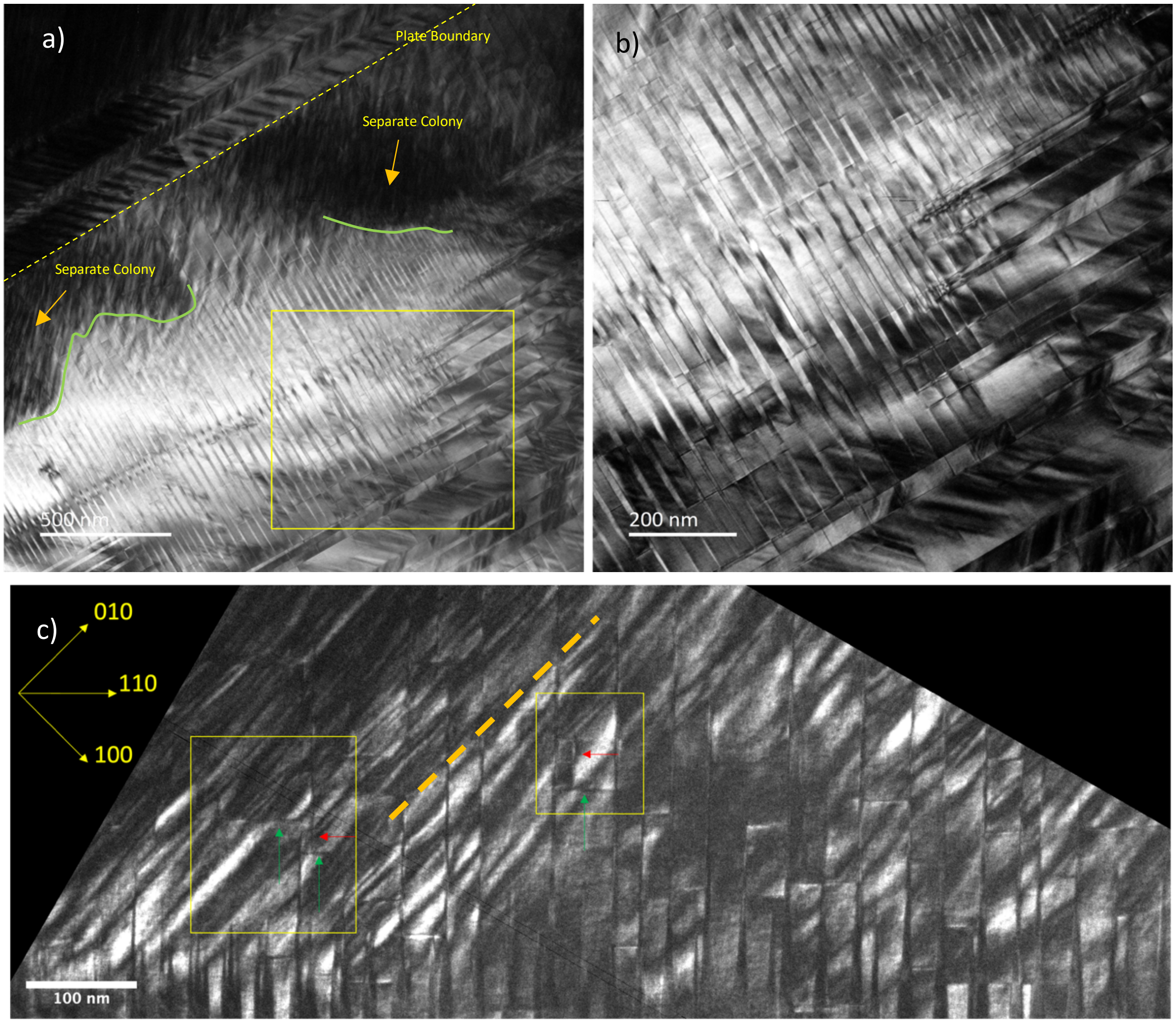

Figure 3.11. In this micrograph a region is showing where one colony of *c*-domains is growing into an adjacent colony. Traces of the adjacent colony habit plane can be observed by the orange dashed lines. The two regions highlighted in the yellow rectangles form the crux of the argument explaining the faceting mechanism observed in L1’. Red/green correspond to different *c*-domain platelets, with habit planes (110) and $(\underline{1}10)$ planes respectively. A ‘squared off’ region is also shown within these yellow rectangles.

3.11a. At this interface between adjacent colonies, an interesting observation is made which affords speculation of potential *c*-domain growth mechanisms which may explain microstructures observed in other bulk regions of the L1' sample. Figure 3.11c shows an orange line which connotes the trace of the ODB habit plane for the upper-left colony. The yellow rectangles in Fig. 3.11c show a 'squaring' off penetrating L1' *c*-domains. The red/green arrows connote different habit planes for these growing L1' domains into the colony. It is suspected that L1' domains with different habit planes, (110) or ($\underline{1}$10) for example, should correspond to differently oriented *c*-domains. This hypothesis is supported below in Fig. 3.13.

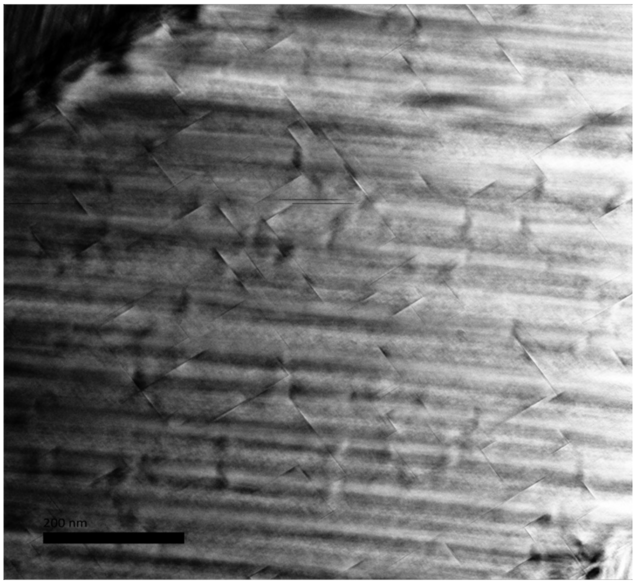

Figure 3.12. Potential growth of *c*-domains into an adjacent colony, with intense polygonization along {110}.

Within all of the single-phase L1' samples, there were large, wide-spread regions found where intricate polygonization of *c*-domains were found (which we originally thought to be anti-phase boundaries). One such region is given in Fig. 3.12. The term 'intra-phase' growth refers to the fact that the domains are L1'-domains growing within L1'. Major justification for *c*-domain growth into adjacent colonies is afforded by a series of DF-images taken down [111] Zone Axis , shown in Fig. 3.13. Dark-field imaging conditions were cycled and individual polygonised sections oriented along {110} lit-up: variant ($L1'_Y$ or $L1'_Z$) identification is afforded by cycling through DF-imaging conditions in Fig. 3.13a,b,c.

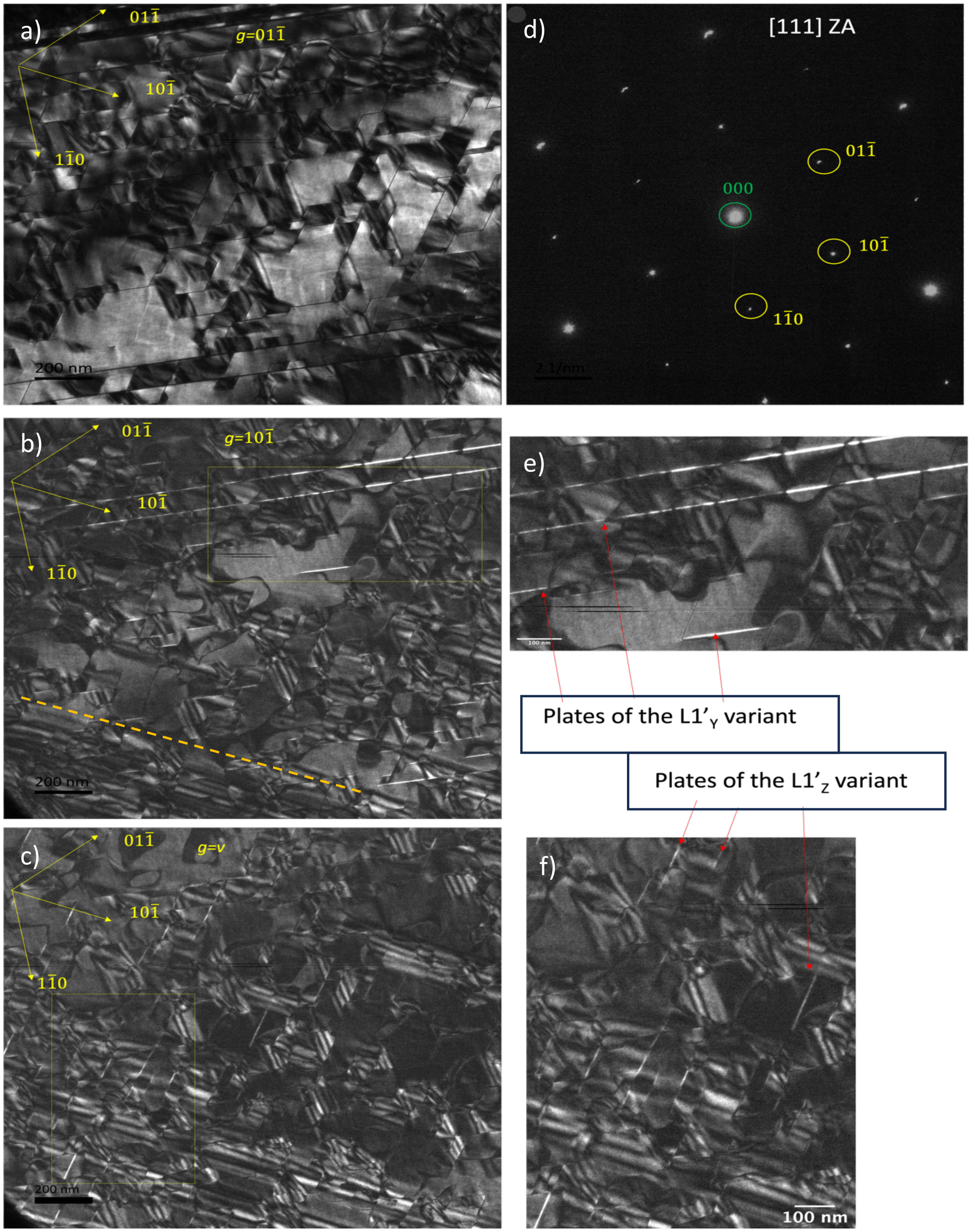

Figure 3.13. The DF micrographs of this figure correspond to different {110} superlattice imaging conditions, made when looking down a [111] zone axis, as shown in d). The different conditions show that the polygonised regions correspond to individual L1' variants which have grown from a neighboring colony into an adjacent, non-co-planar colony.

The SADP of the [111] zone axis is included in Fig. 3.13d. In Figure 13b, obtained using the $g=10\underline{1}$ condition, platelets of $L1'_Y$ variants light up as seen by the white streaks with the corresponding habit plane (inset of Fig. 13e shows this clearer). It is important to note that the long, white streaks observed in Fig. 3.13e provide significant confirmation of the intra-phase growth. While imaging conditions or aberrations may skew quantitative analysis, observation of these >600nm *c*-domains suggests imaging artifacts are not responsible. With the $g=1\underline{1}0$ condition as shown in Fig. 3.13c the $L1'_Z$ variants is seen to light up (inset of Fig. 3.13f shows this clearer, again). It is important to note that the matrix material of these embedded *c*-domains must be a colony of conjugate *c*-domains with orientation domain boundaries aligned along habit planes which are not viewed edge-on. The $L1'_X$ variant appears to be missing from this region of material and while at first this was concerning, this observation is justified given the proposed mechanism, wherein an adjacent colony is only made up of pairs of *c*-domains and thus will always be missing one domain.

The formation mechanism has not been explored explicitly; however a piece-meal mechanism is suggested here. Figure 3.14c shows a region where a colony of edge-on *c*-domains adjoins with a colony oriented along a separate ODW habit plane {110}. At this interface region, the L1’ *c*-domains from the edge-on region appear to grow ‘into’ the conjugate colony (at least at the superficial imagining plane surface). This would suggest that the mechanism is as follows, then. *C*-domains within a colony grow until they are impeded by separate colonies or a plate boundary. It appears that when *c*-domains most likely ‘consume’ any remaining tweed, and are thus strain driven: although surface energy between these *c*-domain/colonies must be high, this should be a strain-relieving transformation. Most likely, strain is minimized if laths are kept thin and long: to account for this, they may need to 'grow' into adjacent colonies. While tweed as a pretransition state has not been observed (microstructure of incipient L1' formation is still lacking), we will assume that the cubic to tetragonal transformation will incorporate the tweed pretransition state.

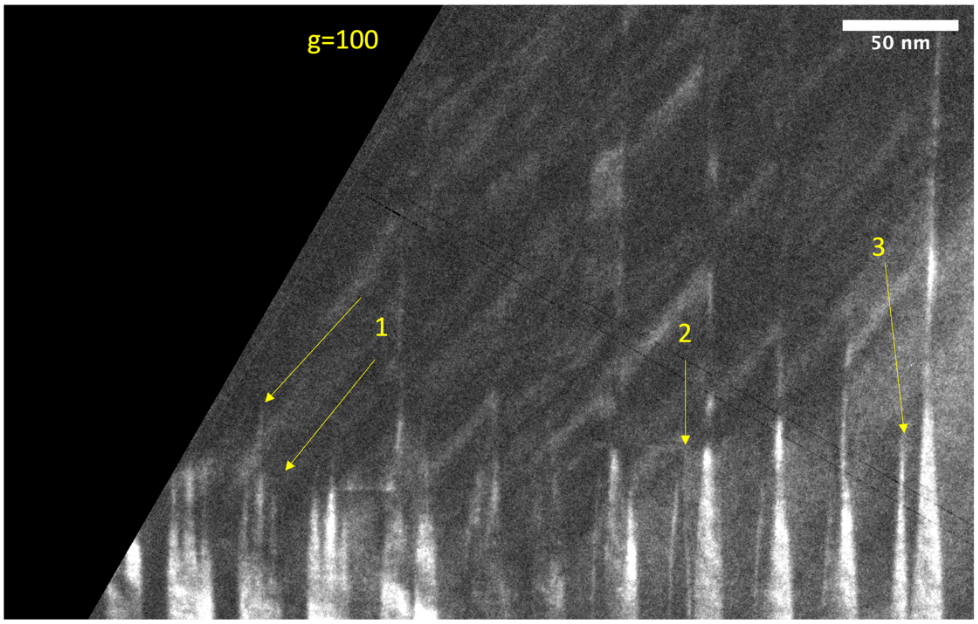

Figure 3.14. Visualization of the L1' plate tips growing into an adjacent colony. Different *c*-domain tips can be observed, denoted by 1,2,3 within the figure. The imaged area in this figure is from the same, larger area, of Fig. 11.

The images included in Figures 3.15a,b,c show more polygonised regions, where 'squaring' of domains and alignment along {110} is visible. The evidence and mechanism provided is not complete: the transformation is suggested based on observations afforded in DF-imaging of i) an incipient domain/colony growth (Fig. 3.11c and Fig. 3.14) and ii) end-state microstructure of *c*-domain / colonies where individual *c*-domains can be identified (Fig. 3.13).

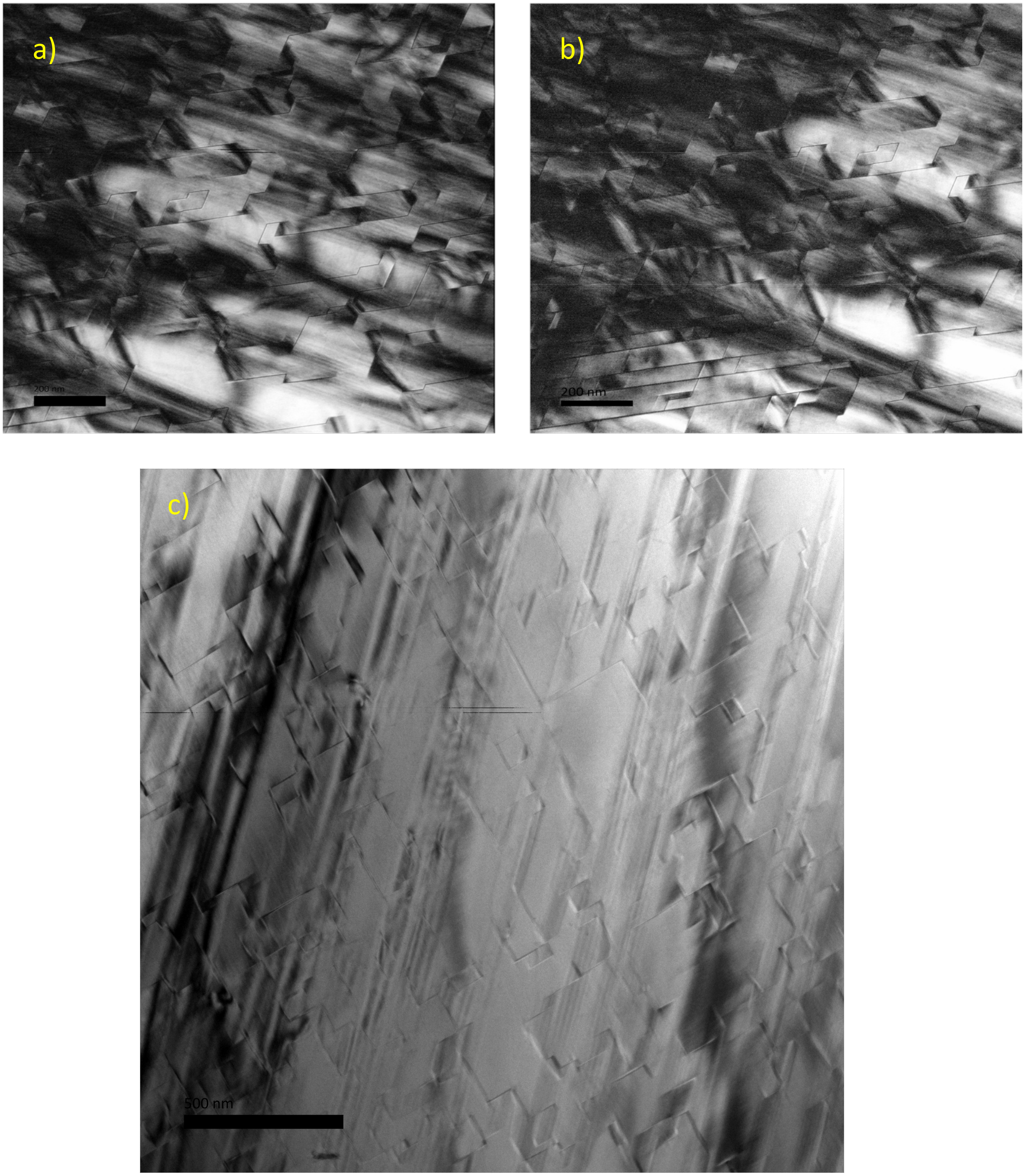

Figure 3.15. BF images taken in a) and b) show different regions where the same polygonization of platelets has occurred. In c) and d), DF micrographs of this region show the same intense polygonization, down a [111] zone axis. In each of these figures, 'squaring' of platelets is observed.

3.4.3. Anti-Phase Boundaries in L1'

Figure 16 clearly displays APBs which exist across all plates. This type of region allowed for an attempt for further identification of the L1' crystal structure. APBs can be characterized by their translation vectors, and L1' has a specific vector not allowed in $L1_0$. Whelan and Hirsch[7] found a relationship between stacking fault contrast and superlattice imaging condition, with direct analogy to anti-phase boundary contrast. Contrast is generated when the diffracted wave is out of phase with the incoming wave, such that the following relationship is non-zero (or 2π): $\alpha = 2\pi\vec{g}\cdot\vec{r}$, where $\vec{g}$ is the reciprocal lattice vector of the diffracted wave *hkl* and $\vec{r}$ the displacement vector

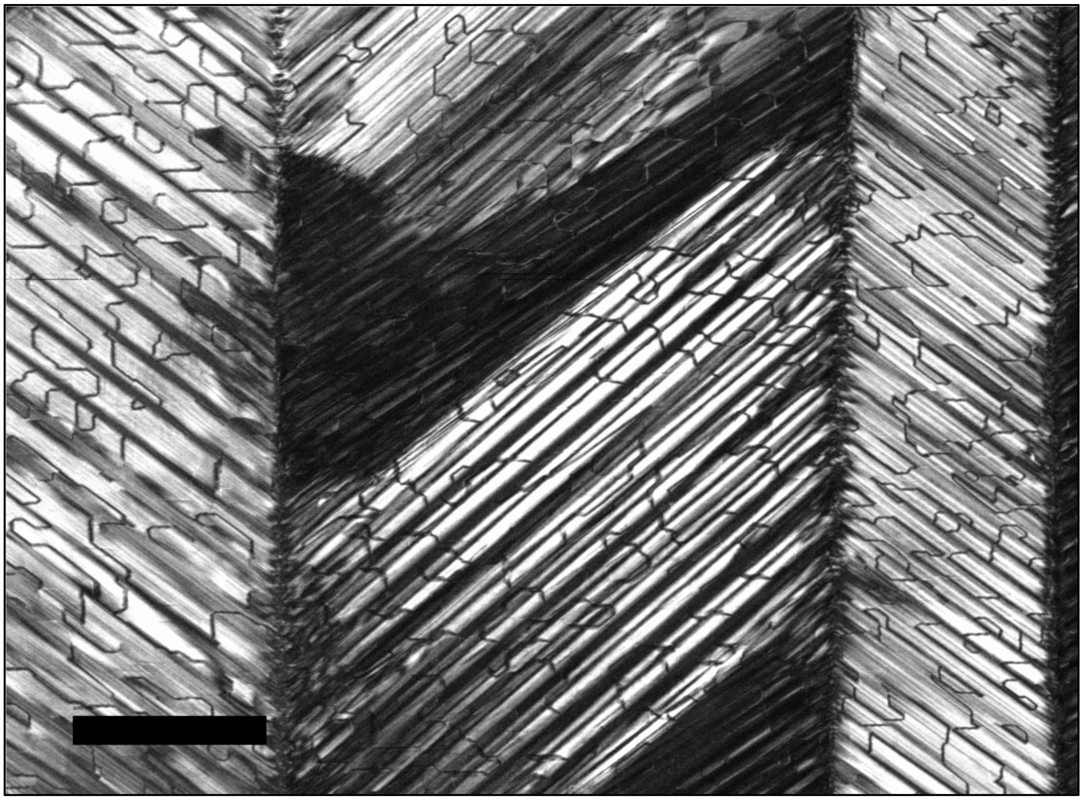

Figure 3.16. This is a bright-field micrograph taken of single-phase L1' showing three connected plates. The dark fringes are anti-phase boundaries, which only slight preference for crystallographic alignment. The majority of the APBs that are easily discernible in this image are transformation APBs.

which describes the relationship between the two lattices bounded by the anti-phase boundary. When $\alpha = \pm\pi$ the boundaries are visible; when $\alpha = 0{,}2\pi$ the boundaries are invisible.

In the $L1_0$ crystal structure there are two discrete ordering sites on the parent FCC lattice : (0,0,0) and (1/2, ½, 0) are synonymous, as are (1/2,0,1/2) and (0,1/2,1/2). However, L1' has three discrete ordering sites on the parent FCC lattice, increasing the type of translation vectors allowed between bounded domains from 2 (for $L1_0$) to 3. The allowed translation vectors $\vec{r}$ for L1' are as follows: **(1)** $\vec{r} = ½\, a < 101 >$, **(2)** $\vec{r} = ½\, a < 011 >$, and **(3)** $\vec{r} = ½\, a < 110 >$. It is this last translation vector that allows for phase identification, as it is disallowed for $L1_0$, but allowed for L1'. The following darkfield images in Fig. 3.17 show APB variation based on superlattice imaging condition. However, APB extinction conditions vary by *c*-domain as the vector $\vec{g}$ varies by *c*-domain, and this analysis becomes non-trivial due to the "mixed" c-domain reflection conditions for L1'. We assume that the two orientation variants in Figure 17 have their c-axes aligned the parent FCC [001] and [100], making them $L1'_Z$ and $L1'_X$ variants respectively. These conditions are summarized in the table below:

Table 3.4 This table shows extinction conditions for different dark-field conditions in L1', where $\vec{g}$ is the imaging condition and $\vec{r}$ the displacement vector.

$\vec{g}$ for Z-variant	$\vec{r}$ Visible	$\vec{g}$ *for X-variant*	$\vec{r}$ Visible
100	2,3	1,2	1,2
010	1,3	010	1,3
110	011	110	2,3

The conditions show, that in order to isolate the 3rd type of translation vector, the *g=010* imaging condition is the most appropriate, as it allows for identification $\vec{r} = \frac{1}{2}\, a < 110 >$ in both orientation variants. However, the above analysis was not particularly fruitful as sample thickness and inconsistencies in intensity frustrated rigorous analysis.

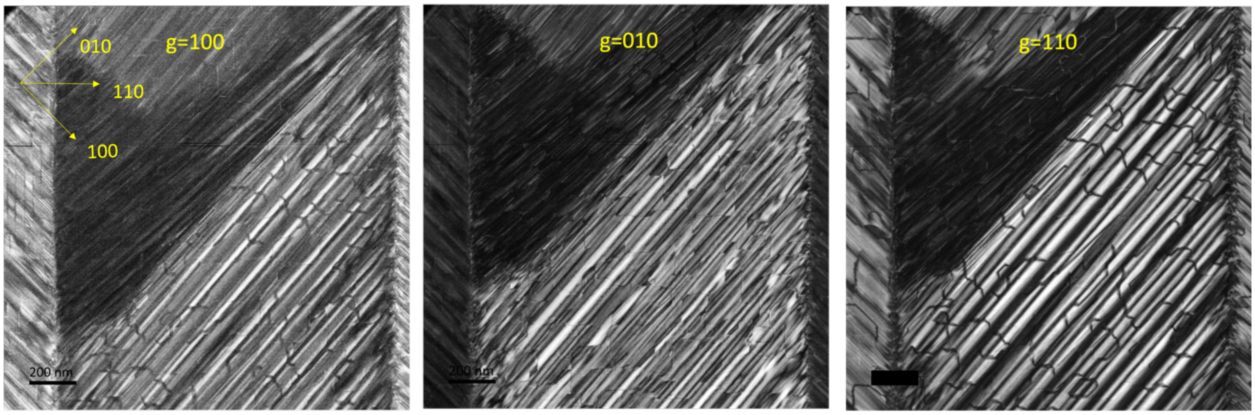

Figure 3.17. A series of DF images is shown in a-c, where visible anti-phase boundaries differ based on extinction conditions. The fundamental observation of 'squared' APBs in b) is evidence of an $L1_0$-forbidden translation vector (based on the logic provided in Table 3.5).

In Fig. 3.17a, the curvilinear transformation APBs are clearly visible, with minor amounts of faceting (trivial amounts by fraction). However, In Fig. 3.17b with *g*=010 imaging condition, a clear 'faceting' or alignment of APBs is visible along {110}, which is not as intensely observed in the other superlattice conditions. With this imaging condition, none of the curvilinear transformation APBs are visible in either of the two dark-field conditions. This would suggest that the intense faceting observed of these APBs was in fact the result of the L1'-only APB type, with translation vector within the (001) plane and thus not allowed for $L1_0$. This analysis is included at a superficial level simply to show that APB fluctuation by dark-field condition did differ in L1' This observation did weakly confirm that the L1' phase identification was correct. Historically speaking, this result spurred further efforts to confirm the L1' ordering.

3.5. Magnetic Measurements & Properties

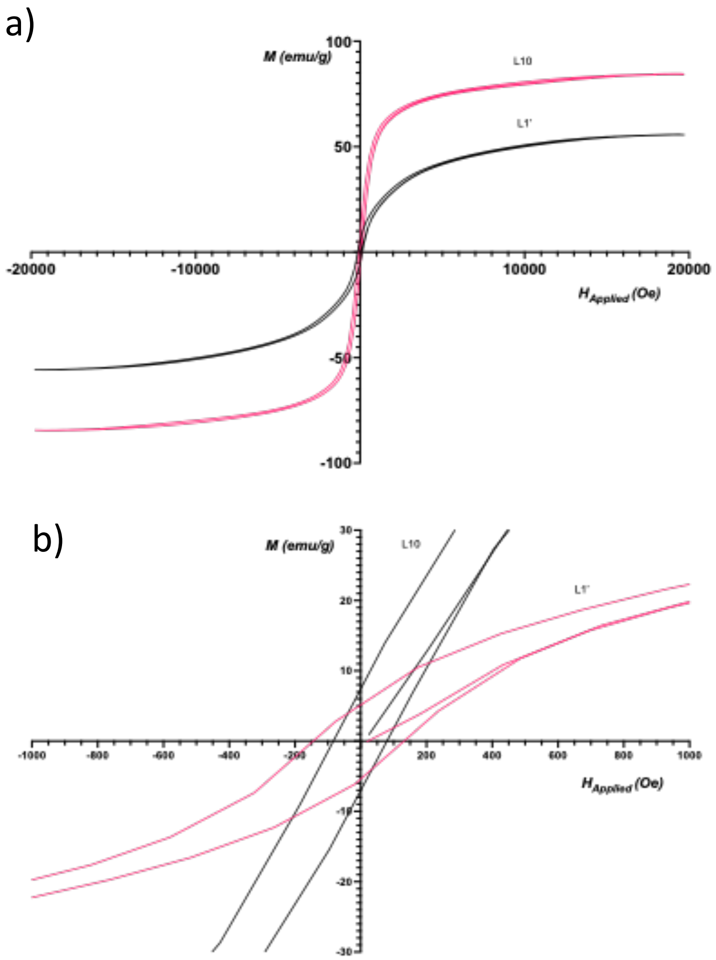

Figure 3.18. This shows hyseteresis loops for single-phase L10 and L1’, measured for samples aged at 650C and 525C for 10 days respectively. The magnetic saturation and coercivity for the samples are quite different, as is the shape of the hysteresis loop.

Figure 3.18 shows two hysteresis loops generated for single-phase $L1_0$ and L1’ at nominally identical compositions. As seen in Fig. 3.18a, the magnetic saturations differ dramatically between these two samples. In Fig. 3.18b, the coercivities may be compared, and again, a general difference in loop-shape and coercivity is found. A simple calculation is required to convert magnetic saturation from emu/g to μ_B/formula unit. The expression is given as follows:

$$\mu_{(f.u.)} = \frac{M_s\left(\frac{emu}{g}\right) * (mol.weight\ \left(\frac{g}{mol}\right))}{(9.274 * 10^{-24}(\frac{J}{T}) * 6.022 * 10^{23}(\frac{1}{mol})} * 10^{-3}$$

This expression gives the Bohr magnetons per formula unit of the crystal structure in question, and allows for some quantitative analysis of magnetic structure (given some assumptions). The calculated values are given below in Table 5. The discrepancies between Moment / unit cell differ dramatically between the two different crystal structures (Table 3.5 column 5). These differences cannot be explained by compositional variations: instead, it is suggested that anti-ferromagnetic (ferrimagnetic) coupling may have occurred between Fe & Pd atoms for L1'. The coercivity differences between $L1_0$ and L1' are non-negligible but non-trivial to deconvolve as they are inherently structure-sensitive properties.

In order to generate the values for table 3.5, It should be stated that molecular weights were calculated for a formula unit of $Fe_{1.512}Pd_{2.488}$ (roughly corresponding to the composition in question).

Table 3.5. This shows extracted magnetic saturation values and calculated magnetic Bohr Magnetons per unit cell and Fe-atom for the given crystal structures above ($L1_0$ and L1').

Crystal Structure	M_S (emu/g)	Coercivity (Oe)	Mol. Weight (g/mol)	Total Moment / Unit Cell (μ_B)
$L1_0$	85.544	81.457	349.2	5.389
L1'	55.819	138.10	349.2	3.519

In order to probe the ordering mechanism (and confirm phase identification for L1') a single-phase L1' sample was shipped to Oak Ridge National Lab User Facility, to use the Spallation Neutron Source (SNS) Inelastic Neutron Scattering beamline, which would allow for magnetic structure determination of this phase and the $L1_0$ phase. In Figure 3.19 the raw data for the neutron scattering of single-phase L1', with the appropriate fit is shown. The background and calculated peaks are shown in red and green curves along the data, respectively. The quality of the diffraction peak is given as an *R* value, in this instance *R=9.7%*, which is considered satisfactory. Again, direct observation of the {100}/(001) and {101}/(110) splitting confirms L1' phase identification.

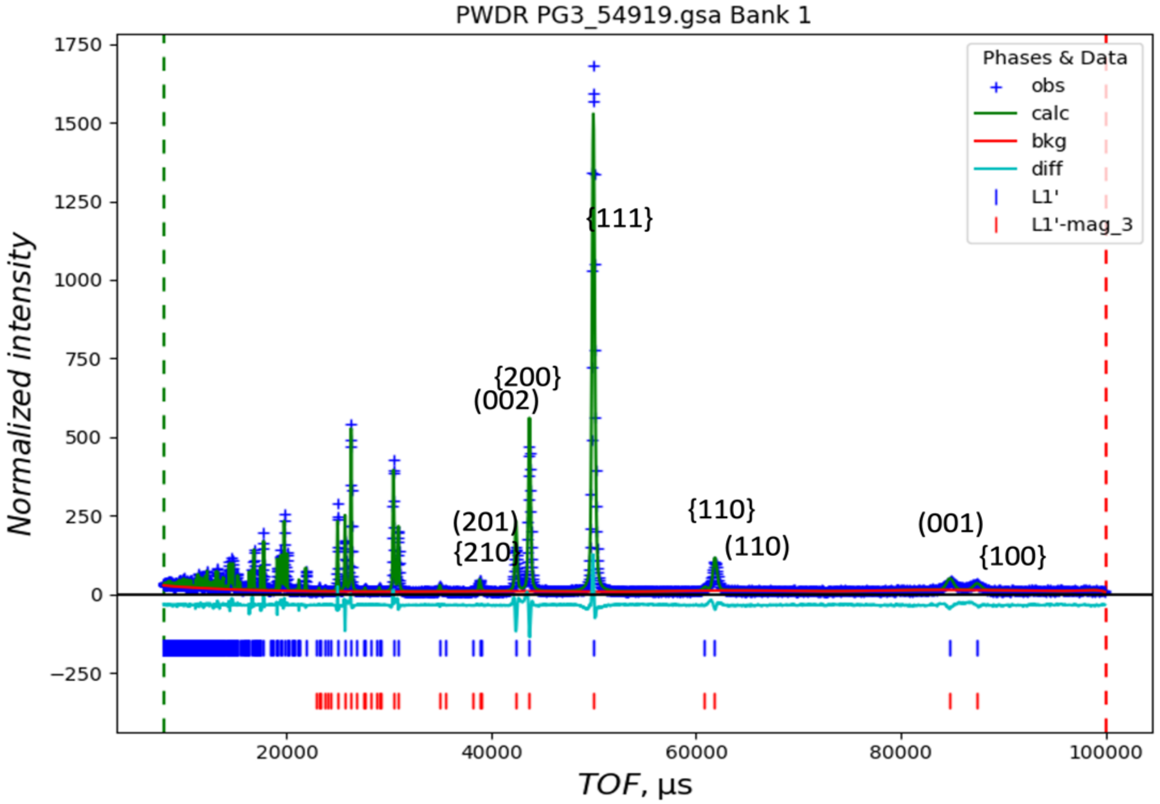

Figure 3.19. This shows the neutron scattering data for single-phase L1', with many of the low Q reflections are labelled. For the scattering peak fits in blue and red, we see contributions from nuclear and magnetic scattering events respectively.

There were key constraints employed to generate a quality fit: namely, that the Fe/Pd shared site (1/2,1/2,0) had equal moment contribution for both Fe & Pd. The blue lines below the diffractogram correspond to the nuclear scattering, whereas the red lines correspond to the planes which have contributions from the magnetic structure. From these magnetic reflections, it is possible to construct a magnetic structure, as shown below in Figure 20. The space group is given as P4/mm'm' and ferromagnetic coupling is observed between all Fe & Pd species is seen. While the structure below suggests ferromagnetic coupling between species for L1', we show with simple calculations that this may in fact be incorrect. The different magnetic saturation measurements observed in Fig. 18 are easily explained using known values for Fe & Pd moments in the Fe-Pd system. Greater refinement of the neutron data should be done, to see if a better fit is capable.

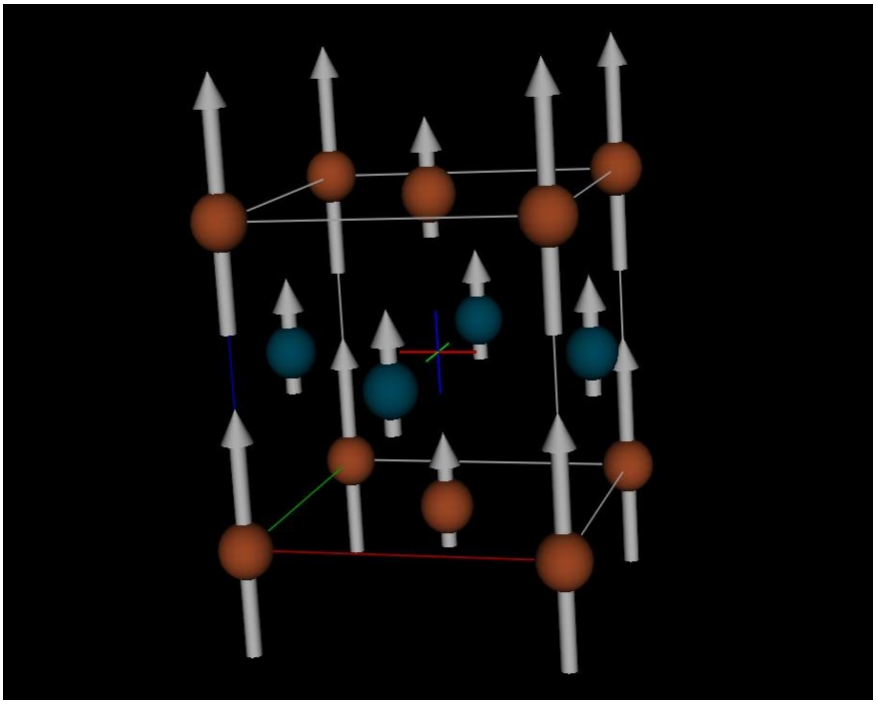

Figure 3.20. This shows the magnetic structure for L1' generated from the neutron diffraction data where Fe,Pd species are shown to couple ferromagnetically.

Inelastic neutron scattering allows for determination of not only chemical & magnetic structure, but also derivation of magnetic moment per species (and site). These results are shown below in Table 4. The $\overline{\mu_{Fe}}$ values generated from the neutron scattering experiments are generally in agreement with previously reported values in the literature, however there is a major disagreement for $\overline{\mu_{Pd}}$ moments.

Table 3.6. *Magnetic moment per species & site, as determined by inelastic neutron scattering at ORNL SNS Facility.*

Species	**Site**	**Moment in Z (μ_B)**
Fe	(0,0,0)	2.819
Pd	(0,1/2,1/2) & (1/2,0,1/2)	1.4702
Fe	(1/2,1/2,0)	3.7879
Pd	(1/2,1/2,0)	3.7879

The literature on magnetic moments shows that with Fe concentrations up to 50 at%, $\overline{\mu_{Fe}} \approx 3\mu_B$ however $\overline{\mu_{Pd}}$ rises to a limiting value of $0.35\mu_B$[80]. More detailed neutron investigations suggest that Fe-Pd interactions (as Fe-Pt) interactions differ significantly by Fe concentrations[81]. Peak magnetization was observed for ~65at% Fe (similarly for Fe-Pt)[82]. It has also been suggested that Fe-Fe interactions in Fe-Pd & Fe-Pt are in fact anti-ferromagnetically coupled and at sufficiently large Fe-rich compositions, override the otherwise ferromagnetic coupling between neighbors[83]. However, work on ordered FePd ($L1_0$) found ferromagnetic coupling between species, with Fe and Pd moments as $2.85\mu_B$ and 0.35 μ_B respectively[83]. These reports find a magnetic saturation for equiatomic FePd at about 110 emu/g.

It is clear from comparisons between neutron scattering moments and generated magnetic saturation moments of the L1’ samples, that the values measured by magnetometry and neutron scattering are not in concert. However, by using the calculated moments from the literature as shown above[80], we can re-evaluate the major hysteresis loop results shown in Figure 3.18.

By simply assuming for our samples that $\overline{\mu_{Fe}} = 3\mu_B$, and $\overline{\mu_{Pd}} = 0.35\mu_B$ and L1_0 exhibits ferromagnetic coupling between all species, we report **1.5 Fe atoms = 3*1.5 = 4.5**$\boldsymbol{\mu_B}$ and **2.5 Pd atoms** = $\boldsymbol{0.35 * 2.5 = 0.875\mu_B}$ which combined gives **4.5**$\boldsymbol{\mu_B}$+ $\boldsymbol{0.875\mu_B} =$ **5.375**$\boldsymbol{\mu_B}$**.** This is in near perfect agreement with the magnetic saturation calculated from the hysteresis loop for L1_0 (Table 3 Column 4). Applying similar logic but for anti-ferromagnetically coupled Fe & Pd moments (as typically seen in L1_2 samples[84]), we would expect to see **1.5 Fe atoms = 3 * 1.5 = 4.5**$\boldsymbol{\mu_B}$ but 2.5 Pd atoms with moment aligned anti-parallel to the Fe-moments: thus, **4.5**$\boldsymbol{\mu_B} -$ $\boldsymbol{0.875\mu_B = 3.62\mu_B}$ which is again, nearly direct agreement with the magnetic saturation measured for the L1’ single-phase sample (Table 5 column 4). While it is clear that the neutron data has not been refined satisfactorily, it should be noted that these relatively straight-forward

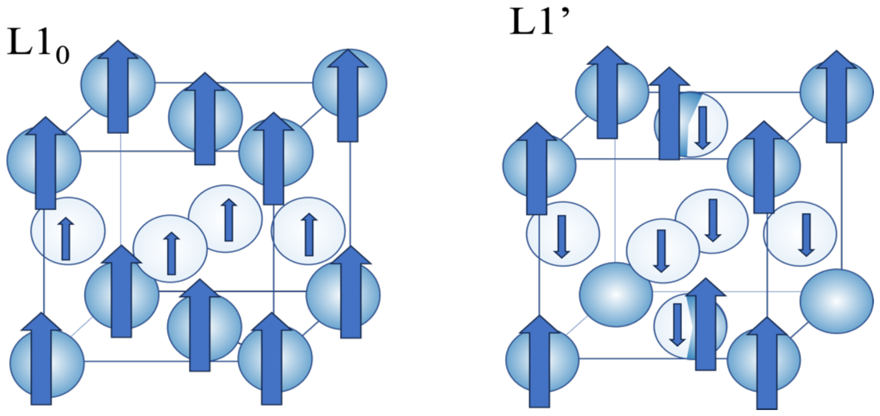

Figure 3.21. Expected magnetic structure based on magnetic hysteresis loop saturation magnetizations and the Bohr magnetons found in the literature.

calculations allow for decent agreement for measurements, showing that magnetic moments are aligned differently between the atomic species for $L1_0$ and L1'.

Figure 3.21 shows the predicted and expected magnetic structures for the differing crystal structures. While L1' is typically displayed as a 'mixed' site phase (1/2,1/2,0), in reality a lattice site cannot 'share' a species. As such, whenever Pd is occupied on that site it would have co couple anti-ferromagnetically with the neighboring Fe atoms, whereas when Fe is present it would need to couple ferromagnetically.

Figure 3.22 shows magnetic aging curves for the $L1_0$/L1' phase-field experiments shown in Figure 3.5. While no structural measurements were observed (in Fig. 3.5), a jump in coercivity was observed. As coercivity is a structure-sensitive property, changes in magnetic ordering cannot be deduced. The magnetic saturation values did not change significantly either. To repeat previous

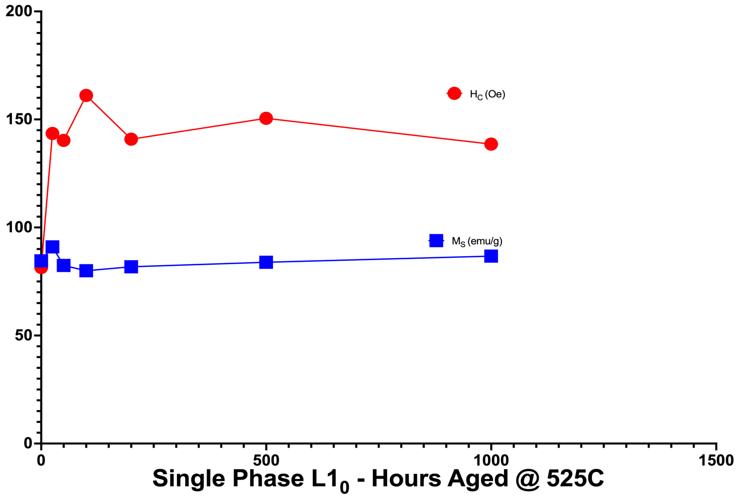

Figure 3.22. This shows the magnetic aging curve for single-phase $L1_0$ as a function of time spent at 525°C, presumably within the single-phase L1' phase-field. While no structural transformations were observed, a clear increase in coercivity (but no change in Ms) was seen.

statements, the lack of change may be described sluggish kinetics and limited driving force between these two phases at temperatures probed.

3.6. Third Law of Thermodynamics Considerations

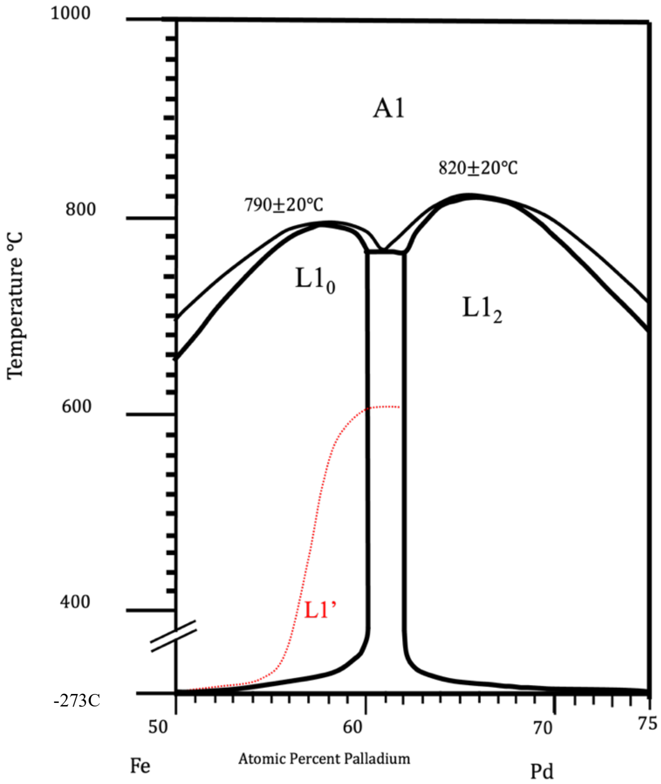

Figure 3.23. This shows the Fe-pd eutectoid region phase diagram snippet down to 0K, where the L1' Order/Disorder boundary is seen to start.

Broadly speaking, the third law of thermodynamics should be considered more in phase diagram calculations and analyses, as suggested by Soffa and Laughlin[85]. Rigorously, the loci of critical points separating the $L1_0$ and L1' phase fields begin at 0K, not at elevated temperatures (this difference is shown in Fig. 3.23). Furthermore, within the two-phase field (either $L1_0 + L1_2$ or $L1' + L1_2$), as 0K is approached, the compositions of $L1_0$ and $L1_2$ solvi should trend towards c=0.5 and c=0.75 respectively. This is shown schematically in Figure 3.23, where the solvi boundaries bow out considerably towards the stoichiometric compositions**.** The two-phase field below L1' Order/Disorder boundary would be $L1' + L1_2$, but at 0K would rigorously have to be $L1_0 + L1_2$. This is shown schematically also as the red Order/Disorder boundary is *above* the solvus.

Chapter 4. $L1_0 + L1_2$ and L1' + $L1_2$ Coexistence in the Eutectoid

4.1. Overview of Results from the Eutectoid Region

This chapter shows phase equilibria in the $L1_0$, L1' , & $L1_2$ eutectoid region of Pd-rich Fe-Pd. This chapter shows that aging at 650°C within the eutectoid region coexistence of $L1_0$ and $L1_2$ is observed, while aging at 525°C showed coexistence of L1' , and L1' + $L1_2$. While only two on-eutectoid composition samples were fabricated exhibiting nominal compositions of Fe – 61.8 at% Pd and Fe – 62.2. at% Pd, individual sample compositions may have deviated. While this is

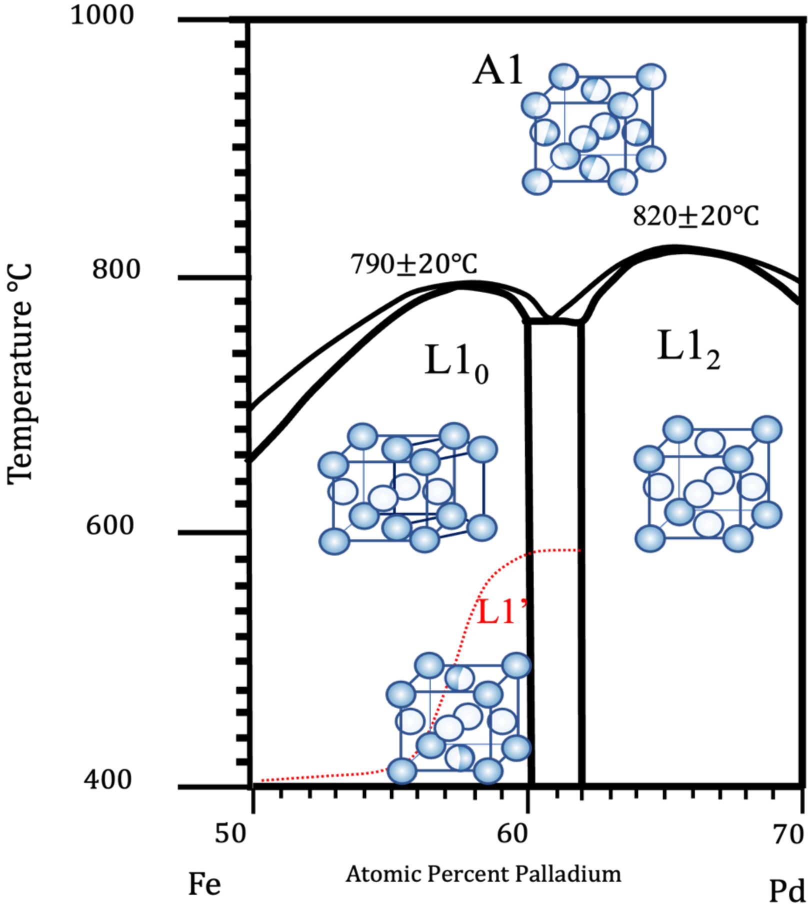

Figure 4.1. This shows the eutectoid region of $L1_0$ and $L1_2$ in Fe-Pd, where the solution phase A1 decomposes into ordered tetragaonal $L1_0$ and ordered cubic $L1_2$ below the eutectoid temperature ~760°C. In addition, the L1' crystal structure is shown at low temperatures. The red dashed lines shows a schematic boundary.

expected for any bulk alloy, small deviations of concentration may significantly affect phase equilibria for on-eutectoid Fe-Pd samples. With a two-phase coexistence region approaching with ~1 at% width, minor concentration variations (on the order of 0.1 at%) may have significantly changed the sample's placement on the tie line. The accepted phase diagram is shown in Figure 4.1, with unit cells for crystal structures shown, where blue(white) corresponds to Iron(Palladium) respectively. In addition, the red dashed line designates the order-disorder boundary between $L1_0$ and L1', but is placed mainly schematically, as the loci of critical points between $0.5 < c < 0.6$ is unknown at this time.

This chapter focuses on characterization and analysis of the two-phase coexistence region in the Pd-rich eutectoid region. An overview of phase equilibria is shown in Figure 4.2, where X-ray diffractograms show $L1_0 + L1_2$ (line 1), single-phase L1' (line 2), $L1_2 + L1_0$ (line 3), and $L1' + L1_2$ (line 4). A note should be made with respect to line 1 & 3. While both show $L1_0 + L1_2$ coexistence, subtle composition differences between these samples displaced the equilibrium value of phase fractions for $L1_0 + L1_2$: as such, line 1 corresponds to a majority $L1_0$ composition, while line 3 corresponds to a majority $L1_2$ composition. Although the Fe-Pd phase diagram given by Massalski[27] is typically accepted, Loebich[86] in 1963 found interesting ordering behavior near the Pd-rich eutectoid region. In his report, Loebich found $L1_0 + L1_2$ two-phase coexistence for Fe – 62 at% Pd samples aged at 600°C , but only single-phase $L1_0$ when identical samples were aged at 500°C. Our results suggest that Loebich may have been probing the order/disorder boundary for $L1_0$ / L1', and observed the narrowing of the two-phase region at low temperatures, as discussed briefly in Chapter 3.

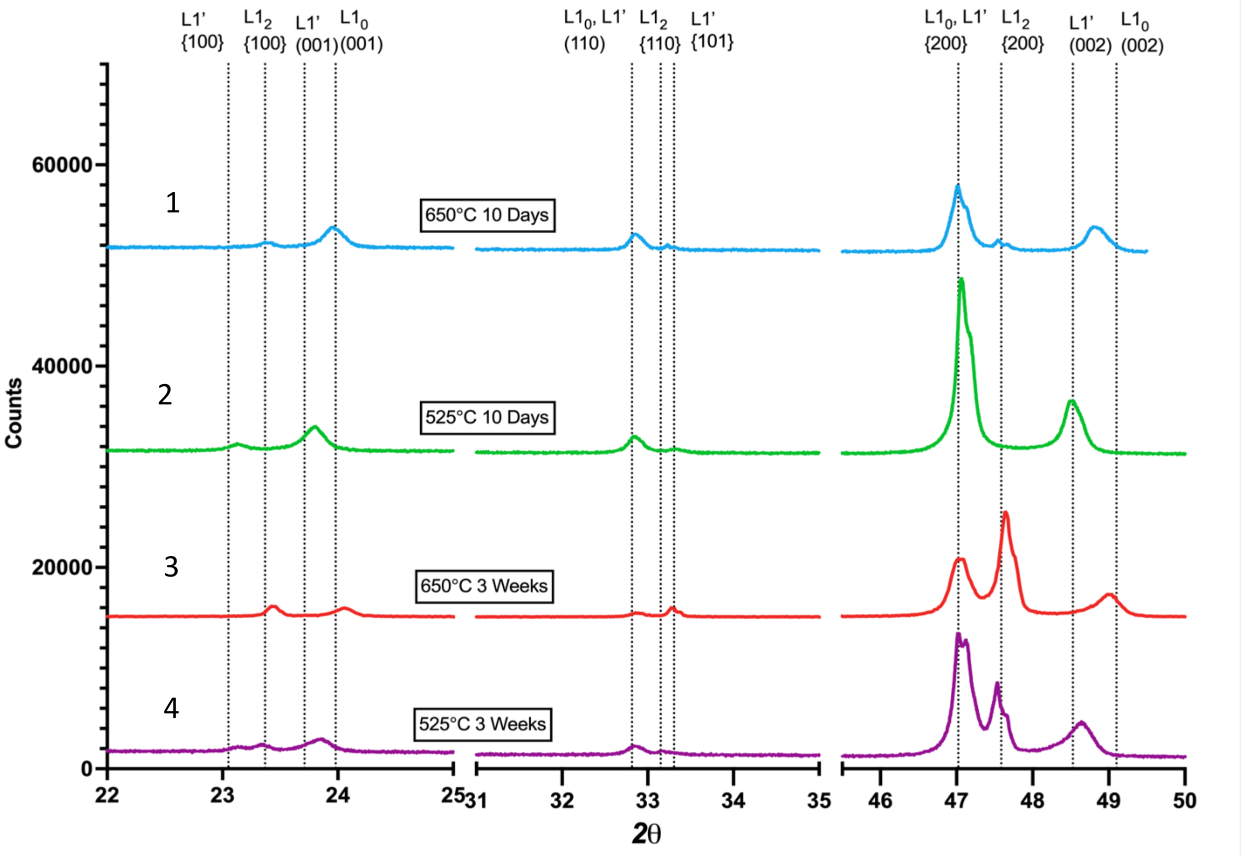

Figure 4.2. This shows phase equilibrium in the eutectoid region. In a) $L1_0$ and $L1_2$ coesxixtence is observed, while in b) single-phase L1’ is reported. In c) a minority $L1_0$ two-phase $L1_0$+$L1_2$ sample is observed, while at low temperatures and identical compositions d) shows L1’ + $L1_2$ coexistence.

The microstructure and energetics of $L1_0$ + $L1_2$ coexistence are explored in Section 4.1. In these Pd-lean $L1_0$ + $L1_2$ samples, a polytwin + nanolaminate layer morphology is found, where $L1_2$ wets all $L1_0$ orientation domain & anti-phase boundaries. The microstructure of $L1_2$ (majority) + $L1_0$ samples are explored in Section 4.2. In these Pd-rich samples, $L1_2$ presents as a bulk matrix where lenticular-shaped $L1_0$ polytwinned plates are spaced quasi-periodically within the matrix. In addition, $L1_2$ is also found to wet the orientation domain boundaries of these plates. L1' + $L1_2$ microstructures are explored in Section 4.3. L1' appears primarily as polytwinned plates where $L1_2$ again forms a wetting layer along all orientation domain and anti-phase boundaries. Interestingly, a significant consequence of identifying L1' + $L1_2$ coexistence is the confirmation that L1' (as explored in Chapter 3 of this dissertation) is most likely an equilibrium phase at low temperatures in the Fe-Pd system, and not a hybrid-ordering phase formed by either kinetics, strain, or anomalous ordering behavior as suggested by Steiner[57].

Table 4.1. Lattice constants and weight fractions of the constituent phases in the two-phase samples are shown below.

Sample # in Fig. 2	**Phase**	***a* (Å)**	***c* (Å)**	**Wt. Frac.**	***c/a***
1	**$L1_0$**	3.872	3.739	0.845	0.965
	$L1_2$	3.832	-	0.159	-
3	**$L1_0$**	3.877	3.735	0.21	0.963
	$L1_2$	3.831	-	0.79	-
4	**L1'**	3.867	3.753	0.711	0.970
	$L1_2$	3.833	-	0.282	-

The table included (4.1) is left as a reference for the two-phase regions explored in this chapter. It should be stated, that for at least the high-temperature aged samples, all transformations began with single-phase $L1_2$. As such, the often-times hierarchical organization of bundles, plates, orientation domains, and wetting layers is non-trivial. In addition, since ordering preceded precipitation, oftentimes quantitative phase analysis, long-range order parameters, or lattice constants are given but may evolve over time as higher degrees of ordering are achieved (in all phases).

4.2. $L1_0$ (majority) + $L1_2$ Coexistence

4.2.1. Structural Evidence of $L1_0$ + $L1_2$

Coexistence of $L1_0$ + $L1_2$ was found for all samples when annealed at 650°C. For Pd-lean composition samples (as explored in this section), $L1_0$ was the majority phase. Interestingly, single-phase $L1_2$ forms first for all two-phase samples, but these results and the attending transformation will be explored in a subsequent chapter (Ch. 5). Pertinent results are shown in Figure 4.3 below, where single phase $L1_2$ is observed on line 1. Fig. 4.3 Line2 shows how continuously cooled ($100°C/$Hr) and aged (+2Hr @ $650°C$) yielded two-phases coexistence. Two-phase coexistence is confirmed by the fundamental & superlattice reflections for $L1_2$ (i.e.{100} & {200}), and similarly for $L1_0$. These reflections are found near the 21-25° 2θ and 45-50° 2θ

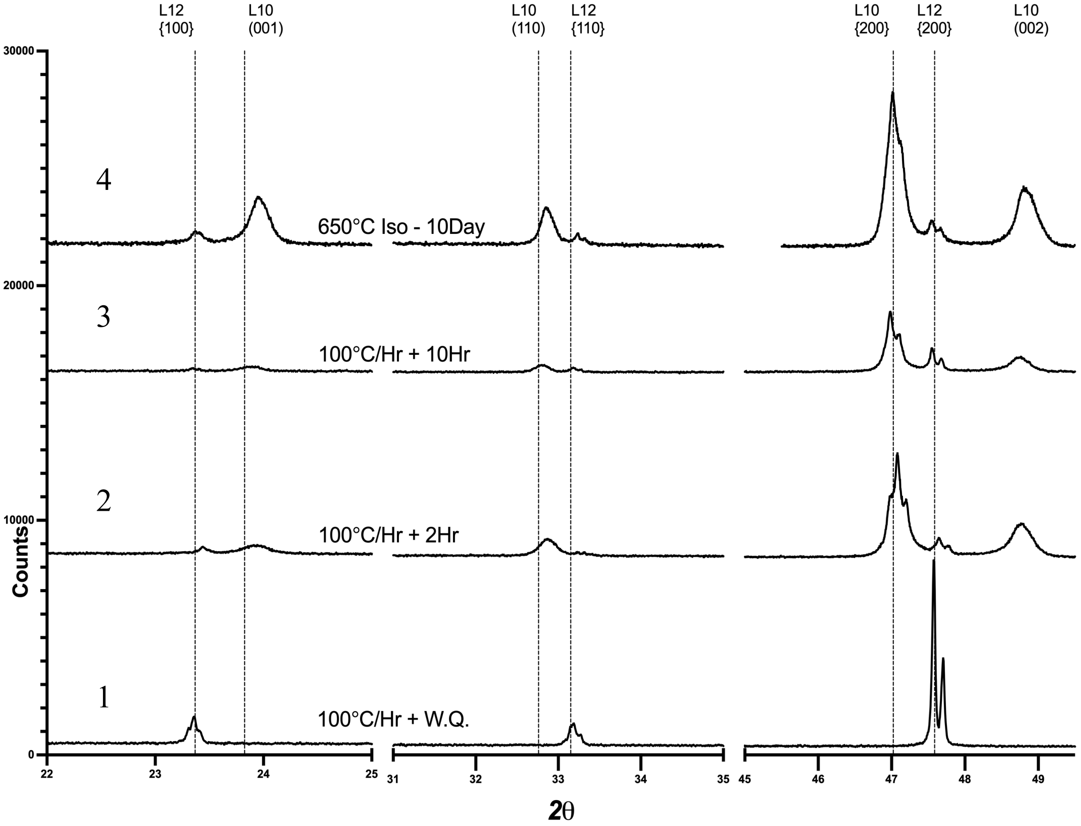

Figure 4.3. This region shows the polytwinned region where some of the colonies within plates are edge-on. Here, the BF images in a) and b) do not allow for identification of any $L1_2$.

regions, respectively. The dashed lines are found from single-phase samples. Fig. 3 lines 3 shows how additional aging at $650°C$ does not significantly alter the structural coexistence (phase fraction, structure), however the degree of long-range order does change. In addition, line 4 of Fig. 4.3 shows how for A1-quenched + isothermally aged samples at $650°C$ two-phase coexistence was observed with similar phase fractions .

Sample (corresponding line on Fig. 3)	$\boldsymbol{\eta} = \boldsymbol{meas.}/\boldsymbol{max.}\left(\frac{\boldsymbol{I_{(001)}}}{\boldsymbol{I_{(002)}}}\right)_{\boldsymbol{L10}}$	$\boldsymbol{\eta} = \boldsymbol{meas.}/\boldsymbol{max.}\left(\frac{\boldsymbol{I_{\{100\}}}}{\boldsymbol{I_{\{200\}}}}\right)_{\boldsymbol{L12}}$
100°C/H + 0min (line 1)	-	0.583
+120min (2Hr) (line 2)	0.46	0.63
+600min (10Hr) (line 3)	0.43	0.56
Iso. 10 Day (line 4)	0.91	1.03

Table 4.2. This table shows calculated long-range order parameters for $L1_0$ and $L1_2$ Fig. 3 line 1.

As described previously, the degree of long-range order η is given by the the ratio of superlattice:fundamental reflections $^{I_{001}}/_{I_{002}}$, and normalized by values of ratios generated from structure factor calculations for on-composition samples. For a completely disordered sample, $\boldsymbol{\eta}$ =0, while for a completely ordered sample $\boldsymbol{\eta}$ =1. Table 1 shows how only after 10 days aging do the long-range order values approach unity. This observation would significantly affect high-fidelity composition measurements (performed with non-destructive methods like EDS, XRF) but should not significantly affect microstructural investigations. However, over-aged samples may exhibit non-trivial changes to the microstructure.

4.2.2. Microstructure of of $L1_0 + L1_2$

$L1_0 + L1_2$ two-phase coexistence samples (with majority $L1_0$ phase) exhibited a prototypical polytwin morphology as shown in the bright-field micrographs of Figure 4.4a,b. A grain in these samples exhibited multiple plates (in the language of Vlasova[41] these would be called bundles), and each plate consisted of conjugately paired *c*-domains aligned along {110} twin boundaries. As observed in Figure 4.4a, many times each plate consisted of multiple colonies, where conjugate pairs of *c*-domain pairings shared one of the 12 {110} habit planes locally within a plate. For example, the green arrow in Fig. 4.4a points to one colony within a plate, while the orange arrow in Fig. 4.4a points to another colony with different twin habit planes within the same plate. These bundle thicknesses can differ, based on growth rate, as suggested by Vlasova[41].

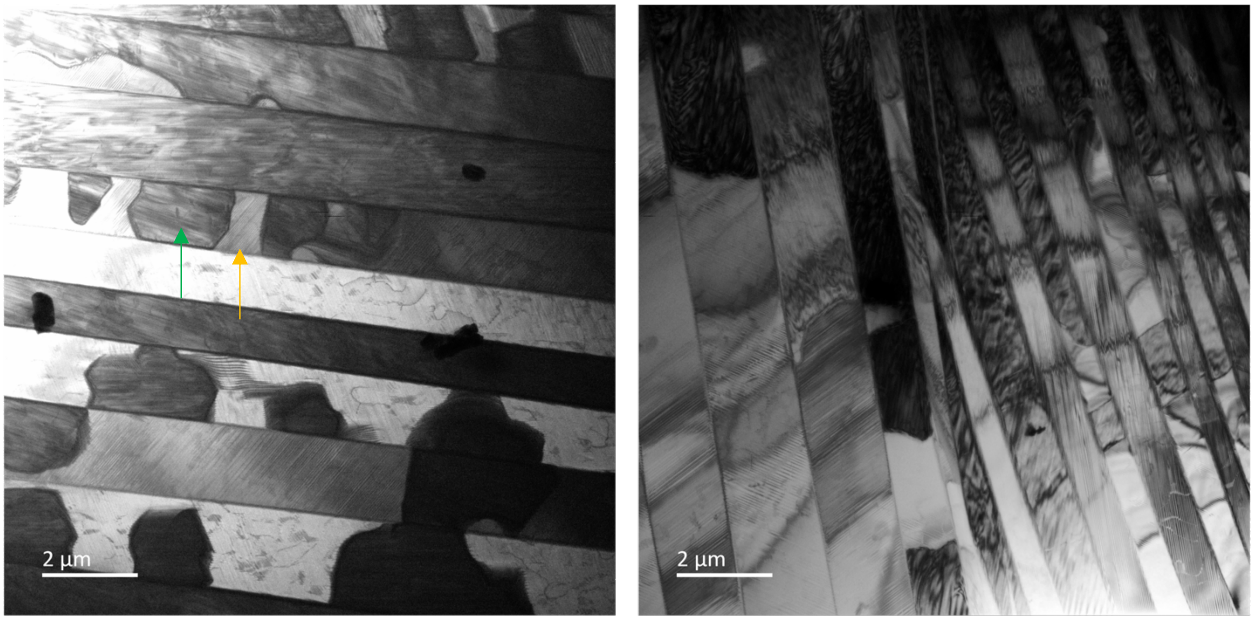

Figure 4.4. This region shows the polytwinned region where some of the colonies within plates are edge-on. Here, the BF images in a) and b) do not allow for identification of any $L1_2$. Yellow and Green arrows designate differently oriented *c*-domain colonies bounded within a single plate.

At magnification and imaging plane of Figure 4.4a,b, it is impossible to observe the $L1_2$ wetting layers which lie directly along the orientation domain and anti-phase boundaries of the polytwinned microstructure. Proper characterization of this microstructure is possible with DF-TEM as shown Figure 4.5, where a series of micrographs allow for identification of individual *c*-domains and the $L1_2$ wetting layer. It should be stated, that there is clearly no bulk matrix region seen in Figs 4.3, 4.4 and suggests that all regions of $L1_2$ exist in stead as the nanometer wetting layer which will be shown below. The associated SADP for this series of images is shown in Fig. 4.5e, with ther zone axis aligned down [001]. Dark-field imaging shown in Fig 4.5a,b,c with *g=100,010,110* allows for identification of the $L1_{0,X}$, $L1_{0,Y}$ and $L1_2$ structures respectively. The conjugate pair of c-variants exhibit an $L1_2$ wetting layer on their {110} interfaces. Orientation domain boundaries (orange arrow in Fig. 4.5d) separate conjugate pairs of *c*-variants, whereas the horizontal faceted regions spanning the width of orientation variants (green arrow in Fig. 4.5d) are anti-phase boundaries and separate regions of the same *c*-variant that are out of phase. These APBs have also aligned along {110}. In Fig. 4.5f, a schematic of the [001] zone axis SADP is attached, with fundamental (green), superlattice (yellow), and $L1_2$ (orange) reflections clearly labelled. The polytwinned structure is such that the diffraction pattern becomes an overlap of the diffraction patterns for the individual variants which constitute the polytwin microstructure (in this case, $L1_x$ and $L1_y$ variants). As shown by Tanaka[40], the {220} reflection shows clear splitting at angle 2φ. There exist relationships between the splitting angle φ, the intersectional angle ϕ (see bottom of Fig. 4.5f, which is the angle a pair of *c*-domains make with one another at their ODB), and the *c/*a ratio. The relationships are as follows: $\phi + \varphi = {}^{\pi}/_{4}, {}^{c}/_{a} = tan\phi = \tan({}^{\pi}/_{4} - \varphi)$. The value 2φ was extracted from the SADP in Fig. 5e, and found to be 2φ =3.6°, so $\varphi = 1.8°$. As such, the angle individual *c*-domains will make with one another $2\phi = tan^{-1}(\pi/4 - 1.8) = 45.41527261° * 2 = 90.83054522$. This is taken as correct (and what is expected) within the

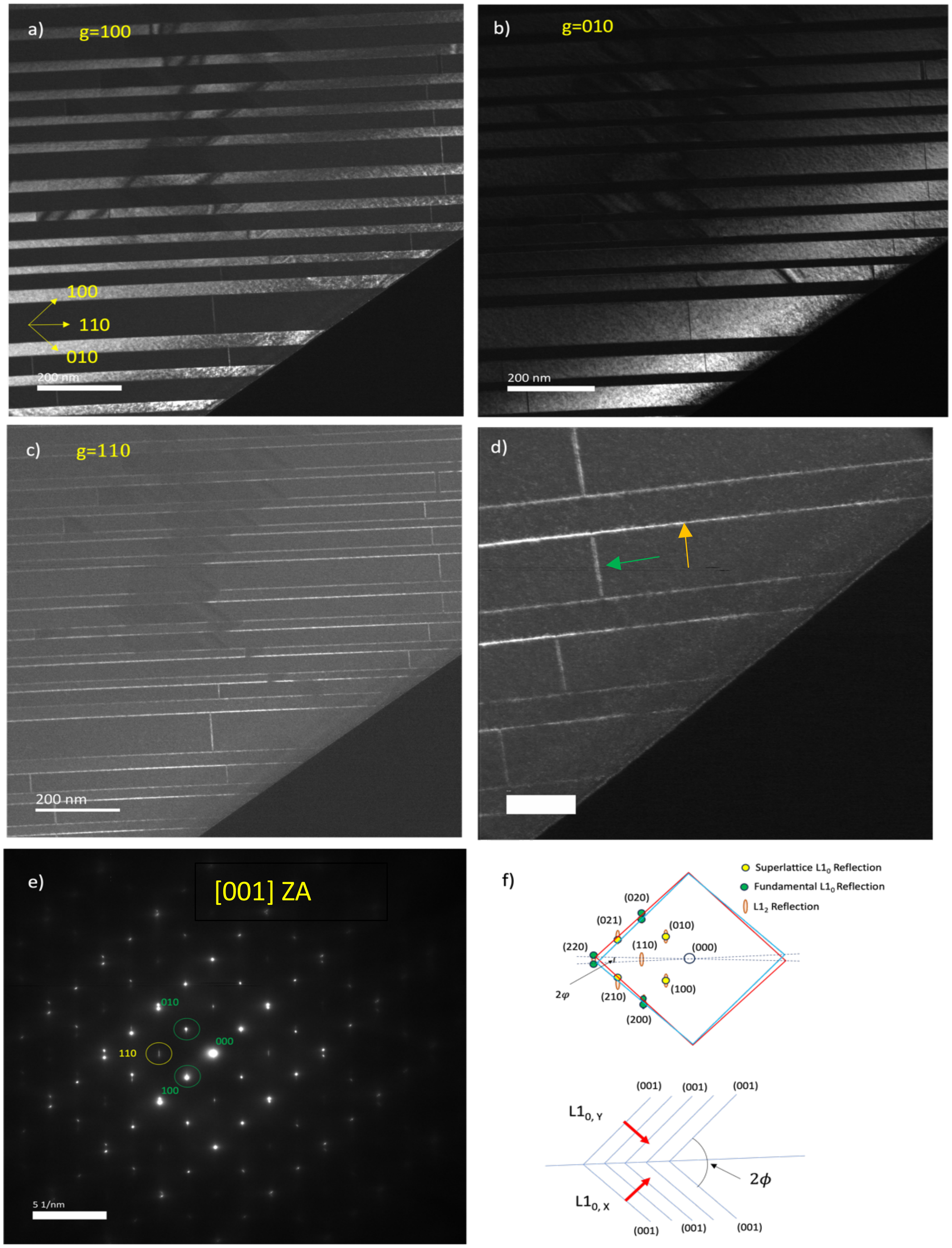

Figure 4.5. A series of DF-TEM images which allow for identification of the individual $L1_0$ variants , and the $L1_2$ wetting layer. In d), orange and green arrows articulate orientation domain and anti-phase boundaries, respectively. The SADP down a [001] Zone Axis in e) is given as a schematic in f), where superlattice + fundamental reflections are labellled.

bounds of measurement error. When calculating intersectional angle from *c/a* we find slightly different values: $tan^{-1}\left(\frac{c}{a}\right) = tan^{-1}(0.9654) = 43.991°$, or an angle $2\phi = 87.98296334°$. An intersectional angle for $L1_0$ polytwin of 88° was also reported by Tanaka[40]. The discrepancy between these values can be attributed to errors in angle measurement using image processing software.

A schematic for the single-phase $L1_0$ polytwin microstructure is shown in Fig. 4.6a, where conjugate pairs of orientation variants are twinned along {110}, exhibiting transformational (curvilinear) anti-phase boundaries. In contrast, a simple $L1_0$ + $L1_2$ wetting layer schematic is shown in Fig. 4.6b, where all orientation domain and anti-phase boundaries have been wetted by a thin layer of $L1_2$ as shown by the orange strips. In addition, APBs are now visibly faceted along {110}. The thin lines labelled A/B/A in the top right of Fig. 4.5a and b correspond to the atomic sheets of Fe/Pd/Fe atoms which (when aligned <100>) constitutes the $L1_0$ crystal structure.

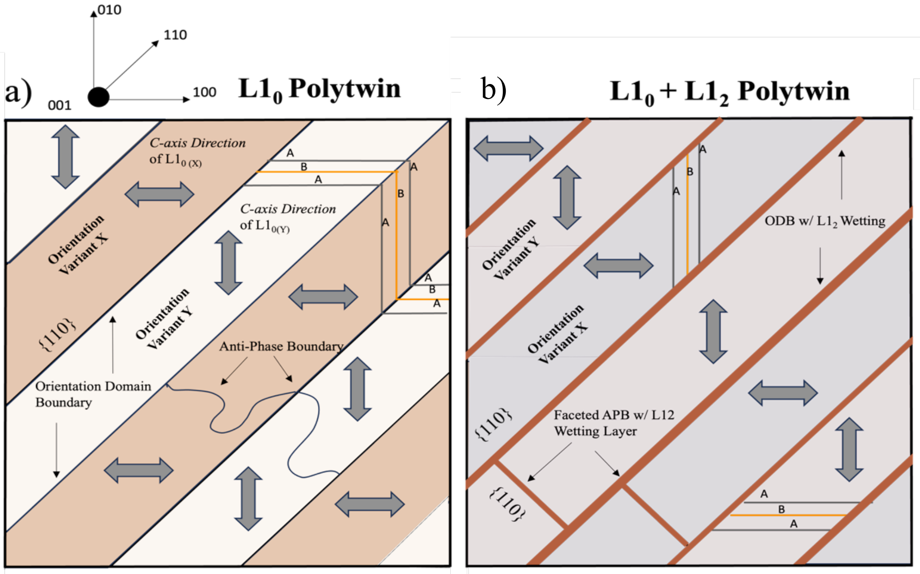

Figure 4.6. A schematic polytwin microstructure for single-phase $L1_0$ in a) , and a $L1_0$ polytwin + $L1_2$ wetting layer schematic shown in b).

Coherency across ODBs is shown in Fig. 6a, where A sheets continue unimpeded, but not for sheets in Fig. 4.6b. This difference will be explored below, where many it is possibly for A/B sheets may be out of-phase at the ODBs between conjugate pairs of variants in the $L1_2$ wetted samples. These schematics are helpful references for polytwin terminology, and show a snippet of the hierarchical nature of the polytwin microstructure.

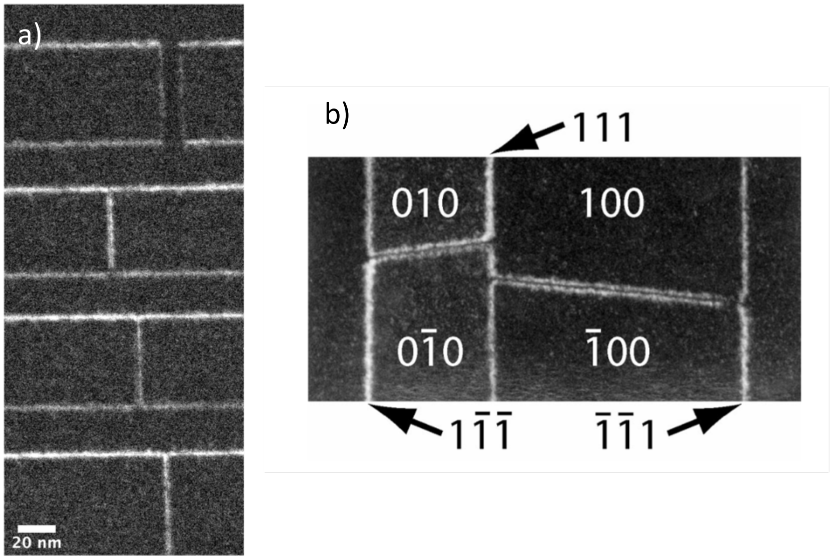

Figure 4.7. In a), $L1_2$ is seen to wet all $L1_0$ ODB and faceted APB interfaces. In b), the all ODB + APBs are wet in Co-Pt[87], but the APBs are angled 5° with respect to {110}.

The faceting observed in these Fe-Pd alloys was similarly observed in Co-Pt, and reported by Le Bouar[87]. Le Bouar found that when on-eutectoid composition samples (Co – 60 at% Pt) were continuously cooled (at a rate of 10 or 40°C/Day) through the eutectoid isotherm in Co-Pt and then held for a long duration (2-4 weeks aging) at temperatures between 690℃ and 600℃, the $L1_0$ polytwin microstructure was decorated by a cubic $L1_2$ layer along orientation domain and anti-phase boundaries (as shown in Fig 4.7b for reference). Interestingly, the anti-phase boundaries in Co-Pt appear to align 5° with respect {110}, as seen by the slight tilt in the DF image of Fig. 4.7b. Utilizing HRTEM and an Ising Model developed elsewhere[88] they were able to identify the preference for (002) Pt-rich planes to continue unimpeded between $L1_0$ and the $L1_2$ wetting layer.

This preference for continuation of (002) sheets from one orientation variant into the cubic wetting layer unimpeded, then dictates wetting behavior rules, whereby specific $L1_0$/$L1_2$ pairings (of orientation & translation variants) becomes favorable or unfavorable. Subsequently, a vectorial ordering approach for the different $L1_0$ and $L1_2$ orientation and translation variants was given. The possible orientation variants are given below in Figure 4.8.

$L1_0$ forms with its *c*-axis oriented along the <100> directions of the parent phase, forming 3 orientation variants within a single grain. As an ordered structure, $L1_0$ ordering can begin any one of the four FCC sublattice sites, which will be organized in this example as simply (0,0,0), (1/2,1/2,0), (1/2,0,1/2), (0,1/2,1/2). However, due to the nature of $L1_0$ ordering (A/B sheets stacked along *c*-axis), there are only two discrete sub-lattice sites. Any ordering that begins on (001) will be out-of-phase with any domain that begins ordering on the FCC (002). As such, there are two translation variants possible per orientation variant, forming a total of 6 possible variants for the $L1_0$ structure within one grain (see Fig. 4.8). Since $L1_2$ is cubic, preferred orientation of the lattice along crystallographic directions is not possible. However, $L1_2$ ordering can begin on any of the four FCC sublattice sites. As such, there are a total of four possible $L1_2$ variants within a single

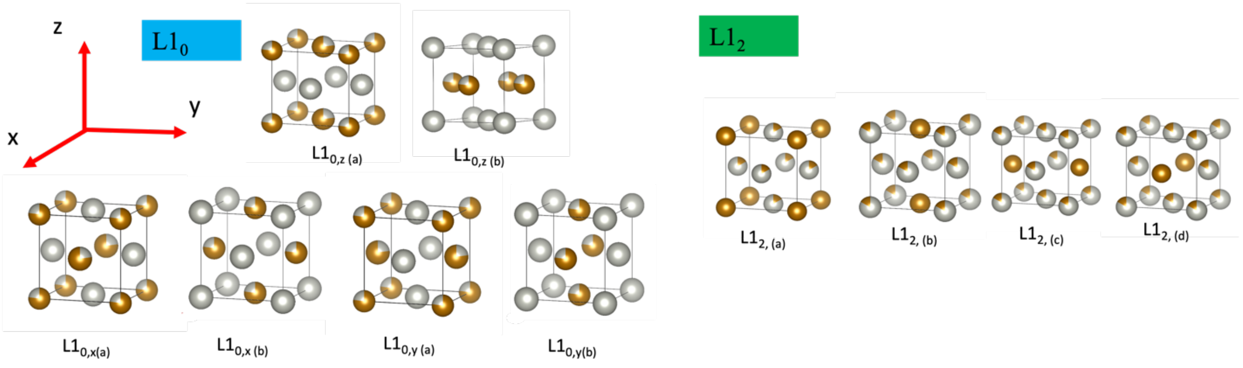

Figure 4.8. Schematic articulating all possible $L1_0$ and $L1_2$ variants within a single grain. $L1_0$ forms with three possible orientation variants, which each have two possible translation variants forming 6 in total. $L1_2$ can only form as four separate translation variants.

grain (as shown below in Fig. 4.8). Wetting logic for the cubic $L1_2$ structure along $L1_0$ orientation domain and anti-phase boundaries can be summed as in the table below.

Table 4.3. Designation of orientation and translational variants

$L1_0$ Type	$L1_2$ Type
$L1_0$x,a	$L1_2$,a or $L1_2$,b
$L1_0$x,b	$L1_2$,c or $L1_2$,d
$L1_0$y,a	$L1_2$,a or $L1_2$,c
$L1_0$y,b	$L1_2$,b or $L1_2$,d
$L1_0$z,a	$L1_2$,c or $L1_2$,d
$L1_0$z,b	$L1_2$,b or $L1_2$,c

Table 4.3 shows the wetting schematic logic for the different $L1_0$ and $L1_2$ variants within a grain. Le Bouar[87] shows this logic identically, but vectorially. Direct visualization of the wetting logic is shown directly in Figure 4.9, where two {110} interfaces between $L1_0$ and $L1_2$ are shown, highlighting a preferential (low-energy) interface in a), and unfavorable (high-energy) interface in b). In this atomic schematic, continuation of the Pd-rich (002) sheets can be seen to continue unimpeded from the $L1_0$ variant directly into the wetting $L1_2$ wetting layer for the low-energy case. For the high-energy choice in b), Pd-sheets do not traverse the boundary into $L1_2$, coherently. This visually explains the choice for wetting schematics as given in Table 2.

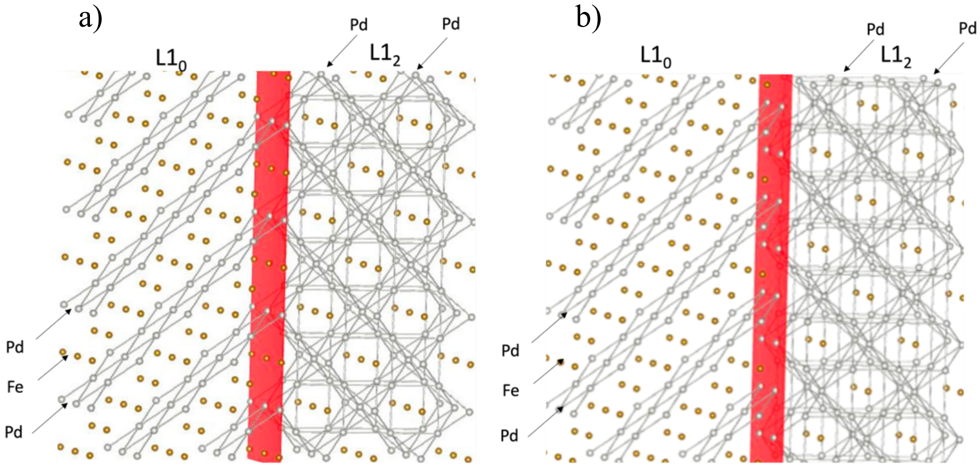

Figure 4.9. Two {110} interfaces between $L1_0$/$L1_2$, showing a low-energy (preferential) interface in a) and unfavorable (high-energy) interface in b).

One of the salient features missing from the report on wetting layers in Co-Pt[87] two-phase alloys, is the consideration of $L1_0$ channels formed by the wetted APB structures. This can be seen in DF imaging, in Figure 8, where a clear 'channel' is formed between $L1_2$ wetting layers that have decorated the boundaries. The inner $L1_0$ channel, and the *c*-domains that are above/below it may be in or out of phase (different translation variants of the same orientation variant). Figure 4.10 shows an $L1_0/L1_2/L1_0$ on{110} interfaces (arrows are included to designate *c*-axis direction of the orientation variants), which forms one half of the channel + wetting APB structure. Although wetting schematics can be clearly articulated based on the logic above, there exist (and have been experimentally observed), boundaries that can form at APB channel + orientation variant interfaces. When wetting is present at this present, the structure is referred to as being 'closed', whereas if there is no wetting layer present the region is described as 'open'.

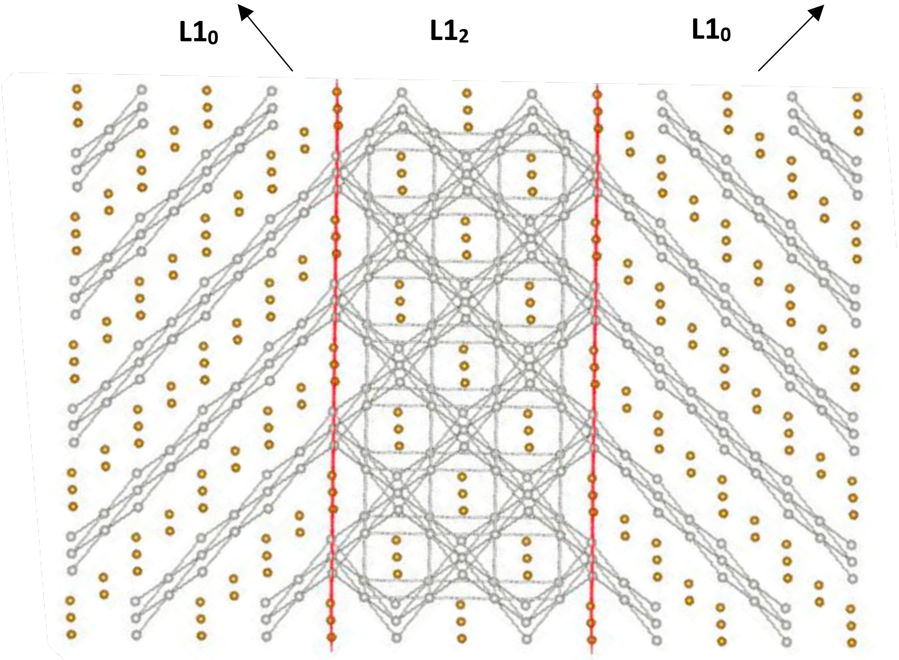

Figure 4.10. This atomic model shows two {110} interfaces between conjugately paired $L1_0$ orientation variants that have an $L1_2$ wetting layer between them. This structure forms one half of the APB channel structure seen in the HRTEM image Fig. 11.

Examples of the "open" and "closed" channels are shown respectively by HR-TEM images shown in Figure 4.11a,b respectively. A simple schematic articulating wetting layer and channel structures is shown directly above it. The arrows within Fig. 4.11 articulate the *c*-axis direction for the individual $L1_0$ variants, designating the orientation variant (translation variant will be unknown, though the APB does separate out-of-phase variants). In the schematics of Fig. 4.11a,b, the blue regions correspond to $L1_0$ of one orientation variant, while grey regions correspond to the conjugate pairing of the $L1_0$ orientation variant. The black regions are strictly $L1_2$, and do not have explicit correspondence to any $L1_2$ translation variant. The open/closed structures can be seen by

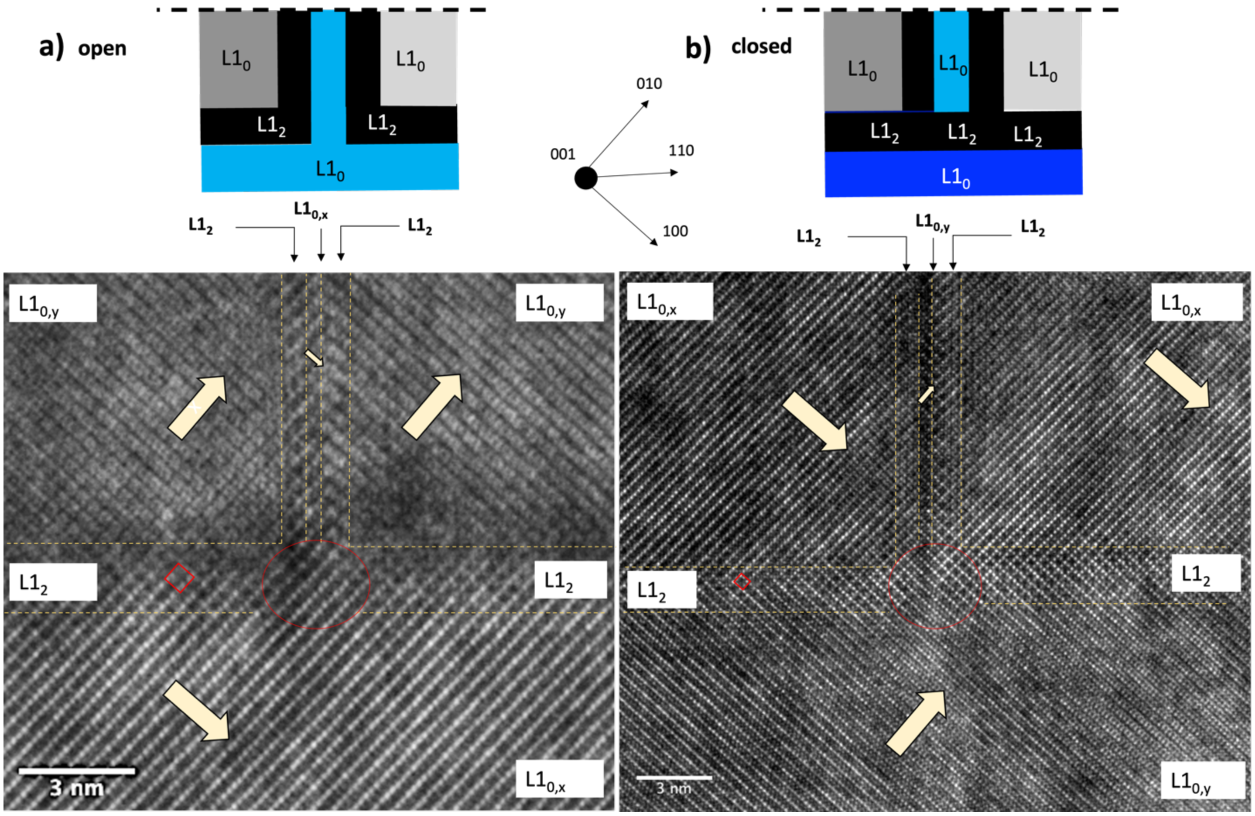

Figure 4.11. HRTEM of APBs showing open/closed structure. The schematics in a), b) are included to show a general overview of the wetting layers that yield an open/closed structure. The HRTEM images in a), b) show atomic ordering changes within the orange lines, which serve as a guide to the eye. Arrows are included to show the direction of the *c*-axis which designates the orientation variant.

the change in atomic ordering in the red ellipses included on the HRTEM images, which show direct continuation of tetragonal layers, or a cubic region at this interface. These cubic wetting layers appear to be roughly ~1-3nm thick in in these samples. The formation of these wetting layers however, is non-trivial, and may be directly related to the incipient $L1_2$ parent (ordered) material (Fig. 3 line 1). This would be in disagreement with the suggested transformation for this polytwin + wetting microstructure as found in phase field models buy Khachaturyan[36], however this transformation will be explored more in depth in a subsequent chapter.

As seen in Figure 4.11a (and Fig. 4.7a,b) the central $L1_0$ region continues unimpeded from one variant to the next. This is in contrast to Fig. 11b, where the $L1_0$ region from the *c*-domain below the APB is 'blocked' by cubic regions pertaining to the $L1_2$ wetting layer. A schematic of this wetting layer across APB channels generating open/closed structures is given in Figure 4.12, where the possible $L1_{0,X(a)}$, $L1_{0,X(B)} + L1_2$ wetting scenarios are clearly shown. The colors given above the schematic articulate the different variants for $L1_0$ and $L1_2$. This figure does not explore all possible $L1_0$ variants.

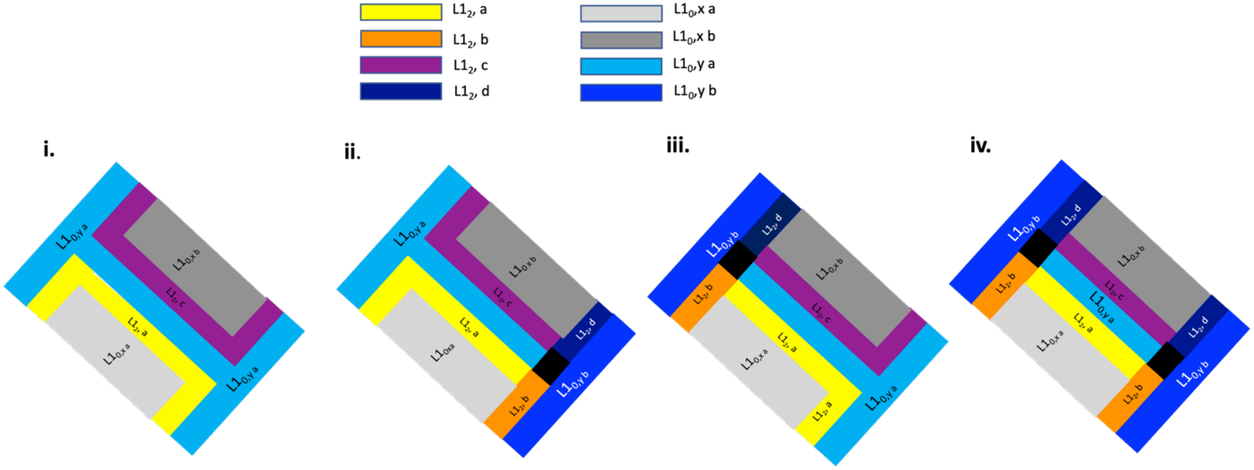

Figure 4.12. A series of open/closed APB structures is shown in i)-iv), where different colors are used to identify orientation/translation variants for $L1_0$ and $L1_2$. The wetting logic for these structures is tabulated clearly in Table 2.

4.3. $L1_2$ (majority) + $L1_0$ Coexistence

4.3.1. Structural Evidence

For Pd-rich composition samples aging at 650℃ saw coexistence of $L1_0 + L1_2$ with majority $L1_2$ phase, as shown in the X-ray diffractogram of Fig. 4.14. The fundamental $L1_2$ reflection is much more intense than the fundamental {200} reflection for $L1_2$ seen in Pd-lean samples (Fig. 4.3 line 1). Minute changes in Pd concentration drastically shift the quantity of the equilibrium phase fractions (location of the composition on the two-phase tie-line). There are minor structural changes found for the $L1_2$ majority two-phase samples, namely a slightly smaller *c/a* ratio (increased tetragonality). Changes in long-range order were minimal, as found by the ratio of superlattice:fundamental reflections.

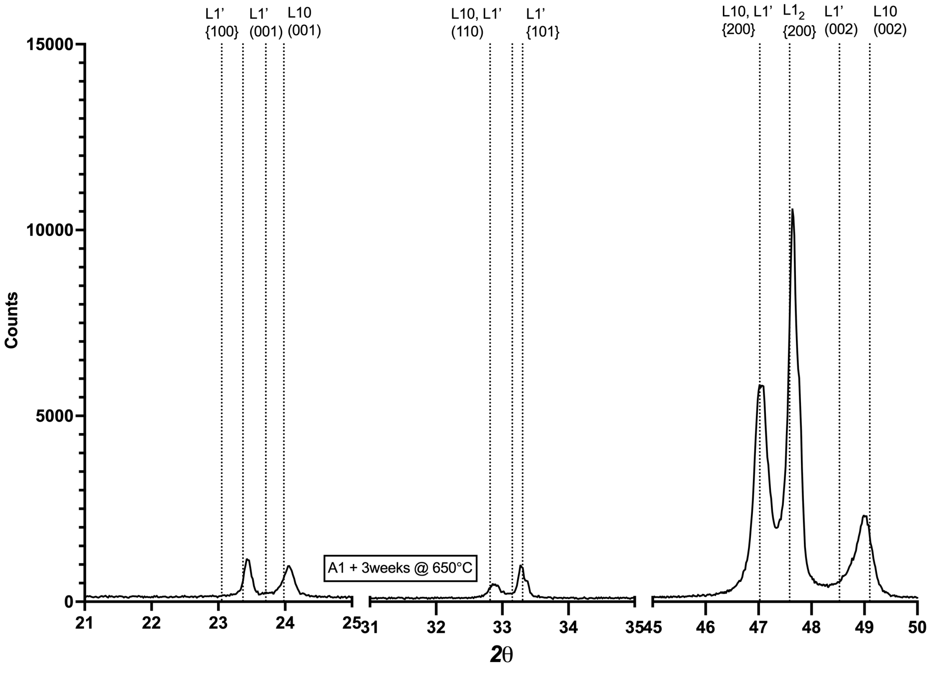

Figure 4.13. X-ray diffractogram of the $L1_2 + L1_0$ samples, with $L1_2$ as a majority phase. Although this diffractogram is included within Fig. 3, it is shown here stand-alone for ease of phase ID.

While quantitative comparisons between two two-phase coexistence samples (and their respective composition) gives satisfactory insight into the width of the two-phase region, a more rigorous analysis was undertaken to give a better understanding of the width of the two-phase region.

Phase	$\frac{meas.}{max.}(I_{001}/I_{002})$	*c*	*a*	*c/a*
$L1_0$	0.85	3.877	3.735	0.963
$L1_2$	0.33	3.831	-	1

Table 4.4. This shows proxy long-range order values for $L1_0$,$L1_2$, and the respective lattice constants.

Figure 4.14a shows a BF-TEM micrograph with the overarching morphology of the Pd-rich $L1_2$ + $L1_0$ samples, with three $L1_0$ plates spaced quasi-periodically apart from one another, enmeshed within an ordered cubic $L1_2$ matrix. Fig. 4.14b shows a Titan TEM EDS map made from a similar but non-identical $L1_2$ matrix/ $L1_0$ plate region. In this micrograph the dashed orange lines serve as guides to the eye, delineating the plate from the matrix. Since thickness of the sample varied significantly, only measurements 4.16 & 4.17 were trusted. The X-ray spectra from these regions is shown to the right in Fig. 4.14c,d 4.16 & 4.17 and correspond to plate & matrix respectively. The $L1_0$ plate was given as $Fe_{39.23}Pd_{60.77}$, whereas the $L1_2$ matrix gave a composition of $Fe_{38.64}Pd_{61.36,.}$ This gives a two-phase width of ~0.6 at%. This finding is in general agreement with a diffusion couple sample made previously, which showed similarly narrow two-phase regions. ThermoFisher reports a sensitivity of EDS measurements of up to 0.1% atomic concentration. However, since the $L1_0$ plate morphology is such that tiny wetting layers are present, the overall composition may slightly

deviate from the solvus boundaries for $L1_0$ and $L1_2$, which constitute the boundaries of the two-phase region. However, since these samples are relatively well ordered (according to superlattice:fundamental reflections), we suggest that these values are trustworthy.

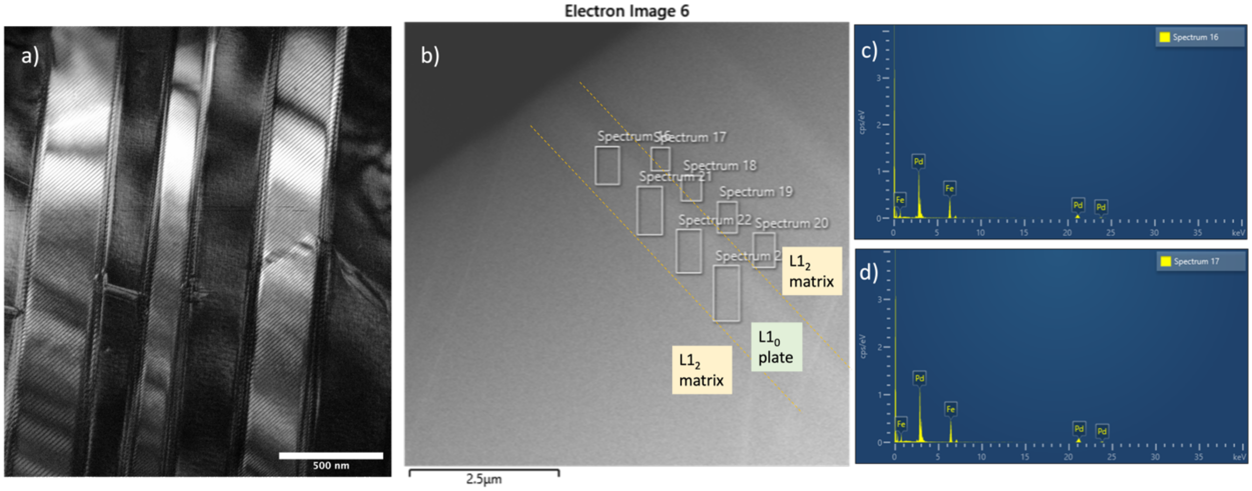

Figure 4.14. The matrix + plate morphology in a) is included as an introduction to the microstructure. In b), EDS maps taken in the Thermofisher Titan TEM are shown, although only spectrum 16 & 17 are considered valid. In c) and d) the X-ray spectra are shown for the areal EDS maps 16 & 17.

4.3.2. Microstructure of $L1_2 + L1_0$

A microscopic (overview) image of the $L1_0$ + $L1_{2(\text{majority})}$ microstructure is displayed in Figure 4.15a,b below. $L1_0$ plates, exhibiting internal twinning along {110} are seen to be quasi-periodically enmeshed within the $L1_2$ matrix. While majority $L1_2$ samples were identified first structurally with X-ray diffraction and follow logically with the increase in Pd-concentration, this matrix + plate morphology is unexpected and so far unreported in the literature. The $L1_0$ plates are lenticular in shape, with tapered edges and a bulging of the midsection; that is, they are three-dimensional saucer-like precipitates that are internally twinned along {110}. The dimensions of

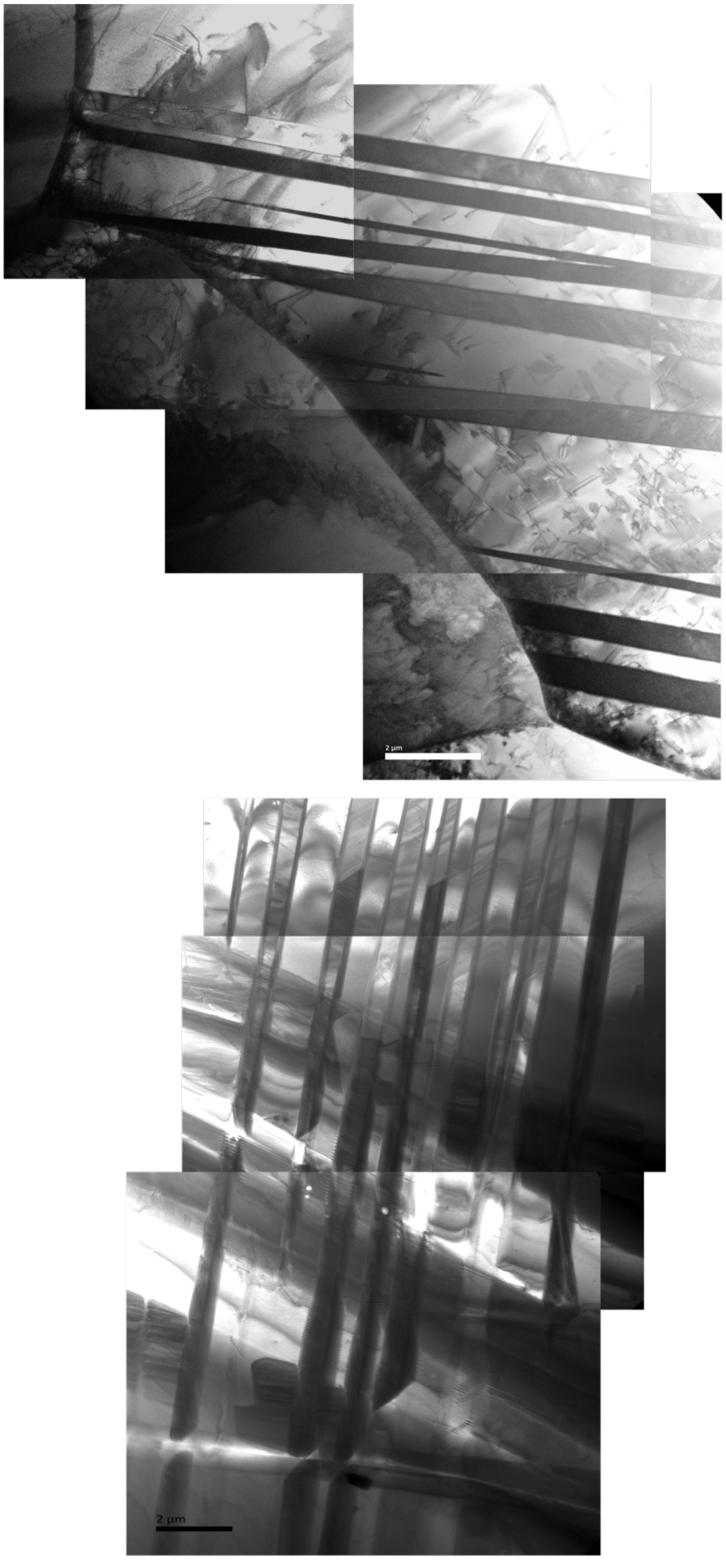

Figure 4.15. In a), a composite BF-TEM image showing the $L1_2$ matrix + $L1_0$ plate microstructure. The $L1_0$ plates appear to be spaced quasi-periodically, to minimize volume-driven elastic strain energy. In b), another BF-TEM composite image is shown, where length of plates can be approximated, with lengths > 30um.

the plate are calculated across multiple specimens: average plate widths are shown to be 512nm, with average inter-plate (center-to-center) spacing to be 1215nm. In Figure 15a, the matrix + plate grain boundary with readily discernible features is shown. Plates appear to terminate (and spawn) on these boundaries. In Figure 4.15b, another composite BF-TEM image is shown , probing the

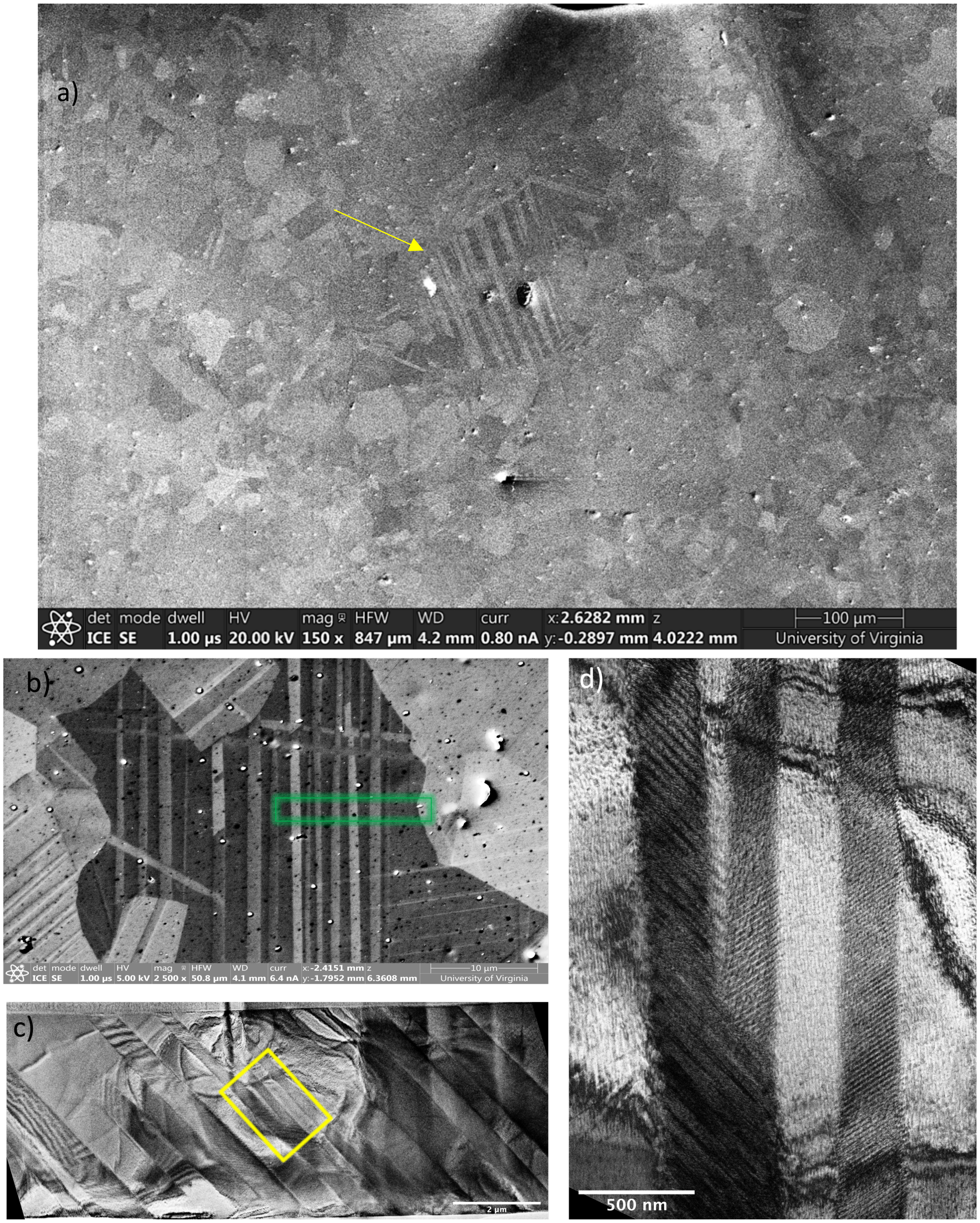

Figure 4.16. This series shows two SEM (a,b) and two TEM (c,d) images of the plate + matrix morphology. The green rectangle in b) was FIB-ed out to form the sample viewed in c,d. This allowed direct visualization of the plate + matrix morphology in X,Y (planar) dimensions (as seen in a) and in Z (depth as seen in c,d).

plates in profile for longer sections, giving information on the distance spanned by any plate. Dimensions gathered from Fig 4.15b. suggest $L1_0$ plates can easily span >30um in length. This is corroborated by SEM micrographs which show plates are typically bounded by the grain boundaries. The individual *c*-domains exhibit {110} twinning planes, and are bounded within the plate boundaries. Greater detail into the *c*-domain + matrix morphology is shown in Fig. 4.16, 4.17. Interestingly, the *c*-domains orientation domain boundaries are also wetted by an $L1_2$ layer. The wetting layer along orientation domains gives insight into transformation pathways, suggesting a long-range self-assembly within the ordered cubic matrix, rather than a super-saturated $L1_0$ product that subsequently forms $L1_2$ along its boundaries.

Figure 4.16 shows SEM (a,b) and TEM (c,d) micrographs made of the matrix + plate microstructure, giving insight into plate + matrix relationship in three dimensions. The micrograph in Figure 16a shows a wide-surface microscopic view of the matrix + plate grains, where individual $L1_0$ plates are resolved in the center grain (yellow arrow). In order to probe the plate morphology in three dimensions, a section of the plate region was 'cut' using a focused ion beam. The region of interest is shown in Fig. 4.16b, where a green rectangle is included as a marker. Interestingly, Figure 4.16b shows there to be 'crossing' of $L1_0$ plates within a single grain. This may be energetically preferable as strain-relieving mechanism (e.g. a 'hatch-work' of polytwinned plates may alternate tension & compression if perpendicular directions). In Figure 4.16c the FIB-ed specimen is seen with TEM BF imaging mode, whereby the plates viewed 'long-wise' in Fig. 16b are now viewed 5um 'into' the imaging plane of Fig. 4.16a,b. This affords direct visualization of the relationship of plates in both X,Y directions and now Z directions as well. This experiment gave satisfactory confirmation of the lenticular nature of these $L1_0$ plates. Spacing of the plates is again seen to be quasi-periodic. The energetics of plate-spacing and growth may be related to: 1) compositional limitations whereby $L1_0$ plate spacing is determined by supersaturation of Fe-species within the $L1_2$ matrix, or 2) inter-matrix strain accommodation, whereby plates are spaced at an equilibrium distance to minimize the volumetric dependent elastic strain energy. Interestingly,

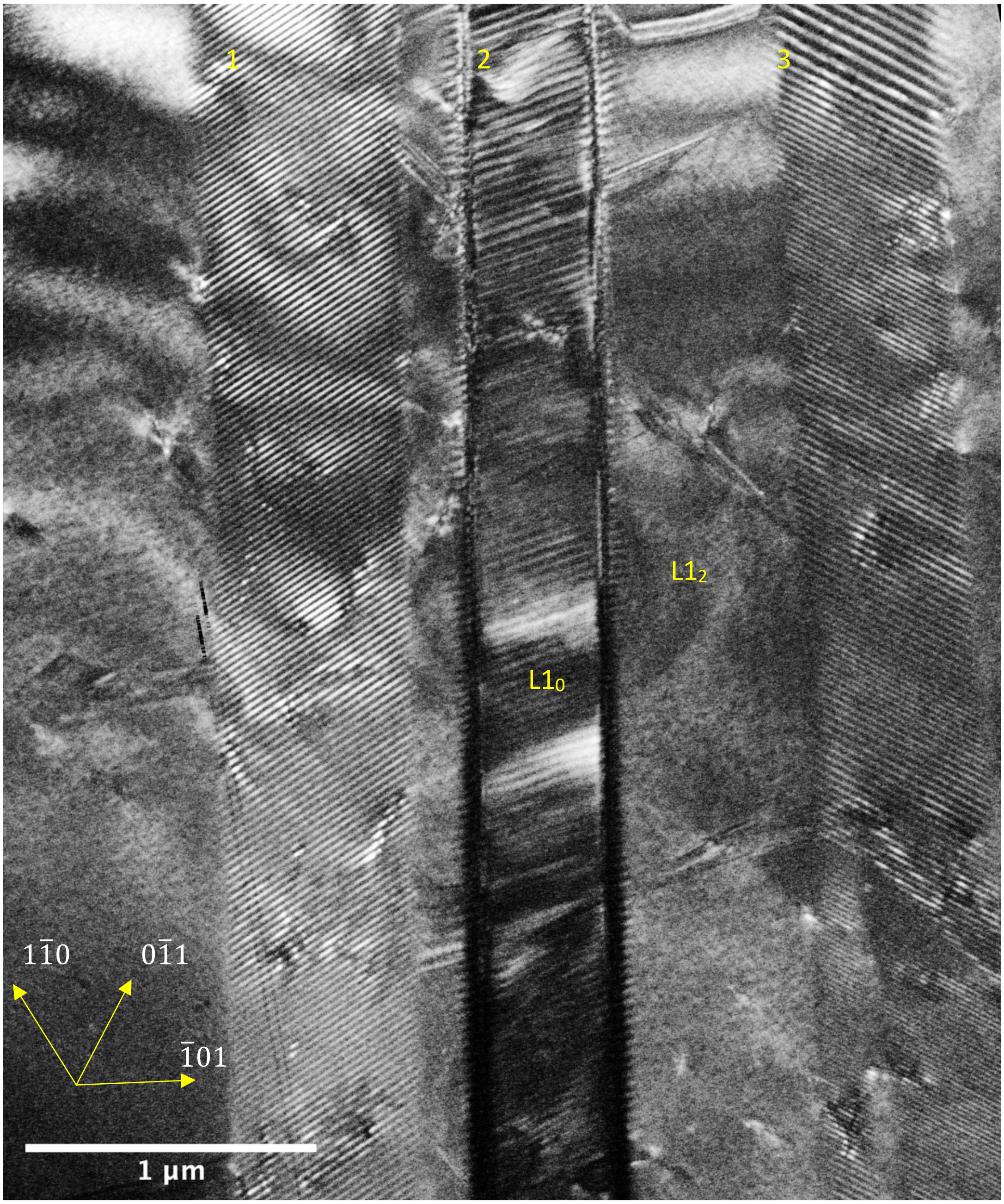

Figure 4.17. A DF-TEM image showing three $L1_0$ plates arranged within the $L1_2$ matrix. Interestingly, plates 1,3 share identical conjugate pairs of orientation variants but dissimilar orientation domain {110} boundaries.

plate/plate interfaces can be coherent, exhibiting invariant-plane strain according to Vlasova[41], when nucleated from the same center. As such, it is relatively unexpected for matrix/plate interfaces to be energetically preferable over plate/plate interfaces. However, a confluence of factors may affect plate growth and spacing, as mentioned above. Figure 4.17 is included to show

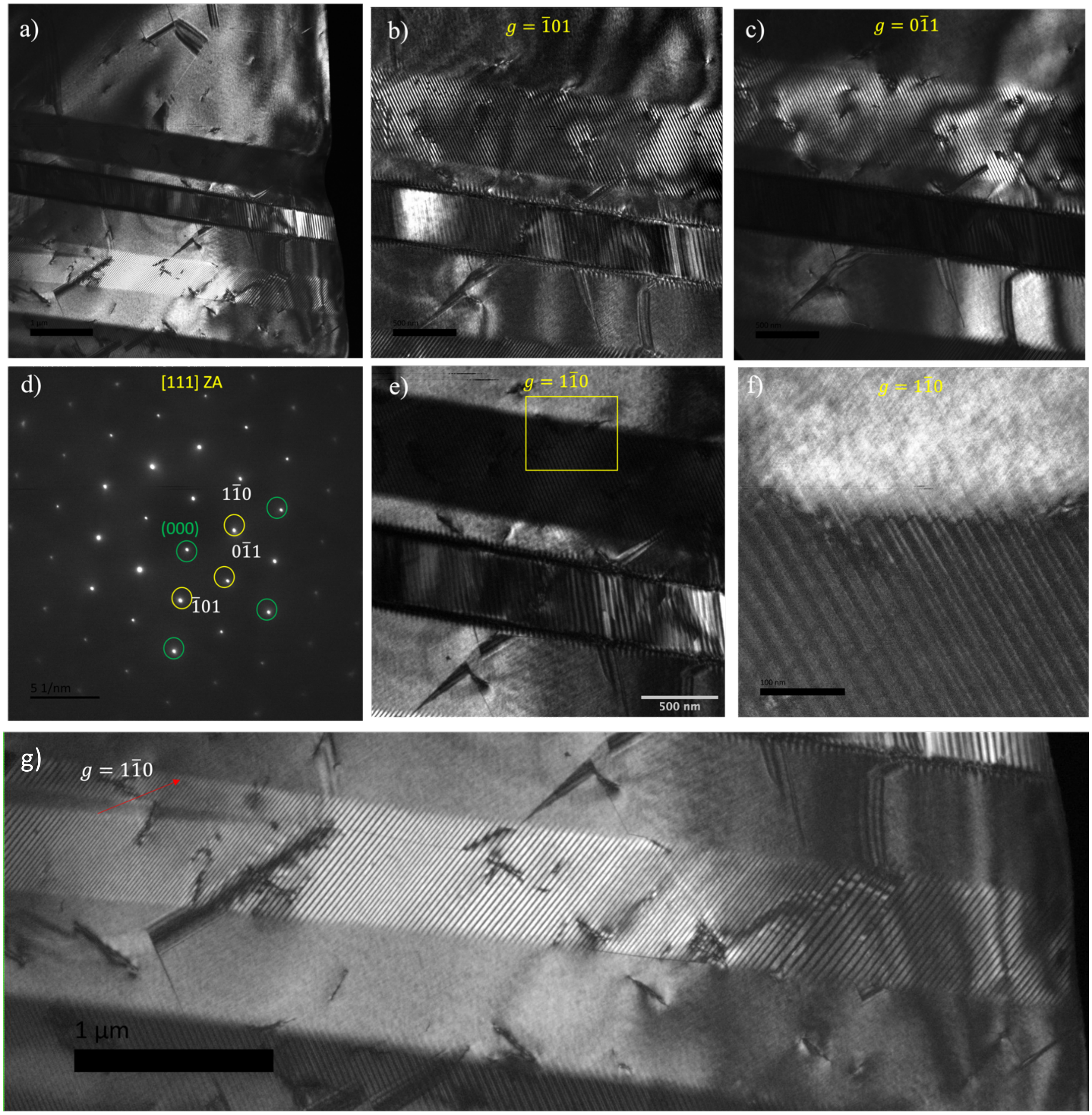

Figure 4.18. This series of DF-TEM images taken down a [111] zone axis (include in d)), show the conjugate pair of orientation variants, and the L1$_2$ wetting layer along ODBs in f). in g), a plate is shown, where branching is seen in the left half of the image. This phenomenon is most likely tied to the formation mechanism and will be discussed in an a subsequent chapter.

a very clear visualization of the plate/matrix microstructure. Interestingly, plates 1,3 share conjugate pairs of orientation variants, with different orientation domain {110} boundaries.

A series of dark-field micrographs of the plate/matrix morphology is shown in Figure 18, with imaging done down a [111] zone axis (Fig. 4.18d). Fig 4.18a shows the general view of the region of interest, where three plates are clearly resolved. In all of the DF imaging conditions, the $L1_2$ matrix appears bright because $L1_2$ contributes to all superlattice reflections. Explicit assignment of *c*-domains within a plate is possible with careful cycling of superlattice reflection *g*-imaging conditions.

Figure 4.18b,c are included for direct visualization of the individual $L1_0$ variants that constitute a conjugate pair. Figure 18b shows the dark-field image with $g=\underline{1}01$ condition, which generates intensity from the (110) plane of the $L1_{0,Z}$ variant. The conjugate c-domain lights up with the $g=0\underline{1}1$ imaging condition shown in Fig 4.18c, with intensity from the (110) plane of the $L1_{0,X}$ variant. In both *g*-vector imaging conditions the surrounding $L1_2$ matrix appears light, given that the bulk ordered matrix should contribute equally to all of these superlattice reflections. Imaging with $g=1\underline{1}0$ in Fig. 4.18e makes the $L1_0$ plate appear dark compared to panels a and b; however, magnifying this plate provides direct visualization of the nanometer lengthscale $L1_2$ wetting layers that decorate the orientation domain boundaries between the two $L1_0$ variants (see Fig. 4.18f for a higher magnification image). The wetting layers appear to terminate within the matrix without abrupt microstructural features, suggesting coherency between wetting layer + matrix. However, without proper lattice imaging this is not directly observed. While the majority of plates embedded within the matrix appear to be singular 'units', bounded by discrete boundaries, several times a ‘forked’ or ‘branched’ region will grow from an original plate (see Fig. 4.16d or Fig. 4.18g). These regions are seen throughout all samples, and are most likely linked to the growth/transformation mechanism. Interestingly, within the forked region, the habit planes for the *c*-domains may change, although direct observation of conjugate pairing flipping has not been explicitly confirmed. As seen in Fig. 4.16d, the periodic contrast periodicity changed directions within the branched region, suggesting an alteration of habit plane for the conjugate pair of $L1_0$ variants (the trace of the plane appears to deviate by roughly ~100° between bulk plate and forked plate). It does not appear that the reorientation of habit planes is necessary or the direct reasoning for this branching, as Fig. 4.18g shows a forked plate but no direct reorientation of habit planes (DF imaging shows *c*-domains edge-on in this micrograph).

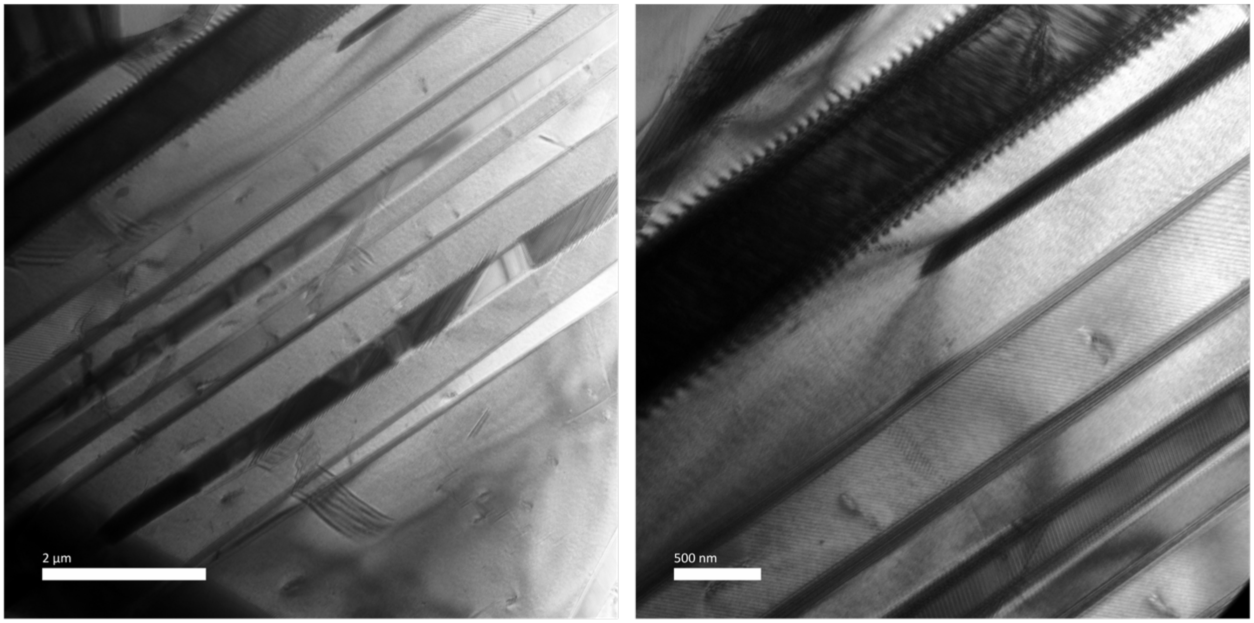

Figure 4.19. These two BF-TEM images show another section of plate + matrix microstructure, where in b) a clear plate tip is shown.

Another region of interest is shown in Fig. 4.19b, where a plate tip is readily imaged within the matrix. At this point, a direct transformation mechanism is only hypothesized, and will be explored more earnestly in subsequent chapters (Chapter 5). However, this micrograph is important as it gives general insight into the plate formation.

4.4. L1’ + $L1_2$ Coexistence

4.4.1. Structural Evidence

At Pd-rich compositions, aging specimens at 525℃ saw marked differences appear from the specimens aged at 650℃. First, the tetragonal $L1_0$ phase was replaced by the tetragonal but

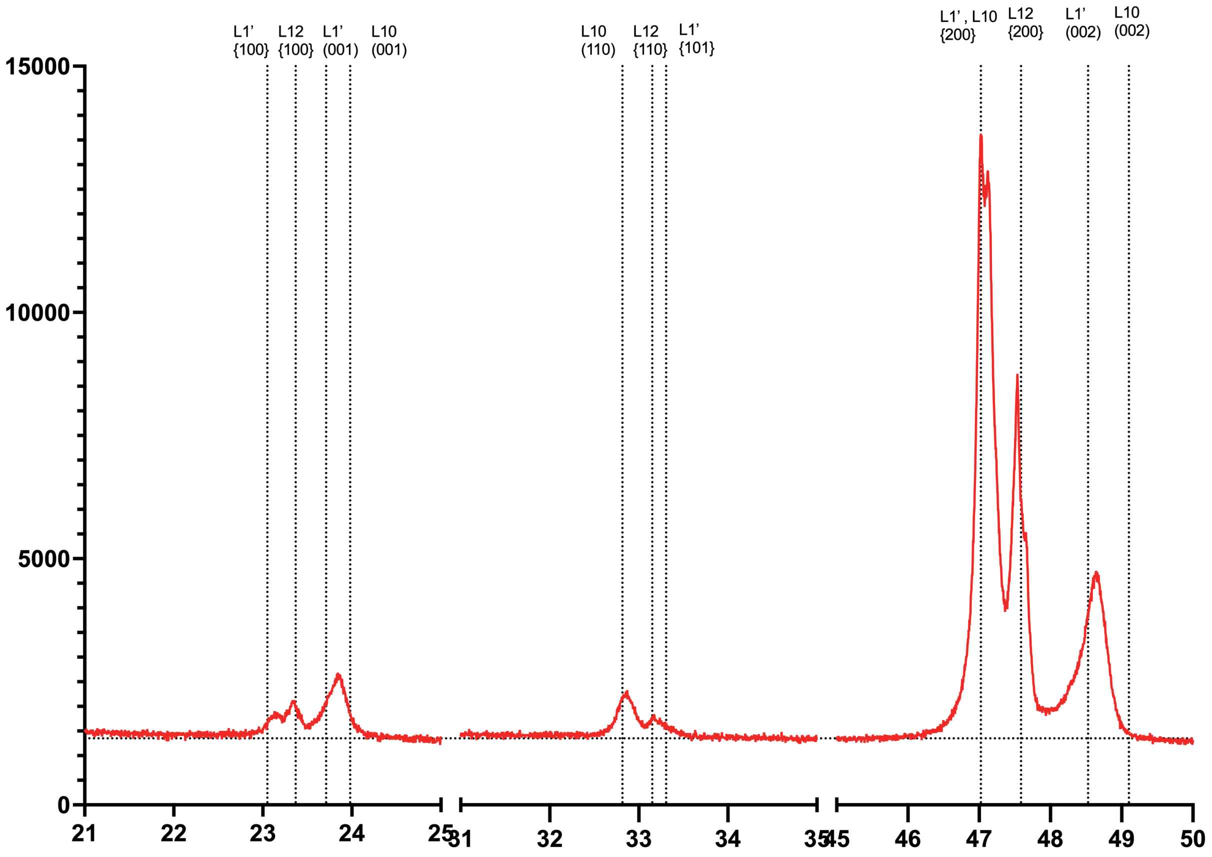

Figure 4.20. X-Ray diffractogram showing L1’ + $L1_2$ coexistence. L1’ phase ID is justified from the superlattice reflection splitting {100}/(001) , (110)/{101} and the structural changes made (increase in *c/a* ratio indicating a more cubic structure). $L1_2$ phase ID is afforded by both superlattice & fundamental reflections.

differently ordered L1’ phase, as documented in Chapter 3 of this dissertation. In addition, the weight fraction of $L1_2$ saw a marked decrease vis-à-vis the $L1_0$ + $L1_{2(\mathrm{majority})}$ samples, discussed in Section 4.2. These changes are shown explicitly in the structural evidence shown by X-ray scattering in Figure 4.20.

Chemical changes in ordering whereby excess (off-stoichiometric) Pd is placed solely on the (½, ½, 0) site to form the L1’ crystal structure, relax superlattice reflection conditions such that *H+K=2n* (necessary for $L1_0$) is no longer required. As such, the {100} and {101} reflections are observed for the L1’ phase as seen in Fig. 11 near 21-25° (2θ) & 31-35° (2θ) regions respectively. As mentioned and explored in Chapter 3, structural changes are evinced in L1’, such that the *c/a* ratio is raised, yielding a less tetragonal structure relative to $L1_0$ (approaching the *c/a* value of unity as seen for $L1_2$). The degree of order for this sample can be taken as the ratio of superlattice:fundamental reflections, namely $^{I_{001}}/_{I_{002}}$, which is a satisfactory measure of order as it probes identical grains (diffraction from (002) and (001) must rigorously occur within the same set of grains). In addition, phase identification for L1’ can be probed by comparison of L1’-only reflections (namely {100}/(001) and {101}/(110)), such that if they are greater than structure-factor produced ratios, an alternative explanation would need to be explored. Lattice constants, measured reflection ratios, and weight fractions are shown in Table 3 below.

Phase	$\frac{meas.}{max.}(^{I_{001}}/_{I_{002}})$	$\frac{meas.}{max.}(^{I_{100}}/_{I_{001}})$	***a***	***c***	***c/a***
L1’	0.87	0.97	3.867	3.753	0.970
$L1_2$	0.72	-	3.833	-	1

Table 4.5. This shows proxy long-range order values for L1’,$L1_2$, and the respective lattice constants.

4.4.2. Microstructure of L1' + $L1_2$

The overall microstructure is displayed in the BF-TEM micrographs in Figure 4.20. With L1' being a dominant (phase fraction) phase, the samples exhibited bundles of L1' polytwinned plates, where $L1_2$ was present as thin wetting layers along orientation domain and anti-phase boundaries (as seen in for Pd-lean samples discussed in Sec. 4.1 of this dissertation). In Fig. 4.21a shows one of these polytwinned bundles, with multiple L1' plates. Another BF-TEM image is shown in Fig. 4.21b, however one can resolve multiple-colonies within a single plate (see red arrow), which suggests similar transformation pathways to $L1_0$ polytwin bundles. In addition to these polytwinned regions, there exist multiple 'block' or 'matrix' regions, where no direct visualization of *c*-domains or

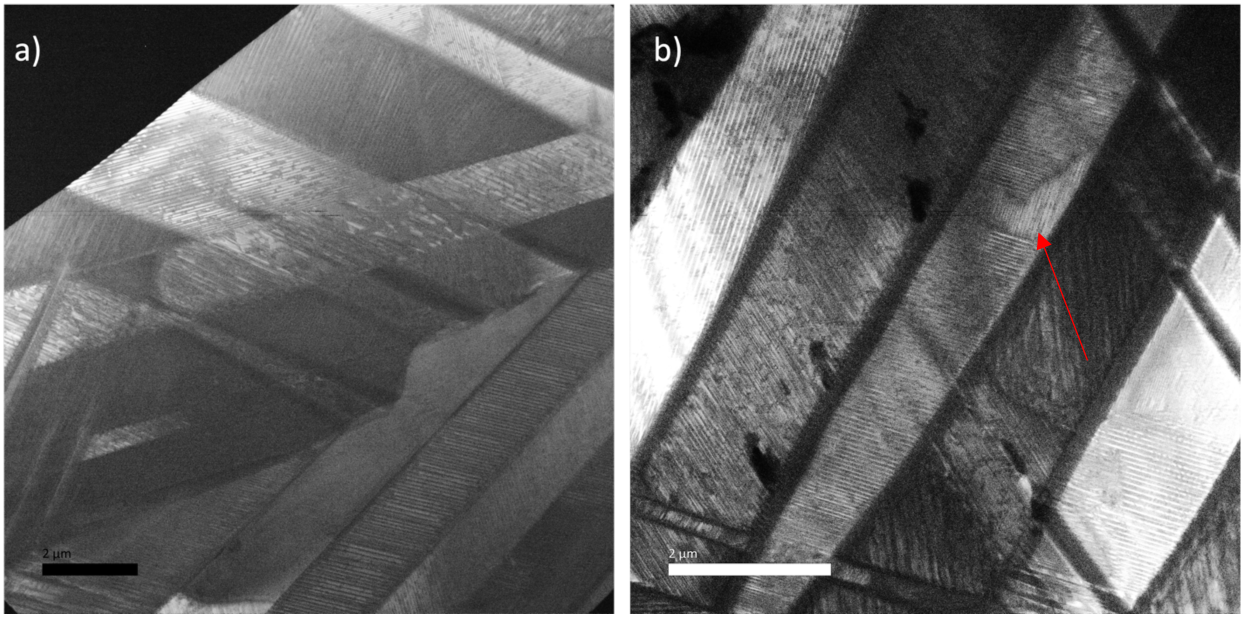

Figure 4.21. BF-TEM images of the polytwinned + wetting microstructure found for bulk L1' + $L1_2$ coexistence.

twinning. These regions mirror similar morphologies observed in single-phase L1’, discussed in Chapter 3. They will also be briefly explored later in this chapter.

While phase identification can be made accurately with X-ray diffraction, electron microscopy allows for quantitative agreement and characterization of the oftentimes hierarchical nature of these microstructures. Figure 4.22a,b shows a series of DF-TEM images that cycle through superlattice imaging conditions , which allow for identification of L1’ and $L1_2$ as well. For example, the *g=010,100* allow for direct observation of the $L1'_Y$ & $L1'_X$ variants respectively. The DF-imaging condition *g=110* allows for L1’ phase ID confirmation, as this superlattice reflection

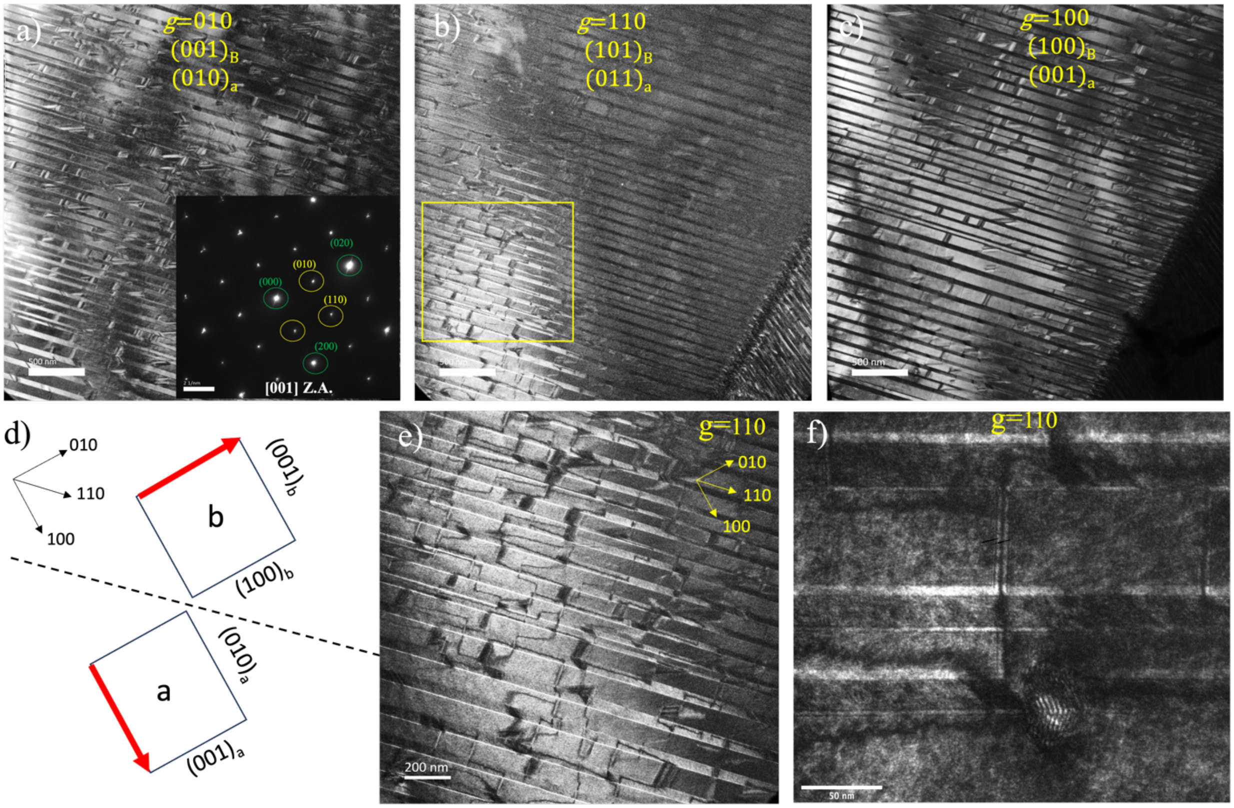

Figure 4.22. This series of DF-TEM images show the conjugate pair of L1’ orientation variants which constitute the polytwin microstructure. In addition, DF imaging with *g=110* allows for direct visualization of both variants and the $L1_2$ wetting layer, which ‘sits’ along the ODB and APBs of the microstructure. In f), an open APB channel structure, as found in Sec. 4.1 of this manuscript.

would not be allowed for phase-pure $L1_0$. In these samples, since both variants contribute to the intensity, phase ID can be confirmed[76].

While Phase ID is important, morphology characterization is afforded through these images as well. As there are an increased number of translation vectors allowed for L1' vis-à-vis $L1_0$, there is an increase in the observed faceted (and curvilinear or non-planar) APBs present in these micrographs. For example, Fig. 4.22e shows a DF-TEM image with g=110 imaging condition, where both L1' variants and the $L1_2$ wetting layer are visible. The wetting layers show 'channel' formation for {110}-oriented APBs, and in addition, non-faceted APBs which appear as the black fringes within the variants of this image. Interestingly, there appears to be a propensity for these curvilinear APBs to align and pass through the faceted APB channels. Most likely, the APBs were actually 'pushed' into these positions by the aligning APB channels which have faceted. Figure 4.24 articulates this formation. Figure 23 shows a DF-TEM micrograph where again, the polytwinned + wetted morphology is present, and an analysis of an associated SADP is given in Fig. 4.23c. Phase ID of L1' is also possible in this SADP image, as multiple reflections corresponding to (110), (210), (120) are visible, which would not be possible for polytwinned $L1_0$. In addition, a rel-rod is partially visible for the $L1_2$ phase, though it is relatively weak for all reflections except the strong fundamental reflections (e.g. {220}). A similar orientation domain boundary analysis is carried out for these two-phase samples as in Sec 4.1. However, the sample is tilted such that it is *close* but not directly on a [001] zone axis. As such, measurement of angles

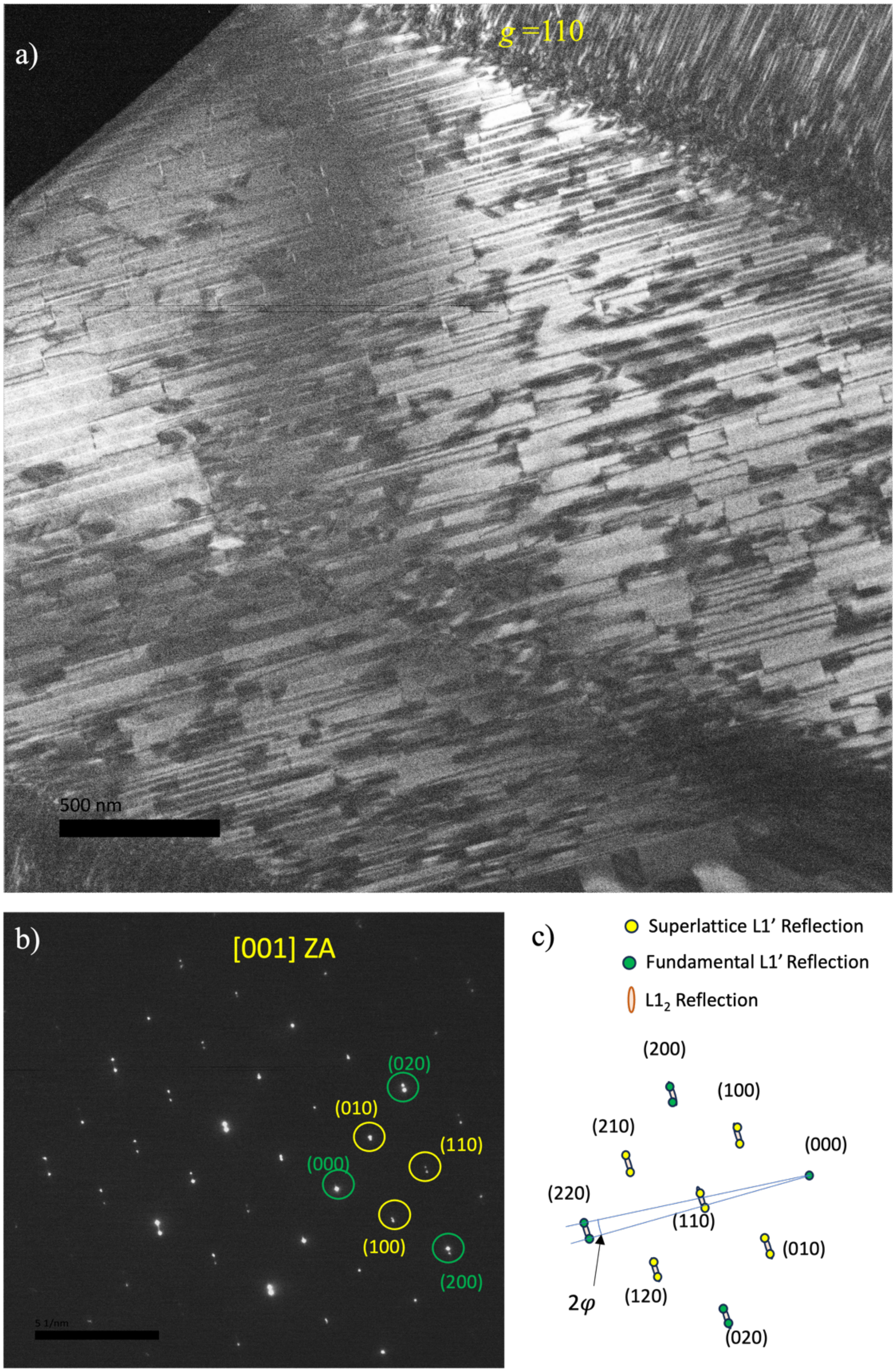

Figure 4.23. A DF-TEM image and accompanying SADP down a [001] zone axis are shown in a) and b) respectively, where important reflections are labelled. A schematic SADP is attached in c), where doubling of superlattice reflections is visible (as it should be for single-phase L1’) as well. It is hypothesized

between {220} reflections is highly variable, and values ranging between 88 - 95° have been measured. However, computing angles from lattice constants, we find $tan^{-1}\left(\frac{c}{a}\right) = tan^{-1}(0.970) = 44.12°$, such that the angle formed between the *c*-axes at the ODB for L1' + $L1_2$ is $2\phi = 88.2°$. Though ostensibly similar, it is slightly larger and this follows logically, since for exactly cubic crystals we would expect 90°.

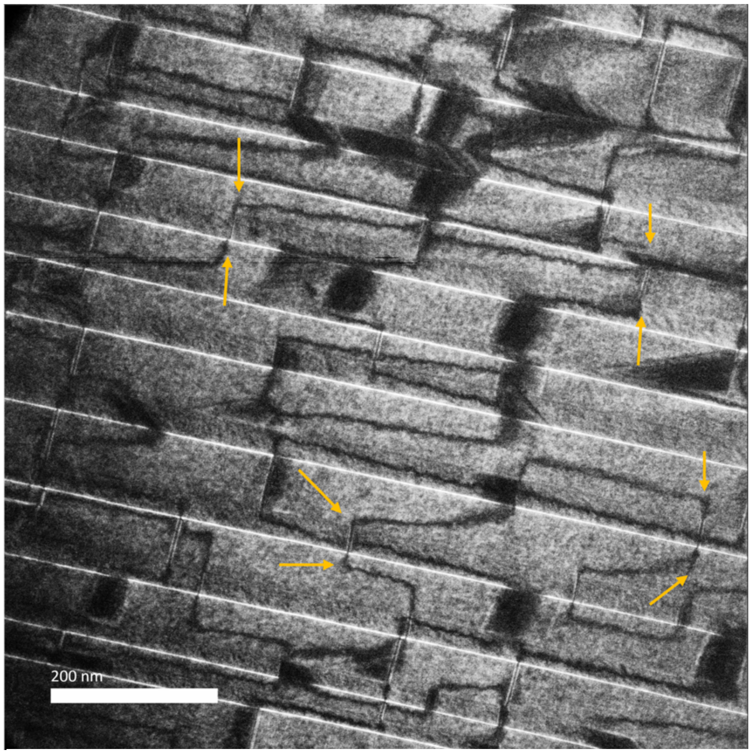

Figure 4.24. APB Faceting in L1' + $L1_2$ samples which shows non-wetted APBs that have been 'pushed' through the channels.

Figure 24 shows regions where the transformation APBs which have not faceted and wetted by $L1_2$ appear to pass through the wetted APBs from one orientation variant, into the adjacent variant. This morphology appears most likely, because during the formation of the faceted APBs, the pre-existing APBs were impinged upon on opposite end, until they were 'trapped' by the faceted + wetted structure. This observation is interesting, as channel APBs fundamentally undergo a transformation process whereby a second phase is either nucleated or re-arranged until all interfaces are decorated by this phase. APBs many times are envisioned, or modelled, as a disordered parent cubic material, which are typically one lattice constant thick. This implies that in many of these channel APB structures in L1' + $L1_2$ the inner channel region is actually an interface between out-of-phase but similarly oriented variants of L1'. The energetics of this structure would be non-trivial, as coherency is suggested across all phase interfaces. Additionally, as coarsening would progress, APB density would trend negatively as equilibrium values are reached, however the APB channel + transformation APB morphology involves multiple interfaces and thus surface energy considerations are critical. The high density of faceted APBs has another significant consequence: orientation variants begin to segment into much smaller 'blocks'. The once large orientation variants now appear as 'blocks', with $L \approx 200 - 400nm$. This higher density of APBs has significant consequences for domain wall propagation within these polytwinned materials.

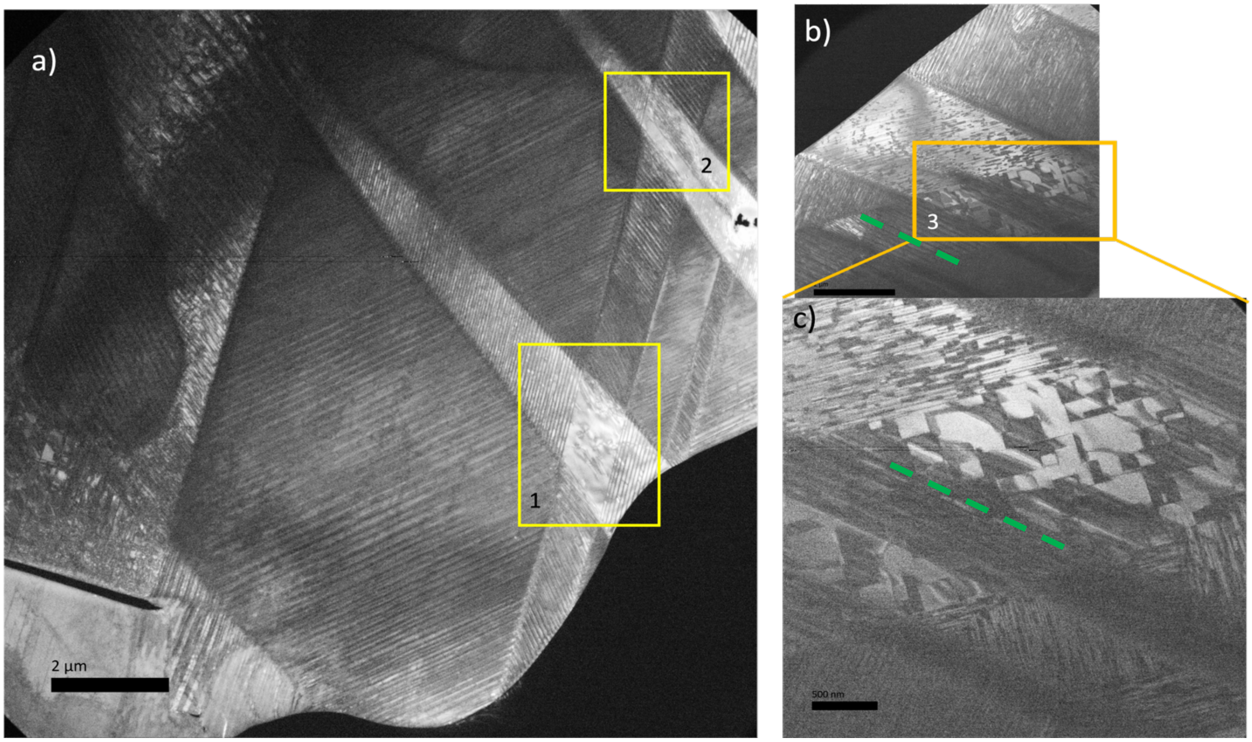

Figure 4.25. In a) a region is shown where polytwinned plates appear to cross each other, in squared regions 1 & 2, where twinning appears to disappear. In b) & c) a similar region is shown where polygonization of APBs or platelets appears. These matrix regions may in fact exhibit a vestige of twinning from bounding regions, as visible in the trace shown by the green line in b) & c).

The overall microstructure present in these samples appears with a polytwinned morphology, there were non-negligible regions of ‘matrix’ or block-like structures which on first glance appear to be single-phase (either $L1_2$ or L1’). However, analysis in single-phase L1’ regions suggest that in fact these matrix regions are in fact polytwin colonies with habit planes on one of the 12 {110} habit planes not visible edge-on in the imaging plane. As such, a faint twinning ‘trace’ is visible, as the habit plane is still visible in these matrix regions. Much like in single-phase L1’, there again appear platelets that form and grow within this matrix region. It is suggested that these platelets are actually growths of individual orientation variants from a separate colony into adjacent colonies

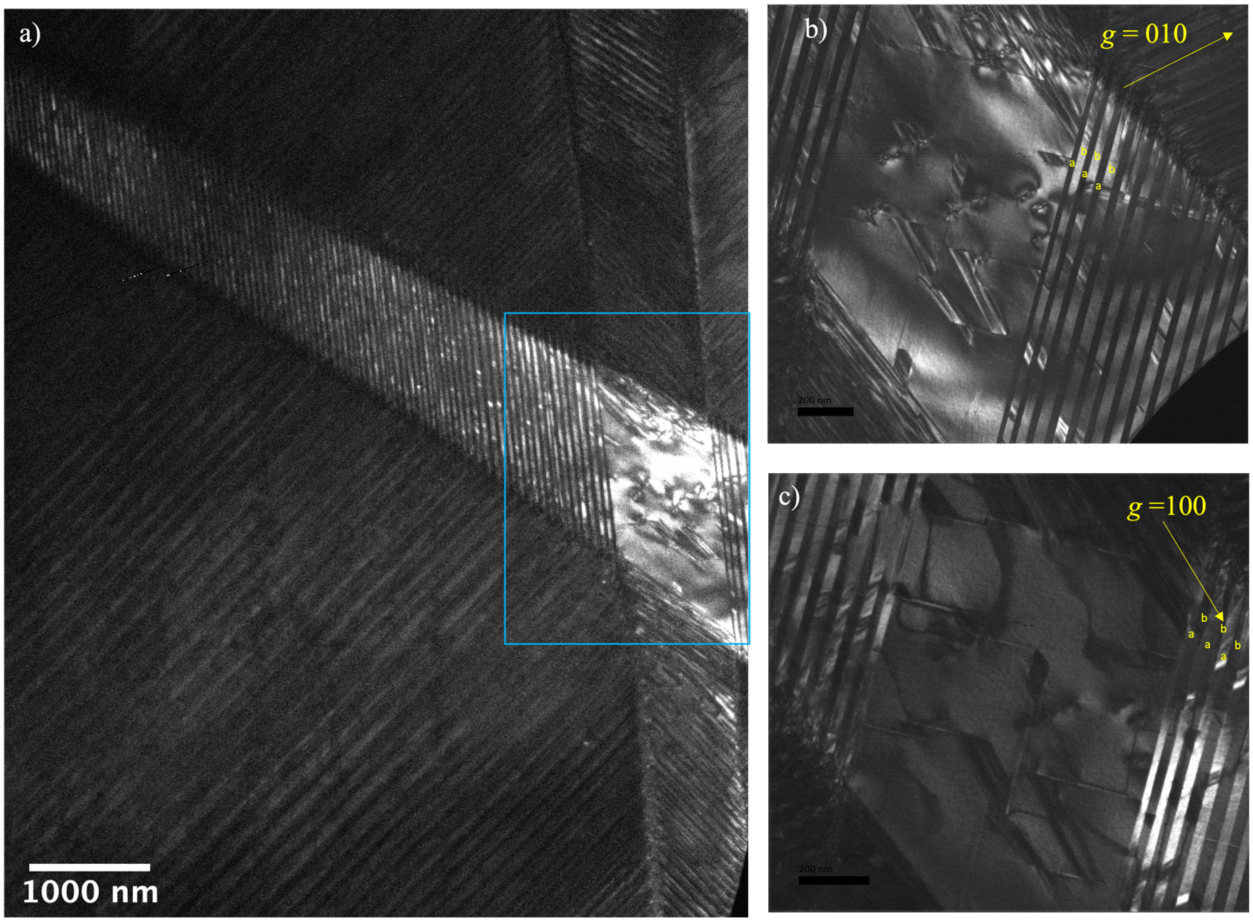

Figure 4.26. This series of DF-TEM images shows a matrix region, where in c) platelets can be seen (inside the matrix). The trace of twins is visible in b) & c), although a direct transformation mechanism is still not fully understood for these regions. This region may be single-phase L1’, as evinced by the similar contrast generated from *g=100* for the central region and $L1'_B$ orientation variant (see Fig. c)).

(as observed in Chapter 3 , single phase L1’). These regions are described + characterized broadly below. Figure 4.24 shows regions where matrix or block morphologies in the L1’ + $L1_2$ samples appear. From Fig. 4.25a (region 1,2) it is readily apparent that these blocks appear where polytwinned plates cross one another. The transformation mechanism for these regions will be explore more in depth in a subsequent chapter (Chapter 5). It is hypothesized that the matrix regions are not in fact single-phase $L1_2$, but a colony of twinned orientation variants aligned along {110} at an angle with respect to the imaging plane. Figure 4.25b,c shows one such region, where ‘squaring’ of platelets or APBs appears, and is bounded by edge-on polytwinned regions. However, closer inspection reveals a trace of a habit plane, which is shown and exaggerated by the green dashed line in the figure. The habit plane of this green figure is in alignment with a polytwinned plate bounding this matrix region, as shown clearer in Fig. 4.25b.

Figure 4.26 shows a a small collection of DF-TEM images which allow for visualization of one of the matrix regions under DF imaging conditions. The macroscopic region is shown in Fig. 4.26a, where the blue rectangle is used to highlight the magnified regions of Fig. 4.26b,c which are imaged with *g=010,100* imaging conditions respectively. While conjugate pairs of L1’ orientation variants are seen to contribute to the intensity for both conditions, clear variant assignment is allowed due to intense bright variants which appear when imaging under *g=010,100* conditions. However, what is gleaned from this series of DF images is that the series of platelets directly observable in Fig. 4.26c, which appear to partially span the central block. The platelets are denoted by green arrows. From this micrograph it is readily observable that platelets habit both (110) and $(\underline{1}10)$, as seen by the horizontal and vertical regions found within the matrix region. There are a number of hypotheses put forward that may explain this morphology. One of them was mentioned previously, above. However, due to the intensity generated with *g=100* imaging condition, it is suggested that the platelets may be single-phase $L1_2$ which has wetted and aligned along APBs that have formed along the and within this cross-polytwinned-plate region. Clearly, the investigation of this particular microstructure is non-trivial, and simple BF/DF-TEM micrographs do not allow for unassailable phase assignment or characterization of the different phases within this matrix/platelet morphology. However, this does not suggest that this is intractable question. Most likely, careful HR-TEM may allow for direct observation of the platelets within this matrix region. In addition, careful FIB-ing of samples from the matrix region, to inform morphology in 3-dimensions may give fundamental insight into the matrix microstructure.

Chapter 5. Order to Order Transformation ($L1_2 \rightarrow L1_0$ and $L1_2$)

This chapter will focus on the transformation sequence observed for all samples aged at 650°C within the $L1_0 + L1_2$ two-phase field. Surprisingly, solid solution FCC always ordered to single-phase $L1_2$ prior to the growth of any tetragonal $L1_0$ material. Several potential mechanisms for preferred $L1_2$ ordering are given and discussed, including the calculation of instability temperatures for both ordered phases. The structural transformation (measured with X-ray diffraction) will be shown and analyzed first. Following this, transmission electron microscopy images will be presented and analyzed at various stages along the transformation (displaying incipient, middle, and end-state microstructures). Key observations made from each stage of the transformation are summarized and listed, which serve as the blueprint for the transformation mechanism hypothesized.

5.1. Structural Evidence of $L1_2$ transforming to $L1_2 + L1_0$

All samples that were initially cooled through the eutectoid isotherm displayed ordering to $L1_2$ before any formation of $L1_0$. This behavior was seen in continuously cooled + aged samples, in addition to A1-quenched + isothermally aged samples, suggesting non-equilibrium processing conditions are not the sole culprit. Continuous cooling rates were varied (cooling from 850°C to 650°C) between 400°C to 50°C per hour as shown in Figure 5.1: all samples yielded single-phase $L1_2$ at different states of long-range order. The long-range order values were characterized by typical Bragg-Williams[77] long-range order parameters, which we are giving as $\frac{measured}{maximum}\left({I_{001}}/{I_{002}}\right)$.

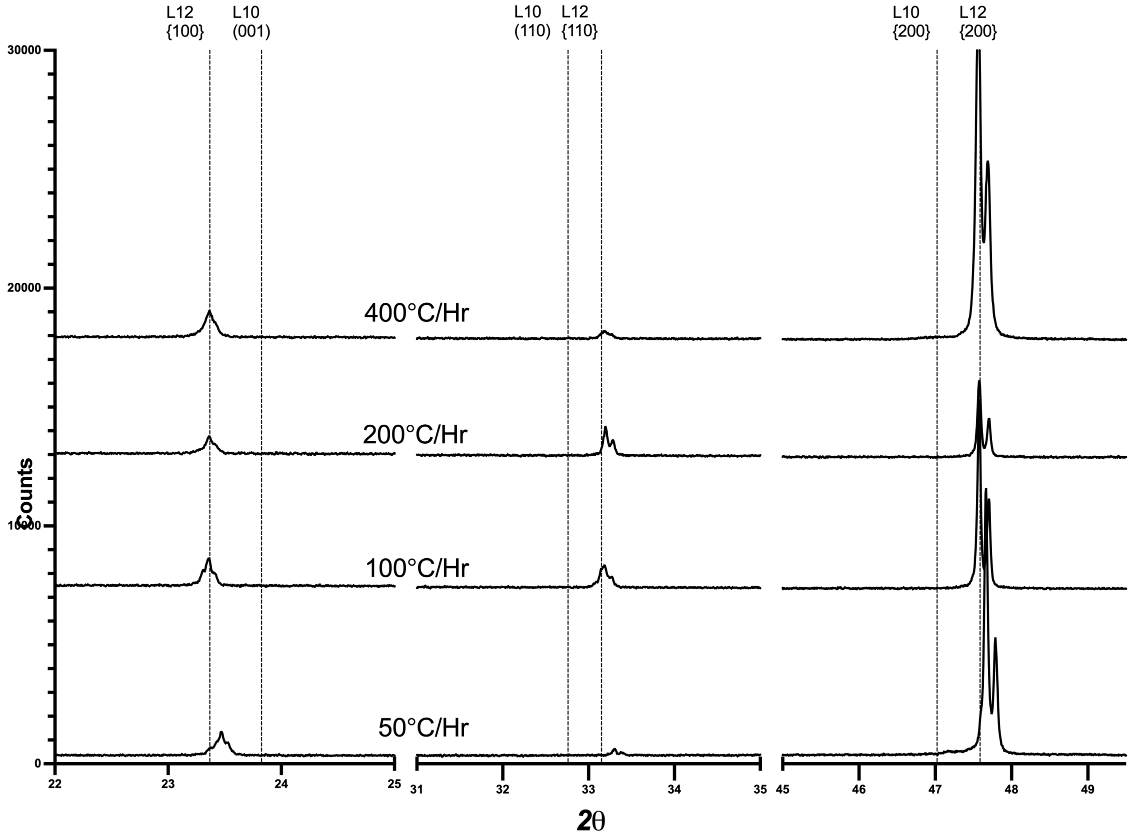

Figure 5.1. XRD Spectra of samples continuously cooled through the eutectoid isotherm at various rates (400℃ - 50℃). All samples exhibited single-phase L1_2, as seen by the superlattice {100},{110}, and fundamental {200} reflections.

Sample (Cooling Rate)	Long-Range Order
400C/Hr	0.347
200C/Hr	1.66
100C/Hr	0.90
50C/Hr	0.67

Table 5.1. Long-range order parameter values for continuously cooled Fe-Pd through the eutectoid isotherm.

These long range order parameter values are given below, where the maximum superlattice:fundamental ratios are determined from structure factor calculations, done for on-composition crystal structures. As seen in table 5.1, all samples exhibited a non-negligible degree of order, which was quite surprising.

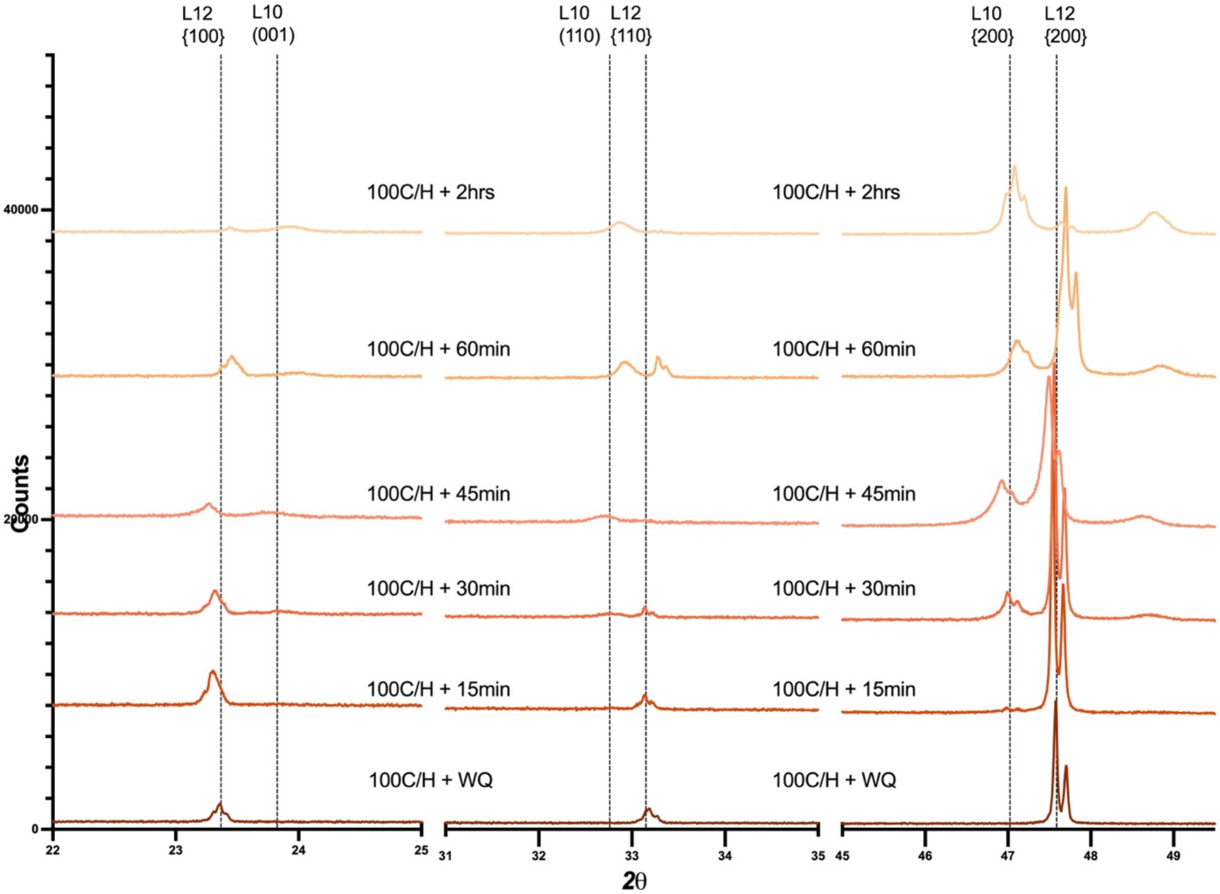

Figure 5.2. X-Ray Diffraction spectra of the continuously cooled ($100℃/H$) and isothermally aged samples. $L1_0$ can be seen to grow from the single phase $L1_2$ parent phase. Two phase coexistence of $L1_0 + L1_2$ is the equilibrium state for this composition.

These results spurred further inquiry into the transformation mechanism. As envisioned by phase-field models done by Khachturyan[36], eutectoid decomposition of *cubic* → *cubic* + *tetragonal* typically begins with either a displacive transformation or a diffusional ordering and to the tetragonal phase within the cubic parent (with an attendant tetragonal distortion).

The tetragonal $L1_0$ phase did appear after additional isothermal aging at $650℃$ following the continuous cooling process, as seen in Figure 5.2. After 15 minutes aging, the $L1_0$ {200} reflection is just visible, as a minor hump in the diffraction pattern: no additionalsuperlattice reflections appear at this aging time. However, after 30 minutes aging, tetragonality is observed for $L1_0$ with {200}/(002) peak splitting. Superlattice reflections (001) and (110) become readily visible for $L1_0$

around 45 minutes, but are more pronounced for 1 hour. As can be seen in Fig. 5.2, the transformation produced structural re-organizations resulting in strains in lattice constants for both $L1_0$ and $L1_2$.

It can be shown that non-equilibrium cooling conditions were not strictly responsible for this ordering behavior, as in Fig. 5.3 isothermally aged samples (post A1-quench) also ordered to $L1_2$ prior to $L1_0$ formation. The sample shown in Fig. 5.3 is Pd-rich with respect to samples studied in Fig. 5.2 (though still within the two-phase coexistence region), exhibiting higher equilibrium phase fraction of $L1_2$ vis-à-vis the equilibrium phase fraction of $L1_2$ found in Fig. 5.2. In Figure 5.3, the bottom line shows the A1+5Hr annealed samples, which exhibit single-phase $L1_2$ as can be seen by the fundamental {200} reflection, and superlattice {100},{110} peaks as well. After 10 hrs aging (second line of Fig. 5.3), a minority $L1_0$ amount is observed, as a small (002) shoulder emerging from {200}, although no superlattice reflections can be seen. For the third spectra in Figure 5.3, 3 weeks aging at 650℃ showed two-phase coexistence of $L1_0$ + $L1_2$, with majority phase fractions of $L1_2$. Interestingly, the transformation rates were much slower for Pd-rich samples, which may be attributed to a weaker driving force for $L1_0$ ordering at the far end of the two-phase coexistence region.

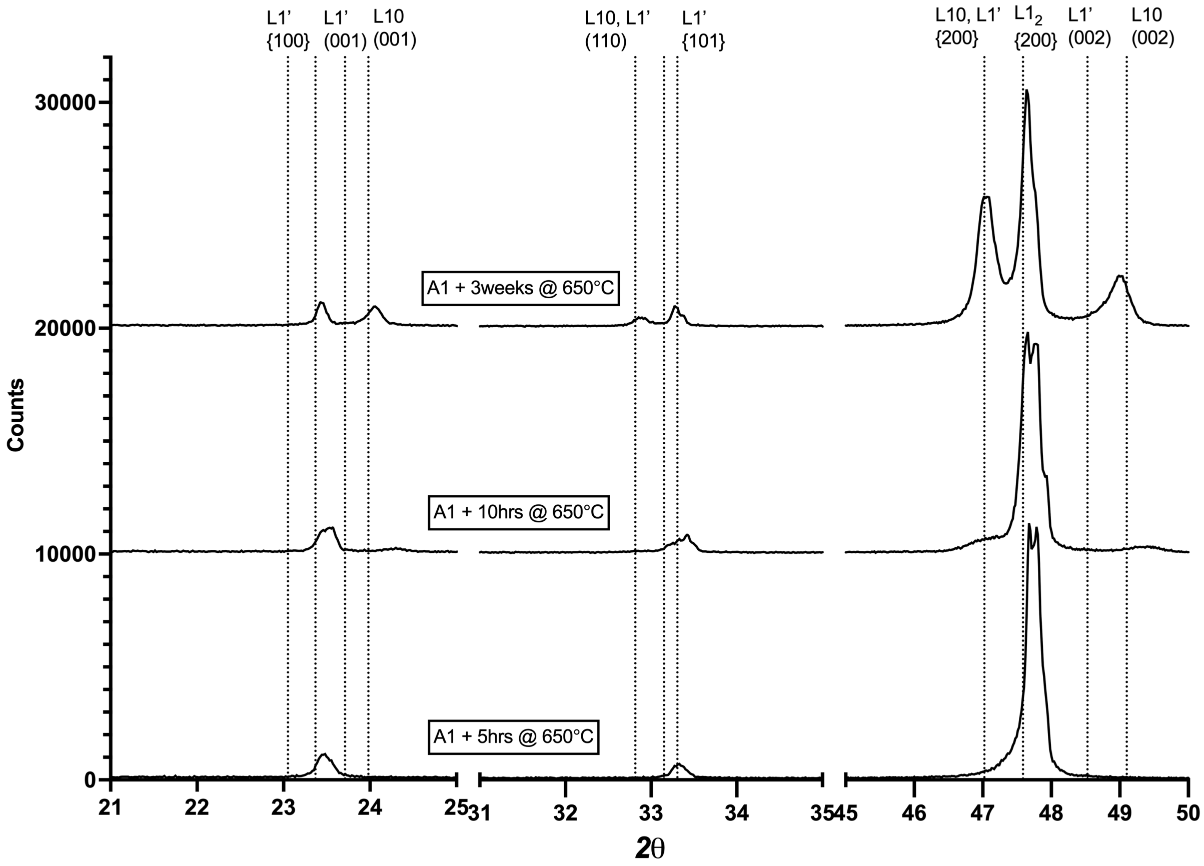

Figure 5.3.XRD spectra of the A1 quench + isothermally annealed samples at 650°C, showing that even isothermally aged samples exhibited preferential ordering to $L1_2$. This finding suggests non-equilibrium processing conditions may not be the sole reasoning for the ordering sequence from solid solution.

5.2. Calculation of Instability Temperatures for First-Principles Calculations

Numerous mechanisms can be suggested to explain the preference for $L1_2$ ordering to precede $L1_0$ formation. A recent publication exploring ordering from liquid employing molecular dynamic simulations found that ordered $L1_2$ precursor nuclei formed in liquid and facilitated the formation of the critical nucleus of the crystalline solid solution[89]. The authors of this work found that the formation energies for $L1_2$ clusters were much lower than $L1_0$ clusters or the medium-range order icosahedra in the supercooled liquid[89]. In a qualitative fashion, it is hypothesized that short-range order $L1_2$ clusters may have also been preferred over other short-range order formations in *solid solution*, which served as nuclei for $L1_2$ ordering below the critical temperature T_C. Interestingly, this preference for $L1_2$ ordering to precede $L1_0$ formation was also observed in on-eutectoid composition Co-Pt alloys that yielded the nanochessboard microstructure[63].

Although the transformations $A1 \rightarrow L1_0$ & $A1 \rightarrow L1_2$ are both rigorously defined as first order transformations (in the Ehrenfest sense), there exist conditions far from equilibrium (where $T=T_i^-<T_C$) where the kinetic behavior of the system will mimic that of a second/higher order transition[90]. That is, the ordering from disordered solution into the ordered phase can occur continuously/homogeneously throughout the system rather than a discrete partitioning into ordered/disordered regions (as would occur for a 1st order transformation)[90]. It is suggested that the preference for $L1_2$ ordering may have occurred because the system was undercooled far from equilibrium (below its instability temperature T_i^-), allowing continuous ordering to occur. Utilizing Landau theory, the instability temperature T_i^- curves can be calculated using first principle (density functional theory generated) values for enthalpies of formation. The static concentration wave model & Bragg-Williams[77] model as shown by Khachaturyan[91] were employed below.

The Helmholtz Free energy of mixing in solution of A & B atoms is given as equation 1,

$$F_m = E_m - TS_m \quad (1),$$

where E_m is the energy of mixing that has 1st and 2nd nearest-neighbor components. This E_m energy of mixing term is expressed as the sum of $E_m = E_1 + E_2 = E_O + E_D$, where $E_O + E_D$ correspond to the Ordered and Disordered energy states. This expression can be rewritten by introducing a composition term C and a long-range order term η:

$$E_D^{L1_2} = NC(1-C)\{12V_{1st} + 6V_{2nd}) \qquad E_D^{L1_0} = NC(1-C)\{12V_{1st} + 6V_{2nd}) \quad (2)$$

$$E_O^{L1_2} = \frac{3}{16}N\eta^2\{4V_{1st} - 6V_{2nd}\} \qquad E_O^{L1_0} = \frac{1}{4}N\eta^2\{4V_{1st} - 6V_{2nd}\} \quad (3).$$

In the above expression, the 1st and 2nd nearest neighbor interchange energies in the FCC crystal are given as V_{1st} and V_{2nd}, respectively. The entropy of mixing term in equation (1) can also be written in terms of composition *C* and η using Sterling's approximations such that

$$S_m^{L1_0} = \frac{-K_bN}{4}\left\{\begin{array}{c} 2\left(C-\frac{1}{2}\eta\right)\ln\left(C-\frac{1}{2}\eta\right)+2\left(1-C+\frac{1}{2}\eta\right)\ln\left(1-C+\frac{1}{2}\eta\right)+ \\ 2\left(C+\frac{1}{2}\eta\right)\ln\left(C+\frac{1}{2}\eta\right)+2\left(1-C-\frac{1}{2}\eta\right)\ln\left(1-C-\frac{1}{2}\eta\right) \end{array}\right\} \quad (4)$$

$$S_m^{L1_2} = \frac{-K_bN}{4}\left\{\begin{array}{c} 3\left(C-\frac{1}{4}\eta\right)\ln\left(C-\frac{1}{4}\eta\right)+3\left(1-C+\frac{1}{4}\eta\right)\ln\left(1-C+\frac{1}{4}\eta\right)+ \\ \left(C+\frac{3}{4}\eta\right)\ln\left(C+\frac{3}{4}\eta\right)+\left(1-C-\frac{3}{4}\eta\right)\ln\left(1-C-\frac{3}{4}\eta\right) \end{array}\right\} \quad (5)$$

The real space site occupation *n(r)* described by Khachatryan[91] utilizes discrete Fourier transforms of the interchange energies formulated in reciprocal *k*-space as shown below.

$$n(r) = C + \sum_k Q(k)\exp\left(ik \cdot r\right) \quad (6)$$

In the previous expression, the average composition *C* is slightly modified by a superposition of concentration waves given by their wave vector *k* and magnitude *Q(k)*. These reciprocal space terms are localized to the first Brillouin zone. This then allows interchange energies to be written as

$$V(k_0) = \sum_r V(r)\exp(ik_0 \cdot r) \quad (7),$$

where first and second nearest-neighbors in the FCC crystal are rewritten below. Following this, the expression for ordered and disordered energy states given in Eq. 2,3 can be written with respect to these new 1st and 2nd nearest-neighbor terms.

$$V(0) = 12V_{1st} + 6V_{2nd} \qquad\qquad V(K_0) = -4V_{1st} + 6V_{2nd} \quad (8)$$

$$E_D^{L1_2} = NC(1-C)V(0) \quad (10) \qquad\qquad E_D^{L1_0} = NC(1-C)V(0) \quad (9)$$

$$E_O^{L1_2} = \frac{3}{16}N\eta^2 V(k_0) \quad (11) \qquad\qquad E_O^{L1_0} = \frac{1}{4}N\eta^2 V(k_0) \quad (10)$$

With enthalpy of mixing terms re-written in this fashion, it is possible to extract interchange energies from these equations, if heats of formation are known. Using values from the literature [92] generated from cluster variation method employing the tetrahedron approximation, the heats of formation for the ordered phases are given in units of Rydberg (Ry) below. The heat of formation for $L1_0$ is given as $E_0(L1_0) = -N(3.5 \cdot 10^{-3})Ry$, while for $L1_2$ this value is extrapolated as $E_0(L1_2) = -N(4 \cdot 10^{-3})Ry$. It should be mentioned that already one can notice a preference for $L1_2$ formation in the system, as there is a lower enthalpy of formation for this ordered phase formed within solid solution (although these values cannot be explicitly compared 1:1 since they are computed for stoichiometric compounds, *AB* & *AB₃* respectively). Furthermore, the disordered states are extrapolated as follows : $E_D(L1_0) = N(4 \cdot 10^{-3})Ry$, and $E_D(L1_2) = -N(1 \cdot 10^{-3})Ry$.

With the ordered and disordered states known, it is possible to substitute into equations (9) and (10) to then extract the interaction energies for first $V(0)$ and second $V(k_0)$ nearest-neighbors. Once these are known, the difference between Helmholtz free energy states of ordered $F_m(\eta)$ and disordered $F_m(0)$ can be calculated. The expression for the Helmholtz free energy is shown below:

$$(11)\qquad F_m(\eta)_{L10} - F_m(0)_{L10} =$$

$$-\frac{1}{4}N\eta^2V(k_0)_{L10} + \frac{k_BNT}{4}\{2(1-1\eta)\ln(\frac{1}{2}-\frac{1}{2}\eta)+2(1+1\eta)\ln\left(\frac{1}{2}+\frac{1}{2}\eta\right)-4\ln(\frac{1}{2})\}$$

$$(12)\qquad F_m(\eta)_{L12} - F_m(0)_{L12} =$$

$$-\frac{3}{16}N\eta^2V(k_0)_{L12} + \frac{k_BNT}{4}\{3(\frac{1}{4}-\frac{1}{4}\eta)\ln(\frac{1}{4}-\frac{1}{4}\eta)+3\left(\frac{3}{4}+\frac{1}{4}\eta\right)\ln\left(\frac{3}{4}+\frac{1}{4}\eta\right)-3\ln\left(\frac{3}{4}\right)+(\frac{1}{4}+$$

$$+\frac{1}{4}\eta)\ln\left(\frac{1}{4}+\frac{3}{4}\eta\right)+\left(\frac{3}{4}-\frac{3}{4}\eta\right)\ln\left(\frac{3}{4}+\frac{3}{4}\eta\right)-\ln(\frac{1}{4})\}$$

The Helmholtz free energies can be plotted as a function of order (η), and then varied by temperature (T). While these results allows us to probe the nature of the transformation order (whether there are thermodynamic restorative forces or not), the Landau free energy curves will not be explored in greater detail, here. They are a requisite step into determining whether $L1_2$ is ordering due to the degree of undercooling in the system, where kinetically-preferential conditions allow for continuous ordering to occur.

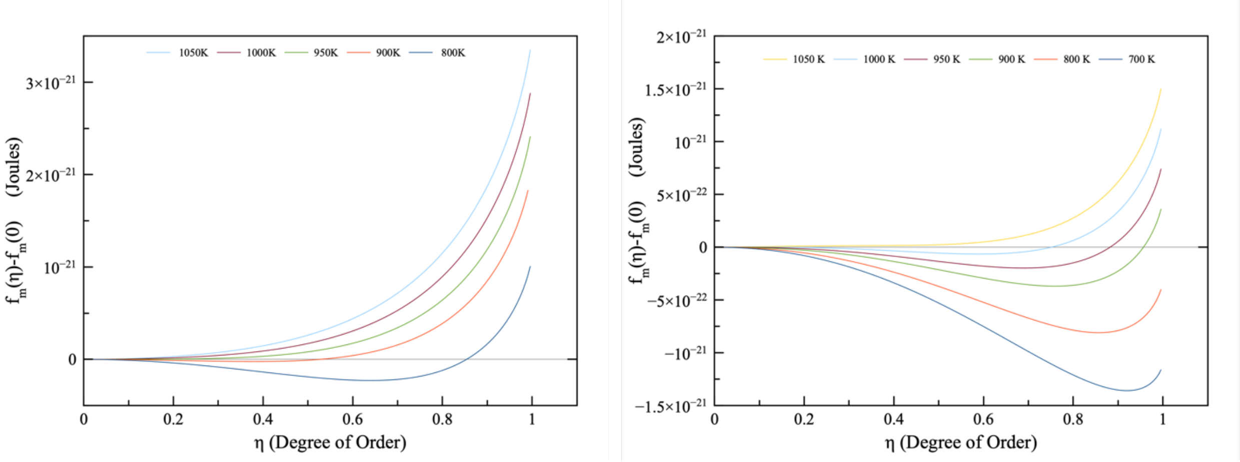

Figure 5.4. Landau free energy plots for a) $L1_0$ and b) $L1_2$. These energy plots are normalized per atom. The instability temperatures for equiatomic compositions are calculated to be 674℃ and 571℃ for $L1_0$ and $L1_2$ respectively.

The results for these calculations are shown in Figure 5.4a & b, for $L1_0$ and $L1_2$ respectively. In order to calculate the instability temperature, the second derivative of the free energy is taken, the degree of order η is set to 0, and the expression can be rewritten as follows:

$$T_i^-{}_{L10} = \frac{V(k_0^{L10})}{2k_B}, \qquad T_i^-{}_{L12} = 3\frac{V(k_0^{L12})}{8k_B} \quad (13)$$

For $L1_0$ the instability temperature is calculated to be 674°C, and for $L1_2$ the temperature is calculated to be 692°C. In similar fashion, it is possible to extrapolate the instability temperatures as a function of composition using the expression as follows:

$$k_B T_i^- = 2C(1-C)V(k_0) \quad (14)$$

In equation (14), the instability temperature T_i^- is calculated as a function of composition *C*. It should be stated that in this expression the interaction energy for the ordered state, generated from the enthalpy for formation extracted from the literature, is varied linearly as a function of composition. A linear interpolation is made between the $L1_0$ and $L1_2$ ground state energies as a function of composition. This gives a rudimentary or 1st-approach understanding of whether or not continuous ordering may have played a part in the interesting ordering observed in the system.

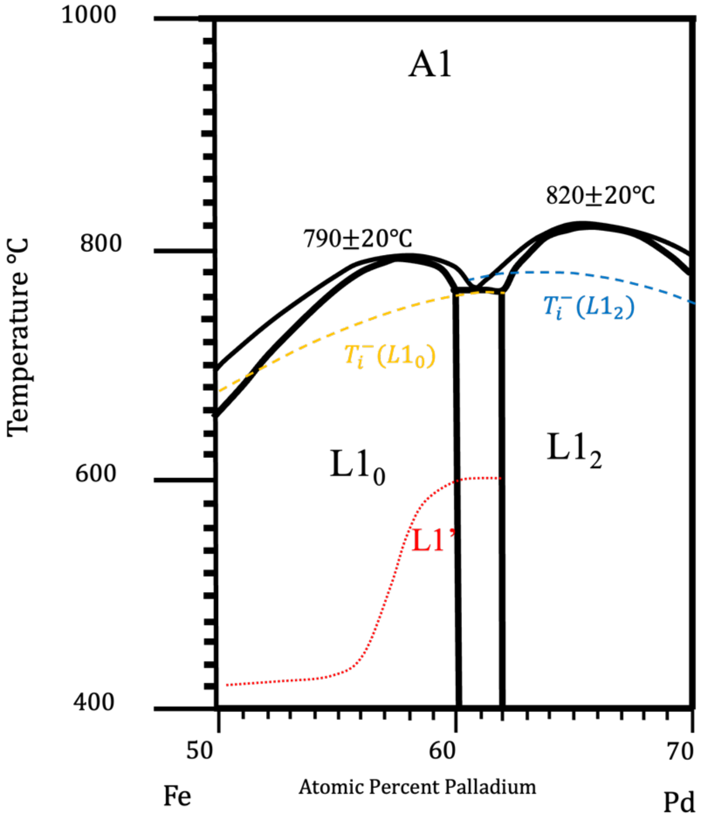

Figure 5.5. Calculated instability temperatures for both $L1_0$ (yellow) and $L1_2$ (blue) extrapolated into the two-phase coexistence region. The extrapolated lines are superimposed onto the commonly accepted Pd-rich eutectoid region. It can be seen that at the two-phase coexistence region, the instability temperature for $L1_2$ is higher than that for $L1_0$, suggesting continuous ordering to $L1_2$ may have occurred.

The results of the calculation for both $L1_0$ and $L1_2$ are shown in Figure 5.5, where the instability temperatures for $L1_0$ (orange) and $L1_2$ (blue line) are extrapolated as a function of composition into the nominal two-phase coexistence region. Interestingly, as the instability temperatures approach this region, the $L1_2$ values begin to surpass those of $L1_0$. While the overall shape of the instability temperatures appears to follow the accepted topology in the literature[10], the temperature values explicitly at the two-phase region may be exaggerated (they are inherently dependent on the ground state enthalpy of formation which was linearly interpolated as a function of composition). That being said, within the bounds of the two-phase coexistence region at exactly Fe – 60 at% Pd, $L1_2$ has an instability temperature of $\sim 780℃$, whereas $L1_0$ has an instability temperature of $\sim 760℃$. With a eutectoid isotherm temperature of $760℃ \pm 30℃$, these calculations may still be significant. These 1st approximation calculations suggest that at the temperatures ordered to in our experiments $L1_2$ may have ordered continuously, explaining the ordering behavior observed.

Interestingly, in Shockley & Nix's[93] seminal work on Order-Disorder transformations in alloys, they found $A1 \rightarrow L1_0$ to occur via a 2nd/higher order transformation. However, when elastic strain energy considerations were included in subsequent reports (Cheong & Laughlin[15]), the transformation order became 1st order. In contrast, the $A1 \rightarrow L1_2$ transformation has always been categorized as a 1st order nucleation + growth process. Rigorously, the order of transformation does not change based on the degree of undercooling. However, with sufficient undercooling thermodynamic barriers are removed and kinetic considerations become greater, allowing a continuous ordering to occur, as may have occurred in these Fe-Pd samples.

Another potential mechanism for the preference of $L1_2$ formation may involve congruent ordering, as hypothesized by Khachaturyan[11] (T_0 line), where decomposition into two ordered phases ($L1_0$ + $L1_2$) in this case_is preceded by single-phase $L1_2$ ordering from solid solution. This would necessitate metastable extension of the T_0 line into the two-phase coexistence region.

5.3. Microstructural Analysis

5.3.1. L1$_2$ + Tweed

A sample continuously cooled through the eutectoid isotherm, exhibiting single phase L1$_2$ was probed microstructurally in the electron microscope, as shown in Figure 5.6 below. Phase ID was suggested visually, by the widespread proliferation of transformation APBs expected in single-phase L1$_2$[7,58]. The selected area diffraction pattern corresponding to a different but similar region of single-phase L1$_2$ is provided in Fig. 6b, where (looking down a [001] zone axis), the superlattice

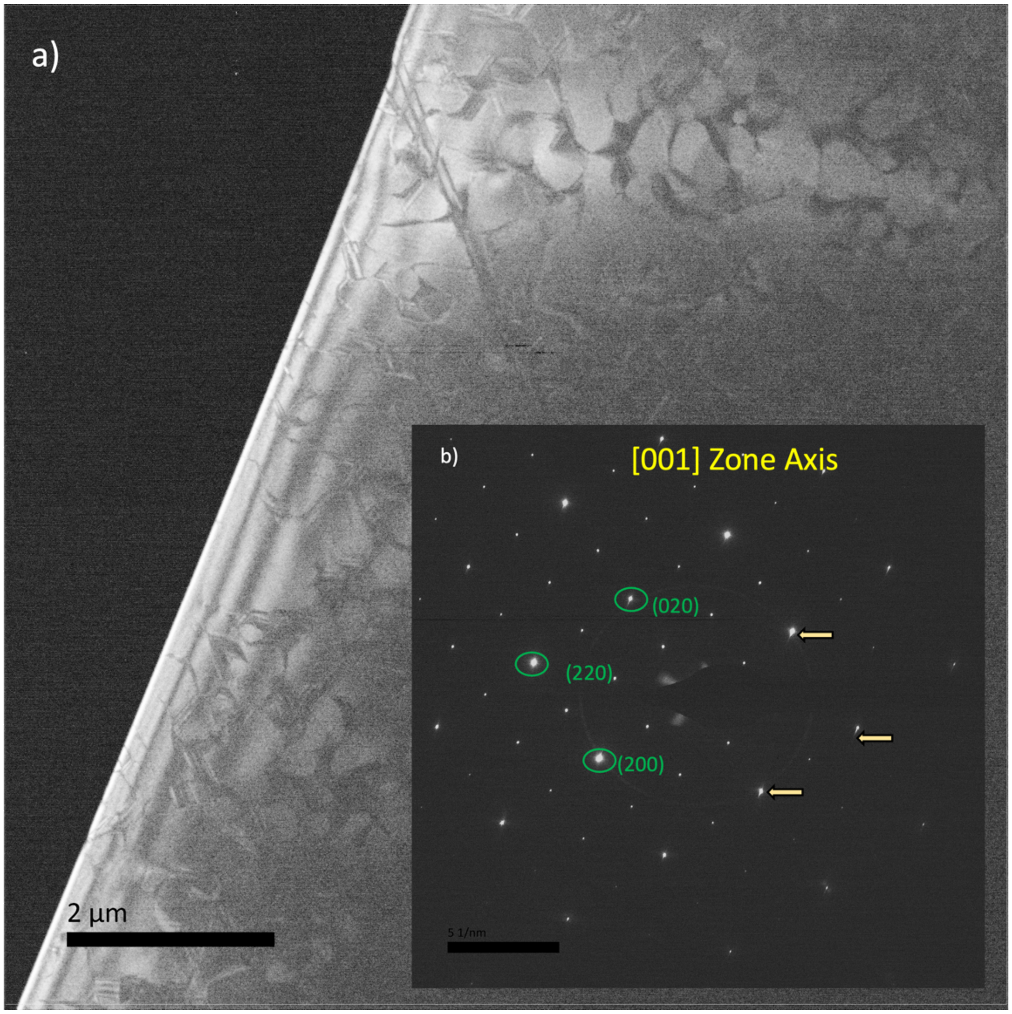

Figure 5.6. BF-TEM micrograph of macroscopic view of L1$_2$, which is identifiable by the SADP down [001] Z.A. in b) and the large proliferation of APBs.

reflections corresponding to the $L1_2$ phase can be identified ((100),(010), (110) etc). Interestingly, as observed for the strongly-diffracting fundamental reflections {200},{220} slight streaking along {110}* can be seen. The arrows included on the SADP are there to highlight the faint but observable streaks, which appear to run parallel to $[\underline{1}10]$. This streaking is normally ascribed to the presence of the tweed 'microstructure', which is in reality a pre-transition state, and will be characterized and explored in greater depth in the following sections.

Tweed is seen as a pre-transitional state known to develop in materials undergoing structural transformations where the loss in point group symmetry results in transformation twinning in the low temperature phase[94]. This is typically found in materials which undergo a martensitic transformation, such as shape memory alloys (NiAl[95], FePd[37], CuAu[ref]), or in high-temperature superconductors $YBa_2(Cu_{0.95}Al_{0.045})_3O_7$[96] . However, different origins may produce a similar tweed or 'basket-weave' microstructure. In spinodally-decomposing solid solutions compositional modulations will occur along elastically soft directions in a crystal, creating a texture with modulations of similar lengthscales to those found for the systems which will undergo transformation twinning, as explained above. Regardless of the transformation type, there are common features found in the observed 'microstructures', such that they are indistinguishable from one another (whether *compositional*[94] or *structural* tweed).

Tweed is typically identified in transmission electron microscopy as cross-hatched strain contrast nearly parallel to the traces of {110} in the parent phase. These striations generate a contrast which bears a close resemblance to the tweed textile[39] fabric. As stated earlier, accompanying modulations are observed in the electron diffraction pattern which is consistent with atom displacements along {110}<110>[38]. This patterning has no strict periodicity, however the striations present with two distinct lengthscales: the longitudinal extent is described by the letter L, while the short width the Greek letter ξ. Measurement of actual lengthscales using electron microscopy can be frustrated by image processing artifacts, but are approximated to be on the order of tens to hundreds of lattice constants[39]. Since tweed has been observed for different transformation mechanisms, observation of tweed does not directly exclude any transformation type.

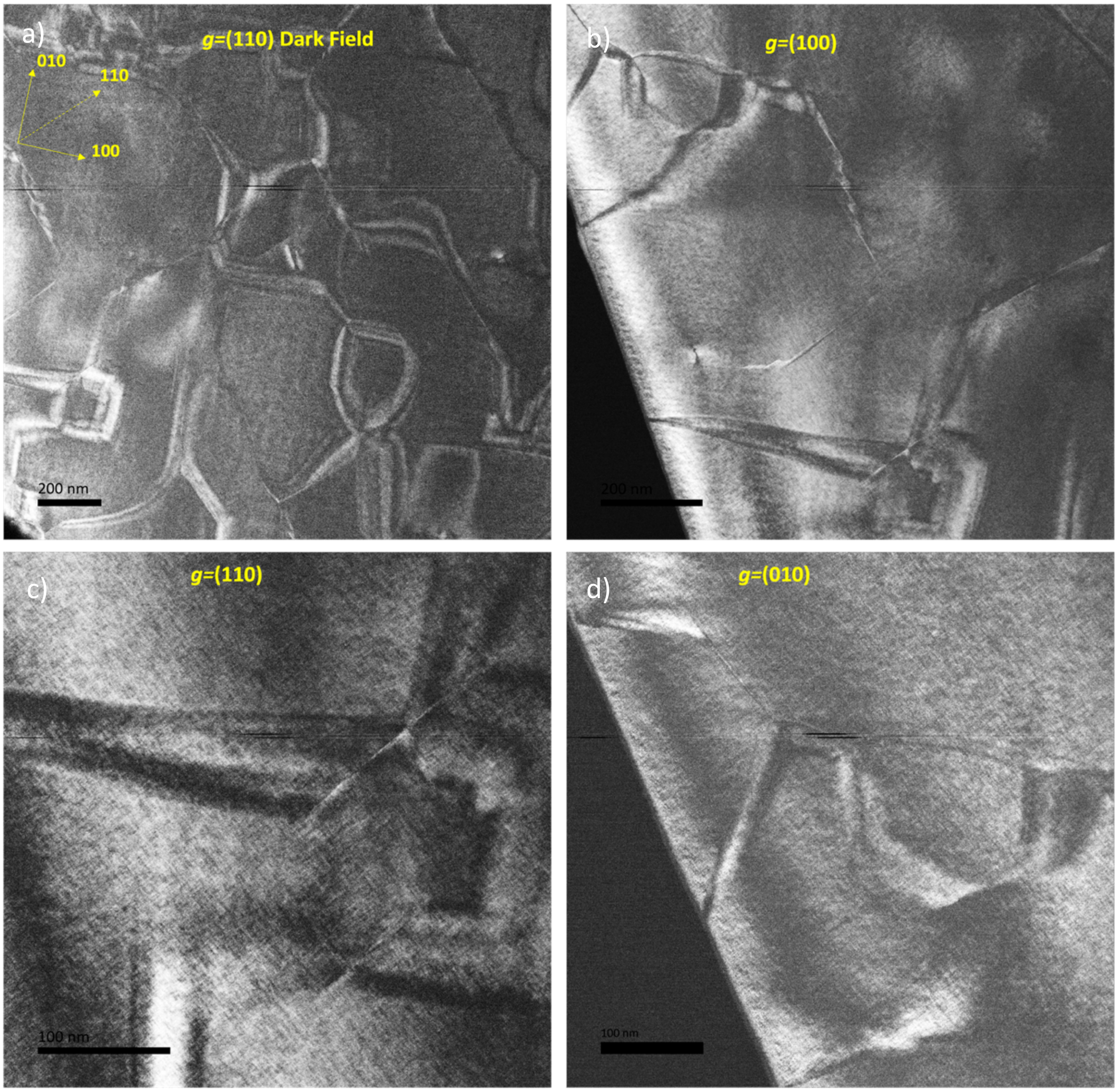

Figure 5.7. DF-TEM micrographs of single-phase $L1_2$ where APBs are visible, and faint modulations or mottling are also visible. The mottling is ascribed to the tweed pre-transition state.

Figure 5.7 shows a series of DF-images taken of the single-phase L1$_2$ where clear mottling is seen along {110}. This type of microstructure (particularly Fig. 5.7c,d) has direct correspondence with tweed structures observed in Co-Pt[97,98], Fe-Pt[4065], Fe-Pd[37–39].

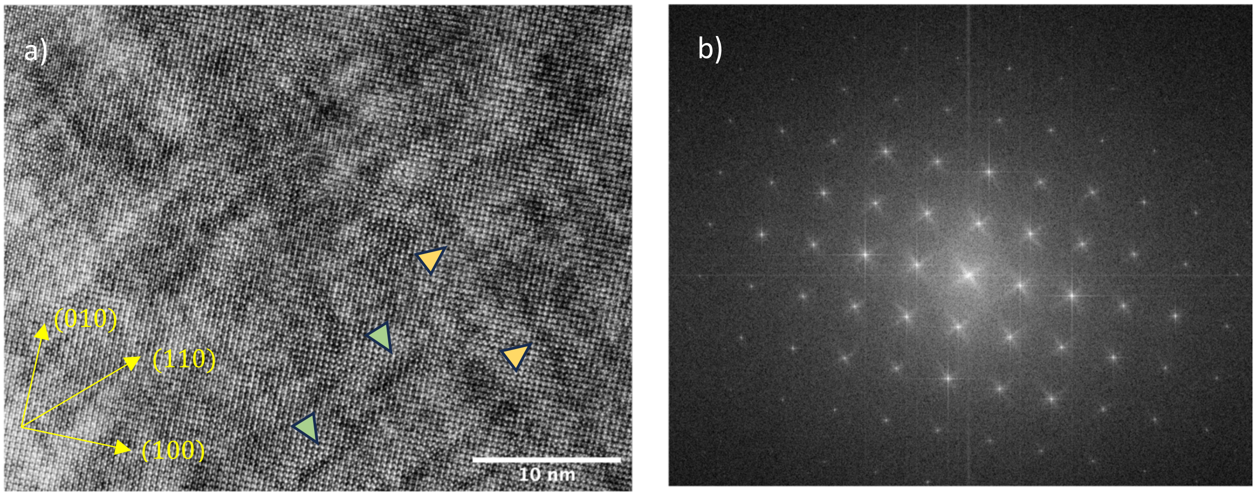

Figure 5.8. HR-TEM in a) of the single-phase L1$_2$, with an accompanying fast-fourier transform (FFT) of the region in b). The modulations along <110> are readily visible in b). The yellow and green arrows in a) correspond to the small structural modulations which are respomsible for the streaks in b).

Further verification of tweed being present is afforded by performing a fast Fourier transform (FFT) on HR-TEM images, as shown in Figure 5.8a,b. In Fig 5.8b, clear striations along {110}* can be observed. In addition, the HR-TEM micrograph shown in Fig. 5.8a shows clear preferential contrast modulation on (110) and ($\underline{1}$10), as shown by the orange and green arrows respectively. The modulations appear on order of 1-3nm, which is agreement with reported[94] modulations of 100-200Å. Although tetragonality of these strain centers has been measured by Muto[38] with spectral filtration, they suggest their reported values may not reflect actual values of the tweed structures because HR-TEM image are typically affected by some aberrations which may influence measurement. As such, calculation of tetragonality (*c/a* ratios) were omitted from the analysis provided here.

Our observation of tweed contrast in ordered $L1_2$ is relatively novel, as tweed has primarily been observed only in *disordered* materials. In fact, Kartha[39]considers tweed to be *disorder*-driven, suggesting that even minor compositional disorder is sufficient to bring about tweed as a pre-transition state. In general, it is suggested that tweed arises from local variations in the effective free energy arising from compositional variation. This may be especially true for martensitic transformations, where (in Fe-Pd at least) compositional deviations on the order of 1 at% have profound effects on martensitic transformation temperatures (up to 100K difference)[39]. Other models in the literature suggest a nucleation-based model[99], where long-range strain interactions induced by vacancies/defects in the lattice create the texturing, and in time will disappear. However, Khachaturyan suggests that the tweed *texture* or state occurs as a spatially correlated patterning of tetragonal nanodomains within a cubic matrix which evolve from their initial composition towards equilibrium values as the system evolves [36]. In this model, ordering interactions are mediated by elastic strains in the material[99].

The tweed pretransition state observed in these $L1_2$ single-phase samples must play a significant role in the $L1_2 \rightarrow L1_0 + L1_2$ transformation. Coordination of both *structural* + *composition* nanodomains across lengthscales via elastic interactions should underlie the formation of the hierarchical structure observed (in the micrographs below). It is the cooperative nature of these tetragonal nanodomains [39] which allows the spatial self-reorganization of this ***ordered cubic → ordered cubic + ordered tetragonal*** transformation. It should be stated explicitly, that while these observations, measurements, and micrographs allow for direct visualization of initial, transformation, and end-states it would be paramount to incorporate a more rigorous free-energy or phase-field model to re-evaluate the conclusions made during this study.

5.3.2. Early-Stage Transformation

For all samples aged above the supposed L1$_0$/L1' Order-Disorder temperature of ~600°C, L1$_2$ ordering preceded the formation of L1$_0$. As explained in Chapter 4, Pd-lean compositions yielded polytwinned L1$_0$ microstructure with L12 existing only as wetting layers, where as for Pd-rich compositions, individual L1$_0$ plates were found quasi-periodically enmeshed within an equilibrium

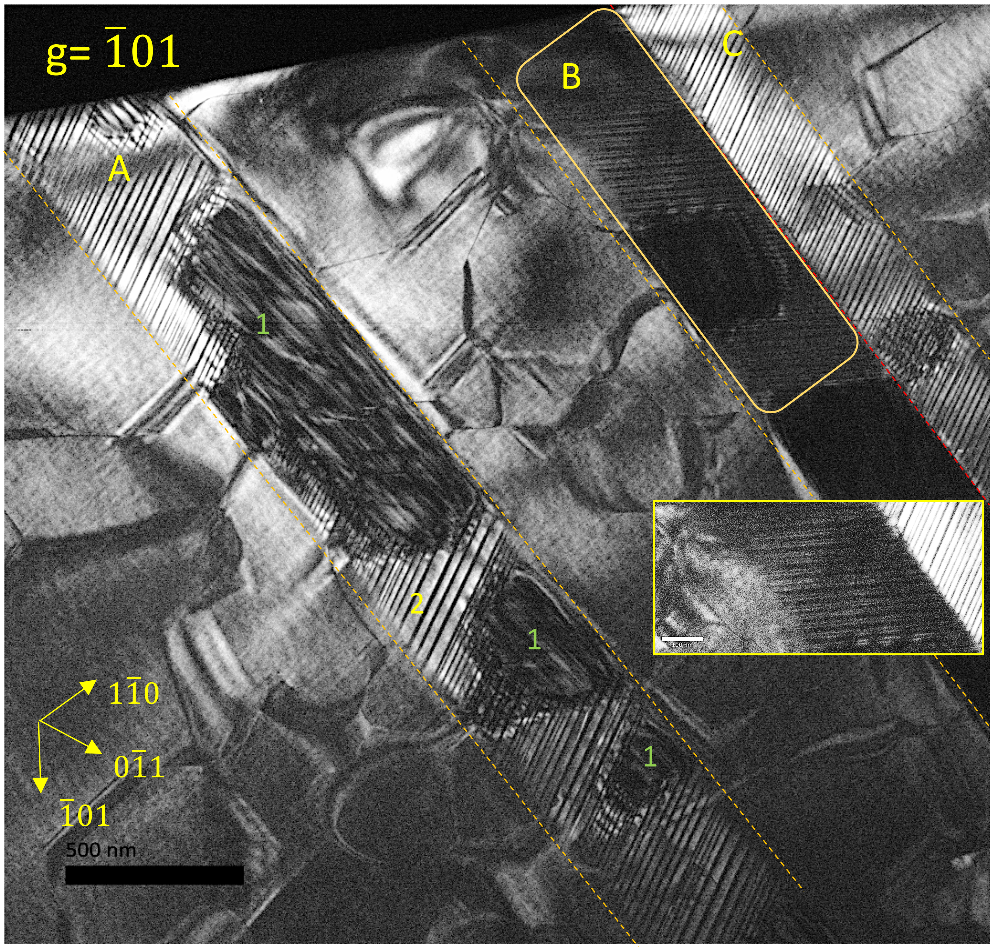

Figure 5.9. A DF-TEM micrograph of the 100°C/Hr + 30min age, where L1$_2$ matrix + L1$_0$ polytwinned plates are found. Interestingly, in contrast with Pd-rich specimens, we observe plate/plate boundaries between B/C plates. This micrograph has captured a moment in the transformation from single-phase L1$_2$ to bulk L1$_0$ polytwinned plates with L1$_2$ wetting layers, with eventual complete consumption of the L1$_2$ matrix seen here.

$L1_2$ matrix. This section will explore the microstructure of samples undergoing the phase transformation from single phase $L1_2$ to the $L1_0$ (polytwinned) + $L1_2$ wetting as observed in Pd-lean compositions. While the microstructure observed and characterized here correlates to this Pd-lean composition, the transformation pathways should be representative of Pd-rich compositions too, albeit with adjustments at critical lengthscales associated with the hierarchical organization. A terminal-state polytwinned $L1_0$ + $L1_2$ wetting layer microstructure is shown for reference in Figure 5.10, where individual plates are demarcated by orange dashed lines (for ease of comparison to Fig. 5.9). In Figure 5.10, none of the original $L1_2$ matrix remains. As such, *all $L1_2$ matrix material observed in Fig.5. 9 will be consumed* in the transformation process towards equilibrium.

A DF-TEM micrograph of the 100C/H + 30min. anneal @ 650°C is shown in Figure 5.9, and serves as a snapshot of the intermediate stage of the $order \rightarrow order + order$ phase transformation. In this micrograph three $L1_0$ polytwin plates are shown, labelled A,B,C respectively. They are bounded within the $L1_2$ matrix, although plates B+C possess an internal plate/plate interface as shown by the red dashed line. The dashed (orange) lines serve as guides to the eye to demarcate the matrix plate/matrix boundaries. It's important to point out that no equilibrium samples explored exhibiting $L1_2$ matrix + $L1_0$ plates for

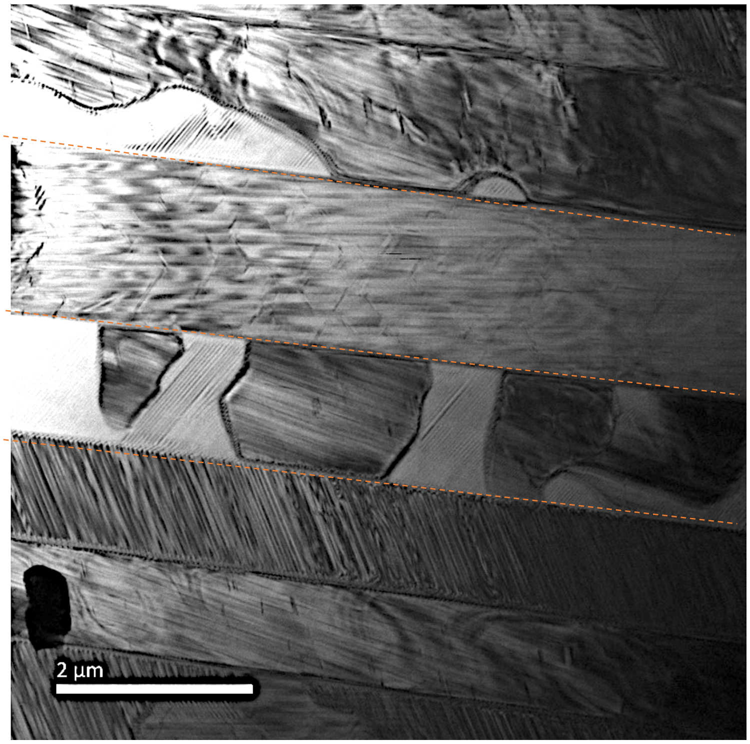

Figure 5.10. A BF-TEM micrograph of the end-state $L1_0$ +$L1_2$ wetting layer microstructure, where no $L1_2$ matrix is left.

Pd-rich compositions ever exhibited plate/plate interfaces (plates were always separated by extended $L1_2$ matrix): as such, the microstructure presented here clearly shows the influence of composition on transformation pathway. For Pd-rich compositions where $L1_0$ is a minority phase, it is suspected elastic strain fields between polytwinned plates select spacing to minimize internal stresses. Whereas for Pd-lean compositions where $L1_0$ will eventually fully consume the $L1_2$ matrix by forming macroscale bundles of polytwinned plates (see Fig. 5.10), plate/plate interfaces must form.. The polytwinned plates exhibit {110}-type matrix/plate & *c*-domain/*c*-domain interfaces, as expected of $L1_0$ polytwins[41]. Another critical observation made of Fig. 5.9 is that in the polytwinned plate labelled 'A' there exist groupings of internally twinned 'colonies', with different {110}-type habit planes, labelled '1' and '2' respectively on the micrograph. This observation gives insight into transformation mechanics, and suggests cooperative growth along plate lengthscales. As additional salient feature of this micrograph is the extreme anisotropy of the plate within the matrix, where plate width *D* (~500nm) is seen to be up to two orders of magnitude narrower than plate length (lower magnification imaging suggested these plates can span entire grains, or order ~10's of μms). This suggests preferential 'growth' in two directions with suppressed growth in the third dimension. In this case, 'easy' or 'fast' growth directions are parallel to plate/matrix boundaries (orange dashed line). Although this extreme anisotropy may suggest growth of the plate, deeper analysis suggests a more complicated structural & compositional evolution. For example, the DF imaging condition used in this image allows for direct visualization of nanometer lengthscale $L1_2$ wetting layer found along all $L1_0$ ODBs (see orange rectangle on plate B of Fig. 5.9 or the inset). This observation complicates a simplistic 'polytwinned plate' growth model, as internal wetting layers would have to be nucleated from Pd-supersaturated $L1_0$, itself forming in Fe-supersaturated $L1_2$. Growth of polytwinned plates with subsequent wetting shows a complex, multi-step pathway that is akin to a cascade transformation: polytwinned plates would nucleate + grow within a *supersaturated* $L1_2$ matrix, with subsequent twinning & wetting of *supersaturated* $L1_0$ *c*-domains. It is hypothesized that the presence of tweed as a pretransition state, in addition to the observed multiple colonies (labelled 1,2 in Fig. 5.9) suggest a cooperative

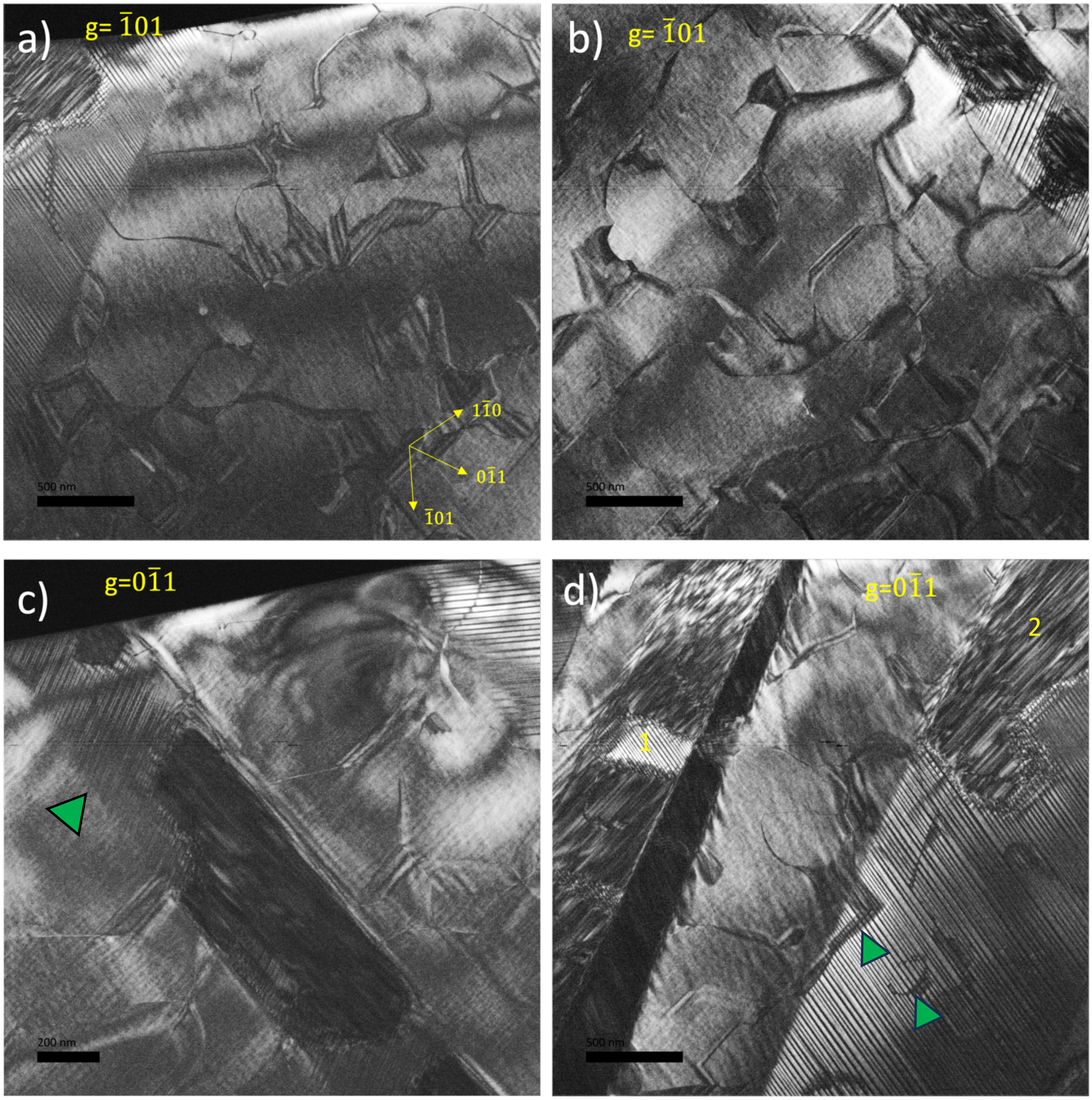

Figure 5.11. BF-TEM micrographs from the 100°C/Hr + 30min aged sample, where polytwinned/matrix regions can be probed more in depth. DF imaging conditions allows for direct visualization of $L1_2$ wetting layers and individual *c*-domains.

elastic-strain mediated tweed → polytwin transformation, where $L1_2$ wetting layers are, in fact, remnant matrix material.

Additional micrographs taken of the 100°C/H + 30min. aged sample (exhibiting a partially transformed state) are included in Figure 5.11, where DF imaging conditions are cycled (for superlattice reflections allowed on [111] zone axis). In Fig. 5.11a &b, a clear view of the extent of the single-phase $L1_2$ matrix region is given. The single-phase $L1_2$ is readily identified by the transformation APBs which present as curvilinear black fringes within the bulk specimen. In Fig. 5.11a (upper left) & 11b (upper righ), L10 plates enmeshed within the matrix are apparent. Figure 5.11c shows that for $g=0\underline{1}1$ imaging condition, the $L1_2$ wetting layers along the $L1_0$ orientation domain boundaries of this enmeshed plate region are directly visualized. The thin striations illuminated in the plate on the top left of the Fig. 5.11c (green arrow) run directly along orientation domain boundaries, connecting the $L1_2$ matrix regions that bound either side of the $L1_0$ plate. In Fig. 5.11d, a complex microstructure is shown, where a central $L1_2$ matrix is observed, bounded by $L1_0$ polytwinned plates on left & right sides. This image is included since it again shows multiple colonies (labelled A,B in this Figure) within a plate, and it also shows how $L1_2$ matrix APBs apparently extend into the polytwinned plate (labelled here with green arrows), crossing many orientation domains.

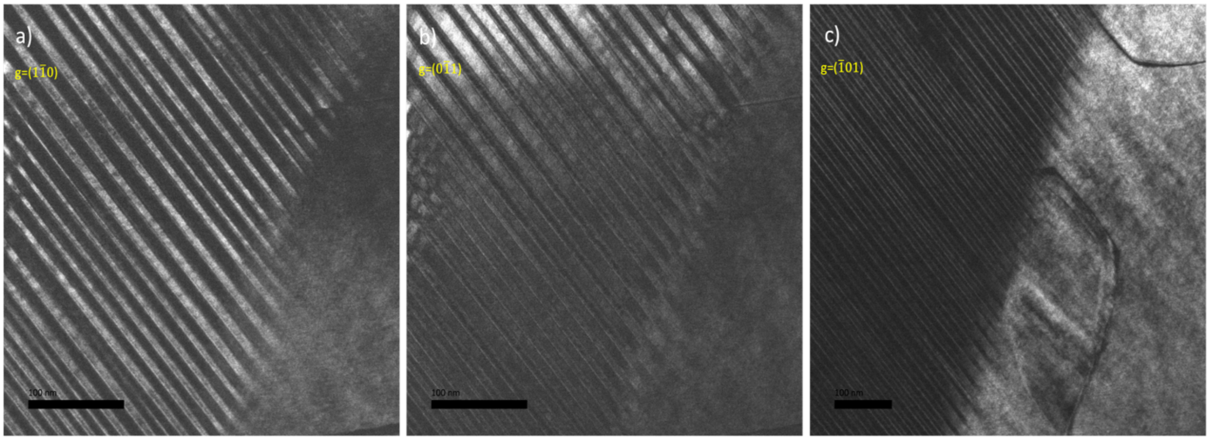

Figure 5.12. DF-TEM micrographs cycling through g= {110} imaging conditions, which allows for identification of individual *c*-domains and the $L1_2$ wetting layer along ODBs. This is a critical result, found for samples at this early stage of the transformation.

Another series of DF-TEM images are shown in Figure 5.12, where imaging conditions are cycled such that direct visualization of the conjugate pairing of *c*-variants is observed. In addition, the narrow $L1_2$ wetting layer is shown explicitly in Fig. 5.11c. Interestingly, Fig. 5.11b shows between the $L1_0$ c-variants and the $L1_2$ wetting layer there may exist a gap of disordered FCC present, however limitations in imaging prevent an unassailable statement on this behavior. While FCC-wetting along $L1_0$ ODBs was observed for CVM calculations in the Co-Pt system[87] this observation would necessitate a potentially energetically unfavorable nucleation + growth of a disordered FCC, since the system has previously ordered to $L1_2$ (see Fig. 5.2, 5.6, 5.7). It is more likely that this observation is simply an artifact from the electron microscope imaging. Another important point to make is that all $L1_2$ matrix regions observed in the micrographs above (Fig. 5.9, 5.11, 5.12) exhibit the tweed strain contrast within the matrix upon close examination.

In order to explore the ordering + structural transformation required to entirely transform the $L1_2$ matrix to macroscale polytwinned $L1_0$ *bundles*, incipiently ordered 100C/H + 15min samples were studied with the electron microscope. As can be seen in the X-ray diffractograms of Fig. 5.2, this stage of the transformation yielded almost entirely single-phase $L1_2$ with only minute amounts of $L1_0$ as noticed by the weak {200} fundamental reflection. Nevertheless, this sample yielded marked polytwinned + matrix regions, despite the weak x-ray reflections. Unfortunately for the series of images discussed in the following section (Fig. 5.13, 5.14, 5.15, 5.16), the large local sample thickness prohibited any DF-TEM micrographs. In addition, with minimal sample tilt conditions due to thickness, no satisfactory zone axis was identified: as such, crystallographic directions were not readily identified. However, ODB & plate/matrix interfaces are assumed to be

{110}-type. At this stage in the transformation no $L1_0$ superlattice reflections were observed (in XRD), although from Figs. 5.13, 5.14 and 5.15, $L1_0$ is clearly present as indicated by the polytwinned plates.

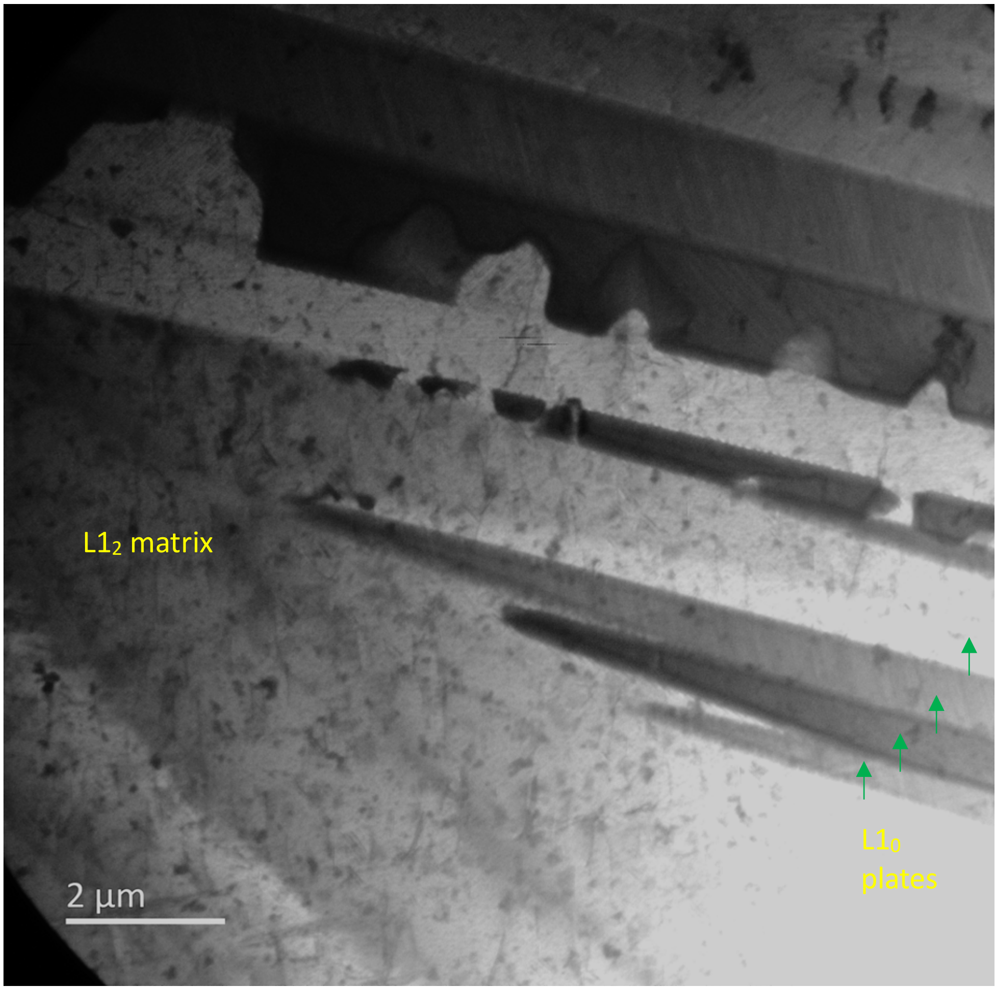

Figure 5.13. A BF-TEM micrograph of an advancing plate tip within the $L1_2$ matrix. The green arrows identify 'trailing' tip growth fronts which have grown laterally to the most advanced plate.

Figure 5.13 shows a crucial observation made when imaging this sample: a bundle of plates growing within the matrix. In this figure, the $L1_2$ matrix is present on the left-hand side of the image, while growing in from the right-hand edge are a collection of internally twinned plates, demarcated with green arrows. It is clear from this micrograph that a 'leading edge' for the bundle is formed. While the term leading edge has direct connotation to precipitate growth within a matrix, the actual transformation process should involve elastically-mediated coordination of tweed domains, most likely influenced by the advancing plate edge. The region probed for this

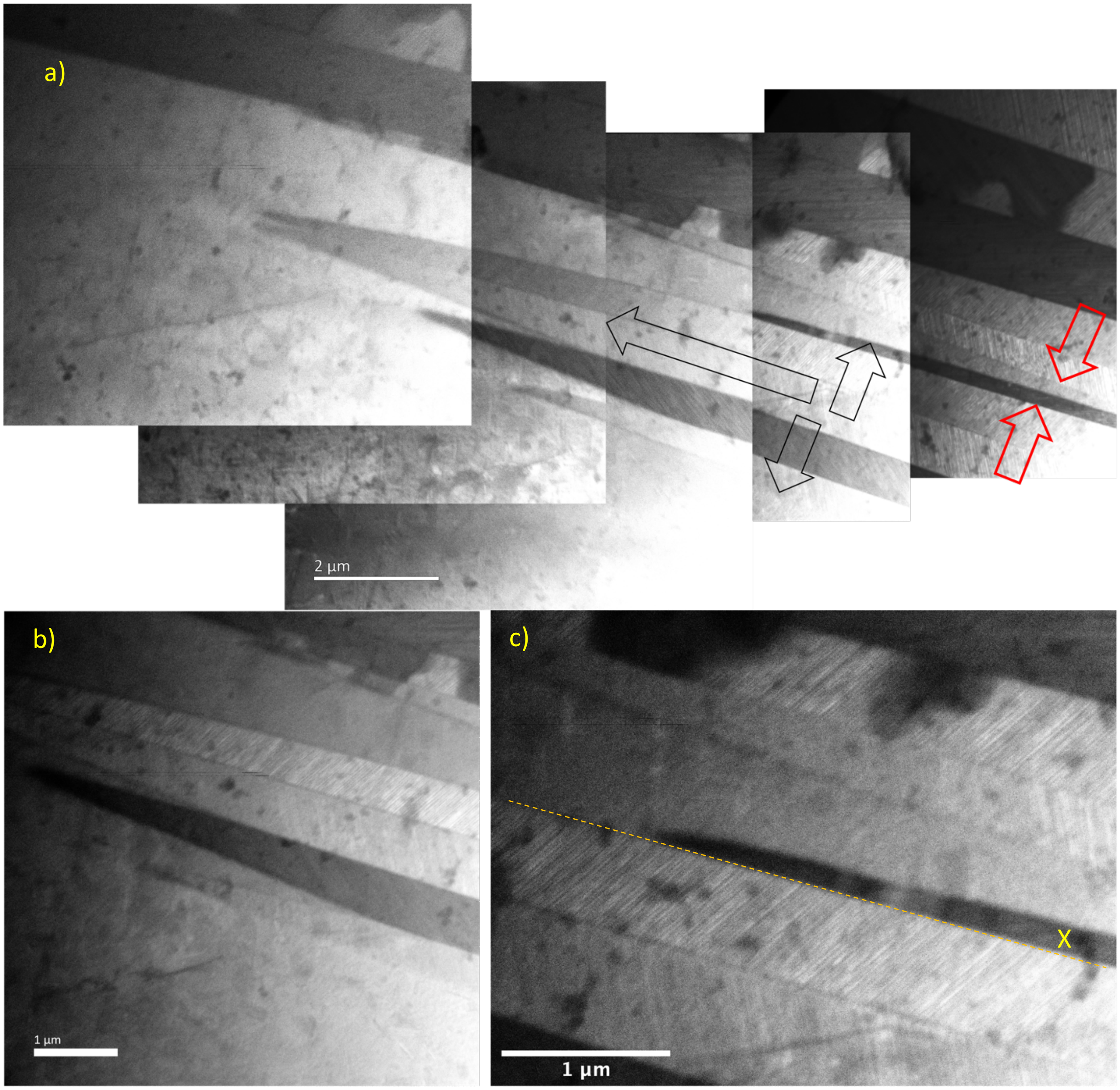

Figure 5.14. Composite images of the region first imaged in Fig. 14, where the extent of the plate growth can be visualized. Arrows in a) are included to show plate growth directions (forward + laterally). The $L1_0$ plate lateral growth appears to form first as a wetting layer along an $L1_0$ plate, consuming the matrix which must contain tetragonal nanodomains (i.e. the tweed pre-transition state). In d) this lateral plate growth is shown by ‘x’.

micrograph gave not only plate/matrix growth transformation information, but evidence for plate/plate growth information as seen in Figure 5.15.

Figure 5.14a shows a composite image of the more magnified region shown in Figure 5.14, where now a greater extent of the advancing plates is seen, in addition to the lateral plate growth, as articulated by the red arrows on the bottom right side of the micrograph. In this context, lateral plate growth is meant to signify growth of plate dimensions not in the radial direction, but an increased in observed 'thickness'. This lateral plate growth is shown in greater detail in Fig. 5.15c, where the dark, band-like region wetting the plate interface (given by the orange dashed line) is another $L1_0$ plate. This newly formed $L1_0$ plate (highlighted with a yellow X in Fig. 5.15c) is assumed to have formed after the larger plate below it, yields insight into the nature of the propagation of these plates and their ultimate consumption of the ordered $L1_2$ matrix. Figure 5.14b,c are also included as the greater magnification resolved the polytwin structure of the various plates . The 'filling in' of the L12 matrix with L10 is a critical detail necessary to explain the end-state microstructure (i.e. Chapter 4 sec 1), where no matrix $L1_2$ is found. Another bundle/matrix interface micrograph is shown in Figure 5.15, where a central matrix region is bounded by bundles of plates.

Another interesting observation in Figs. 5.14, 5.15, and to a lesser extent, Fig. 5.13, is the direct observation of multiple colonies within a bounded plate, which appear as differently shaded regions (owing to the change in habit-plane of the ODBs) within the plate boundaries. Figure 5.15 highlights examples of these as regions 1 and 2 within a single plate). Multicolony plates give insight into transformation mechanisms, specifically, the coalescence of tweed nanodomains.

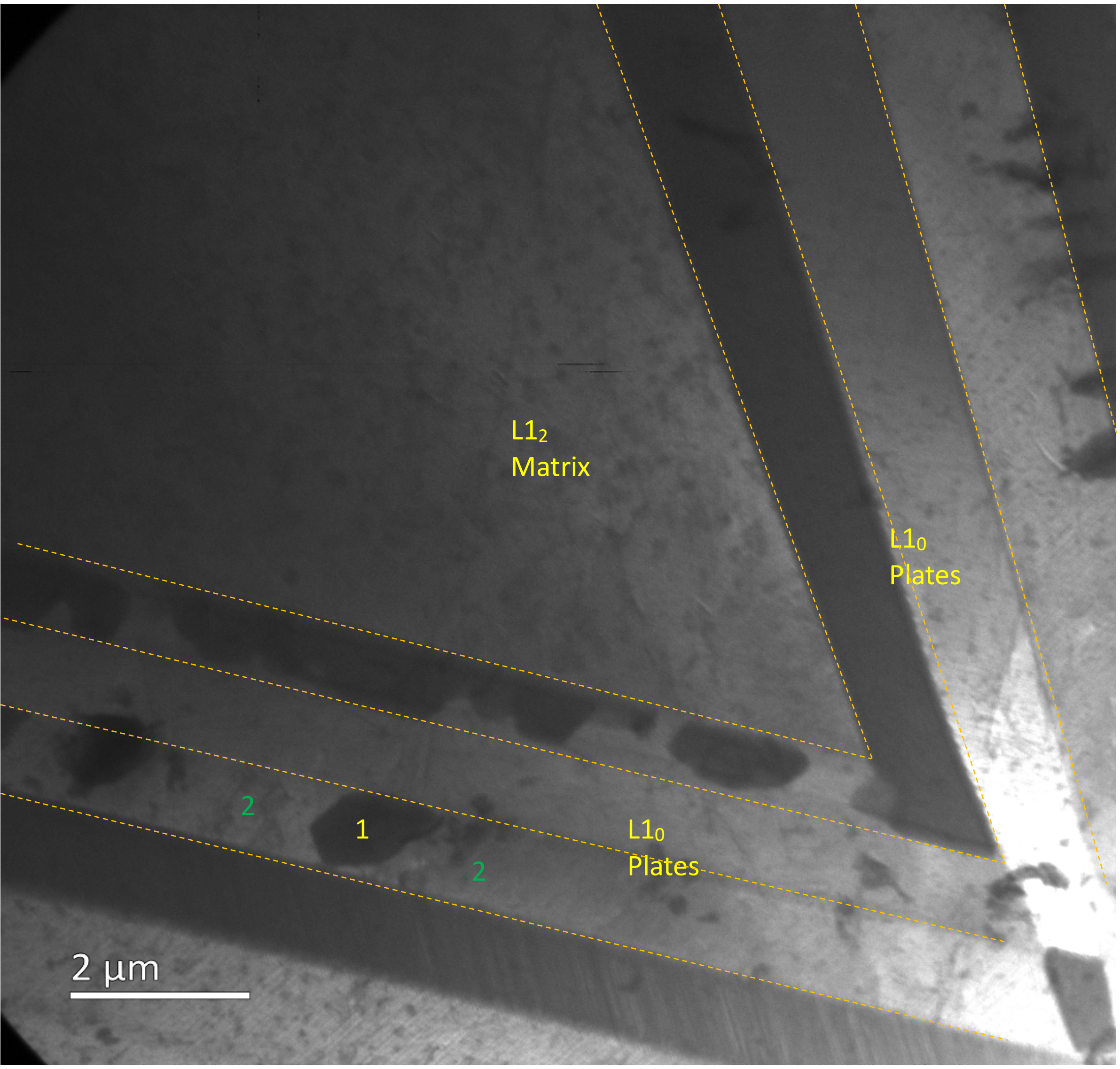

Figure 5.15. Macroscale view of another L1$_0$ bundle + plate matrix region. This micrograph shows that bundles most likely 'fill in' laterally, to consume the L1$_2$ matrix between bundles.

5.4. Transformation Pathway Hypothesis

Although in-situ hot-stage microscopy experiments were performed in efforts to capture the dynamic transformation, the TEM 3mm foils were biased by thin-film constraints and exhibited transformation pathways (and end-state microstructures) not seen in bulk. These type of biasing effects have been observed in other phase transformation in-situ experiments (like in studies on Ni-Al martensite[100]). Direct observation of transformation pathways were therefore stifled.

The hypothesis explaining the $L1_2 \rightarrow L1_0 + L1$ transformation is built upon observations made from incipient, middle-stage, and end-state microstructures imaged and characterized with transmission electron microscopy. The hypothesis that follows is a culmination observations gathered.

Key observations are summarized as follows:

i. $L1_2$ ordering preceded $L1_0$ ordering for all two-phase $L1_0 + L1_2$ samples (see Fig. 5.6, 5.7). $A1 \rightarrow L1_2$ may have transformed by either nucleation + growth within the disordered matrix, or via continuous ordering due to degree of undercooling (below the instability temperature) (see Fig. 5.5)

ii. Within the single-phase $L1_2$ matrix, the tweed pre-transition state, or strain-contrast texture was observed (see Fig. 5.7,5.8).

iii. $L1_0$ plates appear to initiate at grain boundaries and grow into the $L1_2$ matrix radially and laterally (this is shown in a figure further down, see Fig. 5.16) Many $L1_0$ plates contain multiple colonies (differently oriented ODBs) within the plate boundaries (see Fig. 5.9, 5.15, 5.18a)

iv. All $L1_0$ plates exhibit standard internal twinning along {110} that define the orientation domains, and each orientation domain boundary is wet by nm-lengthscale layers of $L1_2$ (see Fig. 5.11, 5.12)

v. $L1_0$ plates consume the $L1_2$ matrix laterally by growth from plate boundaries into the adjacent matrix region, by incorporation of existing tetragonal nanodomains (see Fig. 5.15, 5.18)

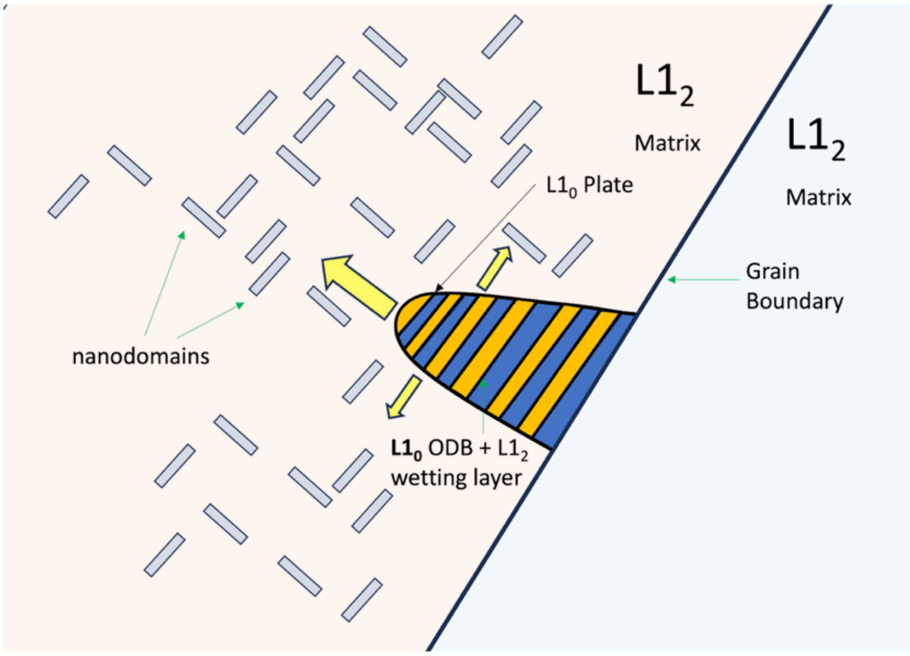

Figure 5.16. Schematic of the $L1_0$ plate growth occurring from a heterogeneous nucleation site along $L1_2$ graim boundary. The growth is considered to be driven by coordination of the elastic strain fields within the system, formed by the tetragonal nanodomains.

An emerging picture of the transformation is given in Figure 5.16, which is a simplified schematic. The transformation hypothesis will be presented in list format, with analysis and discussion to follow. Briefly, Figure 5.16 shows a polytwinned plate growing within an $L1_2$ matrix (given in red), which was spawned on an $L1_2$ grain boundary.

Visible within the red $L1_2$ matrix are the tetragonal nanodomains (in the language of Khachaturyan[36]) or embryos (in the language of Muto[37]) that constitute the tweed pre-transition state. The tetragonal nanodomains are not to scale in this figure, but are exaggerated to accentuate the concept. The yellow arrows in Figure 5.16 show the growth directions (forward and laterally).

In list form, the transformation is hypothesized to progress as follows, where each point (i – iv) will be expounded upon below:

i. Nucleation of an incipient polytwinned plate (at early stages of transformation a *c*-domain) occurs heterogeneously on a grain boundaries.
ii. Forward growth of the plate is mediated by the large, local elastic strain field at the tip of the plate (large yellow arrow in Fig. 5.16), which effectively coordinates or selects nanodomains that will join the propagating tip. Accumulation of new material to the tip occurs as accommodation of pre-existing nanodomains are incorporated into the plate by either re-organization (if not habituated on the relevant {110}) or consumed (if on desirable {110} habit).
iii. As adjacent c-domains are formed, a remnant matrix $L1_2$ boundary wetting layer is left, wetting the ODB's. *C*-domain thickness is dictated by surface energy considerations of the orientation domain boundaries and elastic strain conditions between *c*-domain and matrix material.
iv. The composition of the plates slowly equilibrates as excess (supersaturated) Fe within the $L1_2$ matrix + wetting layer diffuses into the polytwinned regions.
v. Lateral growth (small yellow arrows in Fig. 5.16) of polytwinned plates into the matrix occurs by cooperative nucleation of new plates onto the sides of existing

plates, via a similar reorganization onto appropriate {110}-type boundaries, and eventual diffusion towards equilibrium composition values determined the $L1_0/L1_2$ solvi.

The observation of plate growths on grain boundaries (point i) is observed in a number of sections, with a particularly clear example shown in Figure 5.18, below. A wider base along the grain boundary is seen for the polytwinned plates, with plate projection into the $L1_2$ matrix appears to form a 'spear-like' morphology , with pronounced narrowing of plates occurring at the plate tip. The morphology suggests that growth of the plate began at the grain boundary, and that the narrow plate tip propagates rapidly into the $L1_2$ matrix.

Growth of this plate must occur by strain-field mediated coordination (item ii), as plate B in Fig. 5.18a clearly shows multiple colonies bounded within the plate. Single $L1_0$ plates entrained within the $L1_2$ matrix exhibiting multiple colonies can also be readily observed in Fig. 5.9. No external biasing towards ODB {110} habit planes was possible by adjacent twins, as there are no direct interfaces between plates in this region. As shown by Kartha[39], tetragonal nanodomains exhibit nonlocal interactions as far as 50 lattice constants apart from one another, and plate growth across multiple fronts in isotropic directions, with re-alignemnt of domains may satisfactorily explain the easy growth direction observed. Further evidence supporting nonlocal coordinated rearrangement of tetragonal nanodomains into conjugate pairing of *c*-domains is shown in Fig. 5.18b, where an anti-phase boundary spanning from the $L1_2$ matrix into the polytwinned $L1_0$ plate and back out is shown. This crossing of plate/boundary interface is rigorously impossible if the polytwinned plate boundaries were formed (precipitated) independently of the individual twinning layers, as the anti-phase boundary would be pushed or annealed out. It is expected that growth towards equilibrium composition and degree of tetragonality occurred during the transformation, though composition measurements were not done as variations between phases are minute (as little as 1 at% difference).

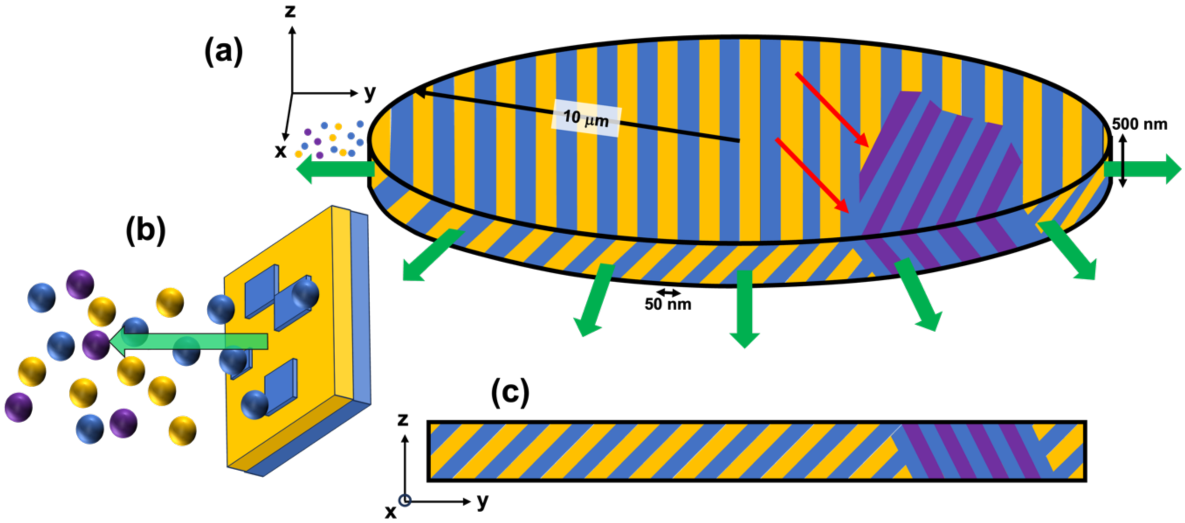

Figure 5.17. (a) A polytwinned plate, where orange and blue regions are conjugate c-domains (L1$_2$ wetting layers are not shown) Blue and purple regions represent another pairing of conjugate *c*-domains which we refer to as ‘colonies’ of *c*-domains. (b) A “zoomed-in” view at the edge of the plate where growth is along the –y direction into adjacent the L1$_2$ matrix. Panel (c) shows a view along the x-direction, and represents what would be observed in a TEM micrograph with x as the zone-axis.

Figure 5.17 gives in a) a polytwinned plate, showing an overall disk shaped envelope, where orange and blue regions are conjugate c-domains (L1$_2$ wetting layers are not shown). A cartesian coordinate system is shown for reference, but is not assigned to any specific crystallographic directions. The plate is drawn with constant thickness along z for simplicity, but in reality the boundary should be lenticular. The plate grows rapidly in the x-y habit plane, eventually reaching 10’s of microns in diameter, while the thickness along the z-direction remains only of order 500 nm (the thickness of the c-domains is not to scale here – they are usually only of order 50 nm thick). Relative dimensions are indicated on the sketch. An embedded colony with a different conjugate pair, and different ODB orientations, has also formed within the plate. In b) a "zoomed-in" view at the edge of the plate where growth is along the –y direction into adjacent the $L1_2$ matrix is given. Small $L1_0$ transformation regions (leading to tweed contrast in TEM) are shown as spheres, colored by their c-axis orientation. At the instant depicted here, elastic strain favors formation of blue on orange to continue the conjugate pairing established earlier, implying that proximal orange and purple regions will dissolve. The process alternates between orange and blue to form mature c-domains, with purple being excluded ahead of the growth front. *However*, the plates grow isotropically in the x-y habit plane, so in other directions (e.g., along x, there must also be addition of new $L1_0$ at the edges of the c-domains, not just on their faces as in b). Growth at edges may provide opportunities for other conjugate pairings to form, perhaps leading to new, entrained colonies, e.g., initiated at the red arrows in a). Panel (c) shows a view along the x-direction, and represents what would be observed in a TEM micrograph with x as the zone-axis.

The remnant layer of $L1_2$ observed all along all ODB's (point iii) is readily visible in Figs. 5.10, 5.11, 5.12. This observation bolsters the tweed → polytwin transformation as growth of Pd-supersaturated $L1_0$ would be energetically unfavorable.

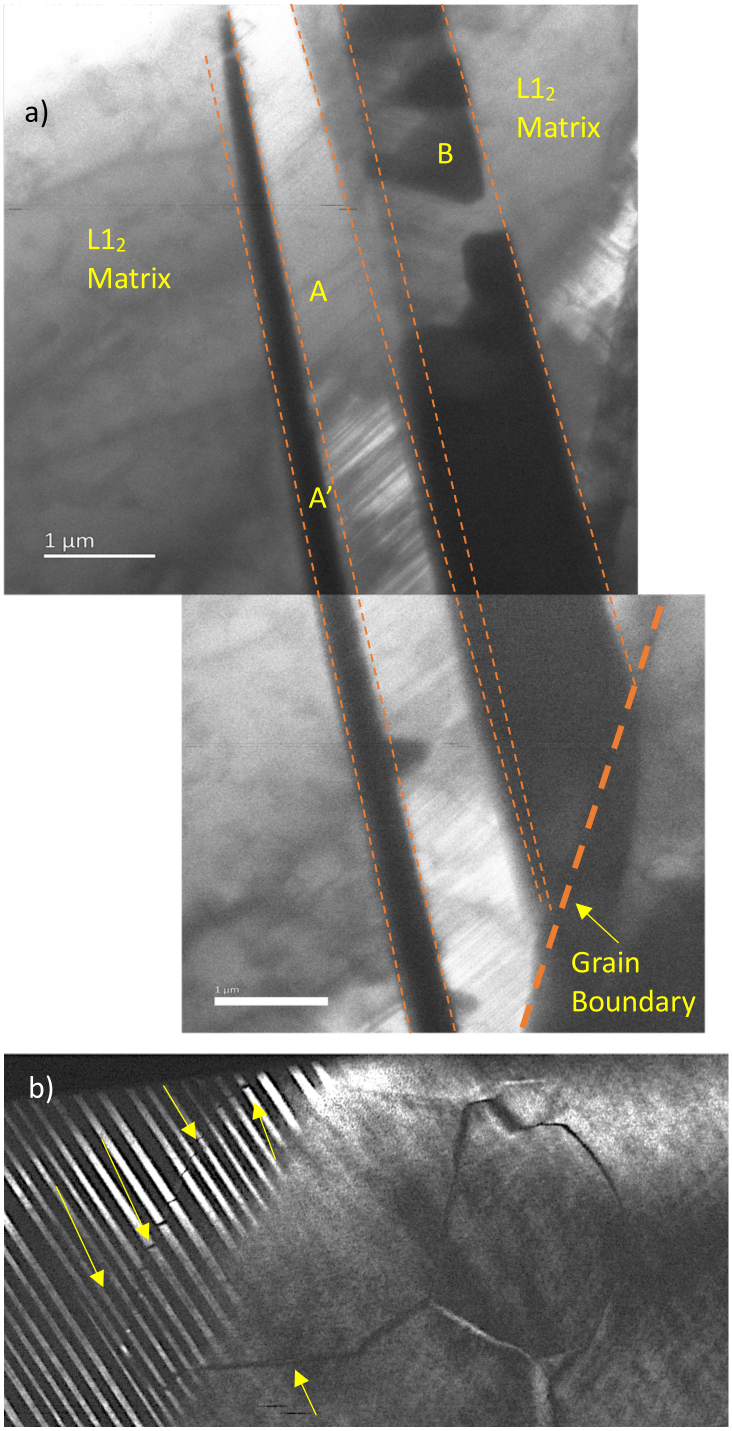

Figure 5.18. **a)** Polytwinned plate growth from a grain boundary into the adjacent $L1_2$ matrix. Lateral plate growth is also observed. b) A DF-TEM micrograph showing an APB progressing from within the single-phase $L1_2$ matrix into the adjacent $L1_0$ polytwin, and cross back out. It is highlighted by yellow arrows.

Lateral growth of the polytwinned plate is readily observed in Figs. 15, 18a. Fig. 5.18a shows a plate A' bounded by orange dashed lines which separate the plates. This growth shows a 'wetting' of adjacent plates along transformed plates where nanodomains are re-incorporated into the growing plate (adjusted if aligned along an unpreferred {110}-type plane). Eventual plate widths were typically envisioned as being growth-rate dependent, as suggested by Vlasova[41], however growth-rate is not variable we have explored in this transformation sequence, alternative factors must influence the selected width. Averaged widths were found to be ~500nm, which is commonly accepted as within the bounds given in the literature (0.1 – 1um)[41].

A schematic exploring lateral plate growth is included in Figure 5.19 where in a) two L1$_0$ polytwinned plates are seen to form in the L1$_2$ matrix: plate 1 (c1 + c2) is shown to have grown first as it is fully formed. A 2nd plate is shown to nucleate on its upper surface (where c1, c2, c3 represent the orientations of the tetragonal c-axes in each conjugate pair). As this plate/plate nucleation process would have to occur concomitantly, different nucleation sites would have preferential {110}-type colonies, with different conjugate pairing of tetragonal domains. This is shown in the schematic by the blue/purple and yellow/blue regions of plate 2. These different palte nuclei will eventually infill completely by lateral growth until impingement. The restriction on growth in the z-direction implies that the different conjugate regions should ultimately have similar thicknesses, even if they nucleate at somewhat different times. Panel (b) depicts what would be seen in a TEM micrograph with direction x as the zone axis, after complete infill of Plate 2 at long times.

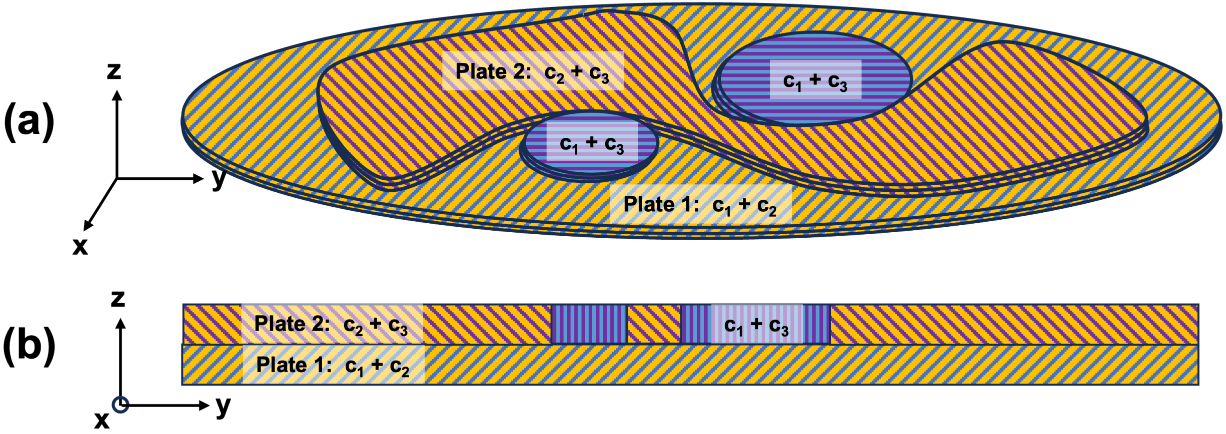

Figure 5.19: (a) Two L1$_0$ polytwinned plates forming in L1$_2$: plate 1 grew first, and then a 2nd plate nucleates on its upper surface. c1, c2, c3 represent the orientations of the tetragonal c-axes in each conjugate pair.. Two different regions nucleate, containing different conjugate pairs than plate 1. These will eventually infill completely by lateral growth to impingement. The restriction on growth in the z-direction implies that the different conjugate regions should ultimately have similar thicknesses, even if they nucleate at somewhat different times. Panel (b) depicts what would be seen in a TEM micrograph with direction x as the zone axis, after complete infill of Plate 2 at long times.

5.5. $L1_0$ Plate Spacing

Although tetragonal nanodomains which constitute the tweed pre-transition state were observed for all single-phase $L1_2$ alloys, one can approximate (to 1st degree) that the $L1_0$ polytwinned plate + $L1_2$ matrix formed as a precipitation from solid solution. This simplification is reasonable since the equilibrium $L1_2$ matrix has an identical structure to the (supersaturated $L1_2$) parent phase but a dissimilar composition, and the precipitated phase differs in crystal structure, composition, lattice parameter, and degree of long-range order[101]. We often observe a quasi-periodic parallel arrangement of polytwinned $L1_0$ plates within the $L1_2$ matrix, see Fig. 5.19. This sample is Pd-rich, so that here the L12 matrix is a stable part of the product microstructure. The origins of this quasiperiodic structure are of interest. This transformation was first envisioned as a cellular or discontinuous precipitation, which can produce somewhat similar results; however these reactions involve grain boundary motion along an advancing precipitation reaction[101]. Although nucleation of the precipitate phase may have occurred heterogeneously along grain boundaries (see Fig. 5.18, 5.21a) the growth and subsequent periodicity may be explainable by elastic strain considerations.

Adapting work done by Khachaturyan[102] on adaptive phase formation in martensitic transformations, we can model the periodicity of the matrix/polytwinned plates using a simple relationship defined by the plate/matrix interface energy $\gamma_{P/M}$, the shear modulus of Fe-Pd μ, and the typical crystal-lattice parent/product strain ε_0. The periodicity λ is then given as

$$\lambda \sim \left(\frac{\gamma_{P/M}}{\mu {\varepsilon_0}^2} D \right)^{1/2}$$

where D is the individual plate width. This is slightly adapted from Khachaturyan's expression, where $\gamma_{P/M}$ is originally given as as γ_{tw}, and is the twin/twin surface energy. A small schematic explaining this relationship, with an accompanying BF-TEM image is shown in Figure 5.20, below.

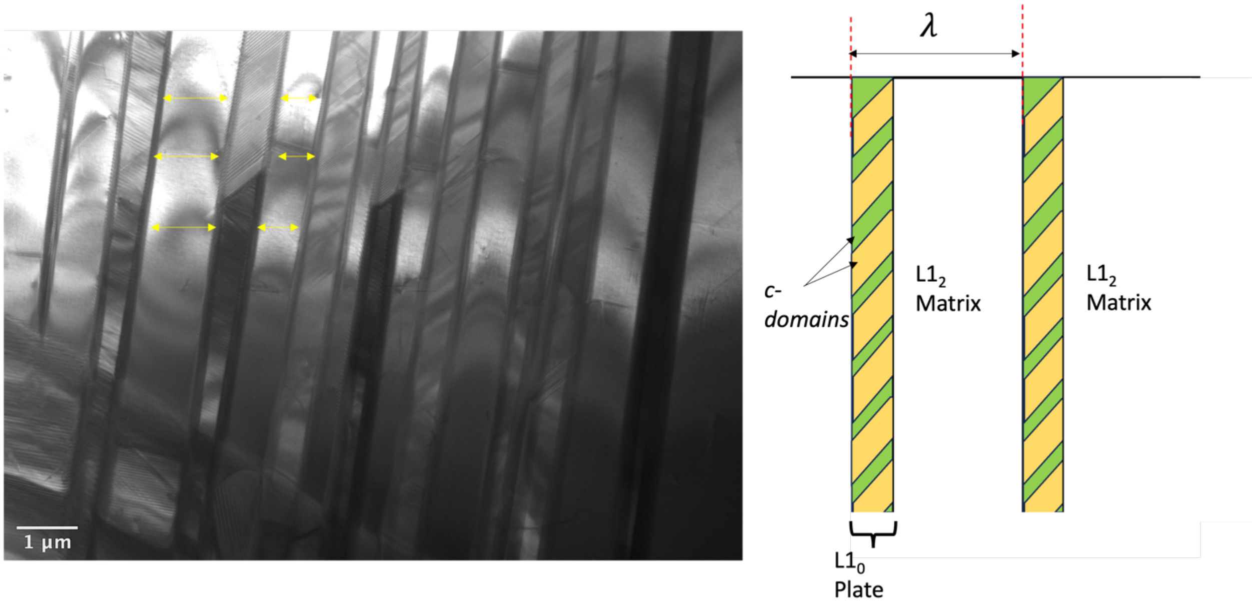

Figure 5.20. For Pd-rich L1$_0$ + L1$_2$ coexistence, plate + matrix microstructures presented with quasi-periodicity of plates within the matrix. A schematic in b) shows a simplified model with period λ.

Taking values from the literature of for shear modulus of bulk Fe-Pd as ~63 GPa[103] on single crystals, a misfit elastic strain of ε_0=0.01, assuming that the surface energy of the plate/matrix is semi-coherent [104] and roughly 500 $\frac{mJ}{m^2}$, and an exaggerated plate width D ~ 600 nm, we get a periodicity of λ = 218nm. This is off by a factor of about 5, as the averaged periodicity of interlamellar spacing (taken from center-center) was measured from Figure 5.20a as ~1200nm. The elastic constants chosen (Shear modulus) varied significantly, and may have contributed to the discrepancy in values. In addition, since the shear modulus is representative of single-phase and we observe two-phase samples, this may be an error. Furthermore, several other assumptions may have negatively influenced the errors in the calculation: namely, semi-coherency at the matrix/plate interface (which may be incorrect). The misfit strain was calculated using the conventional $L1_0$ unit cell and the $L1_2$ unit cell with lattice constants extracted from X-ray diffraction spectra shown in Chapter 4. A major conclusion of this result is that strain considerations *alone* may not be able to accurately describe the periodicity. Nevertheless, strain energy must have significantly impacted the spacing and branching observed (Fig. 5.21) in these Pd-rich composition samples. Branching in martensite/austenite phases has been discussed before[105] and treated elastically, however the microstructures studied deviate significantly

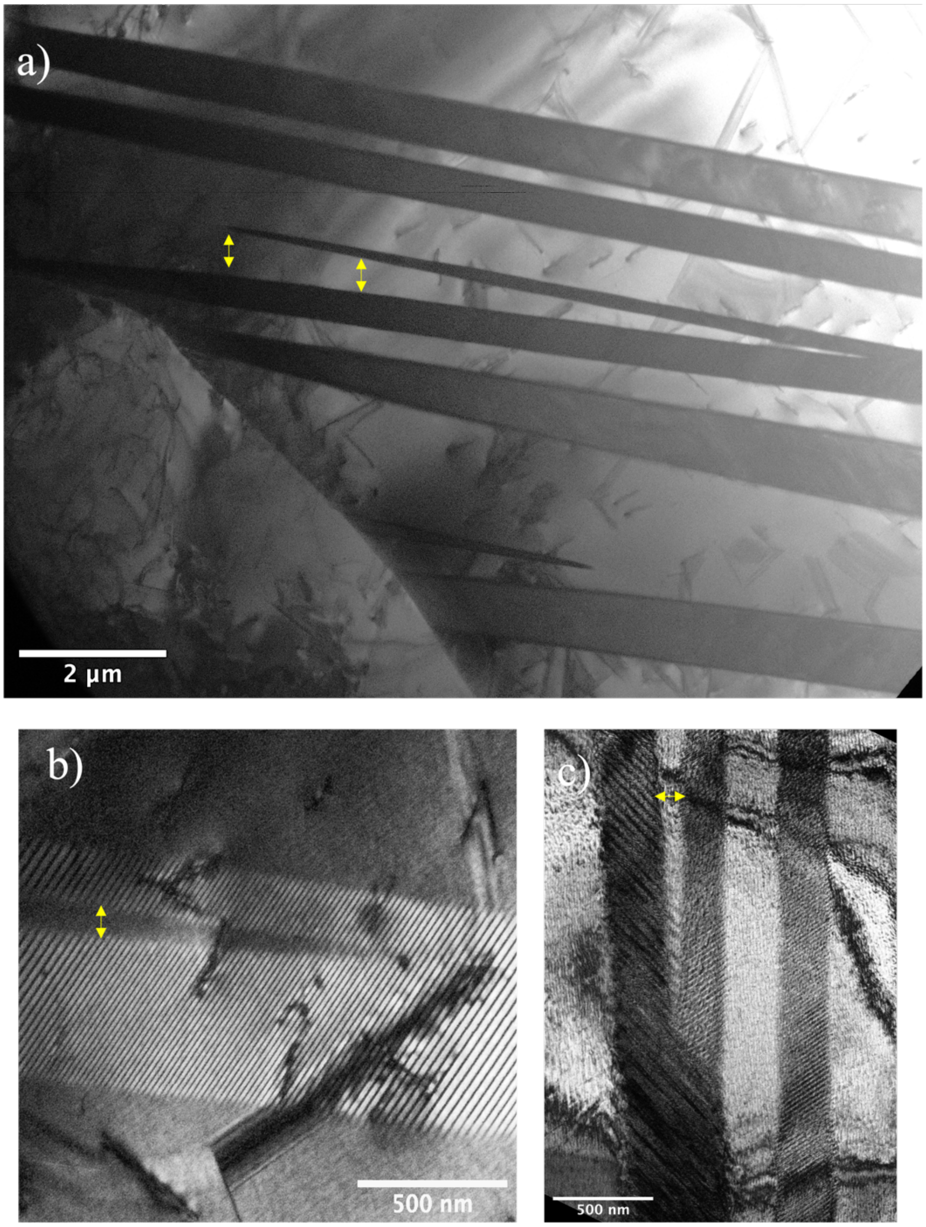

Figure 5.21.BF (a,c) and DF (b)-TEM micrographs of the Pd-rich two-phase coexistence samples which exhibited a plate/plate repulsion most likely formed by fluctuations of the advancing plate tip.The repulsion may be elastically strain driven.

from the observations made here. The branching observed in shape memory alloys studied by Seiner[105] was found between individual *c*-domains, leading to progressively smaller periodicity between lamellae as the parent/product interface was reached. It is suggested in our case (as seen in Fig. 5.21a,b,c), that the branching observed may have formed from an advancing plate-tip that encountered a fluctuation (or defect), and formed a secondary plate tip. As the second plate formed, a repulsive elastic strain field between plates was formed and ‘pushed’ the secondary plate apart from the original plate. This insight does still rigorously fit the proposed transformation model here.

Chapter 6. Summary and Future Work

6.1. Summary

A summary of notable achievements accomplished with this dissertation are provided below.

Firstly, direct observation of the tetragonal L1' phase, first envisioned by Shockley was provided, where at low temperatures the $L1_0$-type ordering is replaced by a different accommodation of off-stoichiometric atoms on the lattice. While identification and verification of this phase is afforded by relatively straight forward analysis of low-angle reflections in X-ray diffraction and Dark-field TEM imaging, there are larger more widespread implications of its existence. For example, while strictly identified in the Fe-Pd system, it may be that all $L1_0$-containing systems (of the *AB*-type rather than ABC_2-type[106]), also contain the L1'-type ordering at low temperatures.

Secondly, the $L1_0 + L1_2$ eutectoid region in Fe-Pd was studied for the first time, and two-phase microstructures for samples aged above and below the order/disorder boundary for $L1_0$/L1' were probed. As mentioned previously, despite nearly a century's worth of study in Fe-Pd, the eutectoid region has never been probed explicitly. Microstructures pertaining to both $L1_2$-poor (Pd-poor) and $L1_2$-rich (Pd-rich) samples were characterized: nm-lengthscale wetting layers for the cubic phase were found for the former, and bulk matrix regions were identified for the latter. While the wetting layer + polytwinned microstructure (for $L1_2$-poor samples) was observed previously in Co-Pt[58]a novel advancement in the consideration of APB channels was given, where translation variants for the channel structure were also considered. The $L1_2$ matrix + polytwinned plate composite material has never been observed in the literature. Characterization of plate/matrix entrainment was considered in three-dimensions, and wetting layers along orientation domain boundaries were identified in this novel microstructure.

In addition to the high-temperature (650℃) two-phase coesxistence results discussed above, low temperature aging (525℃) found coexistence of L1' + $L1_2$. This is novel a result because consideration of L1' phase-fields in the literature have always treated L1' as a low-temperature substitute for $L1_0$ – never as within a two-phase field with $L1_2$. This result further suggests that the L1' phase is not simply a metastable hybrid-ordered $L1_0$ + $L1_2$ phase, but is a stable ordered phase on the FCC lattice (at least in this system, composition, and processing conditions). Our results may be able to assist the development of alloy theory computations with inputs for certain key constraints into models (temperature, species, magnetism, etc), to better predict phase stability and find agreement with experimental results.

The final significant result from our undertakings was the identification of the novel transformation pathway which proceeded as *order* ($L1_2$) → *order* ($L1_2$) + *order* ($L1_0$). Encompassing the total investigation of this transformation, two key results were observed: (i) the novel identification of tweed pretransition state in an ordered $L1_2$ phase, (ii) growth of a polytwinned plate within an ordered matrix. This first result is novel as typically the tweed state is envisioned to be disorder-driven[39] state and is typically identified in solid solution for FCC → $L1_0$ (in Fe-Pd[23], Fe-Pt[40,66], Co-Pt[68], etc.) prior to the formation of the polytwinned phase transformation. Interestingly phase field models predict this behavior as well. To the author's knowledge, there is no identification of tweed in ordered $L1_2$ (or any derivative ordered FCC structure) prior to $L1_0$ formation in the literature. The *order* ($L1_2$) → *order* ($L1_2$) + *order* ($L1_0$) transformation has never been identified in the literature, and is relatively unique as typically phase field models[36,107] done within cubic + tetragonal two-phase regions find the formation of tetragonal regions prior to cubic formation. While the result is novel in and of itself, the pathway found involves the growth of a twinned plate within a matrix, by strain-mediated accumulation of pre-existing tetragonal nanodomains.

6.2 Future Work

Firstly, while L1' phase stability was identified in Fe-Pd, identification of this phase in analogue alloys should bolster the theoretical underpinnings of its stability: whether energetic or entropic components yield the biggest contribution to phase stability. Furthermore, the L1' ordering allows for an additional translation vector (and therefore anti-phase boundary) vis-à-vis $L1_0$, which should boost coercivity as observed in these Fe-Pd alloys. Perhaps this type of investigation will show that in similarly off-stoichiometric $L1_0$ alloys in Fe-Pt, Co-Pt, or Mn-Al, low temperature L1' producing alloys (if identified) are significantly magnetically 'harder' vis-à-vis their $L1_0$ ordering counterparts. This non-trivial though relatively straightforward investigation may shed critical light on permanent magnet design with $L1_0$-containing compounds.

There are a significant number of experiments remaining in Fe-Pd that would further explain key results uncovered in this work. They are listed here:

i. The $L1_0 \rightarrow L1'$ transformation: can it be done in long-time aging? What about $L1' \rightarrow L1_0$? Does the coercivity similarly decrease? Probing the microstructural and structural transformation, and attendant magnetic properties should broaden and solidify the understanding of this fascinating order/disorder boundary.

ii. What does the $L1' \rightarrow L1_0 + L1_2$ phase transformation look like? Microstructurally, how does L1' decompose into these phases? Are there attendant changes in magnetic properties?

iii. Can we identify the order/disorder temperature with Differential scanning calorimetry? Is it 2nd or 1st order (in the Ehrenfest sense) for $L1_0/L1'$ – what about $L1'/(L1_0 + L1_2)$?

iv. Does L1'exist (can it be isolated) near equimolar compositions (but still off) at low temperatures ? Or does it tend to appear strictly near the eutectoid region?

v. Does L1' also transform via a tweed → polytwin process?

vi. What fundamental conclusions can be made with the identification of the tweed pretransition state in ordered material?

The Fe-rich Fe-Pt eutectoid region also, has never been explored. Investigations into this region would be particularly fruitful as both $L1_0$ and $L1_2$ should exhibit higher magnetic moments/unit cell due to the increased Fe content (with decreased cost due to limited Pt content). In addition, the magnetocrystalline anisotropy and magnetic saturation of FePd ($L1_0$) are higher than in Fe-Pd or Co-Pt (refer to Table 1.2). A snippet of the Fe-Pt phase diagram near the eutectoid region is given in Figure 6.1. Does this system also exhibit L1' near its eutectoid region? What type of microstructures does its two-phase region display?

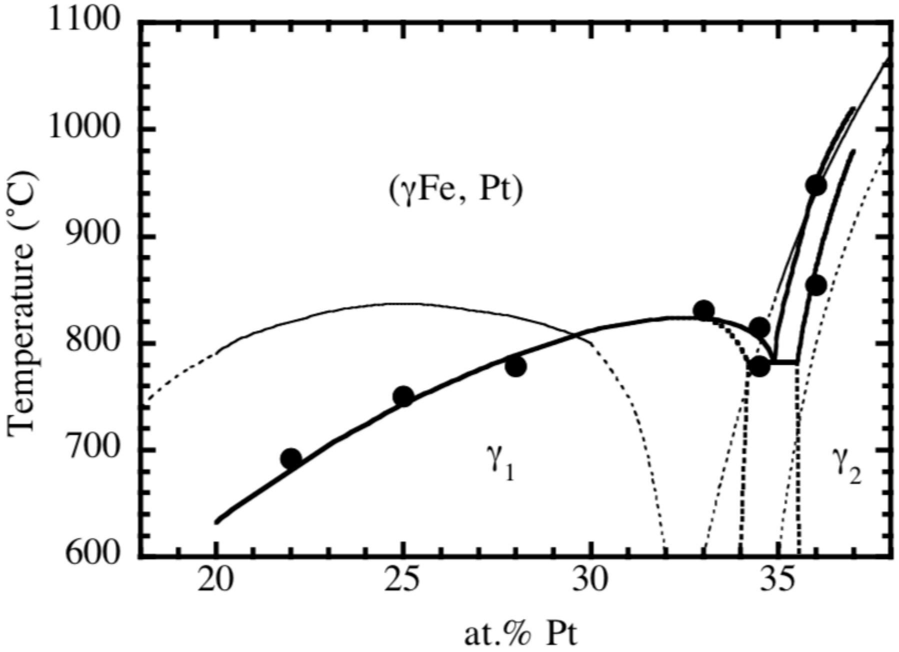

Figure 6.1. The Fe-rich Fe-Pt eutectoid region exhibiting the $L1_0 + L1_2$ phase field, given by Takama[116]

However more importantly, the general push for rare-earth free permanent magnets may have been re-invigorated by recent high visibility published reports on the potential facile formation of tetrataenite (Fe-Ni $L1_0$). While the article's[108] findings were exaggerated or false (alleged report forthcoming by the group), interest in materially abundant, cheap $L1_0$-containing Fe-Ni permanent magnet may have been bolstered by their report. The Fe-Ni phase diagram is attached in Figure 6.2, which shows potential boundaries for the low-temperature *AB* phase field.

Some work done in Fe-Pd may help shed light on ordering in Fe-Ni, which is plagued by limited kinetics due to the low critical temperature. Would aging closer to the Fe_3Ni phase field ($L1_2$) or $FeNi_3$ ($L1_2$) + A1 phase field assist? Would probing general two-phase region compositions in general aid in another order → order + order transformation?

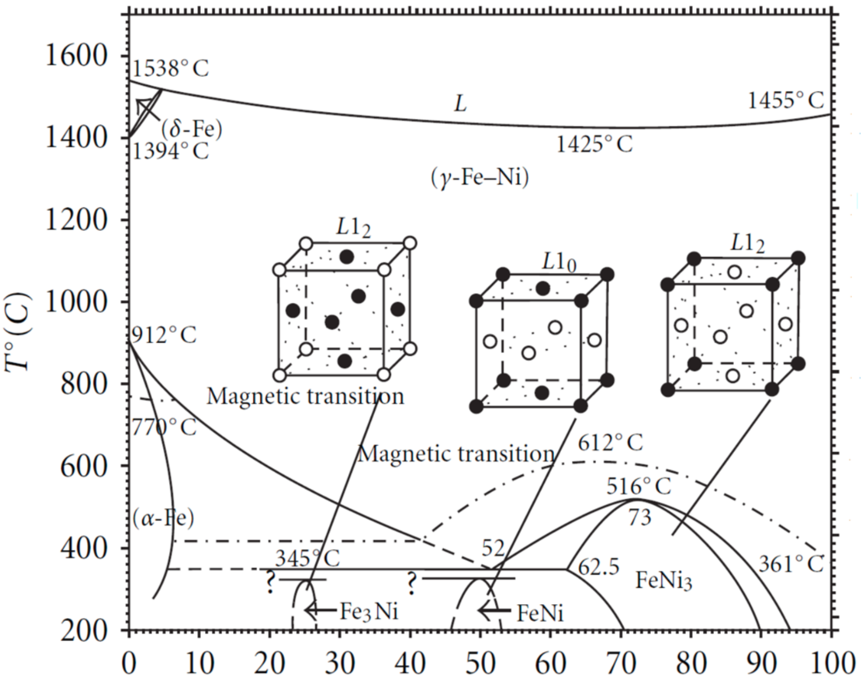

Figure 6.1. The (metstable) Fe-Ni phase diagram [114], showing the expected $L1_0$ (AB) and $L1_2$ (A_3B) phase fields. Note the ? denote the lack of experimental evidence of exact critical temperatures for these phases. Although, Lewis[115] suggests (for Fe – 43 at% Ni) T_{OD} to be ~320℃

Interestingly, reports on meteoritic samples (NWA 6259)[109] containing purported single-phase tetrataenite actually exhibited minute regions of BCC (A2), $L1_0$, $L1_2$, and disordered tetragonal (A6) phases within a tetrataenite matrix. It seems likely that magnetic long-range order affected chemical ordering in Fe-Ni. Although A6 has been identified[110] as a precursor for $L1_0$, it is unclear whether the other precipitates were metastable or not. Applied magnetic[111] + strain fields appear to bolster the ordering process by raising the critical ordering temperature. Furthermore, identification of ordering in tetrataenite is similarly cumbersome: Fe and Ni exhibit nearly identical atomic scattering factors, limiting typical methods used to detect ordering in materials. However, a recent report[112] found nitridation of FeNi nanopowders aided the formation of tetrateanite, where an ordered FeNiN grew (via a massive transformation) as a precursor for the FeNi ($L1_0$). Progress in bulk material synthesis of Fe-Ni $L1_0$ is slow and hard fought. Nevertheless, it seems likely that within this century Fe-Ni $L1_0$ will become a sustainable advanced permanent magnet.

References

1. G. Tammann. Zum Gedächtnis der Entdeckung des Isomorphismus vor 100 Jahren. Die chemischen und galvanischen Eigenschaften von Mischkristallreihen und ihre Atomverteilung. *Z Anorg Allg Chem*. Published online July 1919.
2. E.C. Bain. Cored Crystals and Metallic Compounds. *Chem & Met Eng* . 1923;28(65).
3. H. Johansson JOL. Röntgenographische Bestimmung der Atomanordnung in den Mischkristallreihen Au-Cu und Pd-Cu. *Ann Phys*. 1925;383(21):439-460.
4. J Bradley BA, J ay AH. *The Formation o f Superlattices in Alloys of Iron and Aluminium*. Vol 78.; 1925. https://royalsocietypublishing.org/
5. Jones FW, Sykes C. The Superlattice in β Brass. *Source: Proceedings of the Royal Society of London Series A, Mathematical and Physical Sciences*. 1937;161(906):440-446. https://www.jstor.org/stable/96794
6. Ogawa S, Watanabe D. The Direct Observation of the Long Period of the Ordered Alloy CuAu(II) by Means of Electron Microscope. *Acta Crystallogr*. 1958;11(60):872-875.
7. M. J. MARCINKOWSKI, L. ZWELL. TRANSMISSION ELECTRON MICROSCOPY STUDY OF THE OFF-STOICHIOMETRIC Cu,Au SUPERLATTICES*. *Acta Metallurgica* . 1963;11:373-390.
8. Hultgren R, Zapffe CA. The Crystal Structures of the Iron-Palladium Superlattices. *Zeitschrift fur Kristallographie, Kristallgeometrie, Kristallphysik, Krystallchemie*. 1938;99(1-6):509-512.
9. Tanner LE, Leamy HJ. The Microstructure of Order-Disorder Transitions. In: *Order-Disorder Transformation in Alloys; Proceedings*. Vol 24. ; 1974:180-239.
10. Soffa WA, Laughlin DE. Diffusional Phase Transformations in the Solid State. In: *Physical Metallurgy: Fifth Edition*. Vol 1. Elsevier Inc.; 2014:851-1020. doi:10.1016/B978-0-444-53770-6.00008-3
11. Chen LQ, Khachaturyan A. *KINETICS OF DECOMPOSITION REACTIONS ACCOMPANIED BY A CONGRUENT ORDERING OF THE FIRST-KIND*. Vol 25.; 1991.
12. Francois Ducastelle. *Order and Phase Stability in Alloys*. North-Holland Publishing Co. ; 1993.
13. Shockley W. Theory of order for the copper gold alloy system. *J Chem Phys*. 1938;6(3):130-144. doi:10.1063/1.1750214
14. Guymont M. Phase Transformations in CuAu and Cu3Au. *Z Metallkd* . 1997;88(6):452-454.
15. Cheong B, Laughlin DE. *THERMODYNAMIC CONSIDERATION OF THE TETRAGONAL LATTICE DISTORTION OF THE L10 ORDERED PHASE*. Vol 42.; 1994.
16. Li YY. Quasi-chemical theory of order for the copper gold alloy system. *J Chem Phys*. 1949;17(5):447-454. doi:10.1063/1.1747287
17. Golosov NS, Popov LE, PUDAN Siberian V D Kuznetsov LY. *THEORY OF ORDER-DISORDER TRANSFORMATION IN BINARY SYSTEMS OF THE Cu-Au TYPE-I*. Vol 34. Pergamon Press; 1973.
18. Van Baal CM. Order-Disorder Transformations in Generalized Ising Alloy. *Physica* . 1973;64:571-586.
19. Binder K. *Ordering of the Face-Centered-Cubic Lattice with Nearest-Neighbor Interaction*. Vol 45.; 1980.

20. Finel A, Ducastelle F. On the Phase Diagram of the FCC Ising Model with Antiferromagnetic First-Neighbour Interactions. *Europhys Lett*. 1986;1(3):135-140.
21. Tétot R, Finel A, Ducastelle F. Superdegenerate point in FCC phase diagram: CVM and Monte Carlo investigations. *J Stat Phys*. 1990;61(1-2):121-141. doi:10.1007/BF01013956
22. Tumminello S, Palumbo M, Koßmann J, et al. Dft-cef approach for the thermodynamic properties and volume of stable and metastable Al–Ni compounds. *Metals (Basel)*. 2020;10(9):1-19. doi:10.3390/met10091142
23. Zhang B, Soffa WA. Magnetic Domains and Coercivity in Polytwinned Ferromagnets. *Physica Status Solidi (a)*. 1992;131(2):707-725.
24. Kang S, Jia Z, Nikles DE, Harrell JW. Synthesis and phase transition of self-assembled FePd and FePdPt nanoparticles. In: *Journal of Applied Physics*. Vol 95. ; 2004:6744-6746. doi:10.1063/1.1669306
25. Kakeshita T, Ullakko K. Giant magnetostriction in ferromagnetic shape-memory alloys. *MRS Bull*. 2002;27(2):105-109. doi:10.1557/mrs2002.45
26. Chepulskii R V., Barabash S V., Zunger A. Ab initio theory of phase stability and structural selectivity in Fe-Pd alloys. *Phys Rev B Condens Matter Mater Phys*. 2012;85(14). doi:10.1103/PhysRevB.85.144201
27. T. Massalski HOPS and LK. *Binary Alloy Phase Diagrams, 2nd Ed.* . ASM International; 1990.
28. Ghosh G, Kantner C, Olson GB. Thermodynamic Modeling of the Pd-X (X = Ag, Co, Fe, Ni) Systems. *Journal of Phase Equilibria*. 1999;20(3):295-308.
29. Raub E, Beeskow H, Loebich Jr. O. *The Phase Diagram of Fe-Pd Under 950C.*; 1963.
30. Deshpande AR, Wiezorek JMK. Magnetic age hardening of cold-deformed bulk equiatomic Fe-Pd intermetallics during isothermal annealing. *J Magn Magn Mater*. 2004;270(1-2):157-166. doi:10.1016/j.jmmm.2003.08.013
31. Klemmer T, Hoydick D, Okumura H, Zhang B, Soffa WA. Magnetic hardening and coercivity mechanisms in L10 ordered FePd ferromagnets. *Pergamon Scripta Metallurgica et Materialia*. 1995;33:1793-1805.
32. Laughlin DE. The β Iron Controversy Revisited. *J Phase Equilibria Diffus*. 2018;39(3):274-279. doi:10.1007/s11669-018-0638-z
33. Ozolin¸š VO, Wolverton C, Zunger A. First-principles theory of vibrational effects on the phase stability of Cu-Au compounds and alloys. *Phys Rev B*. 1998;58(10).
34. Barabash S V., Chepulskii R V., Blum V, Zunger A. First-principles determination of low-temperature order and ground states of Fe-Ni, Fe-Pd, and Fe-Pt. *Phys Rev B Condens Matter Mater Phys*. 2009;80(22). doi:10.1103/PhysRevB.80.220201
35. Chepulskii R V., Curtarolo S. Revealing low-temperature atomic ordering in bulk Co-Pt with the high-throughput ab-initio method. *Appl Phys Lett*. 2011;99(26). doi:10.1063/1.3671992
36. Ni Y, Khachaturyan AG. Mechanism and conditions of the chessboard structure formation. *Acta Mater*. 2008;56(16):4498-4509. doi:10.1016/j.actamat.2008.05.035
37. Muto-T S, Takedat S, Oshima$ R, Fujita FE. *High-Resolution Electron Microscopy of the Tweed Structure Associated with the FCC-FCT Martensitic Transformation of Fe-Pd Alloys*. Vol 1.; 1989.
38. Muto S, Takeda S, Oshima R. Analysis of Lattice Modulations in the Tweed Structure of an Fe-Pd Alloy by Image Processing of a High-Resolution Electron Micrograph. *Jpn J Appl Phys*. 1990;29(10):2066-2071.

39. Kartha S, Krumhansl JA, Sethna JP, Wickham LK. Disorder-driven pretransitional tweed pattern in martensitic transformations. *Phys Rev B*. 1995;52(2):803-822.
40. Tanaka Y, Kimura N, Hono K, Yasuda K, Sakurai T. Microstructures and magnetic properties of Fe-Pt permanent magnets. *J Magn Magn Mater*. 1997;170:289-297.
41. N.I. Vlasova, G.S. Kandaurovab, N.N. Shchegolevaa. *Effect of the Polytwinned Microstructure Parameters on Magnetic Domain Structure and Hysteresis Properties of the CoPt-Type Alloys*.; 2000. www.elsevier.com/locate/jmmm
42. Metauurgica S, Soffa WA. (Received July 28, 1993). 1994;30(6):683-688.
43. Ma Y, Ardell AJ. The (Gamma + Gamma')/Gamma' phase boundary in the Ni–Al phase diagram from 600 to 1200 °C. *Z Metallkd*. 2003;94(9):972-975.
44. Kleinerman NM, Serikov V V., Vlasova NI, Popov AG. Mössbauer study of structural inhomogeneities formed upon the FCC–L10 transformation in equiatomic FePd alloy from different initial states. *Philosophical Magazine*. 2018;98(26):2380-2396. doi:10.1080/14786435.2018.1487603
45. Chepulskii R V., Curtarolo S. Revealing low-temperature atomic ordering in bulk Co-Pt with the high-throughput ab-initio method. *Appl Phys Lett*. 2011;99(26). doi:10.1063/1.3671992
46. Pathak R, Golovnia OA, Gerasimov EG, et al. Ab initio study of the magnetic properties of possible phases in binary Fe-Pd alloys. *J Magn Magn Mater*. 2020;499. doi:10.1016/j.jmmm.2019.166266
47. Deshpande AR, Blachere JR, Wiezorek JMK. Texture evolution in combined reaction transformed equiatomic ferromagnetic L10-ordered FePd intermetallics. *Scr Mater*. 2006;54(5):955-960. doi:10.1016/j.scriptamat.2005.10.026
48. Deshpande AR, Xu H, Wiezorek JMK. Effects of grain size on coercivity of combined-reaction-processed FePd intermetallics. *Acta Mater*. 2004;52(10):2903-2911. doi:10.1016/j.actamat.2004.02.036
49. Deshpande AR, Wiezorek JMK. Magnetic age hardening of cold-deformed bulk equiatomic Fe-Pd intermetallics during isothermal annealing. *J Magn Magn Mater*. 2004;270(1-2):157-166. doi:10.1016/j.jmmm.2003.08.013
50. Xu H, Wiezorek JMK. Transmission electron microscopy of room temperature deformed polytwinned L10-ordered FePd. *Acta Mater*. 2004;52(2):395-403. doi:10.1016/j.actamat.2003.09.022
51. Matthew A. Steiner. *Strain-Induced Microstructural and Ordering Behaviors of Epitaxial Fe38.5Pd61.5 Films Grown by Pulsed Laser Deposition*. Doctor of Philosophy. University of Virginia; 2014.
52. Myagkov VG, Zhigalov VS, Bykova LE, Solov'ev LA, Bondarenko GN. Solid-phase synthesis of L10-FePd(001) epitaxial thin films: Structural transformations and magnetic anisotropy. *JETP Lett*. 2010;91(9):481-485. doi:10.1134/S0021364010090109
53. Issro C, Abes M, Pu¨schl W, et al. Atomic Ordering and Magnetism in L1 0 Ordered FePd Alloys. *Metallurgical and Materials Transactions A*. 2006;37A:3415-3422.
54. Kulovits AK, Leonard JP, Wiezorek JMK. Microstructure of pulsed laser deposited FePd thin films on amorphous and crystalline substrates. *Intermetallics (Barking)*. 2007;15(12):1606-1611. doi:10.1016/j.intermet.2007.06.015
55. Takata FM, Pattanaik G, Soffa WA, Sumodjo PTA, Zangari G. Synthesis of L10 Fe-Pd films by electrodeposition and thermal annealing. *Electrochem commun*. 2008;10(4):568-571. doi:10.1016/j.elecom.2008.01.041

56. Steiner MA, Comes RB, Floro JA, Soffa WA, Fitz-Gerald JM, Smentkowski VS. Strain induced microstructural and ordering behaviors of epitaxial Fe 38.5 Pd 61.5 films grown by pulsed laser deposition . *Journal of Vacuum Science & Technology A: Vacuum, Surfaces, and Films*. 2013;31(5):050824. doi:10.1116/1.4819376
57. Steiner MA, Comes RB, Floro JA, Soffa WA, Fitz-Gerald JM. L1′ ordering: Evidence of L10-L12 hybridization in strained Fe38.5Pd61.5 epitaxial films. *Acta Mater*. 2015;85:261-269. doi:10.1016/j.actamat.2014.11.036
58. Leroux C, Loiseau A, Broddin D, Tendeloo G Van. Electron microscopy study of the coherent two-phase mixtures L10 + L12 in Co-Pt alloys. *Philosophical Magazine B*. 1991;64(1):57-82.
59. Vetter E, Ghatwai P, Soffa W, Floro J. Evolution of First-Order Reversal Curves during Self-Assembly of the Co40.2Pt59.8 Nano-Chessboard Structure. *IEEE Magn Lett*. 2015;6:6-9. doi:10.1109/LMAG.2015.2480386
60. Geng LD, Soffa WA, Floro JA, Jin YM. Exchange coupling effects in Co-Pt nanochessboards. *J Appl Phys*. 2018;123(9):0-7. doi:10.1063/1.5019841
61. Member EFK, Hawig R. The Exchange-Spring Magnet: 1991;27(4):3588-3600.
62. Ghatwai P, Vetter E, Hrdy M, Soffa WA, Floro JA. Evolution of microstructure and magnetic properties in Co-Pt alloys bracketing the eutectoid composition. *J Magn Magn Mater*. 2015;375:87-95. doi:10.1016/j.jmmm.2014.09.054
63. Floro JA, Vetter EP, Ghatwai P, Geng LD, Jin YM, Soffa WA. Hierarchical structure and the origins of coercivity in exchange-coupled Co-Pt nanochessboards. *J Magn Magn Mater*. 2019;487(May). doi:10.1016/j.jmmm.2019.165313
64. Nosé Y, Kushida A, Ikeda T, Nakajima H, Tanaka K, Numakura H. Re-examination of phase diagram of Fe-Pt system. *Mater Trans*. 2003;44(12):2723-2731. doi:10.2320/matertrans.44.2723
65. Tanaka Y, Hisatsune K. Remanence enhancement based on L10 ordering in Fe-Pt permanent magnets. *J Appl Phys*. 2003;93(6):3435-3439. doi:10.1063/1.1555675
66. Watanabe K, Masumoto H. On the High-Energy Product Fe-Pt Permanent Magnet Alloys. *Transactions of the Japan Institute of Metals*. 1983;24(9):627-632.
67. Goto T, Utsugi H, Watanabe K. Effect of atomic order-disorder on57Fe hyperfine structure in Fe64Pt36alloy. *J Alloys Compd*. 1994;204(1-2):173-178. doi:10.1016/0925-8388(94)90087-6
68. Ghatwai P. Structure-Property Relationships in Ordered Co-Pt Alloys of Near- Eutectoid Compositions Accepted for the School of Engineering and Applied Science : Dean , School of Engineering and Applied Science. *Phd Dissertation*. 2015;(May).
69. Cantwell PR, Tang M, Dillon SJ, Luo J, Rohrer GS, Harmer MP. Grain boundary complexions. *Acta Mater*. 2014;62(1):1-48. doi:10.1016/j.actamat.2013.07.037
70. Cantwell PR, Frolov T, Rupert TJ, et al. Grain Boundary Complexion Transitions. Published online 2020. doi:10.1146/annurev-matsci-081619
71. Zhang J, Tasan CC, Lai MJ, Dippel AC, Raabe D. Complexion-mediated martensitic phase transformation in Titanium. *Nat Commun*. 2017;8. doi:10.1038/ncomms14210
72. Dillon SJ, Tang M, Carter WC, Harmer MP. Complexion: A new concept for kinetic engineering in materials science. *Acta Mater*. 2007;55(18):6208-6218. doi:10.1016/j.actamat.2007.07.029

73. Toby BH, Von Dreele RB. GSAS-II: The genesis of a modern open-source all purpose crystallography software package. *J Appl Crystallogr*. 2013;46(2):544-549. doi:10.1107/S0021889813003531
74. Bendersky LA, Gayle FW. *Electron Diffraction Using Transmission Electron Microscopy*. Vol 106. http://www.nist.gov/jres
75. Grundy PJ, Jones GA. *Electron Microscopy in the Study of Materials*. Paper Edition. Crane, Russak & Company, Inc. ; 1976.
76. Savovici A, Soffa WA, Floro JA. Direct evidence of the shockley tetragonal L1' phase in a bulk Fe-Pd alloy. *Scr Mater*. 2023;234:115540. doi:10.1016/j.scriptamat.2023.115540
77. Bragg WL, Williams EJ. The Effect of Thermal Agitation on Atomic Arrangement in Alloys. *Proceedings of the Royal Society A*. 1934;145(855):699-730. https://royalsocietypublishing.org/
78. Tanaka Y, Udoh KI, Hisatsune K, Yasuda K. Early stage of ordering in stoichiometric AuCu alloy. *Materials Transactions, JIM*. 1998;39(1):87-94. doi:10.2320/matertrans1989.39.87
79. Finel A, Ducastelle F. On the phase diagram of the fcc ising model with antiferromagnetic first-neighbour interactions. *Epl*. 1986;1(10):543. doi:10.1209/0295-5075/1/10/009
80. Bozorth RM, Davis DD, Wernick JH. . *J Phys Soc Japan*. 1962;17(112).
81. Fallot M. . *Ann Phys* . 1938;10(291).
82. Low GG. . In: *Proc. Intern. Conf. Magnetism*. Inst. Phys. Soc. London; 1964:133.
83. Saito H, Fujimori H. . *J Phys Soc Japan*. 1965;20(293).
84. Crangle J. . *Phil Mag*. 1960;5(335).
85. Laughlin DE, Soffa WA. The Third Law of Thermodynamics: Phase equilibria and phase diagrams at low temperatures. *Acta Mater*. 2018;145:49-61. doi:10.1016/j.actamat.2017.11.037
86. Von Ernst Raub, Hans Beeskow, Otto Loebich jr. Das Zustandsbild Eisen-Palladium unterhalb 950° C. *ZEITSCHRIFT FUR ,METALLKUNDE*. 1963;54(10):549-552.
87. Le Bouar Y, Loiseau A, Finel A. Origin of the complex wetting behavior in Co-Pt alloys. *Phys Rev B Condens Matter Mater Phys*. 2003;68(22). doi:10.1103/PhysRevB.68.224203
88. Le Bouar Y, Loiseau A, Finel A, Ducastelle F. Wetting behavior in the Co-Pt system. *Phys Rev B Condens Matter Mater Phys*. 2000;61(5):3317-3326. doi:10.1103/PhysRevB.61.3317
89. Desgranges C, Delhommelle J. Can Ordered Precursors Promote the Nucleation of Solid Solutions? *Phys Rev Lett*. 2019;123(19). doi:10.1103/PhysRevLett.123.195701
90. Soffa WA, Laughlin DE. Diffusional Phase Transformations in the Solid State. In: *Physical Metallurgy: Fifth Edition*. Vol 1. Elsevier Inc.; 2014:851-1020. doi:10.1016/B978-0-444-53770-6.00008-3
91. A.G. Khachaturyan. *Theory of Structural Transformations in Solids*. Courier Corporation; 2013.
92. Chen Y, Atago T, Mohri T. *First-Principles Study for Ordering and Phase Separation in the Fe-Pd System*. Vol 14.; 2002.
93. Nix FC, Shockley W. Order-Disorder Transformations in Alloys. *Review of Modern Physics*. 1938;10(1):1-71.
94. Putnis A, Salje E. Tweed microstructures: Experimental observations and some theoretical models. *Phase Transitions*. 1994;48:85-105.

95. Tanner LE, Wuttig M. *Workshop on First-Order Displacive Phase Transformations: Review and Recommendations*. Vol 127.; 1990.
96. 3iang, ' X, Wochner P, Moss SC, Zschack P. *Diffuse X-Ray Scattering Study of an Oxygen-Disordered Tetragonal YBa2(Cuo 955Alo 045) 307 Crystal*. Vol 67.; 1991.
97. Le Bouar Y, Loiseau A, Khachaturyan AG. Origin of chessboard-like structures in decomposing alloys. Theoretical model and computer simulation. *Acta Mater*. 1998;46(8):2777-2788. doi:10.1016/S1359-6454(97)00455-2
98. Ghatwai P, Vetter E, Hrdy M, Soffa WA, Floro JA. Evolution of microstructure and magnetic properties in Co-Pt alloys bracketing the eutectoid composition. *J Magn Magn Mater*. 2015;375(January):87-95. doi:10.1016/j.jmmm.2014.09.054
99. Saxena A, Wu Y, Lookman T, Shenoy SR, Bishop AR. Hierarchical pattern formation in elastic materials. *Physica A*. 1997;239:18-34.
100. Sands T, Suresh S, Wagner R, et al. *ELECTRON MICROSCOPY STUDY OF THE FORMATION OF Ni 5 Al 3 IN A Ni 62.5 Al 37.5 B2 ALLOY-I. PRECIPITATION AND GROWTH*. Vol 43.; 1995.
101. Epler M. Structures by Precipitation from Solid Solution. In: *Metallography and Microstructures*. ASM International; 2018:134-139. doi:10.31399/asm.hb.v09.a0003731
102. Khachaturyan AG, Shapiro SM, Semenovskaya S. *Adaptive Phase Formation in Martensitic Transformation*. Vol 43.; 1991.
103. Al-Ghaferi A, Müllner P, Heinrich H, Kostorz G, Wiezorek JMK. Elastic constants of equiatomic L10-ordered FePd single crystals. *Acta Mater*. 2006;54(4):881-889. doi:10.1016/j.actamat.2005.10.018
104. Epler M. Structures by Precipitation from Solid Solution. In: *Metallography and Microstructures*. ASM International; 2018:134-139. doi:10.31399/asm.hb.v09.a0003731
105. Seiner H, Plucinsky P, Dabade V, Benešová B, James RD. *Branching of Twins in Shape Memory Alloys Revisited*.; 2020. https://www.sciencedirect.com/science/article/pii/S0022509620301964
106. Skomski R, Kashyap A, Zhou J. Atomic and micromagnetic aspects of L10 magnetism. *Scr Mater*. 2005;53(4):389-394. doi:10.1016/j.scriptamat.2005.04.036
107. Ni Y, Rao W, Khachaturyan AG. Pseudospinodal mode of decomposition in films and formation of chessboard-like nanostructure. *Nano Lett*. 2009;9(9):3275-3281. doi:10.1021/nl901551j
108. Ivanov YP, Sarac B, Ketov S V., Eckert J, Greer AL. Direct Formation of Hard-Magnetic Tetrataenite in Bulk Alloy Castings. *Advanced Science*. 2023;10(1). doi:10.1002/advs.202204315
109. Kovács A, Lewis LH, Palanisamy D, et al. Discovery and Implications of Hidden Atomic-Scale Structure in a Metallic Meteorite. *Nano Lett*. 2021;21(19):8135-8142. doi:10.1021/acs.nanolett.1c02573
110. Montes-Arango AM, Marshall LG, Fortes AD, et al. Discovery of process-induced tetragonality in equiatomic ferromagnetic FeNi. *Acta Mater*. 2016;116:263-269. doi:10.1016/j.actamat.2016.06.050
111. Vernyhora I V., Tatarenko VA, Bokoch SM. Thermodynamics of f.c.c.-Ni–Fe Alloys in a Static Applied Magnetic Field. *ISRN Thermodynamics*. 2012;2012:1-11. doi:10.5402/2012/917836
112. Wang J, Hirayama Y, Liu Z, et al. Massive transformation in FeNi nanopowders with nanotwin-assisted nitridation. *Sci Rep*. 2022;12(1). doi:10.1038/s41598-022-07479-8

113. Jensen WA. *Hierarchical Engineering of Microstructural Lengthscales in Fe-Si Based Alloys to Minimize Thermal Conductivity for Thermoelectric Applications*. University of Virginia; 2018.
114. Soisson F, Fu CC, Nastar M, Agostini P. Report on the kinetic model of Fe-Ni-Cr implemented in the AKMC simulations Description of the activities: Report on the kinetic model of Fe-Ni-Cr implemented in the AKMC simulations.
115. Bordeaux N, Montes-Arango AM, Liu J, Barmak K, Lewis LH. Thermodynamic and kinetic parameters of the chemical order-disorder transformation in L10 FeNi (tetrataenite). *Acta Mater*. 2016;103:608-615. doi:10.1016/j.actamat.2015.10.042
116. Osaka K, Sakaki D, Takama T. In situ X-ray measurement of order-disorder transition temperature of Fe-rich Fe-Pt alloys. *Japanese Journal of Applied Physics, Part 2: Letters*. 2002;41(2 A). doi:10.1143/JJAP.41.L155